2018

Hierarchical Corannulene-Based Materials

Allison M. Rice
University of South Carolina - Columbia

HIERARCHICAL CORANNULENE-BASED MATERIALS

by

Allison M. Rice

Bachelor of Science
Westminster College, 2014

Submitted in Partial Fulfillment of the Requirements

For the Degree of Doctor of Philosophy in

Chemistry

College of Arts and Sciences

University of South Carolina

2018

Accepted by:

Natalia B. Shustova, Major Professor

Aaron K. Vannucci, Committee Member

Linda S. Shimizu, Committee Member

Peisheng Xu, Committee Member

Cheryl L. Addy, Vice Provost and Dean of the Graduate School

DEDICATION

This dissertation and journey through graduate school is dedicated to my family. My parents, Paul an Diane Rice, have not only been extremely supportive throughout my life, but have always stressed the importance of education. Being able to look up to my parents, who are both in academia, hard-working attitudes has been a great inspiration for me to follow in their footsteps. They have sacrificed so much to provide the best life and education for my twin sister and I, and for this, I am forever grateful. My twin sister, Julie, also has not only been with me for every accomplishment and failure, but has supported me, pushed me, and always loved me. I do not know what I would have done during the tough times in graduate school without her amazing counsel and love. I am also grateful to all of my friends, and my loving boyfriend, Jeffrey DeLuca, who have always shown great support and understanding. The most thanks, though, goes to my Lord and Savior, Jesus Christ, who paid the ultimate sacrifice to give me this life and provided strength and hope during all occasions.

ACKNOWLEDGEMENTS

First and foremost, I would like to thank my major advisor, Dr. Natalia Shustova for her unwavering support and mentorship throughout my time at the University of South Carolina. She not only pushed and challenged me, but truly cared about my success as a graduate student and as a person overall. Thank you for teaching me so much, and for giving me so many great opportunities. I am so grateful to call you my advisor, and I know that we will always be in touch. I would also like to thank the members of my committee: Dr. Vannucci, Dr. Shimizu, Dr. Xu, and Dr. Padak. You were always there to answer questions and provide guidance to me.

A huge thank you is also necessary for my coworkers, both past and present. Derek Williams, as the first graduate student in Dr. Shustova's lab, you had paved the way of success for me, in addition to your great mentorship and friendship. I am also very grateful for the scientific help from Ekaterina Dolgopolova, because without her, I would have struggled very much in many cases. Thank you to Brett Fellows, Otega Ejegbavwo, Brandon Yarbrough, Gabrielle Leith, Corey Martin, and Richard Ly as well for their constant help and support throughout this journey. You all have made this journey such a great experience, and I am blessed to call you lifelong friends.

ABSTRACT

Merging the intrinsic properties of fullerene (buckyball) and corannulene (buckybowl) derivatives with the inherent properties of crystalline metal- and covalent-organic frameworks (MOFs and COFs), including their modularity, porosity, versatility, high surface area, and structural tunability, opens a pathway to unlock a novel class of fulleretic materials. Despite the great interest in MOFs and COFs, as well as fullerene derivatives, this dissertation is focused on crystalline fullerene- and corannulene-containing frameworks, highlighting their potential contributions in the fields of optoelectronic devices, electrodes, and photosensitizers. We have revealed a dual role of fullerene- and corannulene-containing building blocks showing their versatility to act as either a framework linker or a guest inside the pores. The work presented within the following six chapters is focused on the design, synthesis, and characterization of corannulene and fullerene-based MOFs and COFs that target fundamental understanding of ET processes in predesigned pathways, charge transfer processes, and the ability to tune the electronic structures of novel materials. Overall, this work encompasses a rising new field in which fulleretic crystalline frameworks are not only structural and synthetic masterpieces but also valuable potential materials to the ever-expanding technological landscape.

TABLE OF CONTENTS

LIST OF TABLES

LIST OF FIGURES

LIST OF SCHEMES

CHAPTER 1

FULLERETIC MATERIALS: BUCKYBALL- AND BUCKYBOWL-BASED CRYSTALLINE FRAMEWORK

Rice, A. M.; Dolgopolova, E. A.; Shustova, N. B. *Chem. Mater*. **2017**, *29*, 7054.

Because of recent advances in fullerene and corannulene chemistry,[1–9] unlocking the potential of these compounds has become feasible for the practical world. Corannulene, $C_{20}H_{10}$, the smallest curved subunit of fullerene, C_{60} (Figure 1.1), is otherwise known as a buckybowl, similar to the fullerene buckyball.

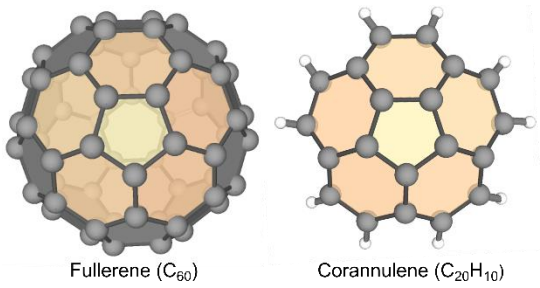

Figure 1.1. Molecular structures of (left) fullerene, C_{60}, and (right) corannulene, $C_{20}H_{10}$.

The curved molecular shape of both buckyballs and buckybowls has led to unique electronic properties in comparison with planar polyaromatic hydrocarbons.[7,10,11] For instance, fullerene C_{60} has a triply degenerate lowest unoccupied molecular orbital (LUMO) and has the ability to stabilize six electrons on its surface, forming a stable hexaanion.[4,12] Because of the low-lying LUMO, fullerene derivatives are commonly applied as electron acceptors.[13–16] For instance, [6,6]-phenyl-C_{61}-butyric acid methyl ester (PCBM) is one of the most explored acceptors for development of bulk heterojunction solar cells.[13,17,18] Along with their superior electron-accepting properties, fullerene and its derivatives are known for ultrafast electron/energy transfer (ET),[14,19,20] which in combination with high electron mobility[21] makes buckyballs attractive candidates for molecular electronics development. The appeal to use fulleretic materials as components for optoelectronic devices also stems from their broad absorption profile and exceptional thermal stability (up to 500 °C).[22–26] Another attractive aspect of

fullerene derivative utilization is their singlet oxygen sensitizing potential.[27] Furthermore, fullerene and its compounds could also be employed to prepare superconductive materials through doping with alkali metals.[22,28] In contrast to buckyballs, properties of corannulene and its derivatives are less studied, despite early discovery,[1,29] mainly because of synthetic challenges. For instance, the first reported wet synthesis of $C_{20}H_{10}$ included 17 steps.[1,29] Corannulene has a doubly degenerate LUMO, allowing it to accept up to four electrons forming a stable tetraanion, which makes it more electron rich per carbon atom than C_{60} (one e− per five C atoms in $C_{20}H_{10}$ vs one e− per 10 C atoms in C_{60}).[13,30−32] Decoration of the buckybowl with perfluoroalkyl chains resulted in corannulene derivatives possessing even better electron-accepting properties than C60.[33,34] In comparison with the more traditional flat aromatic hydrocarbons, buckybowls (e.g., corannulene) and their derivatives (i) possess a significant dipole moment, (ii) provide the possibility to extend the material dimensionality through their nonplanar surface, and (iii) exhibit the potential for effective charge transport.[35−37] Corannulene also forms aggregates with various alkali metals.[31,38,39] For instance, five Li+ cations can be sandwiched between two corannulene tetraanions.[31] Corannulene exhibits a high reversible lithium capacity (602 mAh/g) compared to that of the commonly used graphite material (372 mAh/g),[40,41] which foreshadows the usage of corannulene containing derivatives for anode material development. In addition, there are photophysical studies which revealed the possibility to employ corannulene compounds for the development of organic light-emitting diodes.[42] For this dissertation, we intended to survey, synthesize and study crystalline fulleretic materials, in particular, fullerene- and corannulene-containing metal- and covalent-organic frameworks, i.e., MOFs and COFs. Although

there is great interest in fulleretic supramolecular assemblies,[22,43–49] as well as unique curved molecules, there are not many reports, to the best of our knowledge, specifically highlighting crystalline fulleretic self-assembled materials. There are reviews which include fulleretic hybrid complexes, polymers, dimers, and hybrid frameworks, but the purpose of this dissertation is to highlight the unique nature of fullerene and corannulene-based MOFs and COFs, the challenges to overcome, and the potential for their impact to science, technology, and society.[45,49] Comprehensive review articles on molecular derivatives of buckyballs and buckybowls have been published elsewhere.[4,7,10] Ultimately, this perspective is the first view on the possibility to merge the intrinsic properties of buckyballs and buckybowls with the inherent properties of MOFs and COFs, such as crystallinity, porosity, high surface areas, and structural tunability to unlock new avenues for development of materials with unprecedented electronic behavior. The initial challenge in engineering fulleretic materials lies in the realm of preparation of corannulene- or fullerene-containing building blocks on a scale required for not only material synthesis but also their comprehensive analysis. However, many synthetic procedures reported only preparation of sub-milligram quantities of the buckyball and buckybowl derivatives. In addition, for covalent bond formation occurring in MOF or COF synthesis, the core of interest should be modified with anchors (e.g., carboxylic or pyridyl groups).[50–54] Therefore, another challenge, for instance, in the case of the fullerene building blocks, has arisen due to the possibility of the formation of a large number of isomers (there are 30 C=C double bonds in C_{60} that can be reactive). As a result, high performance liquid chromatography (HPLC)[55] is typically used for isomer separation, especially in the case of a large number of addends on the cage (e.g., > 4),

which also limits the compound quantity available for material preparation. However, recent advances in corannulene synthesis make preparation of its derivatives more feasible even on a kilogram scale.[7] Fullerene and corannulene derivatives as linkers for development of crystalline fulleretic materials will be discussed first. Although almost any type of organic molecules with coordinating functional groups has the potential for self-assembly with metal centers to form a hybrid framework,[50] the work done to date with fulleretic MOFs has only utilized pyridyl and carboxylate anchors (Figure 1.2).[20,55−61]

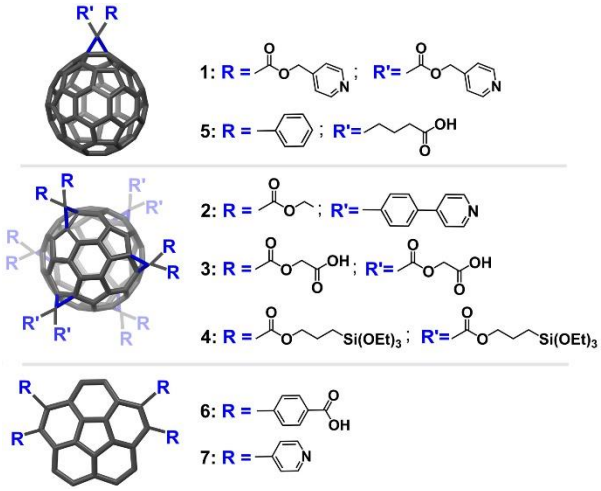

Figure 1.2. Fullerene- and corannulene-based linkers.

In 2007, Schröder and co-workers reported the first example of a chain coordination polymer using a dipyridyl-functionalized fullerene ligand (**1**, Figure 1.2), in which the control of mutual fullerene orientations was achieved through coordination to silver cations.[56] In 2013, Echegoyen and co-workers have also utilized coordination to silver cations as a way to form a fullerene-based framework.[62] An approach combining Krautler¨'s synthetic method with a Bingel-Hirsch reaction for preparation of the trans-1

hexakis-fullerene precursor in a very high yield was developed first[62] in order to prepare a novel hexakis-fullerene derivative **2** (Figure 1.2).[57] This linker containing two phenyl pyridyl groups (2) was employed to make the first example of a two-dimensional (2D) fullerene-linked MOF through coordination to Cd^{2+} (Figure 1.3).[57]

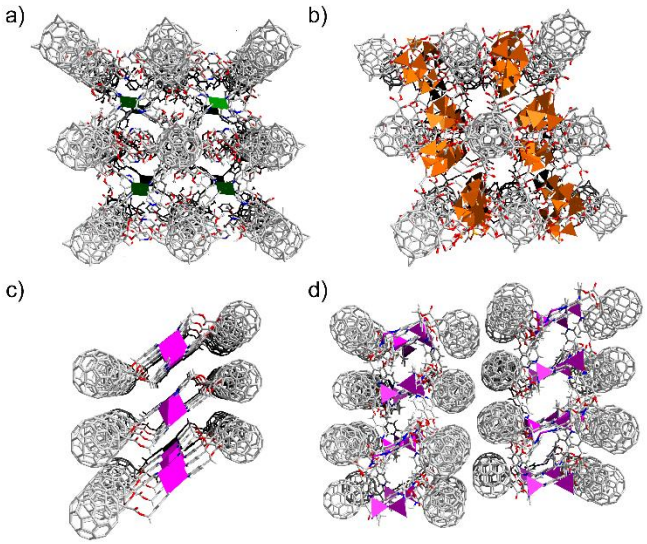

Figure 1.3. Crystal packing of fullerene-linked: (a) two-dimensional $Cd(\mathbf{2})_2(NO_3)_2$; (b) three-dimensional $(Zn_4O)_2(\mathbf{3})$; (c) a molecular complex $Ag(\mathbf{1})_2(PF_6)$; and (d) two-dimensional $Ag_2(\mathbf{1})_2(PF6)_2$. Green, orange, purple, gray, red, and blue spheres represent Cd, Zn, Ag, C, O, and N, respectively. Solvent molecules and hydrogen atoms were omitted for clarity.

Later, Shustova and co-workers used a pyridyl-based fullerene linker (1) to demonstrate its flexibility in the formation of a molecular complex and a 2D coordination framework through silver coordination (Figure 1.3c, d).[55] Beuerle and co-workers synthesized a fullerene-containing linker through decoration of C60 with 12 functional groups (3) as shown in Figure 2 to make a 3D framework through coordination with zinc

cations.[58] In this case, the high connectivity of the linker allows formation of a new inversely cross-linked framework since the number of coordination sites in the ligand surpasses the connectivity of the metal centers (Figure 1.3b).[58] This approach opens the opportunity to design materials with coordination modes of high nuclearity, and the possibility to stabilize a reactive coordination environment, which could lead to their usage in fields ranging from sensing to catalysis.[58] Because of the superior electron-accepting properties of fullerene and necessity of precise donor−acceptor alignment, MOFs can be used as a platform to control donor−acceptor morphology at the nanoscale level. Achievement of such donor−acceptor alignment is crucial for excitonic device performance for efficient energy/charge transfer due to possible effects on the distance of exciton diffusion, π−π stacking, or Förster radius.[55,63] Formation of fullerene stacks can also lead to enhancement of solar cell efficiency as opposed to nonstacking fullerene derivatives.[64] Using a pyridyl-based fullerene linker (**1**, Figure 1.2), Shustova and co-workers have developed the first example of a crystalline metal−donor− fullerene framework where the porphyrin (donor)−fullerene (acceptor) mutual orientation was controlled through metal coordination.[55] Figure 1.4 shows the donor-fullerene crystalline hybrids, which are organized in a way that 2D porphyrin containing layers act as donors for coordinately immobilized fullerene-based acceptors.[55]

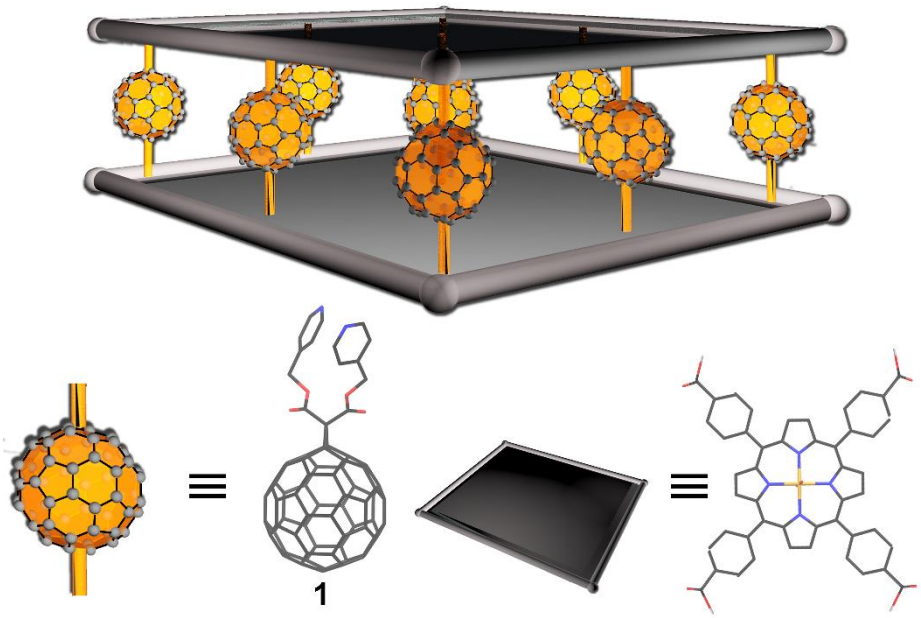

Figure 1.4. Schematic representation of donor/acceptor MOF.

On the basis of time-resolved spectroscopic studies of the donor-fullerene MOFs, we found the estimated rate constant of Förster resonance energy transfer (FRET) to be 49.5%.[55] These studies foreshadow a pathway to control active layer morphology of organic photovoltaics at the nanoscale level. Another possible way for fullerene coordinative immobilization inside the crystalline frameworks is postsynthetic coordination of fullerene derivatives to the metal nodes. This approach was successfully demonstrated by Farha and coworkers using a robust Zr-based MOF (NU-1000, Figure 1.5) as a platform for coordinative immobilization of [6,6]-Phenyl-C_{61}- butyrate (PCBA = 5, Figure 1.5), i.e., through postsynthetical binding of 5 to the metal node.[59] The prepared fullerene-containing hybrid could be utilized as a photosensitizer for oxidation of sulfur mustard, a powerful blistering agent employed as a chemical weapon.[59]

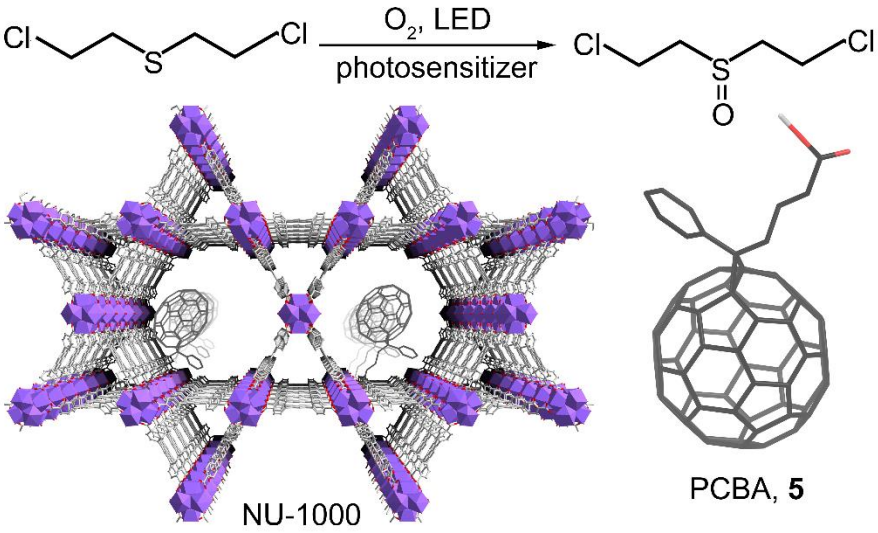

Figure 1.5. (Top) Selective oxidation of sulfur mustard to bis(2-chloroethyl)sulfoxide using the photosensitizer NU-1000-PCBA. (Bottom, left) Schematic representation of PCBA inside the NU-1000 framework. Purple, gray, and red spheres represent Zr, C, and O, respectively. Hydrogen atoms were omitted for clarity. (Bottom, right) Molecular structure of PCBA (**5**).

The use of **5** in this system is vital due to the fact that fullerene derivatives possess a high quantum yield of singlet oxygen generation.[27] Thus, in addition to utilization of fullerene-based frameworks for optoelectronics development, this work revealed the potential for fulleretic materials in the fields of defense and security. Development of crystalline fulleretic materials is not only limited to metal-coordination. Recently, Bein and co-workers reported a well-defined covalent fullerene-containing framework with high porosity through preparation of 4 (Figure 1.2).[60] Notably, fullerene decoration with 12 functional groups in 4 resulted in a drastic decrease of electron mobility, which is in line with previous reports[65,66] concluding that mobility decreases with an increase in intermolecular fullerene distance. As expected, the crystalline framework, prepared by template directed self-assembly, possesses different electronic properties in comparison with unmodified fullerene.[60] Furthermore, the authors reported

that the prepared fulleretic material has a dielectric constant lower than that of the nonporous precursor.[60]

As mentioned above, the recent advances in buckybowl synthesis have allowed a drastic shift for corannulene from a molecule of interest to a candidate for material development. In 2016, Shustova and co-workers performed the first attempt to merge the structural modularity and porosity of MOFs with the intrinsic properties of π-bowls through development of a porous, crystalline corannulene-based material.[61] For that, the corannulene core was modified with four carboxyl groups (6) as shown in Figure 1.2, in which coordination to zinc cations led to the formation of a 2D framework.[61] Preparation of this material allowed, for the first time, to shed light on time-resolved solid-state photophysics of corannulene-based compounds. The performed studies demonstrated that the quantum yield of the prepared corannulene-based MOF is higher than that of parent corannulene.[61] The same corannulene linker 6 was utilized to probe coordination with other metals such as cadmium, which resulted in the formation of a three-dimensional framework.[20] Interestingly, the curvature of the corannulene bowl remains intact inside all reported corannulene-based MOFs, which provides an opportunity to extend MOF dimensionaility[20,61] for applications such as molecular recognition,[67–69] alkali-metal intercalation,[31,39] or separation (Figure 1.6).[70] Those studies are in line with the fascinating report by Petrukhina and co-workers who described preparation of a corannulene "sandwich" intercalated with lithium.[31] Similarly, corannulene-containing frameworks could be considered as an extended "baguette" for alkali-metal intercalation.

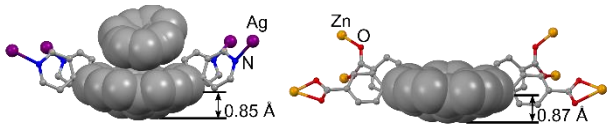

Figure 1.6. (Left) Part of the 2D silver MOF made of 7 and (right) a part of the 2D zinc MOF made of 6, showing the bowl depth of the corresponding corannulene-based derivatives. Purple, yellow, gray, blue, and red spheres represent Ag, Zn, C, N, and O, respectively. Hydrogen atoms were omitted for clarity.

The same tetrabromocorannulene utilized for preparation of 6 was employed for preparation of a pyridyl-containing corannulene derivative (**7**, Figure 1.2).[20] Compound **7** was dually used for both the synthesis of (i) a 2D silver-based MOF and (ii) a donor−acceptor framework. The latter one was explored to study the possibility of FRET in the system through utilization of a two-step synthetic approach, in which a 2D porphyrin-based layered MOF was synthesized first, followed by the immobilization of a new corannulene-based derivative as a pillar.[20] Time-resolved photoluminescence spectroscopy along with spectral overlap function calculations were used to probe the possibility of FRET in the prepared scaffold.[20] As a result, the ET efficiency and rate constant were found to be 85% and 1.01×10^9 s^{-1} , receptively.[20] The reported findings were not only the first time-resolved photophysical studies performed for corannulene-containing materials in the solid state, but they also demonstrated the possibility to achieve a very high ligand-to-ligand ET efficiency in corannulene-containing MOFs.[20] Interestingly, this ligand-to-ligand ET efficiency is 1.7 fold higher than that in a fullerene-porphyrin hybrid material,[55] which could foretell the use of corannulene-based materials molecular electronics development.

Because of MOF porosity, fulleretic materials can be engineered through incorporation of fullerene (or corannulene) and their derivatives as a guest inside the framework while maintaining structural integrity. In 2002, Boyd and co-workers realized this approach and demonstrated that C_{60} can be included as a guest into a 2D framework consisting of tetra-4- pyridylporphyrin linkers connected through lead cations (Figure 1.7).[71]

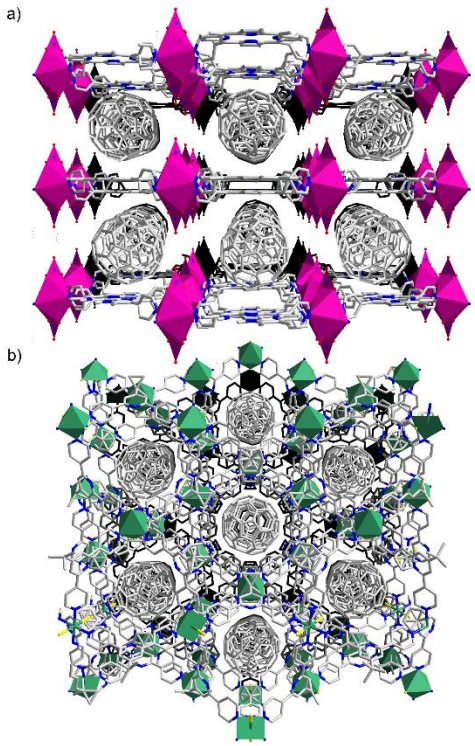

Figure 1.7. Crystal packing in two templated fullerene MOFs: (a) C_{60}@Pb(tetra-4-pyridylporphyrin)$(NO_3)_2$ and (b) C_{60}@3[Ni(4′-tert-butyl4,2′:6′,4″-terpyridine)$_2Cl_2$], respectively. Green, purple, gray, blue, and yellow spheres represent Ni, Pb, C, N, and Cl, respectively. Solvent molecules and hydrogen atoms were omitted for clarity.

In 2004, Yaghi and co-workers were able to monitor inclusion of fullerene C_{60} inside a 3D MOF (MOF-177) through distinct color change of the corresponding framework.[72] In 2012, Zampese and co-workers extended the Boyd's approach to use fullerene as a template for MOF formation (Figure 1.7).[73] As mentioned earlier, fulleretic materials can be utilized to engineer an active layer in organic photovoltaics because of the control of the donor−acceptor alignment, and therefore, morphology at the nanoscale level. Allendorf and co-workers demonstrated this concept by using MOF-177 for incorporation of guests α,ω-dihexylsexithiophene (DH6T) and [6,6]- phenyl-C_{61}-butyric acid methyl ester (PCBM, Figure 1.8).[74]

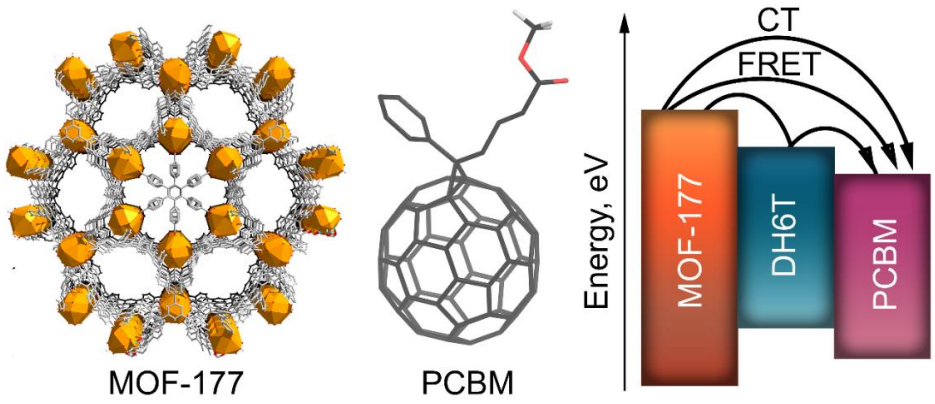

Figure 1.8. (Left) Crystal packing in MOF-177. Orange, gray, and red spheres represent Zr, C, and O, respectively. Hydrogens atoms were omitted for clarity. (Middle) Molecular structure of PCBM. (Right) MOF-177, DH6T, and PCBM band alignment illustrating possibility of energy transfer and charge transfer from the excited linker of MOF177 to incorporated DH6T and PCBM. Adapted with permission from ref 74. Copyright 2014 Royal Society of Chemistry.

The initial studies of ET processes in this designed material show that in the instance of MOF linker excitation, FRET is a possible pathway of ET between the framework and DH6T, while either energy or electron transfer could occur between the MOF and

PCBM.[74] It is possible for DH6T to have a dual role, behaving as an acceptor for MOF-177 and a donor for PCBM, which promotes ET.[74] This example is one of pioneering findings, demonstrating the fulleretic MOF-based materials could be applied for construction of the active layer morphology in organic photovoltaics, and therefore foreshadows a pathway for turning these conceptual studies into a reality.

Since the inception of fulleretic MOFs (and COFs), there have been great strides in novel topologies with unique electronic or physicochemical properties as highlighted in this perspective, but their widespread implementation into device components would require a fundamental shift from synthetic marvels to applicable materials. One of the first challenges, which should be overcome for their practical utilization and mass production, is the low-cost and high-throughput preparation of fulleretic building blocks. Although there has been recent progress, especially in corannulene chemistry,[4,7] its synthesis still relies on a labor-demanding multiple-step procedure. Despite the synthetic challenge, fullerene derivatives offer high thermal stability (>500 °C), possibility for ultrafast charge transfer, opportunity for guest inclusion (endohedral metallofullerenes), charge stabilization due to their unique curvature, and tunability of electron-accepting properties through cage derivatization, which in combination with the crystallinity, porosity, high surface areas, and structural tunability of MOFs (or COFs), provides an appealing prospect for material engineering.[14,19,22–26,31,33,34,55,63] For instance, combination of the unique electron-accepting properties of fullerene derivatives with a controllable and self-assembled process for their alignment with donor molecules through MOF formation provides an opportunity to control active layer morphology in organic photovoltaics at the nanoscale level. Furthermore, well-defined structures of fulleretic

MOFs could facilitate directional charge transport, and therefore, could significantly affect device performance.[64] As mentioned in more detail throughout this perspective, several attempts toward this direction have already been perfomed.[20,55,74] Because of the porous nature, frameworks can act as a host for fullerene inclusion and, for instance, serve as a platform for dispersing endohedral metallofullerenes and steering their electron spin.[76] For example, such endometallofullerene integration inside the rigid matrix can be utilized toward high-density data storage. Another rational to pursue investigations in the field of endometallofullerenes incorporated inside MOFs or COFs could lie in the realm of their possible applications in the medicine sector: for instance, delivery and controlled (and simultaneous) release of multiple drugs or drug grafted on the surface of endohedral metallofullerenes; the latter of which will act as magnetic resonance imaging (MRI) contrast agents.[77] Studies of fulleretic materials can also lead to development of MOF-based stationary phases, i.e., adsorbents for column chromatography applicable for efficient separation of hardly accessible isomers of higher fullerenes (C2n, n > 35) because of the tunability of MOF pore aperture in conjunction with wall derivatization. Furthermore, fullerene-containing MOFs can be also applied in a completely different field as efficient photosensitizers for oxidation of powerful blistering agents employed as a chemical weapon.[59] Although the properties of corannulene and its derivatives are less studied, there has been a recent surge in studies of its photophysical properties, specifically in the solid state.[20,61] Those studies are driven by the attractive outlook for utilization of corannulene-based derivatives in a wide number of applications ranging from solar cells to photocatalysts. The first attempts highlighted herein demonstrated that corannulene-based building blocks can be used for development of materials with

efficient energy transfer.[20] Because the curvature of the corannulene bowl remains intact inside recently reported corannulene-based MOFs,[20,61] it provides an opportunity to extend MOF dimensionality and thereby, to enhance possibilities for guest separation or extraction. Therefore, MOF porosity and tunability relies on a size exclusion effect, whereas corannulene integration offers the additional "bowl recognition effect", which expands the opportunity for guest separation, sensing, and sequestration. Despite the wide variety of the mentioned directions, there are a number of obstacles that must be overcome to harness the full potential of fulleretic frameworks. In addition to the synthetic aspect mentioned above, fulleretic materials should also be easily processable in the form of thin films. Because MOFs are typically grown as single crystals or polycrystalline powders, thin film production is an ongoing effort in the MOF area. Finally, integration of the obtained fulleretic materials into a device is a tough feat in itself, requiring utilization of a multidisciplinary approach. Thus, the attractive prospective for utilization of fulleretic materials described above is just a very promising start.

Through merging the intrinsic properties of buckyball and buckybowl-based derivatives with the inherent properties of MOFs and COFs, such as their modularity, porosity, versatility, high surface area, and structural tunability, there lies the potential to open a new class of fulleretic materials with a broad range of applications. Although there has been paramount interest in MOFs (or COFs) and fullerene/corannulene derivatives, this perspective is the first account highlighting solely crystalline fullerene- and corannulene-containing frameworks, as a novel and almost unexplored class of materials. The dual use of the fullerene- and corannulene-containing building blocks as

either a framework linker or a guest inside the pores, demonstrates multiple facets for their exploration, which could lead to great promise for its implementation into materials for applications ranging from optoelectronics to batteries. The ability to use fulleretic materials as building blocks in these hierarchical assemblies has been fueled by the prominent advances in the syntheses of both fullerene and corannulene since their first development, allowing for their growth beyond just molecules of interest to ones that could be feasible for direct applications in materials. Overcoming the synthetic challenges of these molecules paired with the almost unparalleled growth of the MOF community, has contributed to the knowledge of rationally designing frameworks able to incorporate curved molecules, such as buckyballs and buckybowls, as highlighted in this perspective. Although these materials show abundant potential, the shift from more conventional studies investigating new synthetic routes and topologies to tailored design for specific applications, is still in its rudimentary phases. Both the opportunities and challenges of the surveyed materials are illustrative of the direction this field is going in order to match the continuing interest and ever-changing technological landscape.

REFERENCES

(1) Barth, W. E.; Lawton, R. G. *J. Am. Chem. Soc*. **1966**, *88*, 380−381.

(2) Kroto, H. W.; Heath, J. R.; O'Brien, S. C.; Curl, R. F.; Smalley, R. E. *Nature* **1985**, *318*, 162.

(3) Scott, L. T.; Hashemi, M. M.; Meyer, D. T.; Warren, H. B. *J. Am. Chem. Soc*. **1991**, *113*, 7082−7084.

(4) Wu, Y.; Siegel, J. S. *Chem. Rev*. **2006**, *106*, 4843−4867.

(5) Hirsch, A. *The Chemistry of Fullerenes*; Wiley−VCH: Weinheim, Germany, 2008.

(6) *Fragments of Fullerenes and Carbon Nanotubes: Designed Synthesis, Unusual Reactions, and Coordination Chemistry*; Petrukhina, M. A., Scott, L. T., Eds.; Wiley−VCH: Weinheim, Germany, 2011.

(7) Butterfield, A. M.; Gilomen, B.; Siegel, J. S. *Org. Process Res. Dev*. **2012**, *16*, 664−676.

(8) Yan, W.; Seifermann, S. M.; Pierrat, P.; Brase, S. *Org. Biomol. Chem*. **2015**, *13*, 25−54.

(9) Karunathilake, A. A. K.; Thompson, C. M.; Perananthan, S.; Ferraris, J. P.; Smaldone, R. A. *Chem. Commun*. **2016**, *52*, 12881−12884.

(10) Li, X.; Kang, F.; Inagaki, M. *Small* **2016**, *12*, 3206−3223.

(11) Oshima, H.; Fukazawa, A.; Yamaguchi, S. *Angew. Chem., Int. Ed*. **2017**, *56*, 3270−3274.

(12) *Buckminsterfullerenes*; Billups, E. W., Ciufolini, M. A., Eds.; Wiley−VCH: Weinheim, Germany, 1993.

(13) Liu, T.; Troisi, A. *Adv. Mater*. **2013**, *25*, 1038−1041.

(14) Li, C.-Z.; Yip, H.-L.; Jen, A. K.-Y. *J. Mater. Chem*. **2012**, *22*, 4161−4178.

(15) Troshin, P. A.; Hoppe, H.; Renz, J.; Egginger, M.; Mayorova, J. Y.; Goryachev, A. E.; Peregudov, A. S.; Lyubovskaya, R. N.; Gobsch, G.; Sariciftci, N. S.; Razumov, V. F. *Adv. Funct. Mater*. **2009**, *19*, 779−788.

(16) Wessendorf, C. D.; Eigler, R.; Eigler, S.; Hanisch, J.; Hirsch, A.; Ahlswede, E. *Sol. Energy Mater. Sol. Cells* **2015**, *132*, 450−454.

(17) Dang, M. T.; Hirsch, L.; Wantz, G. *Adv. Mater*. **2011**, *23*, 3597−3602.

(18) Chen, D.; Nakahara, A.; Wei, D.; Nordlund, D.; Russell, T. P. *Nano Lett*. **2011**, *11*, 561−567.

(19) Sukegawa, J.; Schubert, C.; Zhu, X.; Tsuji, H.; Guldi, D. M.; Nakamura, E. *Nat. Chem*. **2014**, *6*, 899−905.

(20) Rice, A. M.; Fellows, W. B.; Dolgopolova, E. A.; Greytak, A. B.; Vannucci, A. K.; Smith, M. D.; Karakalos, S. G.; Krause, J. A.; Avdoshenko, S. M.; Popov, A. A.; Shustova, N. B. *Angew. Chem., Int. Ed*. **2017**, *56*, 4525−4529.

(21) *Handbook of Nanophysics: Clusters and Fullerenes*; Sattler, K. D., Ed.; CRC Press: Boca Raton, FL, 2010.

(22) Diederich, F.; Gomez-Lo´ pez, M. *Chem. Soc. Rev*. **1999**, *28*, 263−277.

(23) Giacalone, F.; Martín, N. *Chem. Rev*. **2006**, *106*, 5136−5190.

(24) Diederich, F.; Thilgen, C. *Science* **1996**, *271*, 317−324.

(25) Kareev, I. E.; Shustova, N. B.; Kuvychko, I. V.; Lebedkin, S. F.; Miller, S. M.; Anderson, O. P.; Popov, A. A.; Strauss, S. H.; Boltalina, O. V. *J. Am. Chem. Soc*. **2006**, *128*, 12268−12280.

(26) Shustova, N. B.; Kuvychko, I. V.; Peryshkov, D. V.; Whitaker, J. B.; Larson, B. W.; Chen, Y.-S.; Dunsch, L.; Seppelt, K.; Popov, A. A.; Strauss, S. H.; Boltalina, O. V. *Chem. Commun*. **2011**, *47*, 875−877.

(27) Prat, F.; Martí, C.; Nonell, S.; Zhang, X.; Foote, C. S.; Gonzalez´ Moreno, R.; Bourdelande, J. L.; Font, J. *Phys. Chem. Chem. Phys*. **2001**, *3*, 1638−1643.

(28) Iwasa, Y. *Nature* **2010**, *466*, 191−192.

(29) Lawton, R. G.; Barth, W. E. *J. Am. Chem. Soc*. **1971**, **93**, 1730−1745.

(30) Xie, Q.; Perez-Cordero, E.; Echegoyen, L. *J. Am. Chem. Soc*. **1992**, *114*, 3978−3980.

(31) Zabula, A. V.; Filatov, A. S.; Spisak, S. N.; Rogachev, A. Y.; Petrukhina, M. A. *Science* **2011**, *333*, 1008−1011.

(32) Guldi, D. M. *Chem. Commun*. **2000**, 321−327.

(33) Kuvychko, I. V.; Spisak, S. N.; Chen, Y.-S.; Popov, A. A.; Petrukhina, M. A.; Strauss, S. H.; Boltalina, O. V. *Angew. Chem., Int. Ed*. **2012**, *51*, 4939−4492.

(34) Kuvychko, I. V.; Dubceac, C.; Deng, S. H.; Wang, X. B.; Granovsky, A. A.; Popov, A. A.; Petrukhina, M. A.; Strauss, S. H.; Boltalina, O. V. *Angew. Chem., Int. Ed*. **2013**, *52*, 7505−7508.

(35) Zoppi, L.; Martin-Samos, L.; Baldridge, K. K. *Phys. Chem. Chem. Phys*. **2015**, *17*, 6114−6121.

(36) Roch, L. M.; Zoppi, L.; Siegel, J. S.; Baldridge, K. K. *J. Phys. Chem. C* **2017**, *121*, 1220−1234.

(37) Zoppi, L.; Martin-Samos, L.; Baldridge, K. K. *J. Am. Chem. Soc*. **2011**, *133*, 14002−14009.

(38) Ayalon, A.; Sygula, A.; Cheng, P. C.; Rabinovitz, M.; Rabideau, P. W.; Scott, L. T. *Science* **1994**, *265*, 1065−1067.

(39) Filatov, A. S.; Zabula, A. V.; Spisak, S. N.; Rogachev, A. Y.; Petrukhina, M. A. *Angew. Chem., Int. Ed*. **2014**, *53*, 140−145.

(40) Gerald, R. E.; Klingler, R. J.; Sandí, G.; Johnson, C. S.; Scanlon, L. G.; Rathke, J. W. *J. Power Sources* **2000**, *89*, 237−243.

(41) Sandí, G.; Gerald, R. E.; Scanlon, L. G.; Johnson, C. S.; Klingler, R. J.; Rathke, J. W. *J. New Mater. Electrochem. Syst*. **2000**, *3*, 13−19.

(42) Mack, J.; Vogel, P.; Jones, D.; Kaval, N.; Sutton, A. *Org. Biomol. Chem*. **2007**, *5*, 2448−2452.

(43) Babu, S. S.; Mohwald, H.; Nakanishi, T. *Chem. Soc. Rev*. **2010**, *39*, 4021−4035.

(44) Wang, W.; Wang, Y.-X.; Yang, H.-B. *Chem. Soc. Rev*. **2016**, *45*, 2656−2693.

(45) Balch, A. L.; Winkler, K. *Chem. Rev*. **2016**, *116*, 3812−3882.

(46) Golan, A.; Goldberg, I.; Vigalok, A. *Supramol. Chem*. **2016**, *28*, 526−535.

(47) Moreira, L.; Calbo, J.; Krick Calderon, R. M.; Santos, J.; Illescas, B. M.; Arago, J.; Nierengarten, J.-F.; Guldi, D. M.; Ortí, E.; Martín, N.́ *Chem. Sci*. **2015**, *6*, 4426−4432.

(48) Sawamura, M.; Kawai, K.; Matsuo, Y.; Kanie, K.; Kato, T.; Nakamura, E. *Nature* **2002**, *419*, 702−705.

(49) Kraft, A.; Beuerle, F. *Tetrahedron Lett*. **2016**, *57*, 4651−4663.

(50) Almeida Paz, F. A.; Klinowski, J.; Vilela, S. M. F.; Tome, J. P. C.;́ Cavaleiro, J. A. S.; Rocha, J. *Chem. Soc. Rev*. **2012**, *41*, 1088−1110.

(51) Platero-Prats, A. E.; Mavrandonakis, A.; Gallington, L. C.; Liu, Y.; Hupp, J. T.; Farha, O. K.; Cramer, C. J.; Chapman, K. W. *J. Am. Chem. Soc*. **2016**, *138*, 4178−4185.

(52) Liang, W.; D'Alessandro, D. M. *Chem. Commun*. **2013**, *49*, 3706−3708.

(53) Stork, J. R.; Thoi, V. S.; Cohen, S. M. *Inorg. Chem*. **2007**, *46*, 11213−11223.

(54) Yamada, T.; Iwakiri, S.; Hara, T.; Kanaizuka, K.; Kurmoo, M.; Kitagawa, H. *Cryst. Growth Des*. **2011**, *11*, 1798−1806.

(55) Williams, D. E.; Dolgopolova, E. A.; Godfrey, D. C.; Ermolaeva, E. D.; Pellechia, P. J.; Greytak, A. B.; Smith, M. D.; Avdoshenko, S. M.; Popov, A. A.; Shustova, N. B. *Angew. Chem., Int. Ed*. **2016**, *55*, 9070−9074.

(56) Fan, J.; Wang, Y.; Blake, A. J.; Wilson, C.; Davies, E. S.; Khlobystov, A. N.; Schröder, M. *Angew. Chem., Int. Ed.* **2007**, *46*, 8013− 8016.

(57) Peng, P.; Li, F.-F.; Neti, V. S. P. K.; Metta-Magana, A. J.; Echegoyen, L. *Angew. Chem., Int. Ed*. **2014**, *53*, 160−163.

(58) Kraft, A.; Roth, P.; Schmidt, D.; Stangl, J.; Müller-Buschbaum, K.; Beuerle, F. *Chem. - Eur. J*. **2016**, *22*, 5982−5987.

(59) Howarth, A. J.; Buru, C. T.; Liu, Y.; Ploskonka, A. M.; Hartlieb, K. J.; McEntee, M.; Mahle, J. J.; Buchanan, J. H.; Durke, E. M.; AlJuaid, S. S.; Stoddart, J. F.; DeCoste, J. B.; Hupp, J. T.; Farha, O. K. *Chem. - Eur. J*. **2017**, *2*3, 214−218.

(60) Minar, N. K.; Hou, K.; Westermeier, C.; Doblinger, M.; Schuster, J.; Hanusch, F. C.; Nickel, B.; Ozin, G. A.; Bein, T. A. *Angew. Chem., Int. Ed*. **2015**, *54*, 7577−7581.

(61) Fellows, W. B.; Rice, A. M.; Williams, D. E.; Dolgopolova, E. A.; Vannucci, A. K.; Pellechia, P. J.; Smith, M. D.; Krause, J. A.; Shustova, N. B. *Angew. Chem., Int. Ed*. **2016**, *55*, 2195−2199.

(62) Peng, P.; Li, F.-F.; Bowles, F. L.; Neti, V. S. P. K.; MettaMagana, A. J.; Olmstead, M. M.; Balch, A. L.; Echegoyen, L. *Chem. Commun*. **2013**, *49*, 3209−3211.

(63) Williams, D. E.; Shustova, N. B. *Chem. - Eur. J*. **2015**, *21*, 15474−15479.

(64) Kennedy, R. D.; Ayzner, A. L.; Wanger, D. D.; Day, C. T.; Halim, M.; Khan, S. I.; Tolbert, S. H.; Schwartz, B. J.; Rubin, Y. *J. Am. Chem. Soc*. **2008**, *130*, 17290−17292.

(65) Chen, S.; Ye, G.; Xiao, Z.; Ding, L. *J. Mater. Chem. A* **2013**, *1*, 5562−5566.

(66) MacKenzie, R. C.; Frost, J. M.; Nelson, J. *J. Chem. Phys*. **2010**, *132*, 064904.

(67) Moon, D.; Kang, S.; Park, J.; Lee, K.; John, R. P.; Won, H.; Seong, G. H.; Kim, Y. S.; Kim, G. H.; Rhee, H. *J. Am. Chem. Soc*. **2006**, *128*, 3530−3531.

(68) Conn, M. M.; Rebek, J. *Chem. Rev*. **1997**, *97*, 1647−1668.

(69) Uemura, T.; Nakanishi, R.; Mochizuki, S.; Kitagawa, S.; Mizuno, M. *Angew. Chem., Int. Ed*. **2016**, *55*, 6443−6447.

(70) Warmuth, R.; Yoon, J. *Acc. Chem. Res*. **2001**, *34*, 95−105.

(71) Sun, D.; Tham, F. S.; Reed, C. A.; Boyd, P. D. W. *Proc. Natl. Acad. Sci. U. S. A.* **2002**, *99*, 5088− 5092.

(72) Chae, H. K.; Siberio-Perez, D. Y.; Kim, J.; Go, Y.; Eddaoudi, M.; Matzger, A. J.; O'Keeffe, M.; Yaghi, O. M. *Nature* **2004**, *427*, 523−527.

(73) Constable, E. C.; Zhang, G.; Housecroft, C. E.; Zampese, J. A. *CrystEngComm* **2012**, *14*, 1770−1774.

(74) Leong, K.; Foster, M. E.; Wong, B. M.; Spoerke, E. D.; Van Gough, D.; Deaton, J. C.; Allendorf, M. D. *J. Mater. Chem. A* **2014**, *2*, 3389−3398.

(75) Dolgopolova, E. A.; Shustova, N. B. *MRS Bull*. **2016**, *41*, 890−896.

(76) Feng, Y.; Wang, T.; Li, Y.; Li, J.; Wu, J.; Wu, B.; Jiang, L.; Wang, C. *J. Am. Chem. Soc*. **2015**, *137*, 15055−15060. (77) Popov, A. A.; Yang, S.; Dunsch, L. Endohedral Fullerenes. Chem. Rev. 2013, 113, 5989−6113.

CHAPTER 2

REDOX-ACTIVE CORANNULENE BUCKYBOWLS IN A CRYSTALLINE HYBRID SCAFFOLD

Rice, A. M.; Fellows, W. B.; Williams, Dolgopolova, E. A.; Vannucci, A. K.; Pellechia, P. J. Smith, M. D.; Krause, J. A.; Shustova, N. B. *Angew. Chem. Int. Ed.* **2016**, *55*, 2195.

A porous crystalline corannulene-containing scaffold, which combines the periodicity, dimensionality, and structural modularity of hybrid frameworks with the intrinsic properties of redox-active π-bowls, has been prepared. Single crystal and powder X-ray diffraction, ab initio density functional theory computations, gas sorption analysis, fluorescence spectroscopy, and cyclic voltammetry were employed to study the properties of the novel corannulene derivatives and the buckybowl-based hybrid materials. X-ray diffraction studies revealed the preservation of the corannulene bowl inside the prepared rigid matrix, which offers the unique opportunity to extend the scaffold dimensionality through the buckybowl curvature. Merging the inherent properties of hybrid frameworks with the intrinsic properties of p-bowls opens a new avenue for preparing redox-active materials and potentially improving charge transport in the scaffold.

The bowl-shaped surface of corannulene, $C_{20}H_{10}$, has attracted a lot of attention owing to its intriguing curvature.[1–6] However, only recently a more practical synthetic route[7] rendered $C_{20}H_{10}$ available for comprehensive studies, which has also boosted its utilization in a wide scope of applications.[8–14] For instance, acceptance of four electrons makes corannulene more electron-rich per carbon atom than the commonly used electron acceptor fullerene.[15,16] Moreover, the electron-accepting properties can be tuned through derivatization of the $C_{20}H_{10}$ bowl.[17] Corannulene also possesses a high degree of lithium intercalation, as exemplified by the sandwich-like structure consisting of two corannulene tetraanions with five lithium cations incorporated between them (Scheme 2.1).[15]

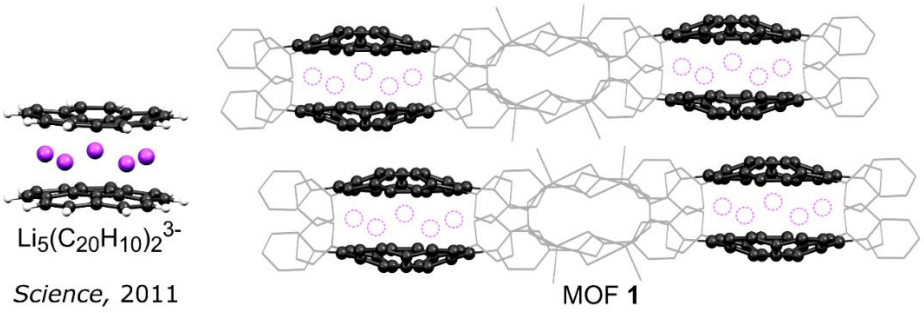

Scheme 2.1. (*left*) The corannulene-based sandwich (adapted with permission from reference [15] . (*right*) The prepared crystalline scaffold suitable for potential guest (e.g., alkali metal) incorporation.

Furthermore, the reversible lithium capacity of corannulene-based materials is almost twice as high as that of lithiated graphite,[18] rendering corannulene derivatives promising building blocks for the preparation of anode materials in rechargeable lithium-ion batteries. Herein, we report the development of a hybrid framework built from novel redox-active corannulene-based ligands. In contrast to previously reported corannulene-containing polymers,[19–23] we have synthesized the first example of a porous crystalline scaffold in which the derivatized buckybowl is covalently linked to metal ions. Coordinative immobilization of the corannulene-based linker inside the metal–organic framework(MOF)preserves the bowl shape, which may offer an extension of scaffold dimensionality through the corannulene curvature. By analogy with the reduced corannulene based "sandwich",[15,24] the prepared crystalline scaffold can be considered a "baguette", for instance, for alkali-metal intercalation (Scheme 2.1). Moreover, incorporation of redox-active corannulene-based ligands opens anew avenue to improve MOF charge-transport properties and develop a new family of electrochromic materials. In the presented work, single-crystal and powder X-ray crystallography, spectroscopic

studies, gas sorption analysis, and cyclic voltammetry were employed for comprehensive analysis of the prepared corannulene-based scaffold. Therefore, these studies are the first attempt to bridge the structural modularity and porosity of MOFs with the intrinsic properties of π-bowls. While milligram-scale reactions are typically reported for the preparation of new corannulene derivatives,[25–27] one of the challenges in the development of corannulene-containing MOFs is the synthesis of the corresponding ligand in multigram quantities. The amount of ligand is dictated by the combinatorial approach typically used for MOF self-assembly[28–31] and, more importantly, comprehensive analysis of the prepared materials.Therefore,1,2,7,8-tetrabromocorannulene,which is accessible on gram scale (Scheme 2.2),[7] was chosen as a precursor for the preparation of the corannulene-based linker with four carboxylic acids for subsequent metal coordination.

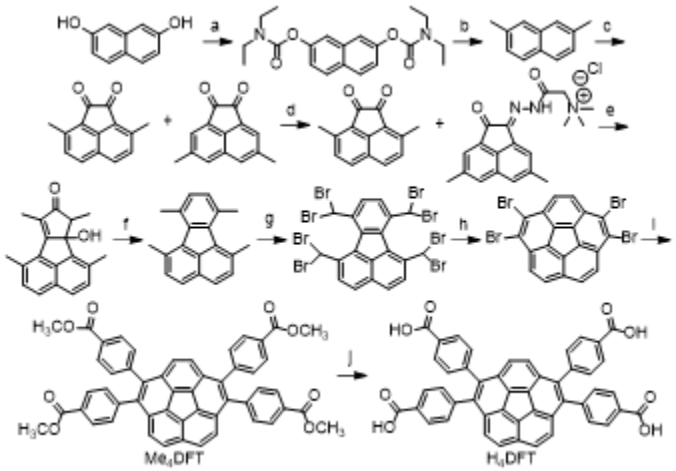

Scheme 2.2. Synthesis of H_4DFT: (a) diethylcarbamoyl chloride, pyridine, 100 °C, 2 d; (b) MeMgBr, $NiCl_2(dppp)_2$, Et_2O, 30 °C, 13 h; (c) $AlBr_3$, $(COCl)_2$, CH_2Cl_2, –15 °C, 8 h; (d) Girard's Reagent T, AcOH, 40 °C, 2 h; (e) 3-pentanone, KOH, MeOH, 2 h; (f) norbornadiene, Ac_2O, 140 °C, 3 d; (g) NBS, benzoyl peroxide, CCl_4, hν, 77 °C, 5 d; (h) NaOH, dioxane/H_2O, 100 °C, 1 h; (i) 4-carboxymethyl phenylboronic acid, methyl 4-iodobenzoate, K_3PO_4, $Pd(PPh_3)_4$, dioxane, 100 °C, 5 d; (j) NaOH, MeOH/THF/H_2O, 80 °C, 3 d.

The ten-step synthetic route employed for the preparation of H_4DFT is shown in Scheme 2.2. The synthetic details for the preparation of Me_4DFT as a precursor for H_4DFT and its structural elucidation by ^{1}H COSY, ^{1}H{13C} HSQC, and ^{1}H{13C} HMBC NMR spectroscopy can found in the Experimental Section (Figures 2.4–2.12).[32] In comparison with naked $C_{20}H_{10}$, decoration of the corannulene core with four electron-withdrawing groups in H_4DFT led to a significantly lowered lowest unoccupied molecular orbital (LUMO) energy level, implying that H_4DFT is a better electron acceptor than unsubstituted $C_{20}H_{10}$ (Experimental, Figure 2.23). As shown in Figure 2.22 (Experimental), H_4DFT has its highest occupied molecular orbital (HOMO) primarily localized on the corannulene bowl. Aside from the corannulene core, significant contributions from two of the benzoic acid groups were observed in the LUMO (Experimental, Figure 2.23). The HOMO–LUMO gap of H_4DFT was calculated to be 3.95 eV, which is in line with the acquired spectroscopic data (Experimental, Figures 2.19 and 2.20). Immobilization of the prepared ligand in a rigid MOF matrix was performed by reacting H_4DFT with $Zn(NO_3)_2$ in a mixture of *N*,*N*-dimethylformamide (DMF) and ethanol, which resulted in the formation of yellow plates of $[Zn_2(DFT)(H_2O)_2(EtOH)]\cdot(H_2O)_{2.85}(DMF)_{0.1}$ (1), which were suitable for single-crystal X-ray diffraction analysis. Crystallographic studies of 1 revealed that coordination of DFT^{4-} to Zn^{2+} led to the formation of a two-dimensional(2D) MOF (Main Text, Figure 2.1; Experimental, Figures 2.25 and 2.26, Table 2.2). Unlike many tetratopic ligands, which typically promote the formation of the common paddlewheel metal nodes,[33–36] the secondary building unit (SBU) in 1 is a strongly distorted ZnO_5 square pyramid. As shown in Figure 2.1, half of the carboxylates are bonded to two Zn^{2+} ions in a similar

motif to that observed in the paddlewheel node, but the other two carboxylates are bonded to one metal ion each, giving rise to a very rare zinc-based SBU.

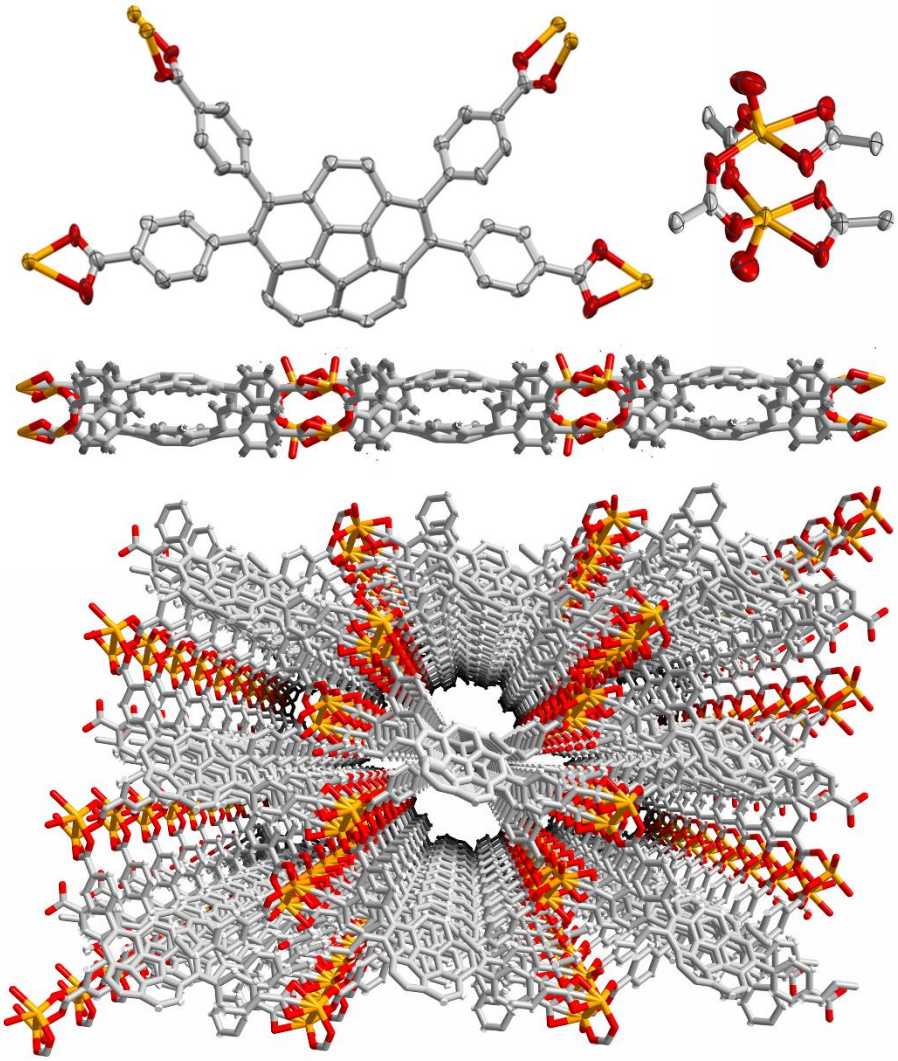

Figure 2.1. The single-crystal X-ray structure of **1**. (*top left*) DFT^{4-} coordinated to Zn^{2+}. (*top right*) The $Zn_2(O_2C-)_4$ SBU. Displacement ellipsoids drawn at the 50% probability level. (*middle*) Infinite 2D layers parallel to the crystallographic (11-1) plane. (*bottom*) Packing of 2D layers forming 1D channels. Grey, red, and orange spheres represent carbon, oxygen, and zinc atoms, respectively. The solvent molecules are omitted for clarity.

Although the rigid structure of MOFs can significantly affect ligand geometry and, in some cases, lead to highly strained organic linkers,[37] the corannulene molecular conformations in 1 are not flattened or distorted. Figure 2.24 and Table 2.1

(Experimental) show a comparison of the DFT^{4-} bowl depth in 1 (0.87 Å)[38] to those in other tetrasubstituted corannulene derivatives,[2,4,39–42] demonstrating that coordinative immobilization has no significant influence on the corannulene bowl curvature. Furthermore, the DFT^{4-} bowl depth in 1 is the same as in parent $C_{20}H_{10}$ (0.87 Å),[38] whereas significant corannulene flattening was previously observed owing to host–guest interactions.[43] The preservation of the undistorted corannulene curvature in DFT^{4-} could perhaps be partially responsible for the significant deviation of the SBU in 1 from the commonly observed paddlewheel metal node. Such preservation of the bowl-shaped DFT^{4-} structure could potentially extend the dimensionality of MOFs and enable the use of corannulene-based linkers as receptors with enclosed cavities for molecular recognition,[44,45] alkali-metal immobilization,[15,46] or selective separation.[47] As shown in Scheme 2.1, Figure 2.1 (Main Text) and Figure 2.26 (Experimental), the crystal structure of 1 contains an unusual, slightly offset subunit consisting of two DFT^{4-} cupped together, forming a clamshell-like unit along the b crystallographic axis. Packing of 2D sheets resulted in the formation of one-dimensional channels oriented along the a crystallographic axis with dimensions of 9×13 Å. Evacuated 1 was utilized to determine the permanent porosity, and despite the 2D structure, gas sorption analysis revealed that 1 is permanently porous with a BET surface area of 224(1) m^2g^{-1}. Aside from single-crystal X-ray and gas sorption analysis, powder X-ray diffraction (PXRD), thermogravimetric analysis, FT-IR spectroscopy ,and elemental analysis were employed to study bulk as-synthesized 1 (Experimental, Figures 2.13–2.18). As shown in Figure 2.18 (Experimental), the PXRD pattern of 1 coincided with the simulated spectrum from the single-crystal X-ray data. Owing to a doubly degenerate LUMO, corannulene can accept

up to four electrons and has three distinct reduction potentials.[48] To test the electrochemical properties of synthesized H_4DFT, Me_4DFT, and 1, cyclic voltammetry measurements were carried out in a DMF solution containing 0.1m tetrabutylammonium hexafluorophosphate, using an H-cell equipped with saturated calomel reference, platinum wire counter, and glassy carbon working electrodes. Cyclic voltammetry studies of MOFs are relatively rare and require significant modification of the commonly used electrochemical setup.[49,50] For the electrochemical studies, a small amount of 1 and Nafion were mixed, followed by placement on the surface of the glassy carbon electrode. The cyclic voltammogram(CV) of 1 shows at least two distinct reduction events with peak potentials of E_p= -1.42 V E_p= -1.69 V (Figure 2.2). Similarly, free H_4DFT undergoes one large, irreversible reduction with a peak potential of E_p= -1.64 V (Figure 2.2). Their reversibility and shape of the CV wave for H_4DFT are consistent with the electrochemistry of related benzoic acids.[51] The cyclic voltammogram of Me_4DFT, on the other hand, exhibits three distinct, reversible reductions at $E_{1/2}$= -1.52 V, $E_{1/2}$= -1.68 V, and $E_{1/2}$ = -1.94 V (Figure 2.2). The charges passed and the peak-to-peak separation of about 30 mV (at 20 mVs^{-1} scan rate) of the third redox wave at $E_{1/2}$= -1.94 Vindicate that this is a two-electron process. Two-electron redox events are indicative of potential inversion, which is typically associated with significant structural changes occurring during the electron transfer processes.[52] Comparing the simulated and experimental CV data of Me_4DFT provides additional support for the two-electron reduction assignment (Figure 2.2).

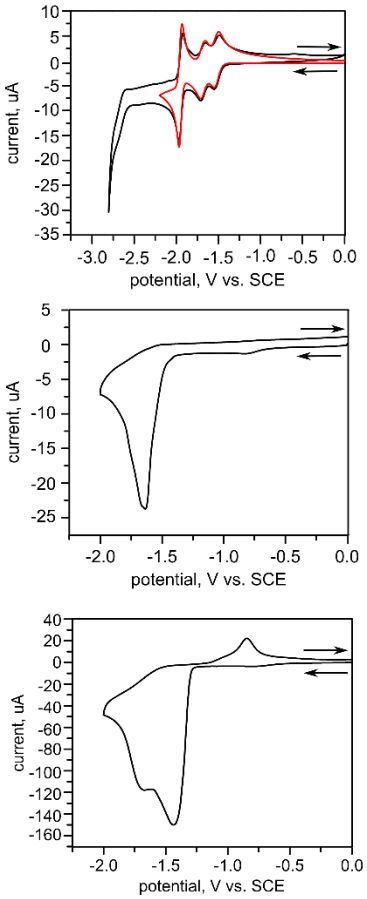

Figure 2.2. Cyclic voltammograms of Me_4DFT (top, black), simulated (top, red), H_4DFT (middle), and **1** (bottom). For performed simulations, diffusion coefficients for all species were set equal to 1×10^{-5} cm^2/s, and all electron transfer rate constants were kept equal to the default value of 10,000 cm/s. Reduction potentials for the four reversible reductions, $Me_4DFT + e \rightleftharpoons [Me_4DFT]^-$; $[Me_4DFT]^- + e \rightleftharpoons [Me_4DFT]^{2-}$; $[Me_4DFT]^{2-} + e^- \rightleftharpoons [Me_4DFT]^{3-}$; $[Me_4DFT]^{3-} + e^- \rightleftharpoons$

$[Me_4DFT]^{4-}$, were set to *E(I)* = –1.52 V, *E(II)* = –1.68 V, *E(III)* = –2.05 V, and *E(IV)* = –1.80 V. The solution resistance was compensated electronically using 100 Ω (electrode area = 0.06 cm^2).

Comparison of the acquired CV data with that of corannulene shows that each reduction potential of Me_4DFT is markedly less negative;[48] $E_{1/2}(I)$, $E_{1/2}(II)$, and $E_{1/2}(III)$ are less negative by +0.35 V, +0.73 V, and +0.62 V, respectively. Similarly, the reduction potentials for 1 are also less negative, with values of $E_{1/2}(I)$ = +0.45 V and $E_{1/2}(II)$ = +0.72 V compared to unmodified $C_{20}H_{10}$. Thus, cyclic voltammetry confirmed the stronger electron-accepting ability of the prepared compounds versus naked $C_{20}H_{10}$. As H_4DFT, Me_4DFT, and 1 exhibit bright emission detectable by the naked eye, their photophysical properties were investigated by fluorescence, UV/Vis, and diffuse reflectance spectroscopy (Figure 2.3).

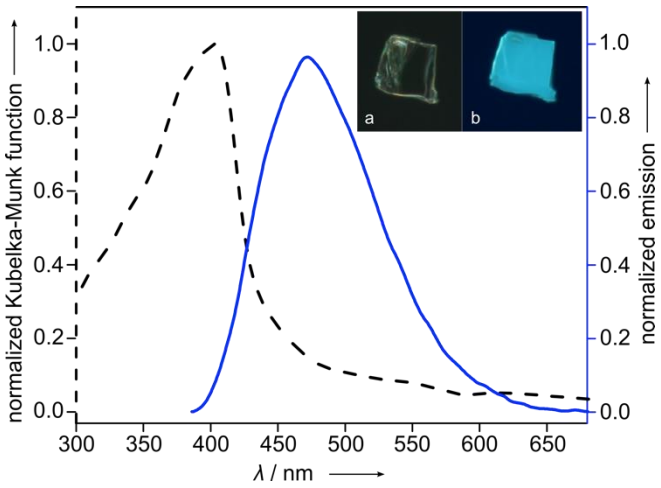

Figure 2.3. Normalized diffuse reflectance (dashed line) and emission (solid blue line) spectra of **1**. The inset shows epifluorescence microscopy images of a crystal of **1** before (a) and after (b) irradiation at λ_{ex} = 370 nm.

The emission maximum of Me_4DFT was located at 443 nm (Experimental, Figure 2.21). The photoluminescence maxima of solid H_4DFT (λ_{max} =470 nm, Experimental, Figure 2.20) and 1 (λ_{max} =472 nm, Figure 2.3) exhibit a bathochromic shift by about 20 nm, in comparison with solid unsubstituted $C_{20}H_{10}$, which could be explained in part by the attachment of electron-withdrawing groups to the corannulene core and the extended π system of the tetra-substituted linker.[53,54] Interestingly, the measured fluorescence quantum yields of H_4DFT and Me_4DFT in solution are more than twice as large as those of the unsubstituted corannulene.[54] Moreover, the quantum yield value of H_4DFT in the solid state is comparable to the value acquired in solution, and therefore, prepared H_4DFT does not suffer from aggregation-caused quenching, which is a common phenomenon for chromophores in the solid state.[55,56] Both in solution and in the solid state, H_4DFT possesses the highest fluorescence quantum yield among these compounds, and the quantum yield as a solid is comparable with that of 1.

In conclusion, we have developed the first example of a porous crystalline hybrid scaffold in which redox-active corannulene-based ligands are covalently coordinated to metal ions. The ten-step synthesis of the corannulene containing linker, which is thus available on a gram scale and necessary for the scaffold preparation, has also been reported. Comprehensive analysis of the new corannulene-based compounds demonstrates their better electron-accepting properties in comparison with unmodified corannulene. Moreover, the photoluminescence quantum yields of the prepared derivatives are almost double that of naked $C_{20}H_{10}$. Single-crystal X-ray analysis revealed the preservation of the corannulene bowl after coordinative immobilization inside the rigid scaffold, which offers an extension of MOF dimensionality through the corannulene

curvature. The preliminary results demonstrate that the doping of 1 with these donor molecules results in a charge-transfer band. Further work in this direction is in progress. The presented work constitutes the first attempt to merge the modularity and porosity inherent to MOFs with the intrinsic properties of π-bowls, which could open anew avenue for the rational design of electroactive multidimensional crystalline porous materials.

EXPERIMENTAL SECTION

Materials.

2,7-dihydroxynapthalene (Chem-Impex International, Inc.), *N*,*N*-diethylcarbamoyl chloride (99%, Acros Organics), dichloro(1,3-bis(diphenylphosphino)propane)nickel (Ark Pharm, Inc), methylmagnesium bromide (Alfa Aesar), aluminum bromide (Strem Chemicals, Inc.), oxalyl chloride (98%, Alfa Aesar), Girard's Reagent T (99%, Acros Organics), 3-pentanone (>98%, Tokyo Chemical Industry Co, LTD), 2,5-norbornadiene (97%, Alfa Aesar), *N*-bromosuccinimide (96%, Oakwood Chemical), benzoyl peroxide (97%, Sigma-Aldrich), 4-methoxycarbonyl phenylboronic acid (Boron Molecules), 4-iodobenzoic acid methyl ester (>99%, Chem-Impex International, Inc.), potassium phosphate (97%, Alfa Aesar), tetrakis(triphenylphosphine)palladium(0) (Matrix Scientific), zinc nitrate hexahydrate (technical grade, Ward's Science), pyridine (99+%, Alfa Aesar), 1,4-dioxane (99+%, Alfa Aesar), diethyl ether (HPLC grade, Fisher Scientific), hydrochloric acid (ACS grade, EMD Chemicals), hexane (ACS grade, BDH), diethyl ether (99% pure, Acros Organics), isopropanol (ACS grade, BDH), dichloromethane (>99.5%, Sigma-Aldrich) and (ACS grade, Macron), methanol (>99.8%, Sigma-Aldrich) and (HPLC grade, Fisher Scientific), acetic acid (ACS grade, Fisher Scientific), acetic anhydride (99.63%, Chem-

Impex International, Inc.), cyclohexane (reagent grade, Malinckrodt), carbon tetrachloride (99.9%, Sigma-Aldrich), ethanol (200 proof, Decon Laboratories, Inc.), chloroform (ACS grade, Macron), tetrahydrofuran (ACS grade, EMD Chemicals), *N*,*N*-dimethylformamide (ACS grade, BDH), sodium hydroxide (ACS grade, Fisher Scientific), anhydrous magnesium sulfate (reagent grade, J.T. Baker® Chemicals), potassium hydroxide (ACS grade, Fisher Scientific), silica gel (Macron), sodium chloride (ACS grade, Fisher Scientific), $CDCl_3$ (Cambridge Isotope Laboratories, Inc.), and DMSO-d_6 (Cambridge Isotope Laboratories, Inc.) were used as received.

The compounds 2,7-bis(diethylcarbamoyloxy)naphthalene (**S1**, Scheme 2.2),[57] 2,7-dimethylnapthalene,[57] acenaphthenequinone,[58] 1,6,7,10-tetramethylfluoranthene,[58] 1,6,7,10-tetrakis(dibromomethyl)fluoranthene,[58] and 1,2,7,8-tetrabromocorannulene[59] were prepared according to the reported procedures.

Synthesis.

4,4′,4″,4‴-(dibenzo[ghi,mno]fluoranthene-1,2,5,6-tetrayl)tetrabenzoate ($C_{52}H_{34}O_8$, Me_4DFT, Scheme 2.1).

The prepared 1,2,7,8-tetrabromocorannulene (0.500 g, 0.884 mmol), 4-methoxycarbonyl phenylboronic acid (3.19 g, 17.7 mmol), potassium phosphate (7.50 g, 35.3 mmol), and 4iodobenzoic acid methyl ester (0.810 g, 3.09 mmol) were placed in dioxane (125 mL) under nitrogen. Tetrakis(triphenylphosphine)palladium(0) (0.408 g, 0.353 mmol) was added to the resulting solution, and heated at reflux for 5 d. The reaction mixture was cooled to room temperature under nitrogen, followed by removal of solvent under reduced pressure, which resulted in a beige solid. The beige solid was then dissolved in dichloromethane and water, and the aqueous layer was extracted with dichloromethane (3

× 100 mL), washed with 1 M sodium hydroxide (100 mL) and water (100 mL), and the dichloromethane was removed under reduced pressure. The resulting solid was then boiled in methanol (250 mL) for 30 min and then filtered. The methanol filtrate was evaporated, followed by the addition of diethyl ether (250 mL), and the mixture was heated at reflux overnight. The diethyl ether suspension was then filtered, resulting in an off-white solid. After drying under vacuum, a yellow solid, Me_4DFT, was isolated in 57.9% yield. ^{1}H NMR (CDCl3, 300 MHz): δ = 8.03–8.00 (2H, d, J = 9.00), 7.93–7.88 (8H, m), 7.52 (2H, s), 7.49–7.43 (8H, m) ppm (Figure S6). 13C NMR (DMSO-d6, 400 MHz): δ = 142.40, 142.39, 138.11, 137.64, 134.39, 134.27, 133.30, 131.57, 131.55, 130.65, 129.66, 129.19, 128.60, 120.59, 128.42, 128.37, 128.35, 127.12, and 126.75 ppm (Figure S7). IR (neat, cm-1): 2953, 1718, 1606, 1565, 1508, 1434, 1404, 1310, 1270, 1179, 1100, 1017, 960, 924, 906, 865, 840, 828, 819, 802, 773, 765, 757, 726, 705, 693, and 654 (Figure S21). HRMS (ESI) m/z: 786.2249 [M^+], calc.: 786.2254. The structural analysis based on the NMR spectroscopic data is given on pages 44-50.

4,4',4",4"'-(dibenzo[ghi,mno]fluoranthene-1,2,5,6-tetrayl)tetrabenzoic acid (C48H26O8, H4DFT, Scheme 2.1).

For the preparation of H_4DFT, 2 M NaOH was added to a solution of Me4DFT (0.739 g, 0.939 mmol) in a 50/50 (80 mL) mixture of MeOH/THF. The resulting mixture was heated at reflux for 2 d. Upon removal of organic solvents under reduced pressure, HCl was added to reach a pH of 1, and the solution was stirred for 2 h. After stirring, the solution was filtered, and the precipitate was collected and washed with water. The precipitate was dried under vacuum at 100 °C, and a yellow solid was isolated in 75.3% yield. ^{1}H NMR (DMSO-d6, 300 MHz): δ = 13.07 (4H, s), 8.09–8.06 (2H, d, J = 9.00),

7.95–7.91 (8H, m), 7.59 (2H, s), 7.57–7.54 (2H, d, J = 9.00), 7.50–7.46 (8H, m) ppm (Figure 2.11). 13C NMR (DMSO-d_6, 400 MHz): δ = 142.08, 142.07, 138.31, 137.85, 134.53, 134.53, 133.36, 131.45, 131.44, 130.72, 129.88, 129.53, 129.50, 129.37, 128.79, 128.78, 128.44, 127.24, and 126.89 ppm (Figure 2.12). IR (neat, cm–1): 3024, 2546, 1689, 1606, 1565, 1510, 1408, 1312, 1268, 1178, 1103, 1017, 924, 905, 868, 816, 802, 774, 750, 720, and 697 (Figure 2.16). HRMS (ESI) m/z: 730.1649 [M+], calc.: 730.1628.

Synthesis of $[Zn_2(DFT)(H_2O)_2(EtOH)] \cdot (H_2O)_{2.85}(DMF)_{0.1}$ ***(1)***.

In a 0.5 dram vial, $Zn(NO_3)_2 \cdot 6H_2O$ (2.5 mg, 8.2 µmol) and H_4DFT (6.0 mg, 8.2 µmol) were dissolved in 0.01/0.19 mL of DMF/EtOH followed by sonication. The resulted solution was heated at 80 °C for 3 d. Yellow crystals (2.0 mg, 2.00 µmol) were isolated in 25.0% yield. IR (neat, cm-1): 2966, 1652, 1606, 1581, 1528, 1511, 1403, 1255, 1176, 1147, 1097, 1046, 1018, 925, 907, 867, 848, 833, 820, 799, 788, 772, 766, 733, 721, 707, and 657. The thermogravimetric analysis plot, FT-IR spectrum, and PXRD pattern are shown in Figures 2.14, 2.17, and 2.18, respectively. Exposure of **1** to solvents such as DEF, ethanol, DMF, and acetonitrile did not result to MOF degradation while soaking in water destroyed the framework. The single crystal X-ray structure of **1** is shown in Figure 2.1. Table 2.2 (Experimental) contains crystallographic refinement data for **1**.

$^1H\{^{13}C\}$ HMBC and HSQC NMR Spectroscopy.

Two-dimensional (2D) Heteronuclear Single Quantum Correlation (HSQC) and Heteronuclear Multiple Bond Correlation (HMBC) spectra were collected on a Bruker Advance III-HD 400 MHz spectrometer operating at 400.27 MHz for ^1H and 100.65 MHz for ^{13}C. Vendor supplied pulse sequences were used and processing was done with

Bruker Topspin 3.2. All data were acquired with temperature controlled at 25 °C. The 2D HSQC spectrum (with pulsed field gradient coherence selection) was collected with spectral widths of 15 ppm and 165 ppm for ^{1}H and ^{13}C respectively. FIDs were acquired with 1024 points and 256 increments were collected in t1. The 2D HMBC spectrum (with pulsed field gradient coherence selection) was collected with spectral widths of 15 ppm and 220 ppm for ^{1}H and ^{13}C, respectively. FIDs were acquired with 4096 points and 256 increments were collected in t_1.

X-ray Crystal Structure Determination.

*Single-crystal X-ray structure of **1**.*

The compound **1** crystallizes as tightly clustered pale yellow rounded plates. Lamellar twinning of the plates was visually evident, and difficulty was encountered in cleaving a single domain specimen. Despite surveying several crystals, the best specimen still showed a contribution from a second, non-merohedrally related domain. The intensity contribution from the second domain was accounted for using the TWINROTMAT program in PLATON.[9] The derived twin law is (-100 / 0-10 / 0.21 0.52 1), which was used to create an HKLF-5 format reflection file with two components for twin refinement in SHELX. The minor twin volume fraction refined to 0.211(3). X-ray intensity data were collected at 100(2) K using a Bruker D8 QUEST diffractometer equipped with a PHOTON 100 CMOS area detector and an Incoatec microfocus source (Mo Kα radiation, λ = 0.71073 Å).[5] The raw area detector data frames were reduced and corrected for absorption effects using the SAINT^{+} and SADABS programs.[6] Final unit cell parameters were determined by least-squares refinement of 9994 reflections taken from the data set. The structure was solved by direct methods with SHELXS.

Subsequent difference Fourier calculations and full-matrix least-squares refinement against F2 were performed with SHELXL-2014[5] using OLEX2[7]. The compound 1 crystallizes in the triclinic system. The space group P-1 (No. 2) was assumed and confirmed by structure solution. The identifiable contents of the asymmetric unit consist of two independent zinc atoms, one $C_{48}H_{22}O_8^{4-}$ ligand, two oxygen atoms from presumably mixed solvent molecules coordinated to the zinc centers, and one interstitial ethanol molecule. The $Zn_2(C_{48}H_{22}O_8)$ connectivity defines a polymeric 2D layered network. Directed into the interlayer gaps is the apical coordination site of the strongly distorted ZnO_5 square pyramids. Difference map electron density suggested that mostly water, but also a smaller amount of DMF/EtOH are coordinated at the apical positions of both Zn1 and Zn2. This disorder could not be modeled well and the apical site was refined as a single oxygen atom (Zn1/O9 and Zn2/O10), with the remaining electron density accounted for by the Squeeze technique (see below). One non-coordinated ethanol molecule located near the oxygen atoms bonded to the metal centers could be refined acceptably (O1S-C2S) using C–O and C–C distance restraints. An additional large volume of diffusely distributed electron density was observed in channel-like voids oriented along the crystallographic a axis. A satisfactory disorder model could not be achieved for these species, which are likely a mixture of crystallization solvents (DMF and EtOH). The Squeeze[8a] program implemented in PLATON was used to account for the disordered solvents, using the LIST 8 functionality for twinned datasets in SHELX 2014. Squeeze calculated a solvent-accessible void volume of 845.1 $Å^3$ (32.0% of the total unit cell volume), representing scattering from 205 electrons per unit cell. The contribution from these electrons was added to the structure factors calculated from the

known structural model during refinement. All non-hydrogen atoms were refined with anisotropic displacement parameters except for the interstitial ethanol carbon atoms (isotropic). Hydrogen atoms bonded to carbon were located in difference maps before being placed in geometrically idealized positions and included as riding atoms. Hydrogen atoms bonded to oxygen could not be located and were not calculated. The largest residual electron density peak in the final difference map is 1.76 e-/Å3, located 1.24 Å from O10, consistent with the small amount of non-water solvent coordinated to zinc, as above.

Other Physical Measurements.

NMR spectra were obtained on a Bruker Avance III-HD 300 and Bruker Avance III 400 MHz NMR spectrometers. 13C and 1H NMR spectra were referenced to natural abundance 13C peaks and residual 1H peaks of deuterated solvents, respectively. FT-IR spectra were collected on a Perkin-Elmer Spectrum 100. Powder X-ray diffraction patterns were recorded from a Rigaku Miniflex II diffractometer with an accelerating voltage and current of 30 kV and 15 mA, respectively. Thermogravimetric analysis was performed on an SDT Q600 Thermogravimetric Analyzer using an alumina boat as a sample holder. Diffuse reflectance spectra were collected on a Perkin Elmer Lambda 45 UV-vis spectrometer referenced to Spectralon®. Emission spectra were obtained on a Perkin Lambda LS 55 fluorescence spectrometer. Quantum yield measurements were collected on an Edinburgh Instruments FS5 spectrofluorometer, using the SC-30 Integrating Sphere Module. Cyclic voltammograms were obtained from a WaveDriver 20 Bipotentiostat combined with Aftermath software. Epifluorescence microscopy images were collected on an Olympus BX51 microscope with a 120 W mercury vapor short arc

excitation light source. Isotherm data were obtained from Micromeritics Analytical Services. Sample was evacuated at 100 °C for 72 hours prior to analysis. N2 adsorption isotherm was measured with the use of a liquid nitrogen bath (77 K).

Theoretical Calculations.

HOMO and LUMO energies of H4DFT were calculated in Spartan 10 using B3LYP DFT calculations with geometry optimized using the 6-31G basis set.

Structural analysis of tetrasubstituted corannulene derivatives.

The Cambridge Crystallographic Data Centre (CCDC) was used to access the crystal structures of the tetra-substituted corannulene compounds. Once identified, bowl depth analysis was performed using Mercury v. 5.36.

Cyclic voltammetry simulations.

Digital simulations were conducted with DigiElch version 7. For performed simulations, diffusion coefficients for all species were set equal to 1×10–5 cm2/s, and. all electron transfer rate constants were kept equal to the default value of 10,000 cm/s. The solution resistance was compensated electronically using 100 Ω (electrode area = 0.06 cm2).

$^{1}H\{^{1}H\}$ COSY, $^{1}H\{^{13}C\}$ HSQC, and $^{1}H\{^{13}C\}$ HMBC NMR Spectra and Structural Elucidation for Me_4DFT.

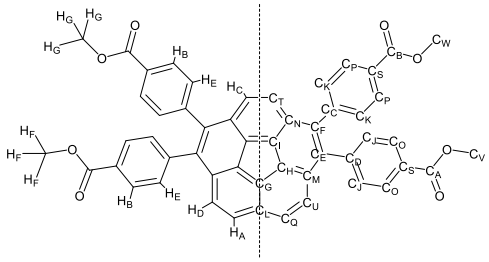

Figure 2.4. Structure of Me_4DFT, showing the symmetry of the

molecule and the carbon (right) and proton (left) assignment labels.

For structural elucidation of Me_4DFT and H_4DFT, ^1H COSY, $^1H\{^{13}C\}$ HSQC, and $^1H\{^{13}C\}$ HMBC NMR were collected. The $^1H\{^1H\}$ COSY NMR was used to assign the protons of Me_4DFT. Phenyl ring protons H_B and H_E (red boxes in Figure 2.5) are coupled to each other (see Figure 2.4 for proton assignment labels). This confirmed that the multiplet observed at 7.9 ppm was from phenyl protons H_B and consists of two overlapping doublets. Similarly, the multiplet observed at 7.4 ppm was ascribed to phenyl protons H_E. The lower rim protons, H_A and H_D are coupled with each other, as highlighted by the blue boxes in Figure 2.5. These doublets are consistent with those observed for tetra-substituted corannulene derivatives and the Me_4DFT precursors.[2,3,4,11] Additionally, upper rim proton H_C produced a singlet at 7.5 ppm, which overlaps with the doublet from lower rim proton H_D (Figure 2.5, blue boxes).

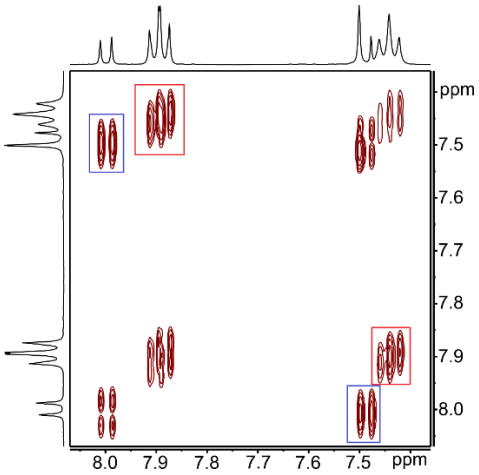

Figure 2.5. ^1H COSY NMR spectrum of Me_4DFT.

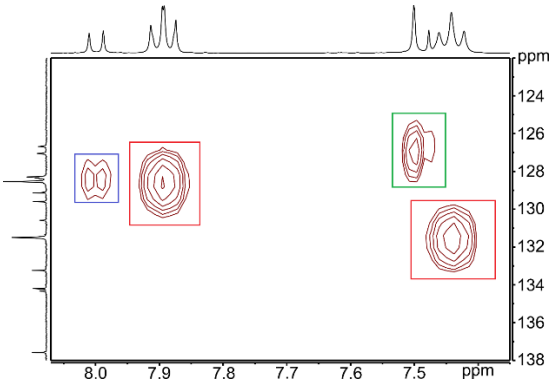

Figure 2.6. $^{1}H\{^{13}C\}$ HSQC NMR spectrum of Me_4DFT.

With the protons identified, the first set of carbons could be assigned, based on the $^{1}H\{^{13}C\}$ HSQC NMR spectrum. Using this data, carbon C_Q was identified as the carbon to which lower rim proton H_A is bonded (Figure 2.6, blue box; see Figure S1 for carbon assignment labels). Phenyl proton H_E is coupled with carbons C_K and C_J, at 129 ppm; phenyl proton H_B is coupled with carbons C_P and C_O, at 131 ppm (Figure 2.6, red boxes). Lower rim proton H_D is coupled to its carbon, $C_{U,}$ at 127 ppm; upper rim proton H_C is coupled to its carbon, C_T, at 126 ppm (Figure 2.6, green box).

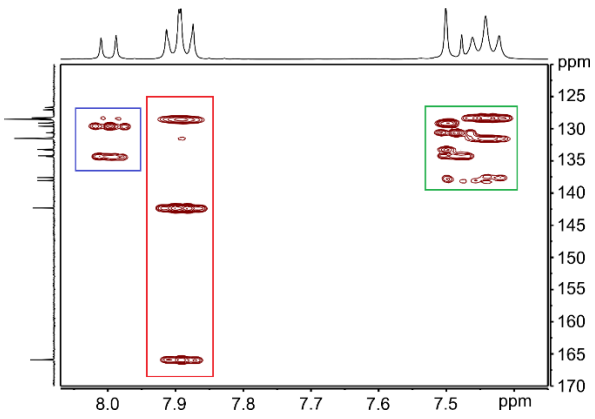

Figure 2.7. $^{1}H\{^{13}C\}$ HMBC NMR spectrum of Me_4DFT.

The $^{1}H\{^{13}C\}$ HMBC NMR spectrum was used to identify all remaining carbons (Figure 2.7). The three-bond couplings show that carbonyl carbons C_A and C_B (167 ppm), phenyl carbons C_C and C_D (142.40 and 142.39 ppm, respectively), and adjacent phenyl carbons C_J and C_K (131.57 and 131.55 ppm, respectively) couple to the H_B protons (Figure 2.7, red box). Lower rim proton H_A shows strong three-bond coupling to hub carbon C_G (134.40 ppm) and spoke carbon C_M (129.66 ppm). Considerably weaker, two-bond coupling of proton H_A to carbon C_U (126.75 ppm) was also observed (Figure 2.7, blue box). Figure 2.8 shows an expansion of the complex region of the $^{1}H\{^{13}C\}$ HMBC NMR spectrum, highlighted by the green box in Figure 2.7.

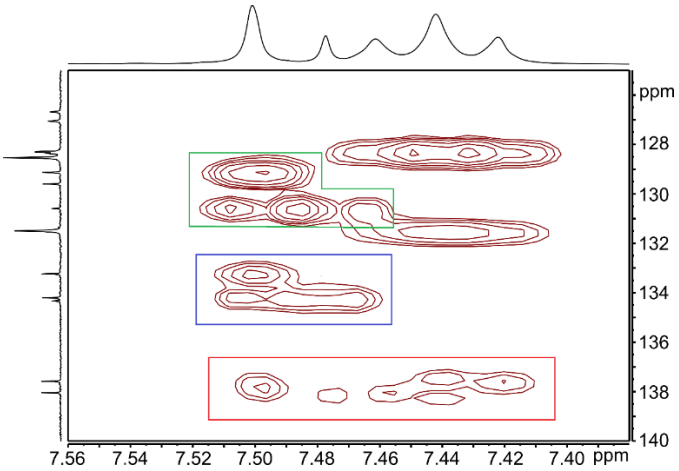

Figure 2.8. Expansion of the $^{1}H\{^{13}C\}$ HMBC NMR spectrum of Me_4DFT.

The expansion was utilized to accurately identify carbons with coupling to upper rim proton H_C, lower rim proton H_D, and phenyl protons H_E. Rim carbon C_E (138.11 ppm) is coupled with both lower rim proton H_D and phenyl proton H_E through a three-bond coupling. Carbon C_F (137.64 ppm) is coupled with upper rim proton H_C and phenyl proton H_E, also through three-bond coupling (Figure 2.8, red box). Lower rim proton H_D is coupled to hub carbon C_H (134.27 ppm) through a three-bond coupling; upper rim

proton H_C was also similarly coupled with carbon C_I (133.30 ppm) through a three-bond coupling (Figure 2.8, blue box). Lower rim proton H_D is coupled to spoke carbon C_L (130.65 ppm) through a three-bond coupling; upper rim proton H_C is coupled to carbon C_N (129.19 ppm) via a two-bond coupling (Figure 2.8, green box).

Using all of the proton and carbon assignments obtained based on the 2D NMR spectroscopic analysis of Me_4DFT, the analogous assignments for H_4DFT were made.

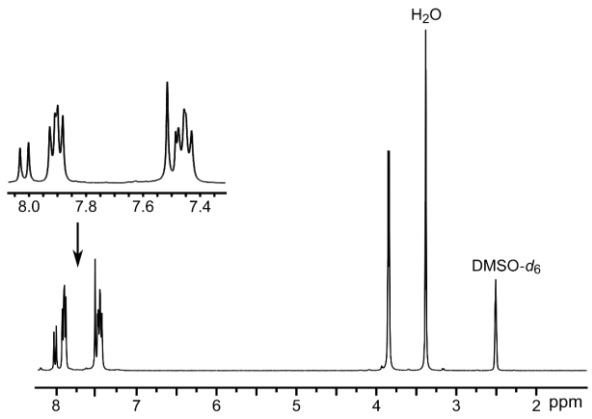

Figure 2.9. ^{1}H NMR spectrum of Me_4DFT.

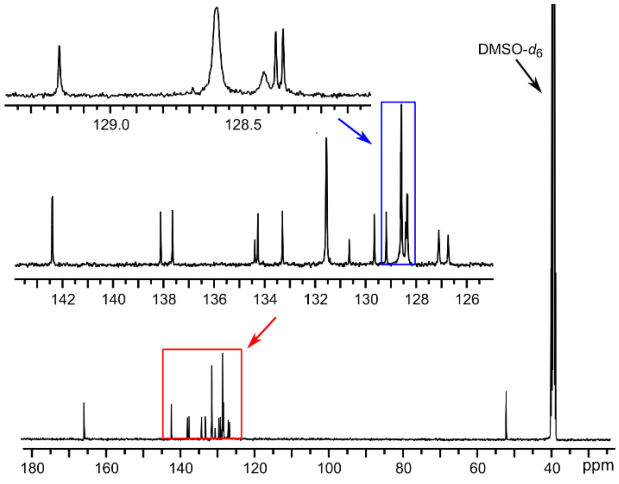

Figure 2.10. ^{13}C NMR spectrum of Me_4DFT.

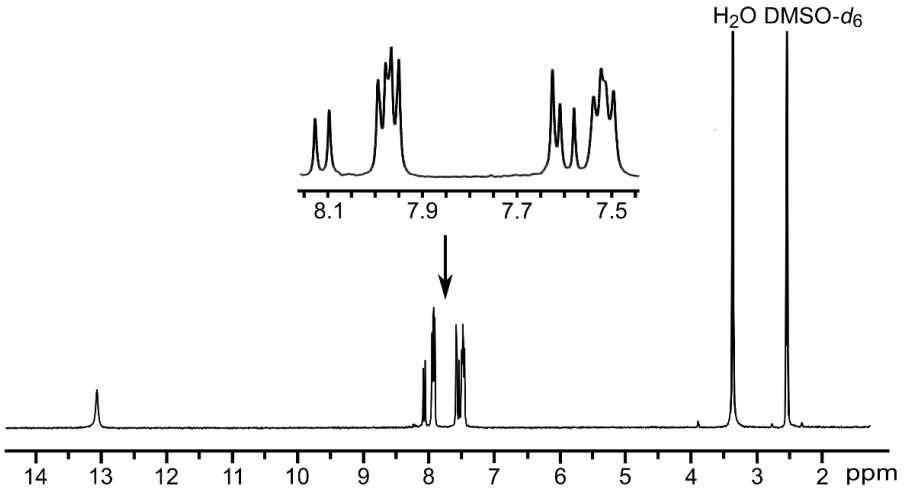

Figure 2.11. ^{1}H NMR spectrum of H_4DFT.

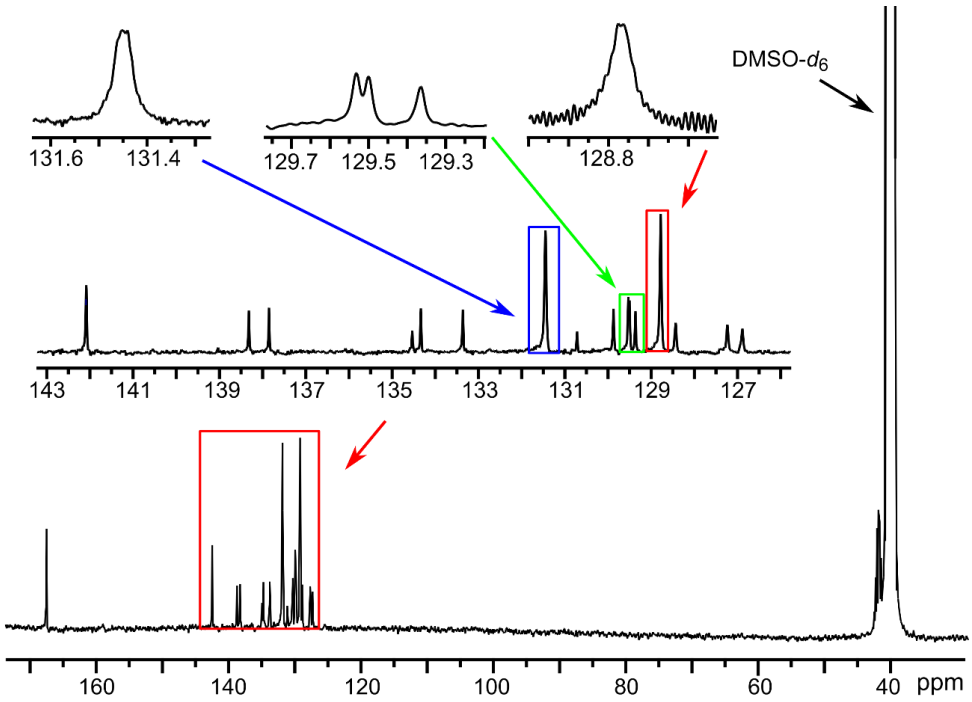

Figure 2.12. ^{13}C NMR spectrum of H_4DFT.

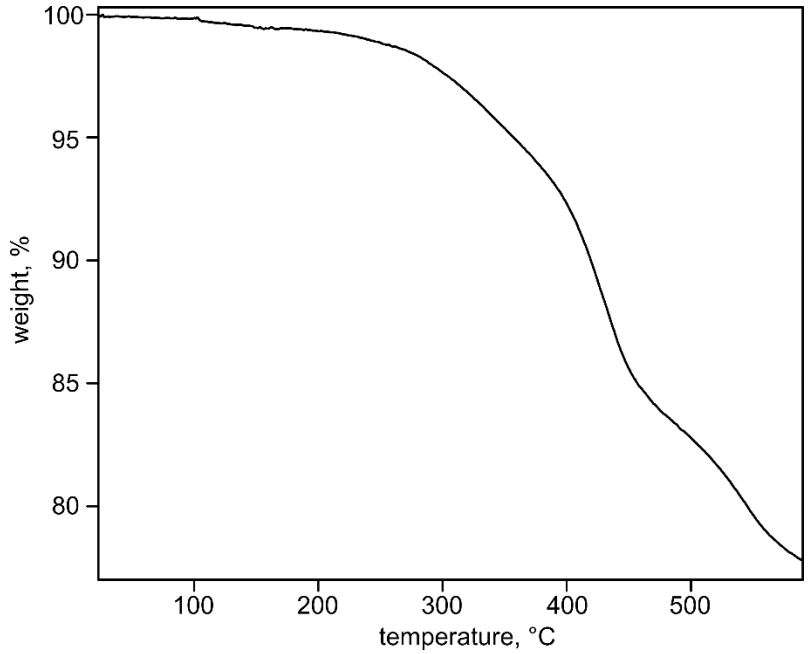

Figure 2.13. Thermogravimetric analysis plot of H_4DFT.

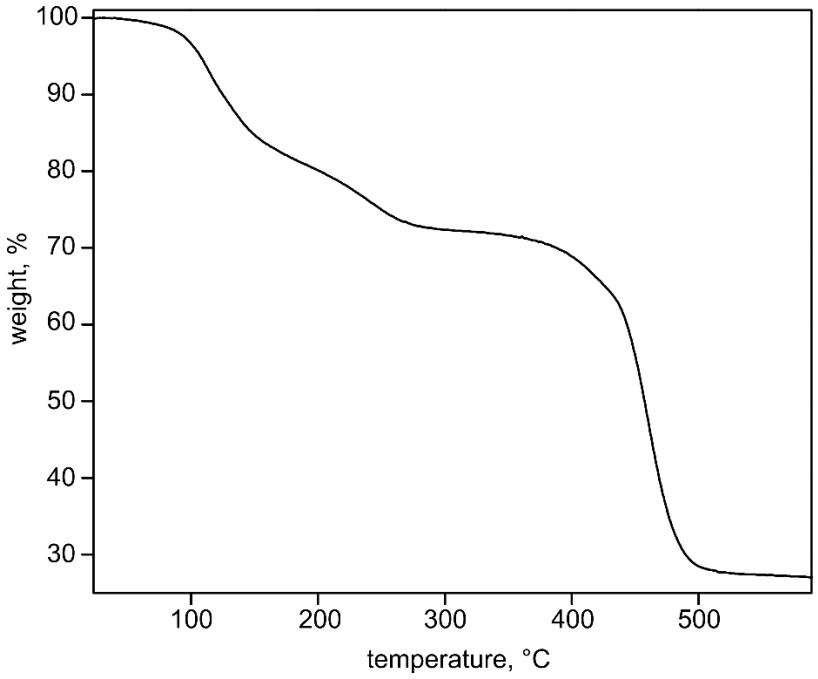

Figure 2.14. Thermogravimetric analysis plot of **1**.

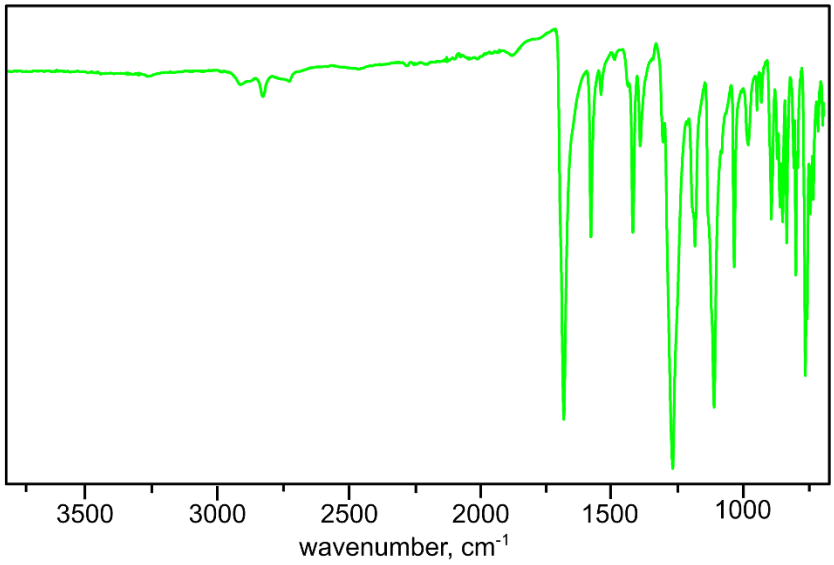

Figure 2.15. The FTIR spectrum of Me_4DFT.

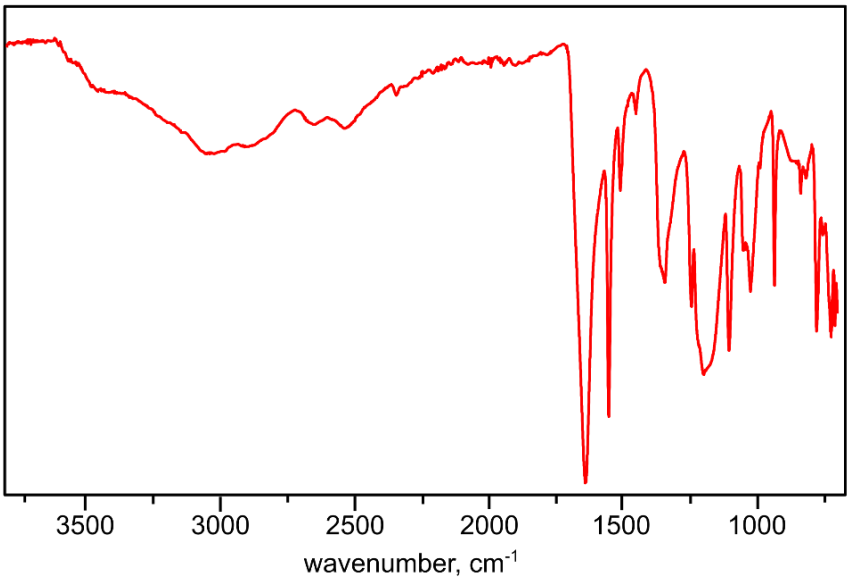

Figure 2.16. The FTIR spectrum of H_4DFT.

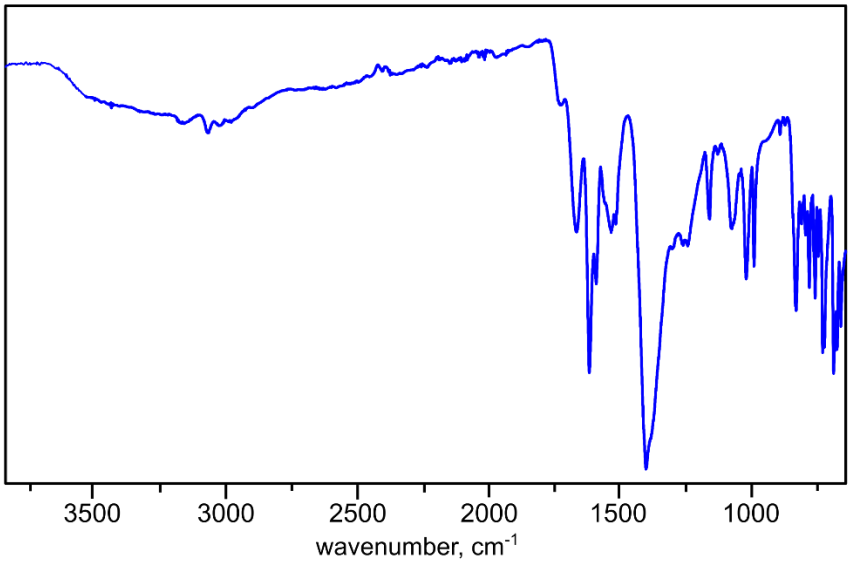

Figure 2.17. The FTIR spectrum of **1**.

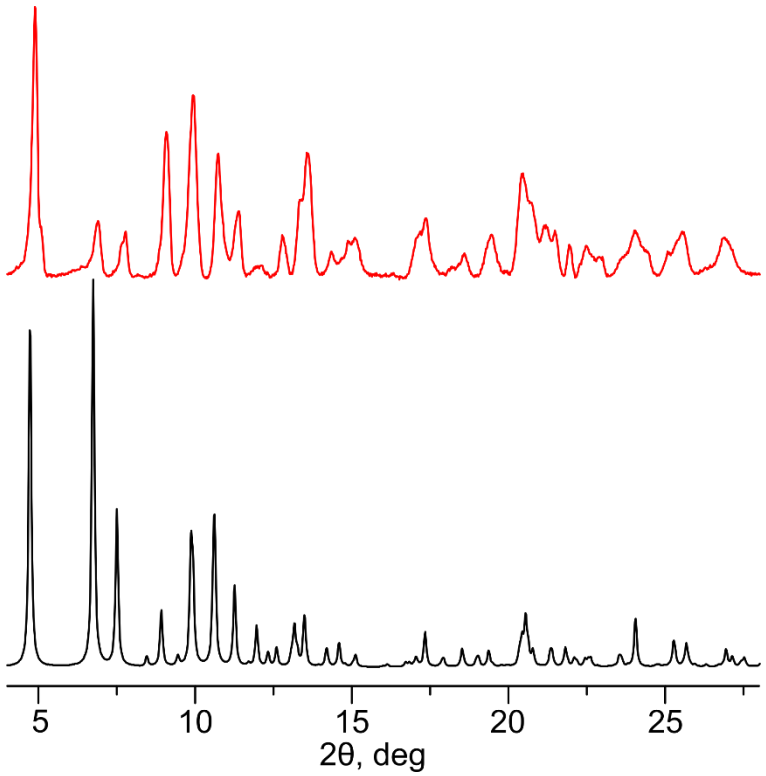

Figure 2.18. PXRD patterns of as-synthesized (red) and simulated (black) **1**.

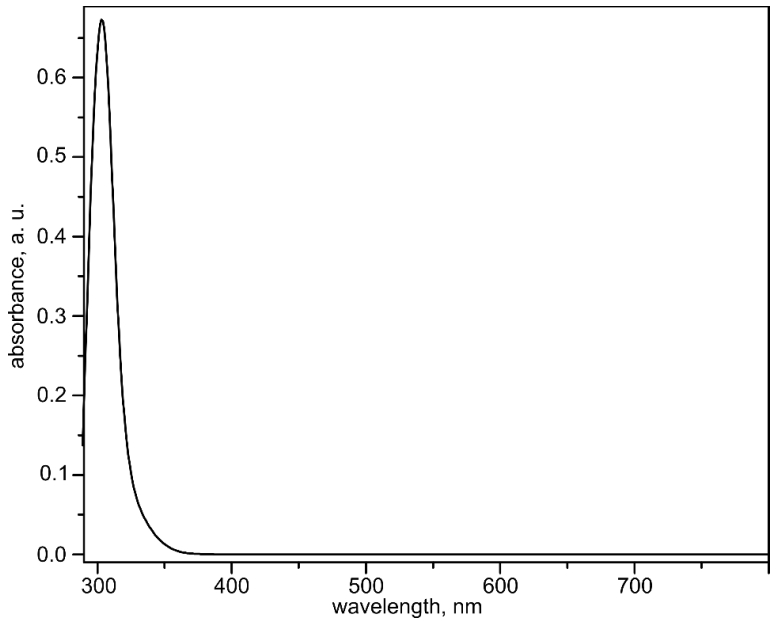

Figure 2.19. UV-Vis spectrum of H_4DFT in THF (1.4×10^{-5} M, λ_{max} = 304 nm).

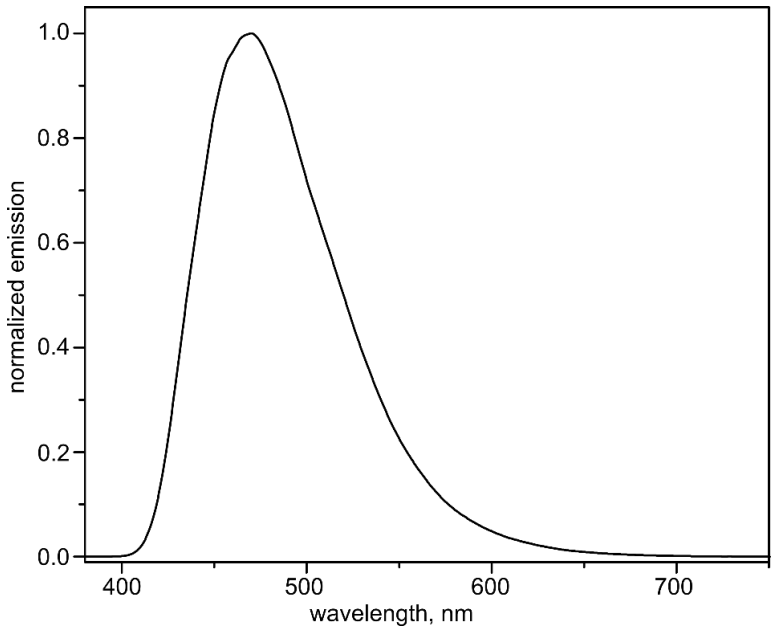

Figure 2.20. Normalized emission spectrum of H_4DFT (λ_{ex} = 408 nm) in the solid state.

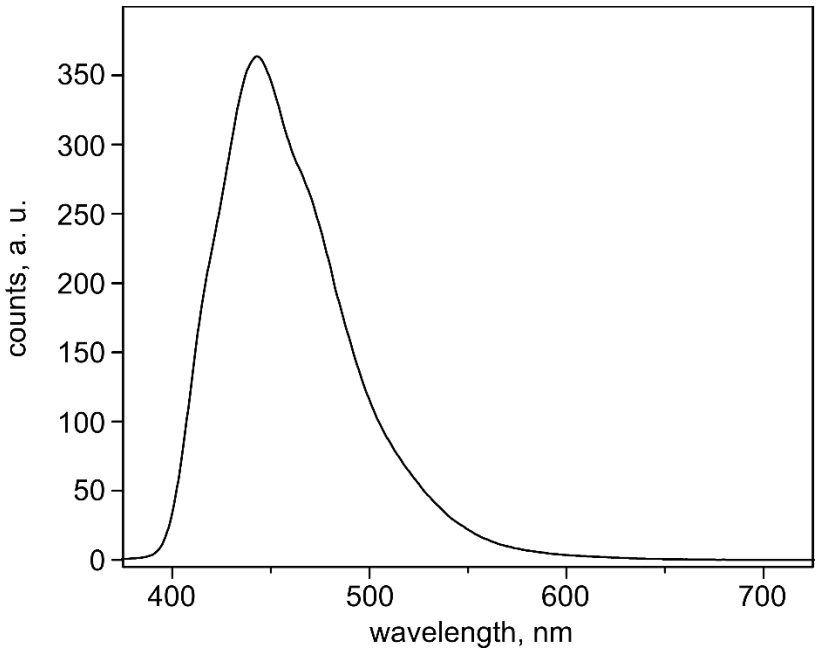

Figure 2.21. Emission of Me_4DFT in THF (1.4×10^{-5} M, λ_{max} = 443 nm).

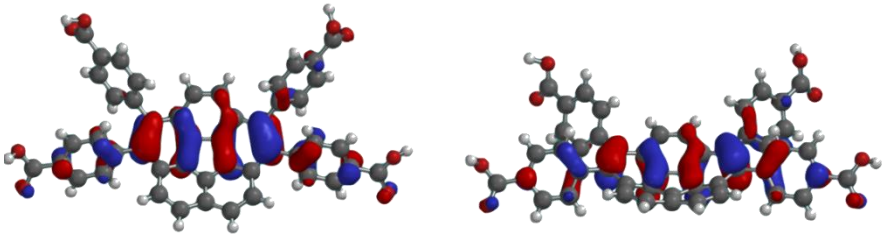

Figure 2.22. HOMO of H_4DFT.

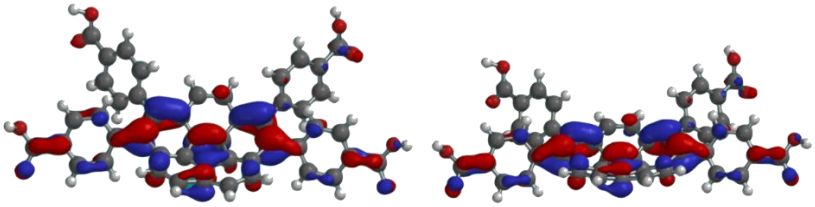

Figure 2.23. LUMO of H_4DFT.

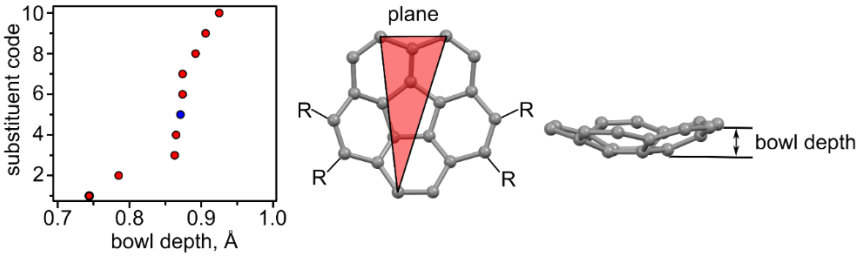

Figure 2.24 and Table 2.1. Bowl depth in the tetrasubstituted corannulene derivatives and **1**

	Substituents, R	Bowl Depth, Å
1	—CH_3	0.744
2	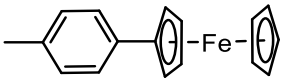	0.785
3	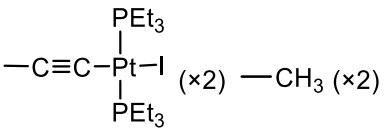	0.863
4	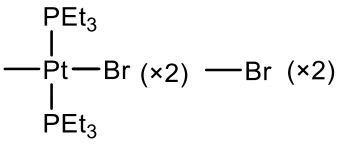	0.863
5	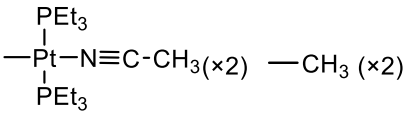	0.865
6	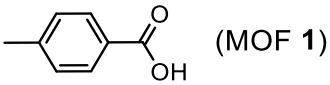	0.871
7	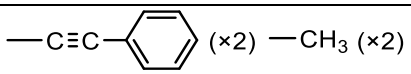	0.874
8	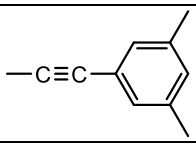	0.874
9	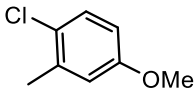	0.892
10	—Br	0.906
11[	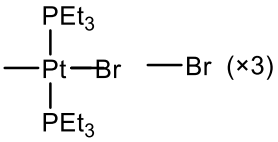	0.925

Table 2.2. X-ray structure refinement data for **1.**

compound	**1**
formula	$C_{50}H_{32}O_{11}Zn_2$
TW	939.49
T,K	100(2)
crystal system	triclinic
space group	P-1
Z	2
a, Å	10.6145(15)
b, Å	13.5062(17)
c, Å	18.996(3)
α, °	100.069(4)
β, °	91.617(5)
γ, °	99.531(5)
V, $Å^3$	2639.8(6)
d,, g/cm^3	1.182
μ, mm^{-1}	0.960
F(000)	960.0
crystal size/mm^3	0.22 × 0.16 × 0.05
theta range	4.354 to 50.266
index ranges	$-12 \le h \le 12$ $-16 \le k \le 16$ $-7 \le l \le 22$
refl. collected	9345
data/restraints/parameters	9345/2/559
GOF on F^2	1.111
Largest peak/hole, e/$Å^3$	1.76/-1.20
Final R indexes [I>= 2 σ (I)]	$R_1 = 0.0943$, $wR_2 = 0.2727$
Final R indexes [all data]	$R_1 = 0.1048$, $wR_2 = 0.2792$

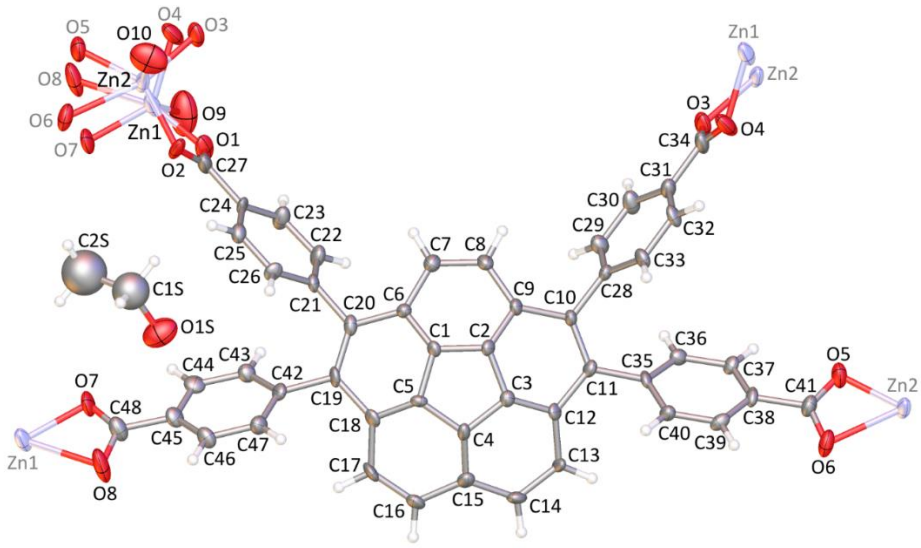

Figure 2.25. Crystal structure of **1**. The asymmetric unit of the crystal, expanded to show coordination environments around zinc and the ligand. Displacement ellipsoids drawn at the 60% probability level. Symmetry-equivalent atoms labeled in grey. O9 and O10 modeled as single oxygen atoms from primarily water.

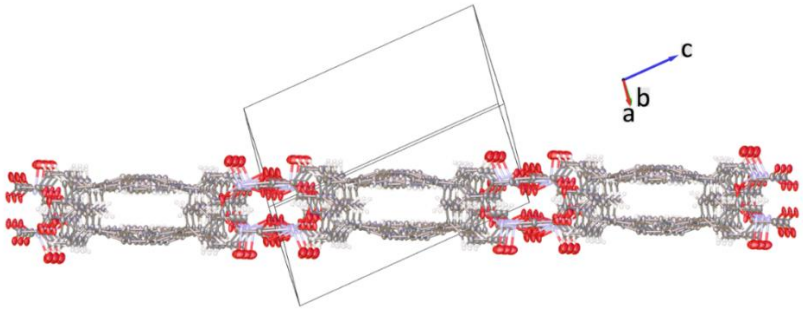

Figure 2.26. Infinite 2D layers of **1** parallel to the crystallographic (11-1) plane.

REFERENCES

1) W. E. Barth ,R. G. Lawton, *J. Am. Chem. Soc*. **1966**, *88*, 380–381.

2) Y. Wu, D .Bandera, R. Maag, A. Linden, K. K. Baldridge, J .S. Siegel, *J. Am. Chem. Soc*. **2008**, *130*, 10729–10739.

3) Y. Wu, J. S. Siegel, Chem. Rev. 2006, 106 ,4843–4867.

4) B. Topolinski, B. M. Schmidt, S. Schwagerus, M. Kathan, D . Lentz, Eur. *J. Inorg. Chem*. **2014**, 5391–5405.

5) C. Dubceac, A. S. Filatov, A. V. Zabula, A. Y. Rogachev, M. A. Petrukhina, *Chem. Eur. J*. **2015**, *21*, 14268–14279.

6) R. Warmbier, A. Quandt, G. Seifert, *J. Phys. Chem. C* **2014**, *118*, 11799–11805.

7) A. M. Butterfield, B. Gilomen, J. S. Siegel, *Org. Process Res. Dev*. **2012**, *16*, 664–676.

8) A. Sygula, F. R. Fronczek, R. Sygula, P. W. Rabideau, M. M. Olmstead, *J. Am. Chem. Soc*. **2007**, *129*, 3842–3843.

9) L. Zoppi, L. Martin-Samos, K. K. Baldridge, *J. Am. Chem. Soc*. **2011**, *133*,14002–14009.

10) G. Valenti, C. Bruno, S. Rapino, A. Fiorani, E. A. Jackson, L. T. Scott, F. Paolucci, M. Marcaccio, *J. Phys. Chem. C* **2010**, *114*, 19467–19472.

11) J. Mack, P. Vogel, D. Jones, N. Kaval, A. Sutton, *Org. Biomol. Chem*. **2007**, *5*, 2448–2452.

12) L. Kobryn, W. P. Henry, F.R. Fronczek, R. Sygula, A. Sygula, *Tetrahedron Lett*. **2009**, *50*, 7124–7127.

13) G. Sande, R. E. Gerald, L. G. Scanlon, C.S. Johnson, R. J. Klingler, J.W. Rathke, J. *New Mater. Electrochem. Syst.* **2000**, *3*, 13–19.

14) H. Yokoi, Y. Hiraoka, S. Hiroto, D. Sakamaki, S. Seki, H. Shinokubo, *Nat. Commun*. **2015**, *6*, 8215.

15) A. V. Zabula, A. Y. Rogachev, M. A. Petrukhina, *Science* **2011**, *333*,1008–1011.

16) Q. Xie, E. Perez-Cordero, L. Echegoyen, *J. Am. Chem. Soc*. **1992**, *114*, 3978–3980.

17) I. V. Kuvychko, S. N. Spisak, Y.-S. Chen, A. A. Popov, M. A. Petrukhina, S. H. Strauss, O. V. Boltalina, *Angew. Chem. Int. Ed*. **2012**, *51*,4939–4492.

18) R. E. Gerald, R. J. Klingler, G. Sande, C. S. Johnson, L. G. Scanlon, J. W. Rathke, *J. Power Sources* **2000**, *89*,237–243.

19) R. Lu, W. Xuan, Y. Zheng, Y. Zhou, X. Yan, J. Dou, R. Chen, J. Pei, W. Weng, X. Cao, *RSC Adv.* **2014**, *4*, 56749–56755.

20) M. C. Stuparu, *Angew.Chem. Int. Ed*. **2013**, *52*, 7786 –7790.

21) E. L. Elliott, G. A. Hernandez, A. Linden, J. S. Siegel, *Org.Biomol. Chem*. **2005**, *3*, 407 –413.

22) Y. Sevryugina, E. A. Jackson, L. T. Scott, M. A. Petrukhina,Inorg.Chim. Acta 2008, 361,3103 –3108.

23) S. N. Spisak, A. V. Zabula, A. S. Filatov, M. A. Petrukhina, *J. Organomet. Chem*. **2015**, *784*, 69–74.

24) A. Ayalon, A. Sygula, P. C. Cheng,M.Rabinovitz, P. W. Rabideau, L. T. Scott, *Science* **1994**, *265*, 1065 –1067.

25) F. Furrer, A. Linden, M. C. Stuparu, *Chem. Eur. J*. **2013**, *19*, 13199 –13206.

26) S. Ito, Y. Tokimaru, K. Nozaki, *Angew. Chem. Int. Ed*. **2015**, *54*, 7256 –7260.

27) S. Da Ros, A. Linden, K. K. Baldridge, J. S. Siegel, *Org. Chem. Front*. **2015**, *2*, 626 – 633.

28) K. K. Tanabe, S.M. Cohen, *Chem. Soc. Rev*. **2011**, *40*, 498 –519.

29) J. Lee, O. K. Farha, J. Roberts, K. A. Scheidt, S. T. Nguyen, J. T. Hupp, *Chem. Soc. Rev*. **2009**, 38, 1450 –1459.

30) D. F. Sava Gallis, L. E. S. Rohwer, M. A. Rodriguez, T. M. Nenoff, *Chem. Mater.* **2014**, *26*, 2943 –2951.

31) K. Lu, C. He, W. Lin, *J. Am. Chem. Soc*. **2014**, *136*, 16712 –16715.

32) D. Pappo, T. Mejuch, O. Reany, E .Solel, M. Gurram, E. Keinan, *Org. Lett*. **2009**, *11*, 1063 –1066.

33) J. L. C. Rowsell, O. M. Yaghi, *Microporous Mesoporous Mater*. **2004**, *73*, 3–14.

34) N. B. Shustova, B. D. McCarthy, M. Dinca, *J. Am. Chem. Soc*. **2011**, *133*, 20126 – 20129.

35) B. Q. Ma, K. L. Mulfort, J. T. Hupp, *Inorg. Chem*. **2005**, *44*, 4912 –4914.

36) T. A. Makal, W. Zhuang, H.-C. Zhou, *J. Mater. Chem. A* **2013**, *1*, 13502 –13509.

37) N. B. Shustova, A. F. Cozzolino, M. Dinca, *J. Am. Chem. Soc*. **2012**, *134*, 19596 – 19599.

38) J. C. Hanson, C. E. Nordman, *Acta Crystallogr. Sect. B* **1976**, *32*, 1147 –1153.

39) A. S. Filatov, A. K. Greene, E. A. Jackson, L. T. Scott, M. A. Petrukhina, *J. Organomet. Chem*. **2011**, *696*, 2877 –2881.

40) R. Maag, B. H. Northrop, A. Butterfield, A. Linden, O. Zerbe, Y. M. Lee, K.-W. Chi, P. J. Stang, J. S. Siegel, *Org. Biomol. Chem*. **2009**, *7*, 4881 –4885.

41) B. D. Steinberg, E. A. Jackson, A. S. Filatov, A. Wakamiya, M. A. Petrukhina, L. T. Scott, *J. Am. Chem. Soc*. **2009**, *131*, 10537 –10545.

42) H. B. Lee, P. R. Sharp, *Organometallics* **2005**, *24*, 4875–4877.

43) M. Juricek, N. L. Strutt, J. C. Barnes, A. M. Butterfield, E. J. Dale, K. K. Baldridge, J. F. Stoddart, J. S. Siegel, *Nat. Chem*. **2014**, *6*, 222 –228.

44) D. Moon, S. Kang, J. Park, K. Lee, R. P. John, H. Won, G. H. Seong, Y. S. Kim, G. H. Kim, H. Rhee, M.S. Lah, *J. Am. Chem. Soc*. **2006**, *128*, 3530 –3531.

45) M. M. Conn, J. Rebek, *Chem. Rev*. **1997**, *97*, 1647 –1668.

46) A. S. Filatov, A. V. Zabula, S. N. Spisak, A. Y. Rogachev, M. A. Petrukhina, *Angew. Chem. Int. Ed*. **2014**, *53*, 140 –145.

47) R. Warmuth, J. Yoon, *Acc. Chem. Res*. **2001**, *34*, 95–105.

48) C. Bruno, R. Benassi, A. Passalacqua, F. Paolucci, C. Fontanesi, M. Marcaccio, E. A. Jackson, L. T. Scott, *J. Phys. Chem. B* **2009**, *113*, 1954 –1962.

49) X. Wang, J. Zhou, H. Fu, W. Li, X. Fan, G. Xin, J. Zheng, X. Li, J. *Mater. Chem. A* **2014**, *2*, 14064 –14070.

50) C. R. Wade, M. Li, M. Dinca, *Angew. Chem. Int. Ed*. **2013**, *52*,13377 –13381.

51) B. D. McCarthy, D. J. Martin, E. S. Rountree, A. C. Ullman, J. L. Dempsey, *Inorg. Chem*. **2014**, *53*, 8350 –8361.

52) D. H. Macias-Ruvalcaba, N. A. Evans, *J. Phys. Chem. B* **2005**, *109*, 14642 –14647.

53) J. Dey, A. Y. Will, R. A. Agbaria, P. W. Rabideau, A. H. Abdourazak, R. Sygula, I. M. Warner, *J. Fluoresc*. **1997**, *7*, 231 –236.

54) A. S. Filatov, E. A. Jackson, L. T. Scott, M. A. Petrukhina, *Angew. Chem. Int. Ed.* **2009**, *48*, 8473 –8476;

55) Y. Hong, J. W. Y. Lam, B. Z. Tang, *Chem. Soc. Rev*. **2011**, *40*, 5361 –5388.

56) J. Luo, Z. Xie, J. W. Lam, L. Cheng, H. Chen, C. Qiu, H. S. Kwok, X. Zhan, Y. Liu, D. Zhu, B. Z. Tang, *Chem. Commun*. **2001**, 1740 –1741.

57) C. Dallaire, I. Kolber, M. Gingras, *Org. Synth.* **2002**, *78*, 42–45.

58) A. M. Butterfield, B. Gilomen, J. S. Siegel, *Org. Process Res. Dev*. **2012**, *16*, 664–676.

59) A. Sygula, G. Xu, Z. Marcinow, P. W. Rabideau, *Tetrahedron* **2001**, *57*, 3637–3644.

60) T. J. Seiders, E. L. Elliott, G. H. Grube, J. S. Siegel, *J. Am. Chem. Soc*. **1999**, *121*, 7804–7813.

CHAPTER 3

HIERARCHICAL CORANNULENE-BASED MATERIALS: ENERGRY TRANSFER AND SOLID-STATE PHOTOPHYSICS

Rice, A. M.; Fellows, W. B.; Dolgopolova, E. A.; Greytak, A. B.; Vannucci, A. K.; Smith, M. D.; Karakalos, S. G.; Krause, J. A.; Avdoshenko, S. M.; Popov, A. A.; Shustova, N. B. *Angew. Chem. Int. Ed.* **2017**, *56*, 4525.

In this chapter, we discuss the first example of a donor–acceptor corannulene-containing hybrid material with rapid ligand-to ligand energy transfer (ET). Additionally, we provide the first time-resolved photoluminescence (PL) data for any corannulene-based compounds in the solid state. Comprehensive analysis of PL data in combination with theoretical calculations of donor–acceptor exciton coupling was employed to estimate ET rate and efficiency in the prepared material. The ligand-to-ligand ET rate calculated using two models is comparable with that observed in fullerene-containing materials, which are generally considered for molecular electronics development. Thus, the presented studies not only demonstrate the possibility of merging the intrinsic properties of p-bowls, specifically corannulene derivatives, with the versatility of crystalline hybrid scaffolds, but could also foreshadow the engineering of a novel class of hierarchical corannulene-based hybrid materials for optoelectronic devices.

While the compromise between strain and aromaticity is a persistent synthetic challenge,[1–3] the bowl shape and electronic properties of corannulene derivatives (buckybowls, Scheme 3.1) imply an unrevealed potential for molecular electronics development similar to their close famous analogues, fullerenes. The main success of the latter in the field of optoelectronics is associated with very fast energy/electron transfer, which has been demonstrated in numerous photophysical studies.[4–6] In contrast, development of buckybowl containing materials with desirable properties is still in its infancy. For instance, during the 50 years since the discovery of the first solution route for corannulene preparation (1966),[1] only around 20 papers[2,7–32] include any photophysical studies, despite nearly 1000 publications focused on corannulene.

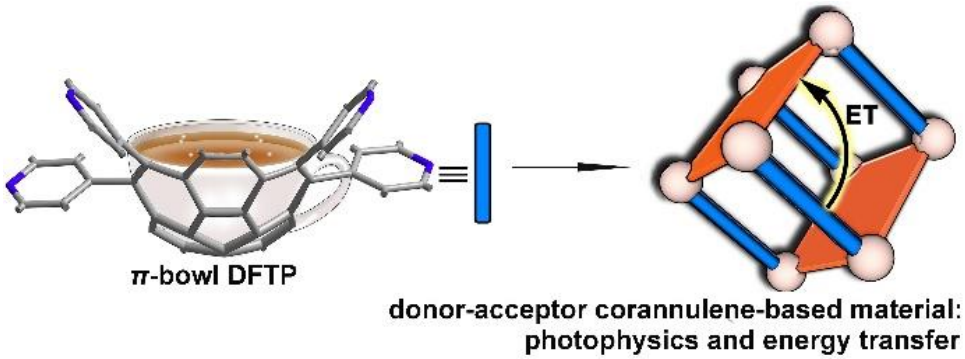

Scheme 3.1. A schematic representation of the hybrid donor-acceptor corannulene-based material with rapid energy transfer prepared from the corannulene-based linker. A blue rod represents the donor while the orange plate is an acceptor.

To the best of our knowledge, there are only two reports[8,10] in the area of corannulene solid-state photophysics. Furthermore, no solid-state time-resolved photoluminescence (PL) data or energy transfer (ET) studies have been reported for any corannulene-containing compounds despite the fact that ET rate and efficiency are crucial fundamental parameters for applications ranging from organic photovoltaics to photocatalysis.[33,34] This gap in material development was the major driving force to initiate the presented study, especially taking into account the recent progress in corannulene chemistry.[35] Our shift from more traditional flat aromatic hydrocarbons[36] towards π-bowls (for example, corannulene) was also driven by 1) their significant dipole moment, 2) the possibility to extend the dimensionality of 3D hybrid frameworks through the p-bowl curvature, 3) potential for charge stabilization on the surface owing to doubly degenerate lowest unoccupied molecular orbitals (LUMOs), 4) anticipated effective intermolecular charge transport, and 5) presence of theoretically predicted super atomic molecular orbitals, which are key factors for intermolecular charge/ energy transport distinct from the conventional mechanisms involving p molecular orbital overlap.[37–41] The latter two facts

were among the main reasons that influenced the choice of the π-bowl, in particular corannulene, in our studies.

Herein, the first example of a donor–acceptor (D–A)corannulene-based material with rapid ligand-to-ligand ET, similar to that observed in fullerene containing compounds will be discussed.[4] The reported hybrid is also the first crystalline buckybowl-containing extended structure, in which control over corannulene(donor)–acceptor orientation is achieved through covalent bonding (Scheme 3.1). A synthetic route to the novel multidentate building block, which provides the necessary versatility for preparation of crystalline corannulene-based multidimensional materials, has also been established. To achieve the required D–A spectral overlap and study ET processes, we utilized the advantages offered by well-defined hybrids including modularity and tunability.[33,34] Based on time-resolved PL data and theoretical studies of D–A exciton coupling, the ET efficiency and rate, key factors for application development in the field of optoelectronics,[42–49] were estimated. Thus, the presented studies provide an opportunity to shed light on ET processes in corannulene-based material for the first time. The initial challenge in the preparation of the aforementioned donor–acceptor corannulene materials mainly lies in synthesis of the versatile corannulene-containing building blocks on gram or larger scales. Therefore, scalability and reaction yield were two initial factors considered for preparation of anovel4,4’,4’’,4’’’-(dibenzo[ghi,mno]fluoranthene-1,2,5,6-tetrayl)tetrapyridinelinker (DFTP, Figure 3.1) Figure 3.2 demonstrates DFTP molecular packing, which consists of layers containing offset “clamshells”, in contrast to many corannulene derivatives exhibiting convex–concave stacking (Experimental, Figure 3.6).[50–52]

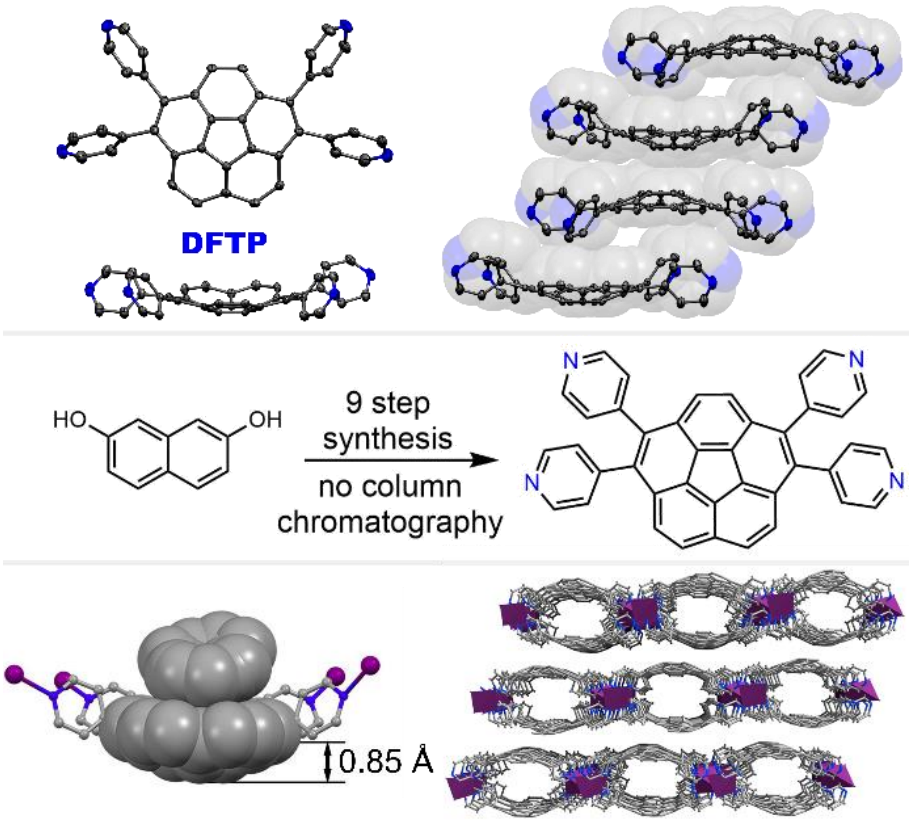

Figure 3.1. (top) The single-crystal X-ray structure and offset "clamshell" crystal packing of DFTP. Displacement ellipsoids are drawn at the 60 % probability level. (middle) A synthetic scheme for the DFTP linker. (bottom) Packing of 1 and a part of 1 showing the bowl depth of DFTP. Space-filling models show the fit of the solvent molecule (benzene) inside **1**. Purple, blue, and grey spheres represent Ag, N, and C atoms, respectively.

Further synthetic and characterization details, including cyclic voltammetry of DFTP, can be found in the Supporting Information (Figures 3.7-3.9, Table 3.2). Since no solid-state time resolved data are available for any corannulene-based materials (including parent corannulene ($C_{20}H_{10}$)), we have studied the photophysical response of DFTP by steady-state and time-resolved photoluminescence spectroscopy, and, therefore, established a reference point for material characterization. The amplitude-weighted average solid-state lifetime was found to be 5.9 ns for DFTP, which is shorter compared

to the measured values for C20H10 itself (9.1 ns) or tetrakis(4-carboxyphenyl)corannulene[8] (9.6 ns, the instrument response function and PL decays are shown in the Supporting Information, Figure 3.11. To test the possibility of DFTP to form extended structures and, therefore, gain structural insights into viable topologies, as well as probe the photophysical properties of DFTP-based materials, we studied the coordination of DFTP to metal ions. The metal was mainly chosen to prevent material photoluminescence quenching (for example, d^0 and d^{10} metals). The synthesized two-dimensional (2D) framework $[Ag_2(DFTP)_2](PF_6)_2 \cdot (C_6H_6)_6 \cdot (CH_3CN)_3$ (**1**) was characterized by single-crystal and powder X-ray diffraction (PXRD), thermogravimetric analysis, and Fourier transform infrared (FT-IR) spectroscopy (Main Text Figure 3.1 and the Supporting Information, Figures 3.12–3.16 and Table 3.3).The single-crystal X-ray studies revealed preservation of the DFTP curvature inside1, despite the possibility to flatten or lock the molecular confirmation with high strain energy imposed by framework rigidity.[53] Indeed, the bowl depth of DFTP inside 1 (0.85 Å, Figure 3.1) is essentially that of parent corannulene (0.87 Å[54]). Owing to the curvature preservation, the DFTP bowl could fit solvent molecules such as benzene (Figure 3.1). Thus, the curvature of corannulene-based linkers could pave the way for an extension of framework dimensionality beyond changing the metal node geometry and linker length. The studies of the photophysical properties of 1 showed ligand-centered luminescence (Figure 3.2a). The emission maximum of 1 was observed at 503 nm (λ_{ex} = 350 nm), similar to that for the free ligand (see above). Analysis of the curves with a reconvolution fit supported a tri-exponential decay model, for which the amplitude-weighted average lifetime of 1 was found to be 3.4 ns (Experimental, Figure 3.11). This lifetime is slightly shorter in

comparison with that(4.1 ns) of another example of a corannulene-based framework, $[Cd_2(C_{48}H_{22}O_8)(DMA)_3]\cdot(DMA)_{1.7}$ (DMA=dimethylacetamide) consisting of tetrakis(4-carboxyphenyl)corannulene linker (see the Supporting Information for Cd-based framework synthesis and characterization, Figures 3.17-3.20, and Table 3.3). As the next step, we applied our findings to the preparation of a crystalline D–A framework, in which the mutual orientation of the donor (D) and acceptor (A) was controlled through covalent bond formation. In general, for synthesis of D–A materials possessing resonance ET, the emission spectrum of D should overlap with the absorption profile of A.[33,55] In our case, to design a material in which the corannulene-based linker, DFTP, could serve as D, we selected 2D $Zn_2(ZnTCPP)$[56] (H_4TCPP = tetrakis(4-carboxyphenyl) porphyrin) as A. Figure 3.2b shows the diffuse reflectance profile of A, which absorbs light up to 650 nm, and therefore provides the necessary spectral overlap of its absorption profile with the emission response of DFTP (D).[55]

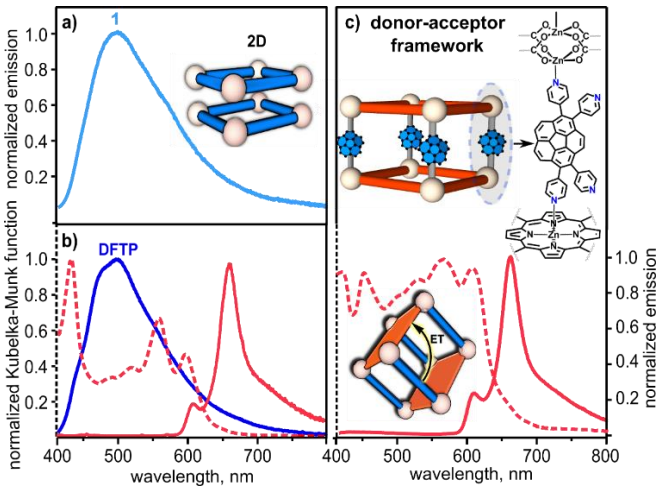

Figure 3.2. (*a*) The normalized emission spectrum of **1**. (*b*) Normalized diffuse reflectance (····) and emission (—) spectra of the porphyrin-based framework (acceptor). The normalized emission spectrum of DFTP (donor, —). (*c*) A schematic representation of donor-

acceptor **2**. The normalized diffuse reflectance (····) and emission (—) spectra of **2**. An excitation wavelength of 350 nm was used to acquire all photoluminescence spectra.

For rational D–A organization, we utilized a two-step synthetic route, which relies on preparation of the Zn_2(ZnTCPP) scaffold, followed by coordinative immobilization of DFTP(D) as a pillar between the layers (Main Text, Figure 3.2c and Experimental, Figure 3.21). In addition to the photophysical requirements, the presence of metal sites, which serve as anchors for coordination of the pyridyl groups, was an additional criterion for framework selection. The coordinative immobilization of DFTP between the Zn_2(ZnTCPP) layers was achieved by coordination of the pyridyl groups of the linker to the metal in the $Zn_2(O_2C^{-})_4$ nodes (Main Text, Figure 3.2c and Experimental, Figure 3.22) and resulted in formation of $[Zn_2(ZnTCPP)(DFTP)_{0.69}(DMF)_{0.31}]\cdot(DMF)_{0.3}\cdot(H_2O)_{26}$ (2). The diffuse reflectance and emission profiles of 2 are shown in Figure 3.2c. The latter shows that the incorporation of both donor and acceptor moieties in 2 resulted in the almost complete disappearance of donor emission (Main Text, Figure 3.2c), which could be attributed to efficient ET. A comprehensive analysis of the prepared D–A material 2 was performed by PXRD, elemental analysis, FT-IR spectroscopy, epifluorescence microscopy, X-ray photoelectron spectroscopy, theoretical modeling, NMR spectroscopy, and mass spectrometry (the latter two techniques were performed on digested samples of 2, Figures 3.22–3.29; more details about characterization of 2 can be found in the Supporting Information). To quantitatively describe the possibility of resonance ET, time-resolved photoluminescence spectroscopy was employed. In particular, analysis of time-resolved PL decays was performed for D(DFTP) in the absence and presence of

A(Zn_2(ZnTCPP)). The emission wavelength channel was configured to capture the DFTP emission and exclude the PL response of the porphyrin-based acceptors. Figure 3.3 shows that the time-resolved photoluminescence curve for coordinatively immobilized DFTP in the presence of the porphyrin containing acceptor decays more rapidly than that of non-coordinated DFTP.

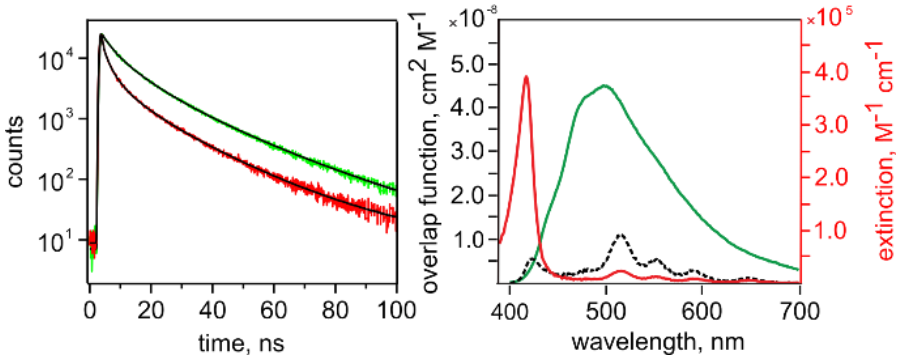

Figure 3.3. (*left*) Fluorescence decays of DFTP in the solid state **(—)** and coordinatively immobilized inside the crystalline donor-acceptor corannulene-based scaffold **(—)**. (*right*) Förster analysis of **2** illustrating the spectral overlap function (- - -, left vertical axis) calculated for the measured emission spectrum of DFTP (—, arbitrary scale) and the molar extinction spectrum of H_4TCPP in ethanol (—, right vertical axis).

Analysis of the curves with a reconvolution fit supported a tri-exponential decay model, which revealed an 85%reduction of the amplitude-weighted average lifetime, from 5.9 ns (DFTP) to 0.85 ns (2). As the first approximation to estimate ET rate (k_{ET}) and efficiency, we applied the classical Förster resonance ET approach [Experimental, Eq. (3.3],[55] in which the corresponding ET efficiency and k_{ET} in 2 were found to be 85% and 1.01×10^9 s^{-1}, respectively. Notably, the observed ligand-to-ligand ET efficiency is approximately 1.7 fold higher than that reported for a recent fullerene-based hybrid material, in which the fullerene-based linker serves as an acceptor.[57] To address the possibility of resonance ET within this model, we estimated the Förster critical transfer radius, R_o, for randomly-oriented point dipoles with the same spectral overlap, *J*, as the DFTP (D) and 2D

porphyrin-based A, which was J=8.3 × 10^{-14} cm^3m^{-1} [Main Text, Figure 3.3, Experimental, Eq. (3.4),].[55] The resulting R_o value of approximately 31 Å [Experimetnal, Eq. (3.5)] is far beyond the D–A distance approximated from the structural data. Therefore, we could attribute the observed changes in the D profile after coordinative immobilization to resonance ET. To apply a more generalized approach, which would allow estimation of k_{ET} beyond the point-dipole model described above, we have also calculated k_{ET} based on $k_{ET} = 2pV^2J_e/\hbar$[58] [where V=D–A exciton coupling and J_e = spectral overlap function,[58] calculated from Experimental, Eq. (3.6)]. While J_e was estimated from the experimental data [Experimental, Eq. (3.6)], *V* was obtained from ab initio calculations based on structural data for 2 [Experimental, Eq. (3.11)]. Previous theoretical studies for a similar class of hybrid systems demonstrated that frontier orbitals have a localized nature near the Fermi level.[57] Similarly, the periodic hybrid material 2 will have no dispersion of relevant bands. Therefore, a truncated model, instead of the complete 3D periodic D–A framework, was utilized for theoretical studies. For estimation of *V*, we employed recent theoretical models focusing on strong orbital coupling, since in our case, D and Aare covalently bonded (the model description and specific equations can be found in the Supporting Information). Figure 3.4 shows an excited state diagram complemented by molecular orbitals contributing to the excitations. The first four excited states of the truncated model of 2 are represented by two-fold degenerated excitations (Q-type and Soret bands) in the H_4ZnTCPP fragment, with energies of approximately 2.2 eV and 3.3 eV, respectively. The excited state that dominated the excitation of DFTP has an energy of 3.7 eV (λ_{ex} = 3.54 eV). Therefore, there are two possible ET mechanisms in the considered model. The first mechanism

involves a direct coupling between S_1^D and S_1^A/S_2^A states. The alternative route includes the formation of a charge transfer (CT) complex, with a CT excitation energy of 3.4 eV. In the latter case, the excitation will still be localized on the DFTP fragment, which could result in PL quenching, assuming large exciton coupling between CT and S_1^A/S_{2A} states. According to our calculations, the S_1^D-S_1^A excitations have a large coupling V=200 meV [Experimental, Eq. (3.11)], while estimated coupling in the case of other possibilities (S_1^D-S_2^A, CT and S_1^A, CT and S_2^A) is much smaller (ca. 1 meV). Moreover, the CT excitation molecular orbitals (HOMO and LUMO-2) are arranged almost orthogonally, which suggests a small probability of electron transfer.

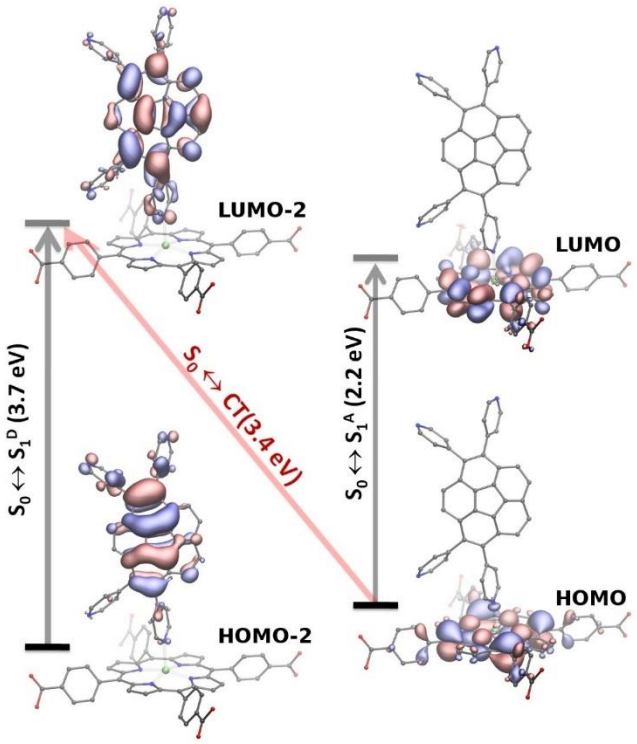

Figure 3.4. A schematic representation of the excitation diagram and most prominent molecular orbitals of each excitation.

Based on those considerations, we may conclude that the ET process, S_1^D-S_1^A, is likely to be a dominating relaxation mechanism in the D–A system. Taking into account the

estimated values of exciton coupling, V, and spectral overlap function, J_e [1.2×10^{-4} eV^{-1}, [Experimental, Eq. (3.6)], we found k_{ET} to be 4.5×10^{10} s^{-1}. Thus, both models for k_{ET} predict rapid ET in the prepared D–A system. In spite of the donating role of DFTP in the presented studies, consideration of corannulene as the smallest bowl-shaped fullerene fragment provoked us to analyze the ET rates previously reported for D–A fullerene-based scaffolds. For instance, k_{ET} in an example with a porphyrin (D)–fullerene (A) system was 5.0×10^{9} s^{-1},[59] which is comparable with the rate observed in our corannulene–porphyrin-based D–A framework. The foregoing results demonstrate the first example of a D–A corannulene-based material 2 with rapid ligand-to-ligand ET. Preparation of 2 was possible due to the synthesis of the novel multidentate building block, DFTP, suitable for the preparation of multidimensional corannulene-based materials such as 1 and 2, available on a gram-scale due to recent achievements in corannulene chemistry. The presented study is also the first report of solid-stale time-resolved PL data collected for any corannulene-containing compound, including parent $C_{20}H_{10}$.Comprehensive analysis of PL decays in combination with theoretical studies of spectral overlap function and D–A exciton coupling revealed that the ligand-to-ligand ET rate estimated from two models is comparable with that observed in fullerene-containing materials, which are generally considered as building blocks for molecular electronics development. In addition, the ligand to-ligand ET efficiency of 2 is 1.7-fold higher than that estimated for the fullerene–porphyrin hybrid material.[57] To summarize, by using theoretical modeling in combination with spectroscopic studies, we shed light on solid-state photophysics (including the possible mechanisms of energy transfer) of a D–A corannulene-containing framework, which is crucial fundamental knowledge required for

the successful implementation of any corannulene derivative in a wide number applications ranging from solar cells to photocatalysts, as well as sensors and photoswitches. Thus, the presented study not only demonstrates the possibility of merging the intrinsic properties of π-bowls with the versatility of metal–organic frameworks but could also foreshadow the engineering of a novel class of corannulene-based hybrid materials for optoelectronic devices.

EXPERIMENTAL SECTION

Materials.

2,7-dihydroxynapthalene (99%, Chem-Impex International, Inc.), *N*,*N*-diethylcarbamoyl chloride (99%, Acros Organics), dichloro(1,3-bis(diphenylphosphino)propane)nickel (99%, Ark Pharm, Inc), methylmagnesium bromide (ACS grade, Alfa Aesar), aluminum bromide (99%, Strem Chemicals, Inc.), oxalyl chloride (98%, Alfa Aesar), Girard's Reagent T (99%, Acros Organics), 3-pentanone (>98%, Tokyo Chemical Industry Co, LTD), 2,5-norbornadiene (97%, Alfa Aesar), *N*-bromosuccinimide (96%, Oakwood Chemical), benzoyl peroxide (97%, Sigma-Aldrich), pyridine-4-boronic acid (95%, Matrix Scientific), sodium carbonate (ACS grade, Macron), tetrakis(triphenylphosphine)palladium(0) (98%, Matrix Scientific), sodium bicarbonate (ACS grade, Macron), tetrakis(4-carboxyphenyl)porphyrin (97%, FrontierScientific), *N*,*N*-diethylformamide (>99%, TCIAmerica), *N*,*N*-dimethylformamide (ACSgrade, BDH), dimethylacetamide (reagent grade, Alfa Aesar), zinc nitrate hexahydrate (technical grade, Ward's Science), cadmium nitrate tetrahydrate (technical grade, Ward's Science), silver hexafluorophosphate (99%, Strem Chemicals, Inc.), pyridine (99+%, Alfa Aesar), 1,4-dioxane (99+%, Alfa Aesar), diethyl ether (HPLC

grade, Fisher Scientific), hydrochloric acid (ACS grade, EMD Chemicals), hexane (ACS grade, BDH), diethyl ether (99%, Acros Organics), isopropanol (ACS grade, BDH), dichloromethane (ACS grade, Macron), methanol (HPLC grade, Fisher Scientific), acetic acid (ACS grade, Fisher Scientific), acetic anhydride (99%, Chem-Impex International, Inc.), cyclohexane (reagent grade, Malinckrodt), carbon tetrachloride (99%, Sigma-Aldrich), ethanol (Decon Laboratories, Inc.), chloroform (ACS grade, Macron), tetrahydrofuran (ACS grade, EMD Chemicals), benzene (ACS grade, EMD Chemicals), acetonitrile (ACS grade, Fisher Scientific), sodium hydroxide (ACS grade, Fisher Scientific), anhydrous magnesium sulfate (reagent grade, J.T. Baker® Chemicals), potassium hydroxide (ACS grade, Fisher Scientific), silica gel (Macron), sodium chloride (ACS grade, Fisher Scientific), chloroform-*d* (Cambridge Isotope Laboratories, Inc.), and DMSO-d_6 (Cambridge Isotope Laboratories, Inc.) were used as received.

The compounds 2,7-bis(diethylcarbamoyloxy)naphthalene (Experimetnal, Scheme 3.2, **S1**),[60] 2,7-dimethylnapthalene (Experimental, Scheme 3.2, **S2**),[60] acenaphthenequinone (Experimental, Scheme 3.2, **S3**),[61] 1,6,7,10-tetramethylfluoranthene (Experimental, Scheme 3.2, **S6**),[61] 1,6,7,10-tetrakis(dibromomethyl)fluoranthene (Experimental, Scheme 3.2, **S7**),[62] 1,2,7,8-tetrabromocorannulene (Experimental, Scheme 3.2, **S8**),[63] and Zn_2(ZnTCPP) [H_4TCPP = tetrakis(4-carboxyphenyl)-porphyrin][64] were prepared according to the reported procedures. Parent corannulene, $C_{20}H_{10}$, was prepared according to a literature procedure.[61] H_4DFT was prepared according to our recently published procedure.[64]

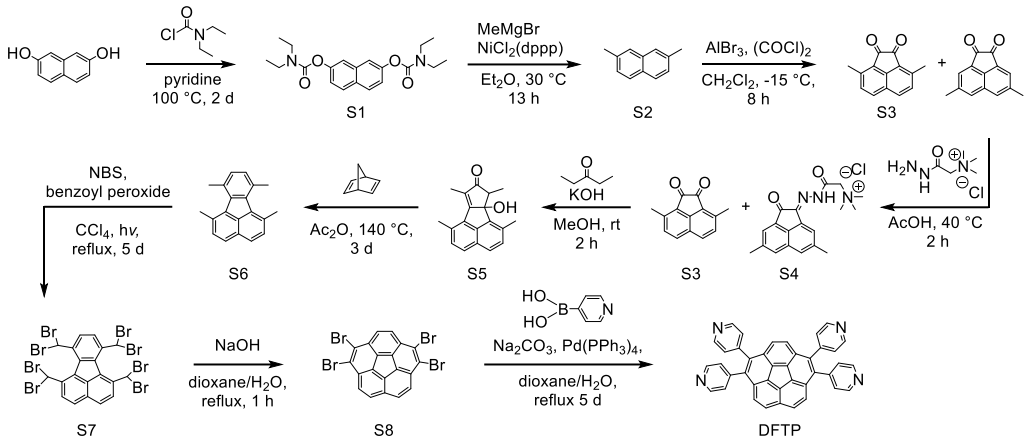

Scheme 3.2. Synthesis of DFTP.

Synthesis.

4,4',4'',4'''-(dibenzo[ghi,mno]fluoranthene-1,2,5,6-tetrayl)tetrapyridine ($C_{40}H_{22}N_4$, *DFTP, Scheme 3.2).*

The prepared 1,2,7,8-tetrabromocorannulene (0.200 g, 0.353 mmol; Scheme S1),[2] pyridine-4-boronic acid (0.869 g, 7.07 mmol), sodium carbonate (1.50 g, 14.1 mmol), and tetrakis(triphenylphosphine)palladium(0) (0.163 g, 0.141 mmol) were heated at reflux in a dioxane/water mixture (20 mL/8 mL) under nitrogen for 5 d. The reaction mixture was cooled to room temperature, followed by the removal of dioxane under reduced pressure, which resulted in a beige solid. The beige solid was then dissolved in 2 M NaOH and dichloromethane, and the aqueous layer was extracted with dichloromethane (3 × 15 mL), washed with 2 M NaOH (2 × 15 mL), and the dichloromethane was removed under reduced pressure. To the resulting brown solid, 3 M HCl (25 mL) was added until most of the solid dissolved. The now acidic reaction mixture was washed with dichloromethane (3 × 15 mL), and then neutralized with 50 wt% NaOH until the formation of a beige precipitate that was then filtered and washed

with saturated aqueous $NaHCO_3$ and water. After drying under vacuum, a yellow solid, DFTP, was isolated in 70% yield. ^{1}H NMR (DMSO-d_6, 300 MHz): δ = 7.37 (8H, m), 7.55 (2H, d, J = 6.6), 7.55 (2H, s) (note: singlet and doublet overlap at 7.55 but are distinguishable), 8.09 (2H, d, J = 6.6), 8.57 (8H, m) (Figure 3.7). ^{13}C NMR (DMSO-d_6, 101 MHz): δ =126.50, 127.17, 127.64, 129.17, 129.42, 129.73, 131.45, 133.97, 134.83, 134.91, 136.61, 137.16, 145.49, and 149.67 (Figure 3.7). IR (neat, cm^{-1}): 669, 694, 722, 757, 790, 802, 813, 825, 834, 852, 881, 993, 1068, 1217, 1407, 1544, and 1594. (Figure 3.24). HRMS (ESI) m/z found: 559.1920 $[M+H]^+$, calc.: 559.1917.

Synthesis of $[Ag_2(C_{40}H_{22}N_4)_2](PF_6)_2 \cdot (C_6H_6)_6 \cdot (CH_3CN)_3$ ***(1).***

In a glass tube (diameter = 10 mm; length = 75 mm), a $AgPF_6$ solution in acetonitrile (7 mg/1 mL) was carefully layered on top of a solution of DFTP in benzene (8 mg/1 mL) and capped with a septum. After one day, transparent yellow crystals (**1**) were isolated in 25% yield. The obtained crystals were suitable for single-crystal X-ray analysis (Figures 3.1 (main text), Experimental, Figures 3.12 and 3.13). Table 3.3 contains crystallographic refinement data for **1**. IR (neat, cm^{-1}): 676, 830, 1012, 1036, 1067, 1218, 1418, 1480, 1544, 1604, and 3036 (Figure 3.15). The PXRD pattern and thermogravimetric analysis plot of **1** are shown in Figures 3.14 and 3.16. More detailed description of the crystal structure can be found in the *X-ray Crystal Structure Determination* section (vide infra). The epifluorescence microscopy image of **1** is shown in Figure 3.25.

Synthesis and structural analysis of $[Zn_2(ZnTCPP)(DFTP)_{0.69}(DMF)_{0.31}] \cdot (DMF)_{0.3} \cdot (H_2O)_{26}$ ***(2)***.

In a 0.5 dram vial, Zn_2(ZnTCPP) (5.0 mg, 5.1 μmol) was added into a solution of DFTP (0.020 g, 0.34 mmol) in 0.5 mL DMF. After 3 days, the mother liquor was replaced with fresh DMF to remove any excess of the DFTP ligand. The described procedure was repeated five times to thoroughly wash away the residual ligand. As a result, the purple square plate crystals of **2** (2.2 mg, 1.2 μmol) were isolated in 23% yield. IR (neat, cm^{-1}): 660, 760, 865, 1064, 1093, 1256, 1388, 1408, 1440, 1496, 1597, and 1657 (Figure 3.24). Comparison of the FTIR spectra of Zn_2(ZnTCPP), DFTP, and **2** are shown in Figure 3.24. The composition of **2** was determined based on a combination of elemental analysis, ^{1}H NMR spectroscopy, and mass spectrometry, in which the latter two were performed on a digested sample of **2**. The ^{1}H NMR spectroscopy has been also used to determine the degree of the DFTP installation between porphyrin-based layers. To study the composition of **2** by ^{1}H NMR spectroscopy, a solution of 500 μL DMSO and 5 μL of concentrated hydrochloric acid was added to ~ 5 mg of **2**, followed by sonication until complete sample dissolution. For mass-spectrometry analysis, the washed crystals of **2** were digested in 500 μL of chloroform by the addition of 3 μL of concentrated HCl. After solvent removal under reduced pressure, the obtained powder was subjected to mass-spectrometry analysis. The spectroscopic studies of digested **2** are shown in Figure 3.26.

Structural analysis was performed using the PXRD pattern of **2** in combination with the single-crystal data for Zn_2(ZnTCPP) (or PPF-1), unit cell paramenters obtained for **2** (by single-crystal X-ray diffraction), and the single-crystal data collected for the

DFTP ligand and framework **1**. As a starting point for our simulation, we utilized the coordinates of the two dimensional porphyrin-based layers in the Zn_2(ZnTCPP) structure and the size of the DFTP linker. The linker size was determined in the present work based on single-crystal X-ray analysis of the structures of DFTP and the silver-containing framework, **1**. As shown in Figure 3.22, **2** consists of two-dimensional layers, made from paddlewheel shaped $Zn_2(O_2C^-)_4$ secondary building units bridged by $TCPP^{4-}$ ligands, which are connected by DFTP pillars. Pillar installation resulted in an increase of interlayer distances from 2.8 Å to 14.9 Å (Figures 3.21 and 3.22), which resulted in the increase of the unit cell parameter *c*. Indeed, based single-crystal X-ray analysis we confirmed an increase of *c* from 17.49 Å to 28.71 Å. The latter value is also consistent with the N···N distance in DFTP determined from the crystal structure (Figure 3.5). All possible orientations of DFTP coordinated to metal nodes within the scaffold of **2** were taken into consideration, and the orientation with the best fit to the experimental data, shown in Figure 3.23, was used. As a result, the simulated PXRD of **2** is consistent with the experimental pattern of **2** (Figure 3.23). Due to the size of the solvent DMF molecules (~2–4 Å) used for synthesis of **2**, solvent coordination cannot be responsible for the drastic increase of the interlayer distance. Based on the similarity of the pillar size with the interlayer distance (in combination with ^{1}H NMR spectroscopy and ESI MS), we conclude DFTP immobilization. In addition, we have performed experiments of immobilization on just parent corannulene, but no changes in the PXRD pattern, as well as the presence of corannulene in the digested ^{1}H NMR spectra, were observed. Furthermore, a shift corresponding to an increase of the interlayer distance was also supported by the PXRD analysis performed on the bulk of **2** (Figure 3.23). We have also

studied the N 1s region of the XPS spectra of DFTP, zinc-coordinated DFTP (prepared by stirring of DFTP with access of zinc nitrate as a control), and framework **2**. As shown in Figure 3.29, the N 1s photoelectron peak consists of one component at a binding energy 398.7 eV, while for the prepared zinc-DFTP salt, it has been shifted and recorded at 399.7 eV, which we attributed to Zn–N bond formation. For framework **2**, the N 1s consists of three main components (Figure 3.29), in which their binding energies in comparison with the N 1s regions in the spectra of DFTP, zinc-coordinated DFTP, and literature analysis, could be attributed to Zn–N bond formation (399.7 eV), the pyridyl groups in free DFTP (398.7 eV), and contribution from the porphyrin fragment (400.6 eV).

In addition to the acquired experimental data, we have also performed modeling of the structure of **2**. We have optimized the unit cell parameter, *c*, at the DFTB level of theory using CP2K code to fit the DFTP linker. For both systems, the porphyrin-based 2D structure and **2**, we have made a molecular dynamic simulation at DFTB level of theory. The systems were integrated with a step size 1 fs for about 100 ps in the canonical ensemble (Nosé-Hoover thermostat). For the runs at room temperature for 100 ps, the trajectories do not show any signs of significant structural changes, which confirm that the reported structures are robust upon external perturbations. The simulated structure of **2** is shown in Figure 3.28. The PXRD spectrum of modeled **2** perfectly matches the experimental one (Figure 3.27).

Photophysical properties of **2** were studied by diffuse reflectance, and steady-state and time-resolved photoluminescence spectroscopy (Figures 3.2 and 3.3). The epifluorescence microscopy image of **2** is shown in Figure 3.25.

Synthesis of Cd-based MOF $[Cd_2(C_{48}H_{22}O_8)(C_4H_9NO)_3]\cdot(C_4H_9NO)_{1.7}$.

In a 20 mL vial, $Cd(NO_3)_2\cdot 5H_2O$ (69.3 mg, 0.224 mmol) and prepared H_4DFT (12.3 mg, 0.0169 mmol) were dissolved in 1.5 mL DMA followed by sonication. The resulted solution was heated at 100 °C for 48 h. Yellow crystals were isolated in 49% yield. IR (neat, cm^{-1}): 678, 720, 730, 776, 801, 804, 854, 871, 926, 962, 1018, 1101, 1178, 1262, 1387, 1547, 1589, 1641, 2930, and 3049. The prepared compound was characterized by single-crystal X-ray diffraction. The detailed picture of the three-dimensional Cd-based framework is shown in Figure 3.17. Table 3.3 contains crystallographic refinement data. More detailed description of data collection well as structure determination could be found in the *X-ray crystal structure determination* section (vide infra). Comprehensive analysis of the prepared framework also includes powder X-ray diffraction and FT-IR spectroscopy (Figures 3.18-3.19). Photophysical properties of Cd-based framework were studied by diffuse reflectance and steady-state and time-resolved photoluminescence spectroscopy (Figures 3.20 and 3.11).

X-ray crystal structure determination.

Single-crystal X-ray structure of DFTP, $C_{40}H_{22}N_4$. X-ray intensity data from a colorless wedge-shaped plate were collected at 100(2) K using a Bruker D8 QUEST diffractometer equipped with a PHOTON 100 CMOS area detector and an Incoatec microfocus source (Mo K_α radiation, $\lambda = 0.71073$ Å).[7] The raw area detector data frames were reduced and corrected for absorption effects using the SAINT+ and SADABS programs.[7] Final unit cell parameters were determined by least-squares refinement of 6674 reflections taken from the data set. The structure was solved by direct methods with SHELXT.[8] Subsequent difference Fourier calculations and full-matrix least-squares

refinement against F^2 were performed with SHELXL-2014[8] using OLEX2.[9]

The compound crystallizes in the monoclinic system. The pattern of systematic absences in the intensity data was consistent with the space group $P2_1/c$, which was confirmed by structure solution. The asymmetric unit consists of one molecule. All non-hydrogen atoms were refined with anisotropic displacement parameters. Hydrogen atoms were located in Fourier difference maps before being placed in geometrically idealized positions included as riding atoms with d(C-H) = 0.95 Å and U_{iso}(H) = 1.2U_{eq}(C). The largest residual electron density peak in the final difference map is 0.33 e^-/Å^3, located 0.96 Å from H40.

Single-crystal X-ray structure of ***1****,* $Ag_2(C_{40}H_{22}N_4)_2](PF_6)_2 \cdot (C_6H_6)_6 \cdot (CH_3CN)_3$.

Crystals of the compound form as light yellow prisms with well-developed facets. X-ray intensity data were collected at 100(2) K using a Bruker D8 QUEST diffractometer equipped with a PHOTON 100 CMOS area detector and an Incoatec microfocus source (Mo K_α radiation, λ = 0.71073 Å).[7] The raw area detector data frames were reduced and corrected for absorption effects using the SAINT+ and SADABS programs.[7] Final unit cell parameters were determined by least-squares refinement of 9498 reflections taken from the data set. The structure was solved by direct methods with SHELXT.[8] Subsequent difference Fourier calculations and full-matrix least-squares refinement against F^2 were performed with SHELXL-2014[8] using OLEX2.[9]

The compound crystallizes in the triclinic system. The space group P-1 (No. 2) was assumed and confirmed by structure solution. The asymmetric unit consists of two crystallographically independent silver atoms, two $C_{40}H_{22}N_4$ ligands, two

hexafluorophosphate anions, six benzene molecules, and three acetonitrile molecules. One PF_6^- anion (P2) is disordered and was modeled with three closely separated orientations A/B/C. The geometry of each PF_6^- disorder component was restrained to be similar to that of the ordered anion (P1) using SHELX SAME instructions. Total site population was constrained to unity. Atoms appearing nearly superimposed were assigned equal displacement parameters, and displacement parameters for these atoms were further restrained to a reasonable form using rigid-bond restraints (SHELX RIGU). Two of the six independent benzene molecules are disordered; one (C131–C136/C231–C236) over two positions and the other (C125–C130/C225–C230/C325–C330) over three positions. Each disordered benzene component was refined as a rigid hexagon with *d*(C–C) = 1.39 Å and the total site population was constrained to one. Atoms C125–C130/C225–C230/C325–C330 were refined with a common isotropic displacement parameter. Two of the three acetonitrile molecules are also disordered, and were modeled with two (N102/N202) or three (N103/N203/N303) positions, with the total site population constrained to one. Acetonitrile atoms (N103/N203/N303) were refined with a common isotropic displacement parameter. Molecular geometry of the disordered acetonitrile molecules was restrained to be similar to that of the ordered acetonitrile using SHELX SAME instructions. In total, 381 restraints were used in disorder modeling. All non-hydrogen atoms were refined with anisotropic displacement parameters except for disordered solvent atoms (isotropic). Hydrogen atoms were placed in geometrically idealized positions and included as riding atoms with *d*(C-H) = 0.95 Å and U_{iso}(H) = 1.2U_{eq}(C) for arene hydrogen atoms and *d*(C-H) = 0.98 Å and U_{iso}(H) = 1.5U_{eq}(C) for methyl hydrogens. The largest residual electron density peak in the final difference map

is 0.91 $e^-/Å^3$, located 0.82 Å from Ag_2.

Single-crystal X-ray structure of $[Cd_2(C_{48}H_{22}O_8)(C_4H_9NO)_3]\cdot(C_4H_9NO)_{1.7}$.

The crystals grown as light yellow blocks were transferred rapidly to the diffractometer cold stream. Several crystals were examined for quality, and all were found to be twinned by non-hydrogen based on manual examination of the area detector diffraction pattern and indexing difficulties. The selected data crystal gave relatively sharp diffraction peaks and could be indexed to two identical unit cells with different orientations. Using the Bruker Cell_Now program, [7] all reflections from a set of 1035 from the data crystal were indexed entirely to two domains with the reported unit cell parameters. The derived twin law, relating indices of one domain to those of the other, is (-1 0 -0.577 / 0 -1 0 / 0 0 1), corresponding to a 180° rotation about the real-space [001] axis. X-ray intensity data were collected at 100(2) K using a Bruker D8 QUEST diffractometer equipped with a PHOTON 100 CMOS area detector and an Incoatec microfocus source (Mo K_α radiation, λ = 0.71073 Å).[7] The raw area detector data frames were reduced and corrected for absorption effects using the SAINT+ and TWINABS programs.[7] TWINABS also constructed SHELX HKLF-4 and HKLF-5 format reflection files for solution and refinement, respectively. Final unit cell parameters were determined by least-squares refinement of 9785 reflections in the range 4.48° < 2θ < 52.63° taken from both twin domains of the crystal. The structure was solved by dual-space direct methods with SHELXT.[8] Subsequent difference Fourier calculations and full-matrix least-squares twin refinement against F^2 were performed with SHELXL-2014[8] using OLEX2.[9] The major twin volume fraction refined to 0.574(1).

The compound crystallizes in the monoclinic system. The pattern of systematic

absences in the intensity data was consistent with the space groups *C*2/*c* and *Cc,* the former of which was confirmed by structure solution. The asymmetric unit consists of two independent cadmium atoms, one $C_{48}H_{22}O_8^{4-}$ ligand, three DMA ligands coordinated to Cd1, and three non-coordinated interstitial DMA molecules. Phenyl ring (C28-C33) is disordered over two orientations with refined occupancies A/B = 0.49(2) / 0.51(2). Atomic coordinates of the 'pivot atoms' (C28 and C31 A/B) and the anisotropic displacement parameters (*adp*s) of pairs of nearly superimposed atoms (*e.g*. C30A/C30B) were held equal. Ring geometry was restrained to be similar to that of ordered ring C42-C47, and the *adp*s for these atoms were further restrained to adopt a spherical shape (SHELX ISOR). All coordinated and interstitial DMA molecules are disordered except for O11/N11/C51-C54. Two coordinated DMA ligands each occupy two positions with occupancies O12A/O12B = 0.70(1)/0.30(1) and O13A/O13B = 0.47(1)/0.53(1). All disordered DMA molecules were restrained to a similar geometry as the ordered DMA using SHELX SAME instructions. Group occupancies of the interstitial DMA molecules (O101, O102/O103, O104) were allowed to refine freely; those of the coordinated disordered DMA molecules were restrained to sum to unity. All non-hydrogen atoms of the $Cd_2(C_{48}H_{22}O_8)(DMA)_3$ framework were refined with anisotropic displacement parameters except for DMA atoms N13/C59-C62 A/B (isotropic). Interstitial DMA atoms were refined with a common isotropic displacement parameter for each group. Hydrogen atoms were placed in geometrically idealized positions included as riding atoms with d(C-H) = 0.95 Å and U_{iso}(H) = 1.2 U_{eq}(C) for aromatic hydrogen atoms and d(C-H) = 0.98 Å and U_{iso}(H) = 1.5U_{eq}(C) for methyl hydrogens. The largest residual electron density peak in the final difference map is 1.62 $e^-/Å^3$, located 1.03 Å from the Cd_2.

Fluorescence spectroscopy.

An Edinburgh FS5 fluorescence spectrometer equipped with a 150 W Continuous Wave Xenon Lamp source for excitation was used to acquire steady-state emission spectra. Emission measurements on solid samples were collected on powders of the desired materials placed inside a 0.5 mm quartz sample holder using the front-facing module. Fluorescence lifetimes were measured using a Mini-τ lifetime spectrometer from Edinburgh Instruments equipped with a 365-nm picosecond-pulsed-light-emitting diode (EPLED 365). Epifluorescence microscopy images were collected on an Olympus BX51 microscope with a 120 W mercury vapor short arc excitation light source (Figure 3.25).

Fitting of fluorescence decays. Energy transfer efficiency, Φ_{ET}.

The fluorescence decays for DFTP and 2 shown in Figure 3 (main text) were fit with the triexponential function:

$$\mathrm{I}(t) = \int_{-\infty}^{\mathrm{t}} \mathrm{IRF}(t') \sum_{\mathrm{i}=1}^{\mathrm{n}} B_{\mathrm{i}} \mathrm{e}^{\left[-\frac{t-t'}{\tau_i}\right]} dt' \qquad \text{(eq. 3.1)}$$

where τ and B are lifetime and amplitude, respectively.

The amplitude-weighted average fluorescence lifetimes were calculated based on the following equation:

$$\langle \tau_{\mathrm{av}} \rangle = \frac{B_1\tau_1 + B_2\tau_2 + B_3\tau_3}{B_1 + B_2 + B_3} \qquad \text{(eq. 3.2)}$$

	B_1	τ_1, ns	B_2	τ_2, ns	B_3	τ_3, ns	$<\tau_{av}>$, ns
DFTP	0.0094	2.71	0.0504	3.64	0.0765	7.81	5.91
2	0.289	0.115	0.128	0.878	0.0343	6.91	0.85

Energy transfer efficiency, Φ_{ET}. Spectral overlap function, J. Förster radius, R_o.

The energy transfer efficiencies, Φ_{ET}, were calculated by the following equation:

$$\Phi_{\mathrm{ET}} = \frac{k_{\mathrm{e}}}{(k_{\mathrm{r}} + k_{\mathrm{nr}} + k_{\mathrm{e}})} = \frac{k_{\mathrm{e}}}{(k_{\mathrm{o}} + k_{\mathrm{e}})} \qquad \text{(eq. 3.3)}$$

where k_r, k_{nr}, and k_e = radiative decay, non-radiative decay, and energy transfer constants, respectively. The k_o and k_e values were found from the lifetimes for the donor molecule (τ_D) and the donor molecule in the presence of acceptor ($\tau_{D\text{-}A}$), which are $\tau_D = 1/k_o$ and $\tau_{D\text{-}A} = 1/(k_o+k_e)$, respectively. The spectral overlap function (J) was calculated from the experimental donor emission and acceptor absorption using the following equation:

$$J = \int f(\lambda) d\lambda, f(\lambda) = F_D(\lambda)\varepsilon_{\mathrm{A}}(\lambda)\,\lambda^4 \qquad \text{(eq. 3.4)}$$

where $F_D(\lambda)$ is the donor emission spectrum normalized to unit area and $\varepsilon_A(\lambda)$ is the molar extinction spectrum of the acceptor (Figure 3 (main text)). The calculated overlap function has been used for estimation of corresponding Förster critical radius (R_o), i.e., the distance at which Φ_{ET} is 50%:

$$R_{\mathrm{o}}(\mathrm{cm}) = (8.79 \times 10^{-25} \times \kappa^2 n^{-4} Q_{\mathrm{d}} J)^{\frac{1}{6}} \qquad \text{(eq. 3.5)}$$

where $Q_d = k_r \times \tau_D$ (k_r = donor radiative rate), κ is an orientation factor, and n is the refractive index. The function f(λ) is plotted in Figure 3.3.

For the more detailed energy transfer calculation described below, a normalized spectral overlap function J_e with units of eV^{-1} was calculated as follows:

$$J_e = \frac{\int_0^\infty f(\lambda)d\lambda}{\hbar c \int_0^\infty F_D(\lambda)\lambda^3 d\lambda \int_0^\infty \frac{\epsilon_A}{\lambda} d\lambda} \qquad (eq. 3.6)$$

where $F_D(\lambda)$ and $\varepsilon_A(\lambda)$ are the emission spectra of the donor and absorption spectrum of the acceptor, respectively.

Other Physical Measurements.

NMR spectra were obtained on the Bruker Avance III-HD 300 and Bruker Avance III 400 MHz NMR spectrometers. ^{13}C and ^{1}H NMR spectra were referenced to natural abundance ^{13}C peaks and residual ^{1}H peaks of deuterated solvents, respectively. FT-IR spectra were collected on a Perkin-Elmer Spectrum 100. Powder X-ray diffraction patterns were recorded from a Rigaku Miniflex II diffractometer with an accelerating voltage and current of 30 kV and 15 mA, respectively. Thermogravimetric analysis was performed on an SDTQ 600 Thermogravimetric Analyzer using an alumina boat as the sample holder. Diffuse reflectance spectra were collected on a PerkinElmer Lambda 45 UV-vis spectrometer referenced to Spectralon®. Cyclic voltammetry (CV) measurements were carried out in N,N-dimethylformamide (DMF) and acetonitrile solutions using a WaveDriver 20 Bipotentiostat combined with Aftermath software. Both solutions contained 0.1 M tetrabutylammoniumhexafluorophosphate and 1 mM DFTP,

and measurements were done in an H cell equipped with Ag/AgCl reference, platinum wire counter, and glassy carbon working electrodes. In DMF, DFTP exhibits two reversible reductions at $E_o(I) = -1.36$ V and $E_o(II) = -1.63$ V vs Ag/AgCl (Figure S6). Upon expanding the potential range to –2.4 V, two more reductions were observed, both of which were irreversible reductions as indicated by the lack of a return wave during the anodic scan. The irreversible reductions also led to new anodic waves at –0.42 V and –0.81 V. These anodic waves could possibly be attributed to decomposition products during further reduction of $DFTP^{2-}$ in DMF. In acetonitrile, four quasi-irreversible reduction waves of DFTP were observed at Ep(I) = –1.49 V (ΔEp = 0.08 V), Ep(II) = –1.66 V (ΔEp = 0.07 V), Ep(III) = –1.93 V (ΔEp = 0.09 V), and Ep(IV) = –2.13 V (ΔEp = 0.12 V) (Figure S6).

Theoretical Calculations.

The truncated model of 2 (Figure 3.4), the DFTP-H_4ZnTCPP, system was optimized at PBE/TZV level of theory using PRIRODA code. The single point TDDFT/CAM-B3LYP/def2SVP calculations were performed on the optimized geometry of the DFTP-H_4ZnTCPP dyad, DFTP molecule, and H_4ZnTCPP fragment, using Gamess-US software. Coulomb-attenuated range separated exchange functional with LYP correlation was chosen to address the well-known TDDFT problems with spatially extended and charge-transfer excitations.

In the approximation of single excitations an expression for the excitation energy transfer coupling, *V*, between corannulene-based linker, DFTP (D), and porphyrin-based, H_4ZnTCPP (A), in the truncated model is given by three parts:

$$V_{full} = V_{Coulomb} + V_{exchange} + V_{overlap} \qquad \text{(eq. 3.7)}$$

The largest contribution by far is coming from the Coulomb part alone:

$$V \sim V_{Coulomb} \int\int dr\, dr' \rho_D^{tr}(r) \frac{1}{|r - r'|} \rho_A^{tr}(r') \qquad \text{(eq. 3.8)}$$

where $\rho_D^{tr}(r) / \rho_A^{tr}(r)$ are donor and acceptor parts transition densities produced by energy transfer relevant excitations. Localized on atomic centers of D and these densities can be approximated through the set of transition atomic charges $q_D^{tr}(r) / q_A^{tr}(r)$.

The original Förster's point dipole model defines the coupling between a donor and acceptor in the following form:

$$V = \frac{\left(\vec{\mu}_D \vec{\mu}_A\right)}{R_{DA}^3} - 3\frac{\left(\vec{\mu}_D \vec{R}_{AB}\right)\left(\vec{\mu}_A \vec{R}_{AB}\right)}{R_{DA}^5} \qquad \text{(eq. 3.9)}$$

where μ_D and μ_A are the transition dipole moments for the D and A excitations, and R_{DA} a distance between two centers. In general, such approximation works for the relative large distances between the coupled chromophores (R_{DA}>> than spatial metrics of the transition densities). At some shorter distances, however, better results can be achieved by using the transition atomic charges $q_D^{tr}(r) / q_A^{tr}(r)$:

$$V = \sum_{i \in D, j \in A} \frac{q_i^{tr}(r_i) q_j^{tr}(r_j)}{|r_i - r_j|} \qquad \text{(eq. 3.10)}$$

here, the integrals in eq. S8 are substituted by the sums.

Despite the fact that both discussed approximations could provide reasonable insights on photophysical processes, both models would neglect the short-range orbital

coupling and only applicable for well-separated D-A pairs with $R_{DA} > 4.0$ Å. In our case, the D and A molecules are connected by a covalent bond. For that reason, we have employed a recent development in the field, which focused on the fragments with strong orbital coupling.

Assuming, that adiabatic excitations can be approximated by linear combination of two diabatic states of the D-A system, and following Voityuk's proposal, the excitation energy transfer coupling can be estimated as:

$$V = (E_i - E_j)\frac{(M_i M_j)(m_D^2 - m_A^2) - (M_i^2 + M_j^2)(m_D m_A)}{(M_i^2 - M_j^2)^2 + 4(M_i M_j)^2} \qquad \text{(eq. 3.11)}$$

In this expression the E_i and E_j are the energies of coupled adiabatic excitations with transition dipole moments M_i and M_j of the D(DFTP)-A(H_4ZnTCPP) system and m_D and m_A are transition dipole moments of D and A parts, respectively. Numerical values of these parameters are provided in the Table S1. Notably, by using eq. 3.11 we have used approximation, that the adiabatic excitations in the D-A (DFTP-H_4ZnTCPP) fragment can be approximated by linear combination of diabatic states. The ratio $(F_i + F_j)/(f_D + f_A)$ should be close to 1, if two states approximation is reliable. However, this ratio for S_1^D and S_1^A states (Figure 3.4) is 1.5 (1.3–1.6 for other states).

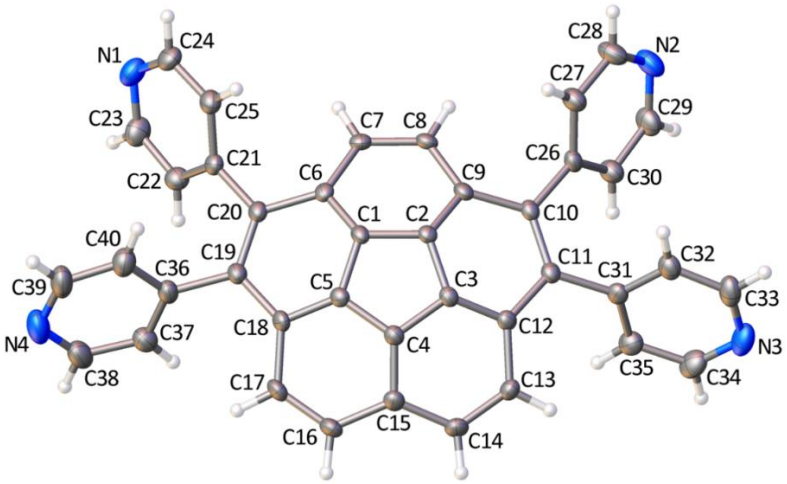

Figure 3.5. Crystal structure of DFTP. Displacement ellipsoids are drawn at the 60% probability level. Grey, blue, and white spheres correspond to carbon, nitrogen, and hydrogen, respectively.

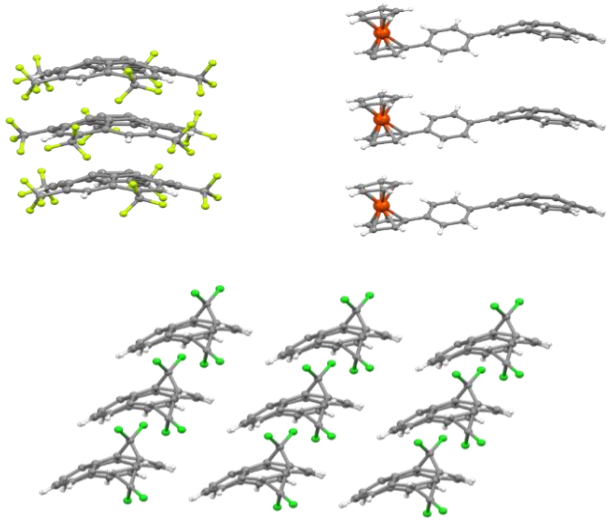

Figure 3.6. (*top left*) Packing of C_5-$C_{20}H_5(CF_3)_5$ molecules. Yellow, grey, and white spheres correspond to fluorine, carbon, and hydrogen atoms, respectively. (*top right*) Packing of 1-corannulenyl-4-ferrocenyl-benzene molecules. Orange, grey, and white spheres correspond to iron, carbon, and hydrogen atoms, respectively. (*bottom*) Packing of $C_{20}H_{10}CCl_2$ molecules. Green, grey, and white spheres correspond to

chlorine, carbon, and hydrogen atoms, respectively.

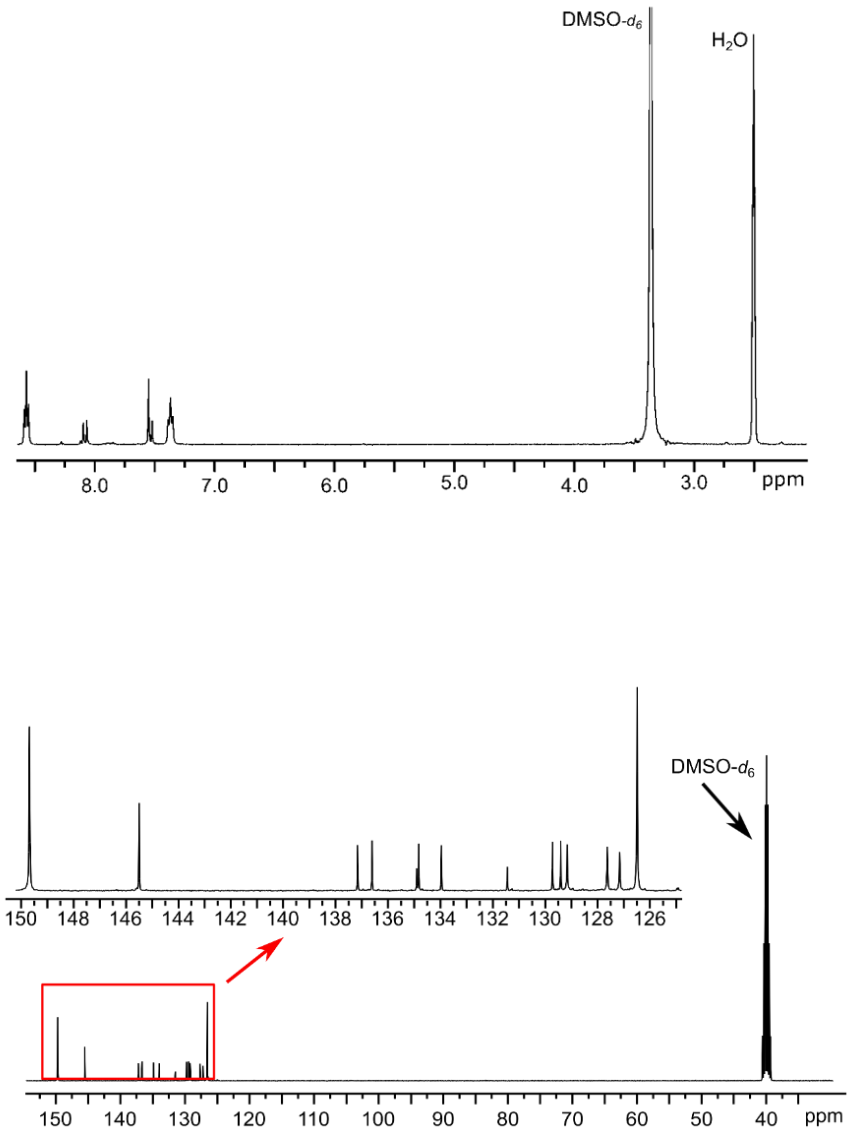

Figure 3.7. ^{1}H NMR (top) and ^{13}C NMR (bottom).

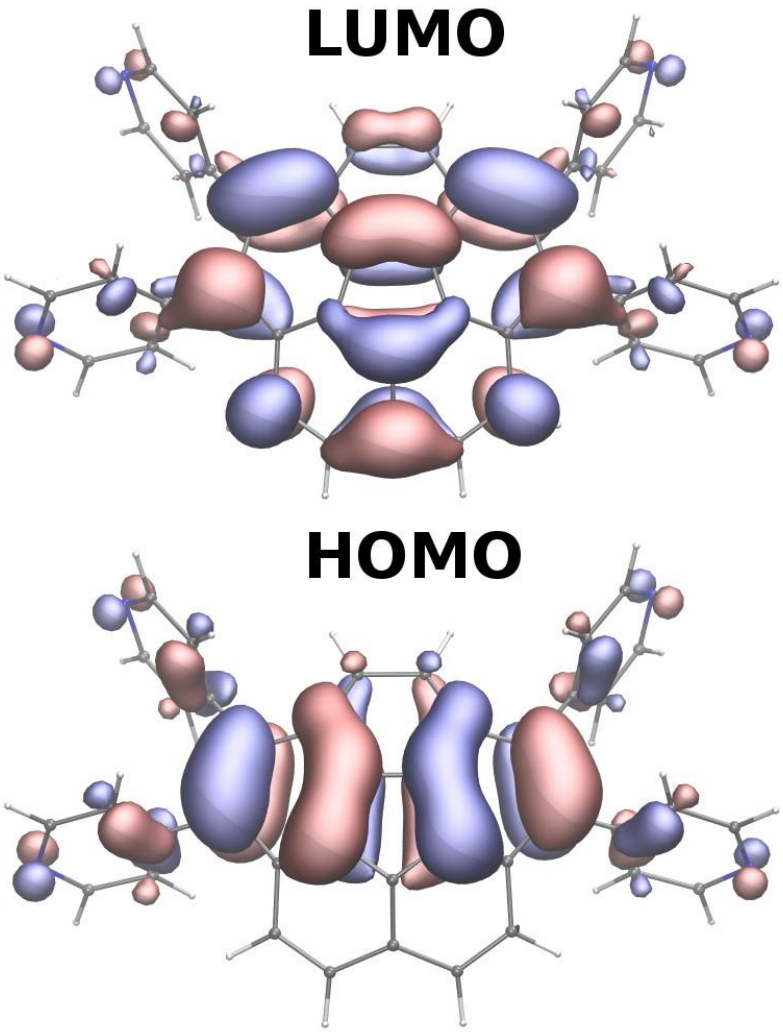

Figure 3.8. LUMO (top) and HOMO (bottom) of DFTP. The LUMO and HOMO of DFTP are primarily localized on the corannulene bowl, and the calculated HOMO-LUMO gap found to be 6.3 eV (CAM-B3LYP/def2SVP). In comparison with unsubstituted $C_{20}H_{10}$, the decoration of the corannulene core with four pyridyl groups led to a significantly higher LUMO energy, illustrating that DFTP is a better electron acceptor than corannulene itself.

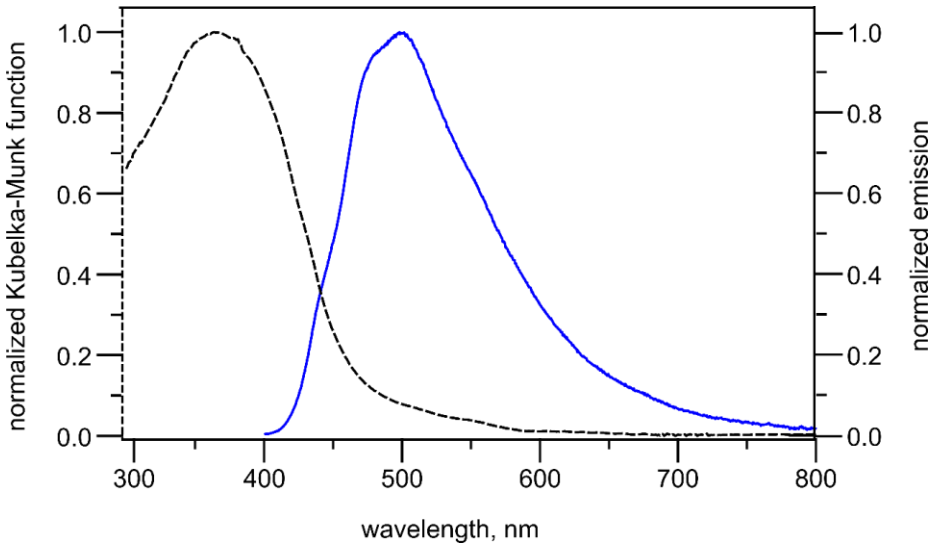

Figure 3.9. Diffuse reflectance spectrum of DFTP (black line) and emission spectrum of DFTP (blue line, λ_{ex} = 350).

Table 3.1. Cyclic voltammetry data for DFTP.

	E_p(I), V	E_p(II), V	E_p(III), V	E_p(IV), V
DFTP (DMF)	–1.41	–1.67		
DFTP (ACN)	–1.49	–1.66	–1.93	–2.13
$C_{20}H_{10}$[22](DMF)	–1.87	–2.41	–3.13	

This CV data confirmed the better electron accepting properties of the prepared corannulene-based derivatives compared to pristine corannulene.

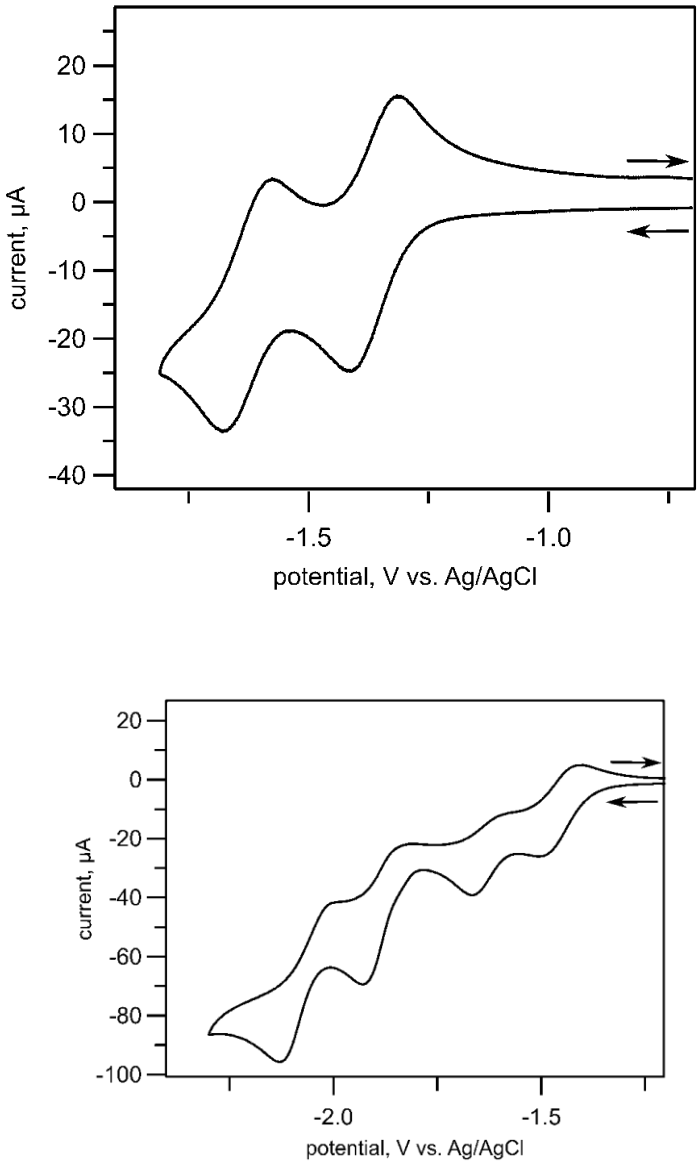

Figure 3.10. Cyclic voltammogram of DFTP in DMF (top) and acetonitrile (bottom).

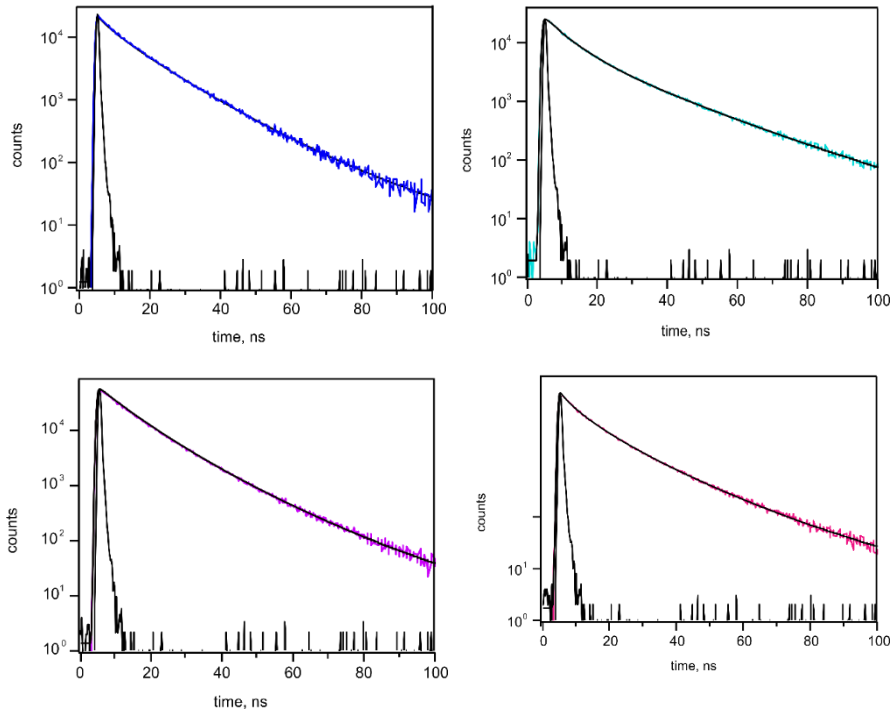

Figure 3.11. Fluorescence decay for 1 (top left), $C_{20}H_{10}$ (top right), H_4DFT (middle left), and Cd-based MOF (middle right).

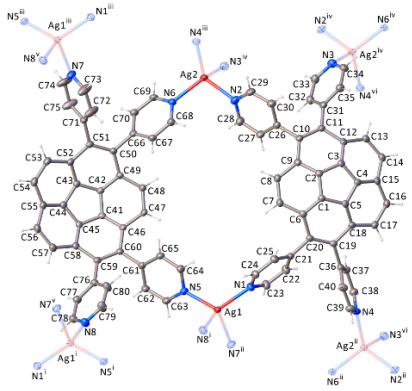

Figure 3.12. A part of the crystal structure of **1**. Displacement ellipsoids are drawn at the 60% probability level. Grey, blue, white, and red spheres correspond to carbon, nitrogen, hydrogen, and silver, respectively.

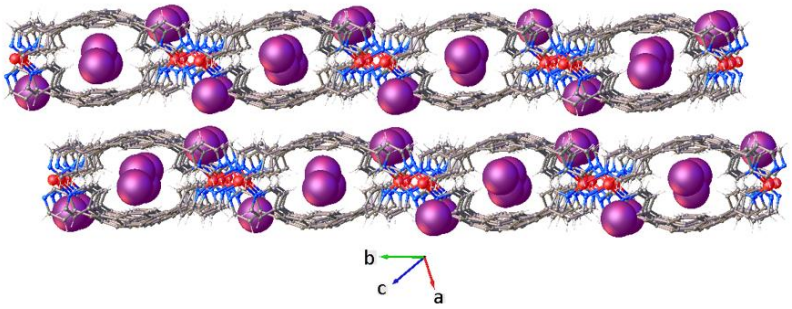

Figure 3.13. The crystal structure of **1** (*top*). Infinite 2D layers in **1**, parallel to the crystallographic (101) plane with PF_6^- anions (large purple spheres) included. Red, grey, blue, and white spheres correspond to silver, carbon, nitrogen, and hydrogen atoms, respectively (*bottom*).

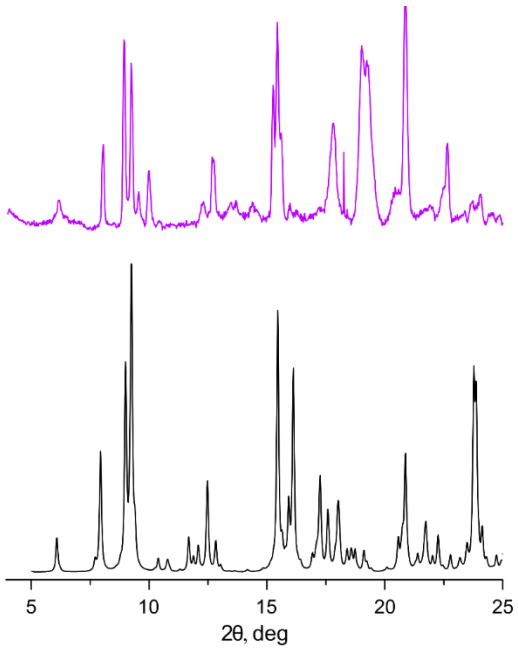

Figure 3.14. PXRD patterns of **1**: experimental (purple) and simulated (black) with preferential orientation along the crystallographic [310] direction.

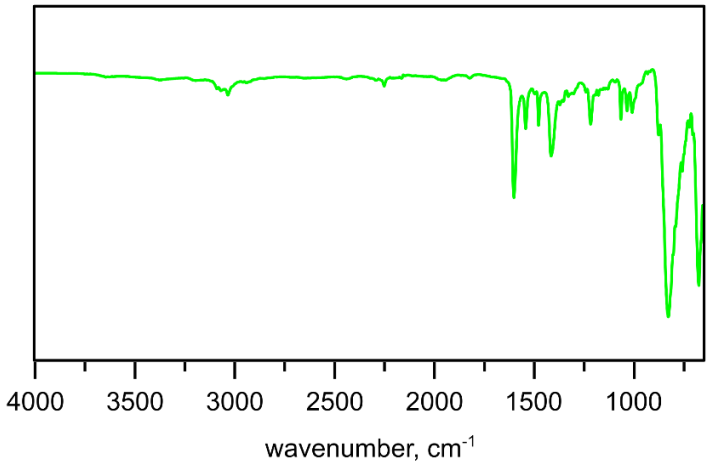

Figure 3.15. FT-IR spectrum of **1.**

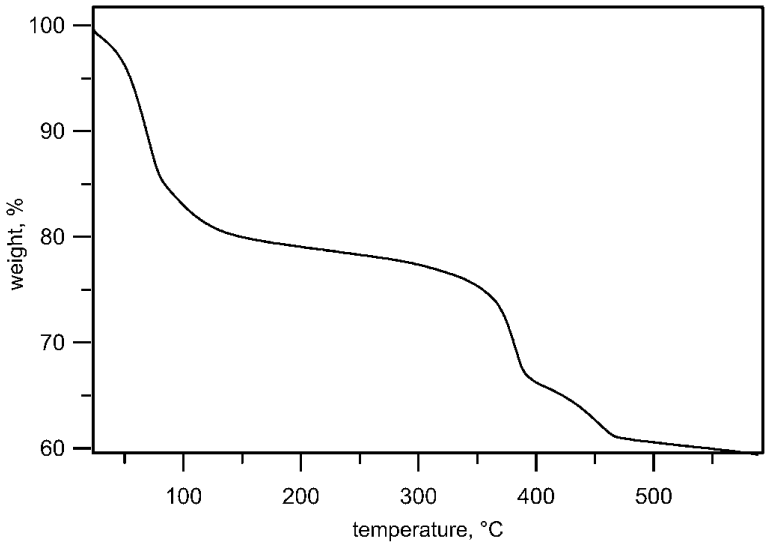

Figure 3.16. Thermogravimetric analysis plot of **1**.

Table 3.3. X-ray structure refinement data[a] for DFTP, **1**, and Cd-based MOF.

compound	**DFTP**	**1**	**Cd-based MOF**
formula	$C_{40}H_{22}N_4$	$C_{122}H_{89}Ag_2F_{12}N_{11}P_2$	$C_{66.75}H_{64.18}Cd_2N_{4.69}O_{12.69}$
FW	558.61	2214.72	1359.73
T, K	100(2)	100(2)	100(2)
crystal system	monoclinic	triclinic	monoclinic
space group	$P2_1/c$	P-1	C2/c
Z	4	2	8
a, Å	10.3044(7)	11.6135(9)	39.062(4)
b, Å	21.2336(15)	17.5633(13)	15.2283(15)
c, Å	13.2924(9)	25.2483(18)	22.817(2)
α, °	90	91.177(1)	90
β, °	109.384(2)	99.446(1)	99.749(2)
γ, °	90	90.350(1s)	90
V, Å^3	2743.5(3)	5078.8(7)	13377(2)
d_{calc}, g/cm^3	1.352	1.448	1.350
μ, mm^{-1}	0.080	0.497	0.698
F(000)	1160.0	2260.0	5560.0
crystal size, mm^3	0.16 × 0.08 × 0.04	0.44 × 0.24 × 0.18	0.38 × 0.34 × 0.18
theta range	4.608 to 51.362	4.15 to 55.02	4.232 to 52.916
index ranges	$-12 \le h \le 12$ $-25 \le k \le 25$ $-16 \le l \le 16$	$-15 \le h \le 15$, $-22 \le k \le 22$, $-32 \le l \le 32$	$-48 \le h \le 48$, $0 \le k \le 19$, $0 \le l \le 28$
refl. collected	54988	151806	21769
data/restraints/ parameters	5202/0/398	23306/381/1347	21769/348/804
GOF on F^2	1.021	1.013	1.061
R_1/wR_2, $[I \ge 2\sigma(I)]^b$	0.0461/0.1101	0.0367/0.0854	0.0644/0.1676

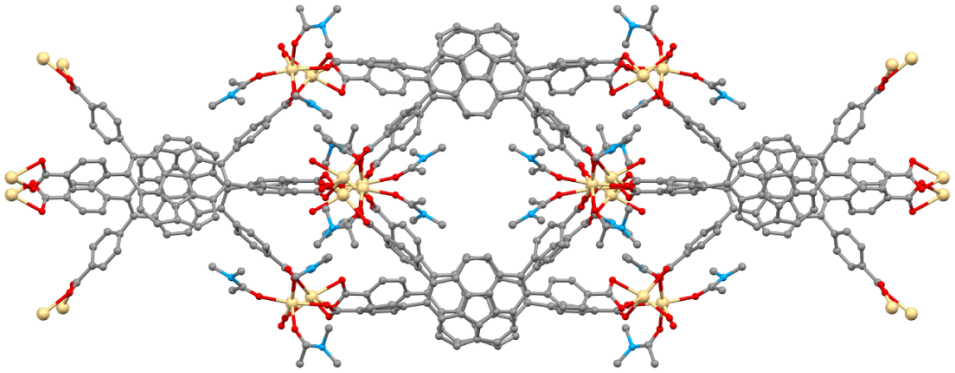

Figure 3.17. A part of the crystal structure of Cd-based MOF (top) and packing (bottom). Red, orange, blue, and grey spheres correspond to oxygen, cadmium, nitrogen, and carbon atoms, respectively.

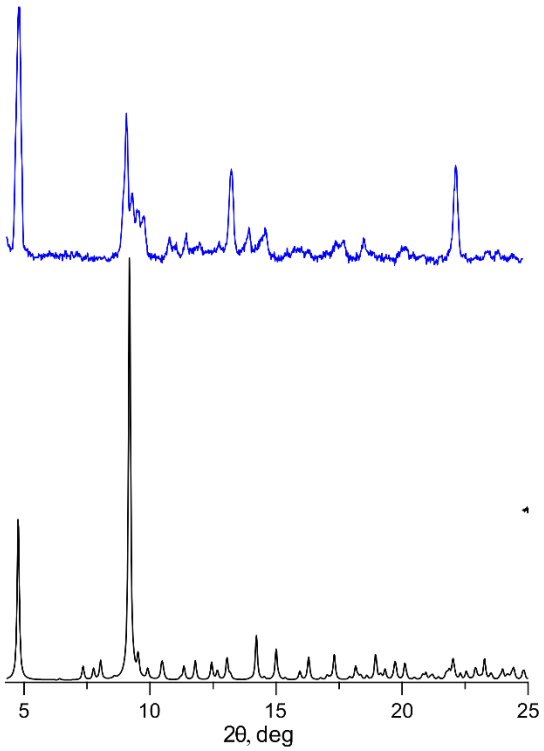

Figure 3.18. Simulated (black) and experimental (blue) PXRD patterns of Cd-based MOF.

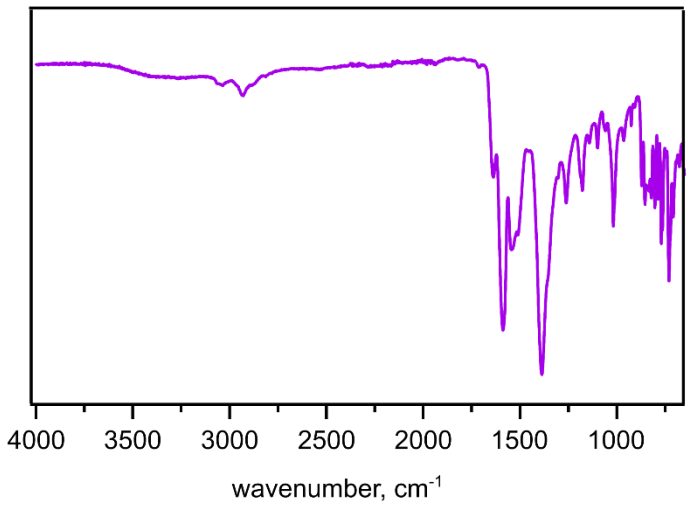

Figure 3.19. FTIR spectrum of Cd-based MOF.

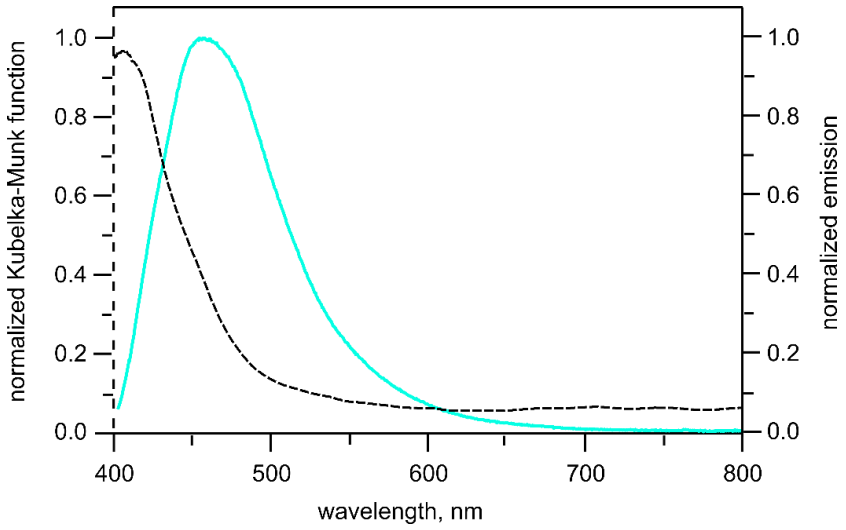

Figure 3.20. Diffuse reflectance (black) and emission spectrum (light blue, λ_{ex} = 350) of Cd-based MOF.

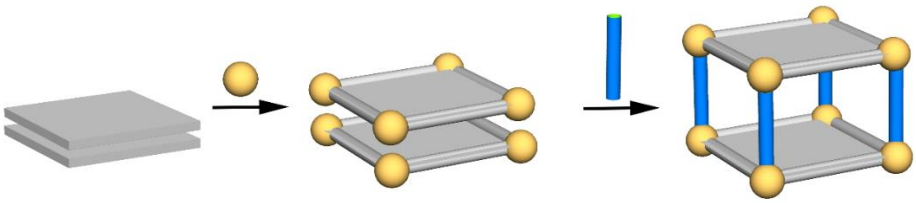

Figure 3.21. A schematic representation of a two-step approach for pillar installation utilized for preparation of **2**.

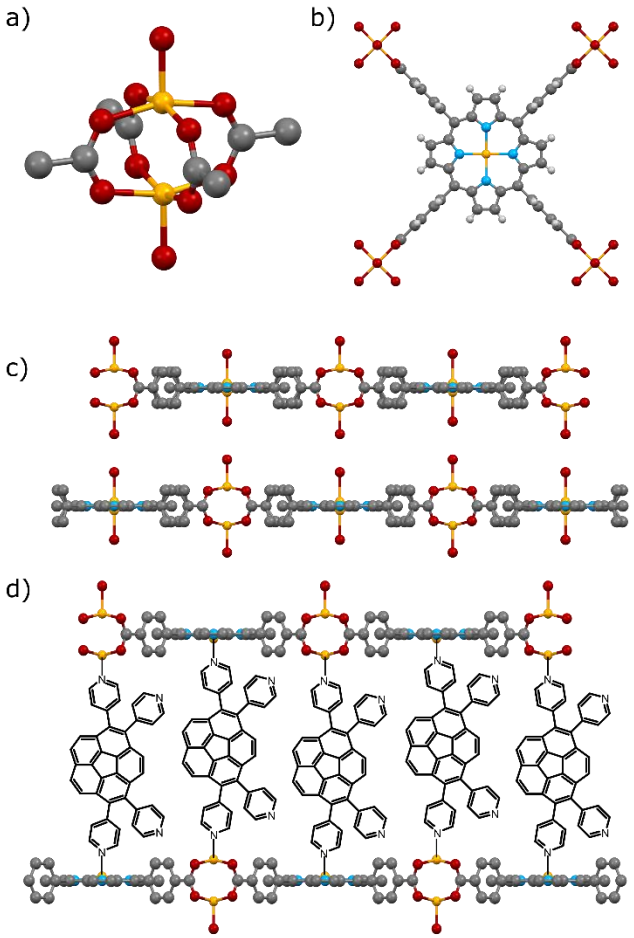

Figure 3.22. *a*) A secondary building unit, $Zn(O_2C^-)_4$, in a porphyrin-based 2D structure shown in c). *b*) A fragment of the porphyrin-based structure showing the porphyrin unit, bridged by $Zn_2(O_2C^-)_4$ secondary building units. *c*) X-ray crystal structure of the porphyrin-based 2D framework.[5] *d*) A schematic representation of DFTP immobilized between the two-dimensional porphyrin-based layers in 2. Notably, DFTP connects all layers

along *c* axis. Yellow, red, blue, and grey spheres correspond to zinc, oxygen, nitrogen, and carbon atoms, respectively.

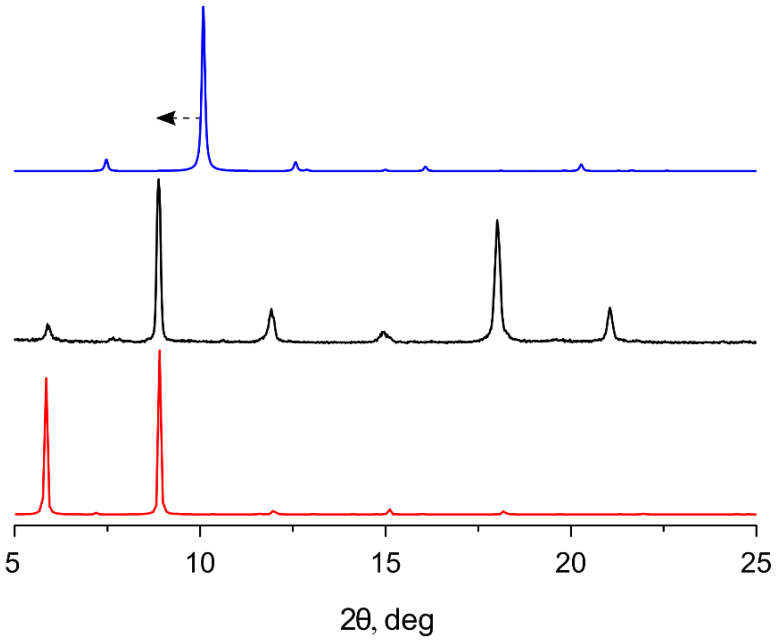

Figure 3.23. PXRD patterns of as-synthesized 2D porphyrin-based Zn_2(ZnTCPP)[5] (*top*, *blue*), as-synthesized **2** (*middle*, *black*), and simulated **2** (bottom, red; preferential orientation along the [00l] direction). The dashed arrow indicates the changes in the PXRD profile associated with the increase in the interlayer distance.

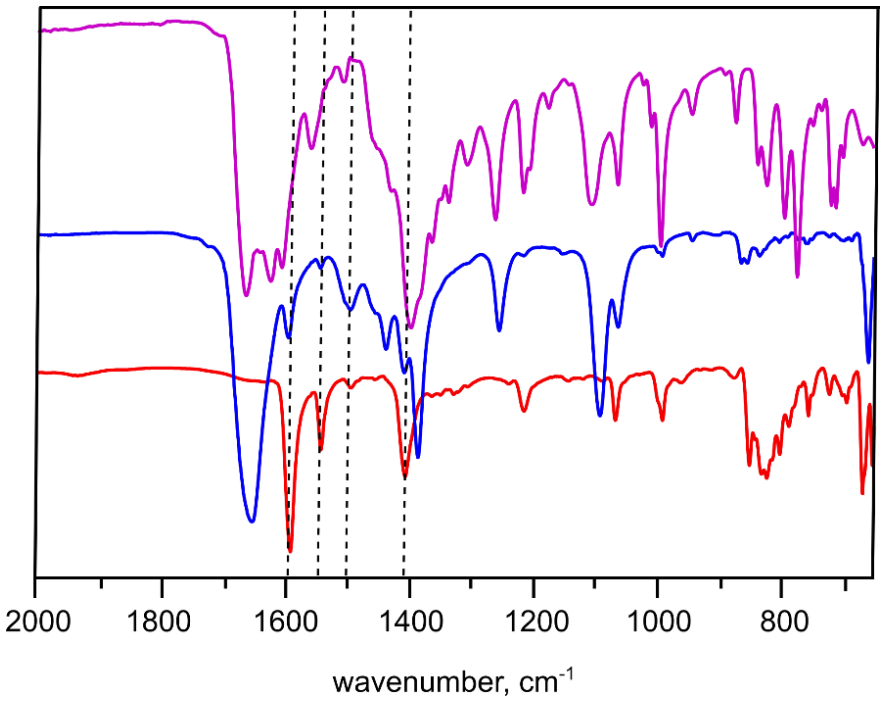

Figure 3.24. FT-IR spectra of Zn_2(ZnTCPP) (top), **2** (middle), and DFTP (bottom). The dashed line indicates the main resonances corresponding to DFTP in **2**.

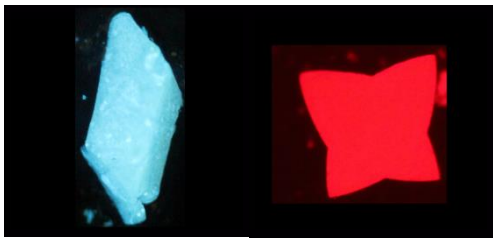

Figure 3.25. Epifluorescence microscopy images of 1.

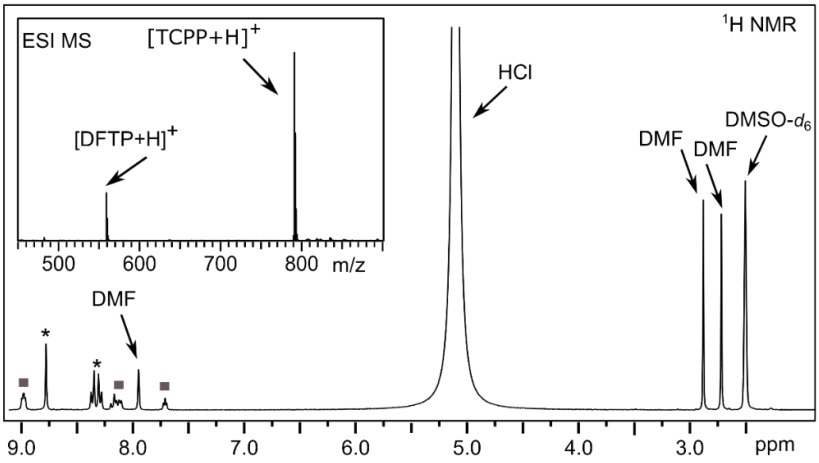

Figure 3.26. ^{1}H NMR spectrum of digested 2. The peak corresponding to H_4TCPP (*) and DFTP (▪) are labeled. The inset shows the electrospray ionization mass-spectrum of digested 2.

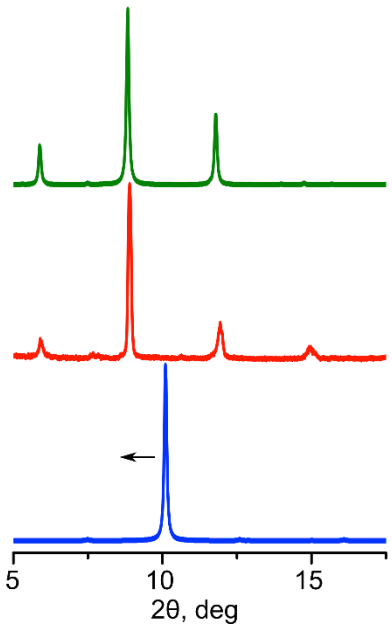

Figure 3.27. PXRD patterns: 2D Zn_2(ZnTCPP)[5] (preferential orientation along the [00l] direction; *bottom, blue*), as-synthesized **2** (*middle, red*), and predicted **2** based on theoretical modeling (preferential orientation along the [00l] direction; *top, green*). The black arrow indicates the changes in the PXRD profile

associated with the increase in the interlayer distance.

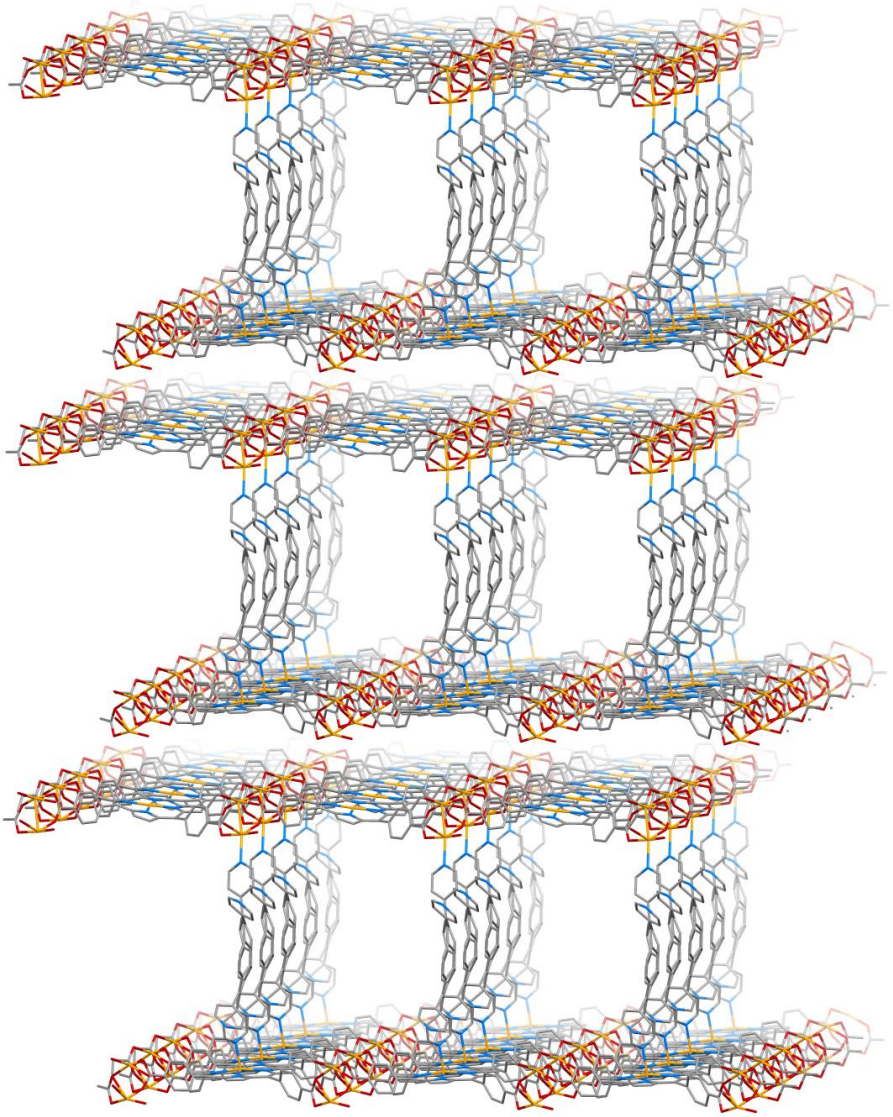

Figure 3.28. Packing of the simulated structure of **2**.

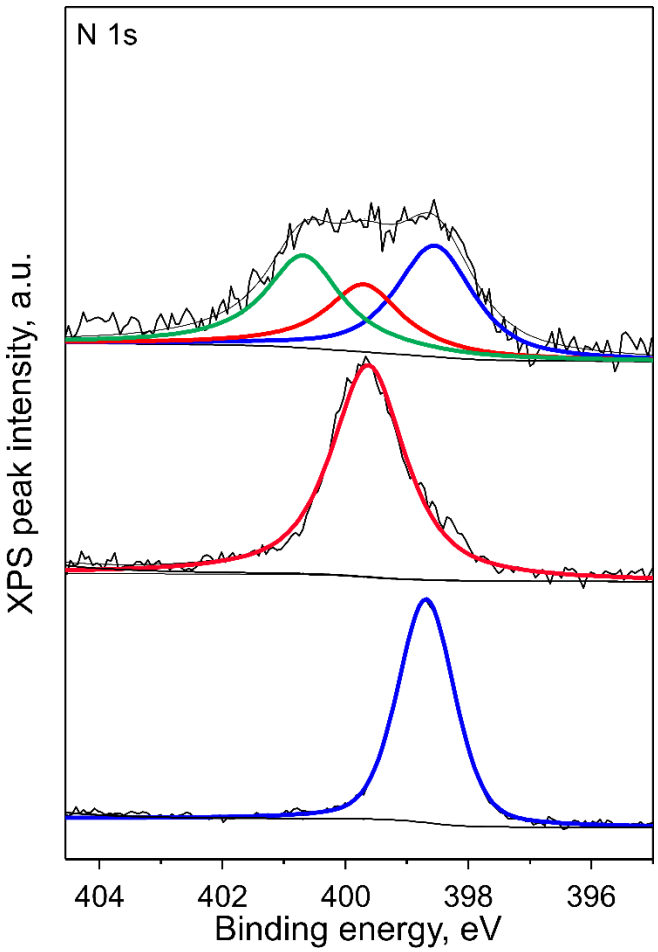

Figure 3.29. The N 1s regions of the XPS spectra for **2** (top), zinc-coordinated DFTP (middle), and DFTP (bottom).

REFERENCES

1) W. E. Barth, R. G. Lawton, *J. Am. Chem. Soc*. **1966**, *88*, 380–381.

2) A. S. Filatov, A.V. Zabula, S. N. Spisak, A. Y. Rogachev, M. A. Petrukhina, *Angew. Chem. Int. Ed*. **2014**, *53*, 140–145.

3) S. Lampart, L. M. Roch, A. K. Dutta, Y. Wang, R. Warshamanage, A. D. Finke, A. Linden, K. K. Baldridge, J. S. Siegel, *Angew. Chem. Int. Ed*. **2016**, *55*,14648–14652.

4) J. Sukegawa, C. Schubert, X. Zhu, H. Tsuji, D. M. Guldi, E. Nakamura, *Nat. Chem*. **2014**, *6*, 899–905.

5) K. P. Castro, Y. Jin, J. J. Rack, S. H. Strauss, O. V. Boltalina, A. A. Popov, *J. Phys. Chem. Lett*. **2013**, *4*, 2500–2507.

6) C.-Z. Li, H.-L. Yip, A. K.-Y. Jen, *J. Mater. Chem*. **2012**, *22*, 4161– 4177.

7) P. Liu, Y. Hisamune, M. D. Peeks, B. Odell, J. Q. Gong, L. M. Herz, H. L. Anderson, *Angew. Chem. Int. Ed*. **2016**, *55*, 8358– 8362.

8) W. B. Fellows, A. M. Rice, D. E. Williams, E. A. Dolgopolova, A. K. Vannucci, P. J. Pellechia, M. D. Smith, J. A. Krause, N. B. Shustova, *Angew. Chem. Int. Ed*. **2016**, *55*, 2195–2199.

9) M. Yamada, K. Ohkubo, M. Shionoya, S. Fukuzumi, *J. Am. Chem. Soc*. **2014**, *136*, 13240–13248.

10) A. S. Filatov, E. A. Jackson, L. T. Scott, M. A. Petrukhina, *Angew. Chem. Int. Ed*. **2009**, *48*, 8473–8476.

11) J. Dey, A. Y. Will, R. A. Agbaria, P. W. Rabideau, A. H. Abdourazak, R. Sygula, I. M. Warner, *J. Fluoresc*. **1997**, **7**, 231–236.

12) M. Yamaji, K. Takehira, T. Mikoshiba, S. Tojo, Y. Okada, M. Fujitsuka, T. Majima, S. Tobita, J. Nishimura, *Chem. Phys. Lett.* **2006**, *425*, 53–57.

13) Y.-T. Wu, D. Bandera, R. Maag, A. Linden, K. K. Baldridge, J. S. Siegel, *J. Am. Chem. Soc*. **2008**, *130*, 10729–10739.

14) Y. Kim, M. Lee, *Chem. Eur. J*. **2015**, *21*, 5736–5740.

15) A. K. Dutta, A. Linden, L. Zoppi, K. K. Baldridge, J. S. Siegel, *Angew. Chem. Int. Ed.* **2015**, *54*, 10792–10796.

16) G. Valenti, C. Bruno, S. Rapino, A. Fiorani, E. A. Jackson, L. T. Scott, F. Paolucci, M. Marcaccio, *J. Phys. Chem. C* **2010**, *114*, 19467–19472.

17) J. Mack, P. Vogel, D. Jones, N. Kaval, A. Sutton, *Org. Biomol. Chem*. **2007**, *5*, 2448–2452.

18) G. H. Grube, E. L. Elliott, R. J. Steffens, C. S. Jones, K. K. Baldridge, J. S. Siegel, *Org. Lett.* **2003**, *5*, 713–716.

19) T. J. Seiders, E. L. Elliott, G. H. Grube, J. S. Siegel, *J. Am. Chem. Soc*. **1999**, *121*, 7804–7813.

20) D. Wu, T. Shao, J. Men, X. Chen, G. Gao, *Dalton Trans.* **2014**, *43*, 1753–1761.

21) Y.-L. Wu, M. C. Stuparu, C. Boudon, J.-P.Gisselbrecht, W. B. Schweizer, K. K. Baldridge, J. S. Siegel, F. Diederich, *J. Org. Chem*. **2012**, *77*, 11014–11026.

22) N. Niamnont, N. Kimpitak, K. Wongravee, P. Rashatasakhon, K. K. Baldridge, J. S. Siegel, M. Sukwattanasinitt, *Chem. Commun*. **2013**, *49*, 780–782.

23) Y. Matsuo,K .Tahara, M. Sawamura, E. Nakamura, *J. Am. Chem. Soc*. **2004**, *126*, 8725–8734.

24) M. C. Stuparu, *Tetrahedron* **2012**, *68*, 3527–3531.

25) F. Hauke, S. Atalick, D. M. Guldi, J. Mack, L. T. Scott, A. Hirsch, *Chem. Commun*. *2004*, 766–767.

26) S. Ito, Y. Tokimaru, K. Nozaki, *Angew. Chem. Int. Ed*. **2015**, *54*, 7256–7260

27) Y. Matsuo, Y. Sato, M. Hashiguchi, K. Matsuo, E. Nakamura, *Adv. Funct. Mater*. **2009**, *19*, 2224–2229.

28) C. S. Jones, E. Elliott, J. S. Siegel, *Synlett* **2004**, 187–191.

29) M. Mattarella, L. Berstis, K. K. Baldridge, J. S. Siegel, *Bioconjugate Chem*. **2014**, *25*, 115–128.

30) Y. Wang, Y. Li, W. Zhu, J. Liu, X. Zhang, R. Li, Y. Zhen, H. Dong, W. Hu, *Nanoscale* **2016**, *8*, 14920–14924.

31) H. Barbero, S. Ferrero, L. Alvarez-Miguel, P. Gomez Iglesias, D. Miguel, C. M. Alvarez, *Chem. Commun*. **2016**, *52*, 12964–12967.

32) R. Chen, R.-Q. Lu, P.-C. Shi, X.-Y. Cao, *Chin. Chem. Lett*. **2016**, *27*, 1175–1183.

33) D. E. Williams, N. B. Shustova, *Chem. Eur. J*. **2015**, *21*, 15474– 15479.

34) T. Zhang, W. Lin, *Chem. Soc. Rev*. **2014**, *43*, 5982–5993.

35) A. M. Butterfield, B. Gilomen, J. S. Siegel, *Org. Process Res. Dev*. **2012**, *16*, 664–676.

36) H. Oshima, A. Fukazawa, S. Yamaguchi, *Angew. Chem. Int. Ed*. **2017**, *56*, 3270–3274.

37) A. V. Zabula, A. Y. Rogachev, M. A. Petrukhina, *Science* **2011**, *333*, 1008–1011.

38) A. Ayalon, A. Sygula, P. C. Cheng, M. Rabinovitz, P. W. Rabideau, L. T. Scott, *Science* **1994**, *265*, 1065–1067.

39) L. Zoppi, L. Martin-Samos, K. K. Baldridge, *Phys. Chem. Chem. Phys*. **2015**, *17*, 6114–6121.

40) L. M. Roch, L. Zoppi, J. S. Siegel, K. K. Baldridge, *J. Phys. Chem. C* **2017**, *121*, 1220–1234.

41) L. Zoppi, J. S. Siegel, K. K. Baldridge, *Wiley Interdiscip. Rev.: Comput. Mol. Sci*. **2012**, *3*, 1–12.

42) L. E. Kreno, K. Leong, O. K. Farha, M. Allendorf, R. P. Van Duyne, J. T. Hupp, *Chem. Rev*. **2012**, *112*, 1105–1125.

43) Z. Guo, D. K. Panda, K. Maity, D. Lindsey, T. G. Parker, T. E. Albrecht-Schmitt, J. L. Barreda-Esparza, P. Xiong, W. Zhou, S. Saha, *J. Mater. Chem. C* **2016**, *4*, 894–899.

44) H. Furukawa, K. E. Cordova, M. Keeffe, O. M. Yaghi, *Science* **2013**, *341*, 1230444.

45) B. Manna, S. Singh, A. Karmakar, A. V. Desai, S. K. Ghosh, *Inorg. Chem*. **2015**, *54*, 110–116.

46) K. Sasan, Q. Lin, C. Mao, P. Feng, *Nanoscale* **2016**, *8*, 10913– 10916.

47) W. P. Lustig, F. Wang, S. J. Teat, Z. Hu, Q. Gong, J. Li, *Inorg. Chem*. **2016**, *55*, 7250–7256.

48) F. Wang, W. Liu, S. J. Teat, F. Xu, H. Wang, X. Wang, L. An, J. Li, *Chem. Commun*. **2016**, *52*, 10249–10252.

49) D. F. Sava, L. E. S. Rohwer, M. A. Rodriguez, T. M. Nenoff, *J. Am. Chem. Soc.* **2012**, *134*, 3983–3986.

50) B. Topolinski, B. M. Schmidt, S. Schwagerus, M. Kathan, D. Lentz, *Eur. J. Inorg. Chem*. *2014*, 5391–5405.

51) C.Dubceac, A. S. Filatov, A. V. Zabula, M. A. Petrukhina, *Cryst. Growth Des*. **2015**, *15*, 778–785.

52) I. V. Kuvychko, S. N. Spisak, Y.-S. Chen, A. A. Popov, M. A. Petrukhina, S. H. Strauss, O. V. Boltalina, *Angew. Chem. Int. Ed*. **2012**, *51*, 4939–4492.

53) N. B. Shustova, A. F. Cozzolino, M. Dinca, *J. Am. Chem. Soc*. **2012**, *134*, 19596–19599.

54) J. C. Hanson, C. E. Nordman, *Acta Crystallogr*. **1976**, *32*, 1147– 1153.

55) J. R. Lakowicz, *Principles of Fluorescence Spectroscopy*, Springer, **2007**.

56) B. J. Burnett, W. Choe, *CrystEngComm* **2012**, *14*, 6129–6131.

57) D. E. Williams, E. A. Dolgopolova, D. C. Godfrey, E. D. Ermolaeva, P. J. Pellechia, A. B. Greytak, M. D. Smith, S. M. Avdoshenko, A. A. Popov, N. B. Shustova, *Angew. Chem. Int. Ed*. **2016**, *55*, 9070–9074.

58) Q. Zhang, C. Zhang, L. Cao, Z. Wang, B. An, Z. Lin, R. Huang, Z. Zhang, C. Wang, W. Lin, *J. Am. Chem. Soc*. **2016**, *138*, 5308– 5315.

59) Y. Kuramochi, A. Satake, A. S. D. Sandanayaka, Y. Araki, O. Ito, Y. Kobuke, *Inorg. Chem*. **2011**, *50*, 10249–10258.

60) C. Dallaire, I. Kolber, M. Gingras, *Org. Synth.* **2002**, *78*, 42–45.

61) A. M. Butterfield, B. Gilomen, J. S. Siegel, *Org. Process Res. Dev.* **2012**, *16*, 664–676.

62) A. Sygula, G. Xu, Z. Marcinow, P. W. Rabideau, *Tetrahedron* **2001**, *57*, 3637–3644.

62) T. J. Seiders, E. L. Elliott, G. H. Grube, J. S. Siegel, *J. Am. Chem. Soc.* **1999**, *121*, 7804–7813.

63) B. J. Burnett, W. Choe, *CrystEngComm* **2012**, *14*, 6129–6131.

64) W. B. Fellows, A. M. Rice, D. E. Williams, E. A. Dolgopolova, A. K. Vannucci, P. J. Pellechia, M. D. Smith, J. A. Krause, N. B. Shustova, *Angew. Chemie-Int. Ed.* **2015**, *55*, 2195–2199.

CHAPTER 4

STACK THE BOWLS: TAILORING THE ELECTRONIC STRUCTURE OF CORANNULENE INTEGRATED CRYSTALLINE MATERIALS

Rice, A. M.; Dolgopolova, E. A.; Yarbrough, B. J.; Leith, G. A.; Martin, C. R.; Stephenson, K. S.; Heugh, R. A.; Brandt, A. J.; Chen, D. A.; Karakalos, S. G.; Smith, M. D.; Hatzell, K. B.; Pellechia, P. J.; Garashchuk, S.; Shustova, N. B. *Angew. Chem. Int. Ed*. **2018**, *57*, 11310.

We report in this chapter, the first examples of purely organic donor–acceptor materials with integrated p-bowls (πBs) that combine not only crystallinity and high surface areas but also exhibit tunable electronic properties, resulting in a four-orders of-magnitude conductivity enhancement in comparison with the parent framework. In addition to the first report of alkyne–azide cycloaddition utilized for corannulene immobilization in the solid state, we also probed the charge transfer rate within the Marcus theory as a function of mutual πB orientation for the first time, as well as shed light on the density of states near the Fermi edge. These studies could foreshadow new avenues for the development of optoelectronic devices or a route for highly efficient porous electrodes.

The unique curvature of p-bowls (πBs) distinguishes them from more traditional flat polycyclic aromatic hydrocarbons (PAHs) and, in combination with an unusual electronic structure, results in a number of intriguing properties including, but not limited to, surface charge stabilization, high reversible lithium capacity, bowl-to-bowl inversion, a significant dipole moment, and high charge mobility.[1–8] This combination of material properties can open a pathway for πB utilization in applications ranging from optoelectronic devices or electrodes to thermoresponsive materials.[4,9,10]

Herein, we demonstrated, for the first time, how πB integration (in particular, corannulene [πB-$C_{20}H_{10}$]) inside insulating porous scaffolds could tune electronic properties resulting in circa 10000-fold conductivity enhancement. Moreover, the porosity of the prepared crystalline hybrids was maintained providing a pathway to re-enforce semiconducting behavior in typically insulating porous materials (for example, covalent organic or metal–organic frameworks (COFs/MOFs)).[11–21] In addition to the

first report of azide–alkyne 1,3-cycloaddition utilized for corannulene integration in the solid state, the described corannulene material is the first member in the family of crystalline (purely organic) donor–acceptor (D–A) corannulene-COFs with the highest surface area among corannulene-based extended structures reported to date (Scheme 4.1).

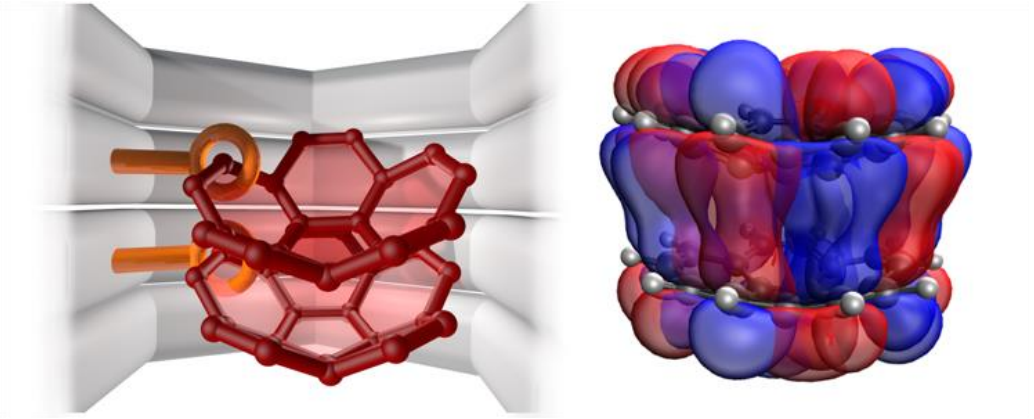

Scheme 4.1. (left) Schematic representation of πB organization inside the crystalline framework through 1,3-cyloaddition. (right) Delocalization of πB molecular orbitals associated with ground state charge transport.

In combination with spectroscopic and structural analysis, we employed theoretical calculations, which allowed us to probe charge transfer rates within the Marcus theory as a function of πB mutual orientation for the first time, as well as to shed light on the density of state distribution near the Fermi edge For engineering corannulene-containing crystalline materials, we considered two methods based on the post-synthetic integration of the πB through 1) utilization of azide-alkyne 1,3-cycloaddition and 2) non-coordinative πB inclusion. To accomplish these strategies, the material used for πB integration should satisfy the following criteria:1) Sufficient pore apertures to accommodate πBs (for example, πB-$C_{20}H_{10}$ diameter is ca. 6.6 Å), 2) structural integrity after πB inclusion, and 3) the presence of functional groups (for example, -C≡C) for πB

integration through covalent bond formation. The covalent organic scaffolds, 1/(x%) (where x = [BPTA]/([BPTA]+[DMTA]) × 100%; Figure 4.1), made from 2,5-bis(2-propynyloxy) terephthalaldehyde (BPTA), 2,5-dimethoxyterephthalaldehyde (DMTA), and tri-(4-aminophenyl)benzene (TAPB) and 1-OMe consisting of DMTA and TAPB, were utilized for coordinative and non-coordinative πB integration, respectively (Supporting Information, Schemes 4.2-4.4 and Figures 4.5–4.23).[22]

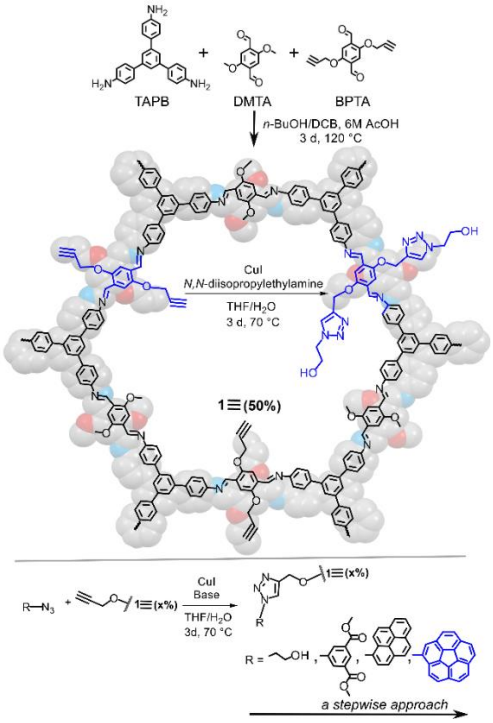

Figure 4.1. (*top*) Synthesis of **1≡(50%)** including the reaction conditions utilized for azide-alkyne cycloaddition reaction in the solid state. Blue color highlights the moieties participating in CuAAC reaction on molecular species. (*bottom*) Building blocks utilized in a stepwise approach for the development of the CuAAC synthetic conditions applicable for the COF

Both selected frameworks, possessing layered structures with a pore aperture of 33 Å, maintain structural integrity under a wide pH range[22] making it possible to explore a number of synthetic conditions for πB immobilization without material degradation. However, several challenges still had to be addressed for not only reaction condition development but also synthesis of corannulene-based building blocks on a gram scale. The latter challenge has been overcome owing to recent advances in πB chemistry,[3,23–26] allowing for the preparation of azide-containing corannulene (πB-$C_{20}H_9N_3$, Figure 4.1, Scheme 4.6) using a 12-step procedure[26] as well as pristine corannulene (π$BC_{20}H_{10}$) by a 9-step approach (Scheme 4.6).[25] A stepwise approach was devised for the investigation of reaction conditions for a copper-catalyzed azide–alkyne cycloaddition (CuAAC), which involved the development of synthetic methods using less bulky and more affordable moieties (for example, 2-azidoethanol, Figure 4.1) before pursuing the reaction with the labor-demanding π$BC_{20}H_9N_3$. Therefore, we started with molecular building blocks, such as 2-azidoethanol and BPTA, to observe reaction progress using solution NMR spectroscopy, in contrast to the insoluble COFs (Supporting Information, Figures 4.24–4.26). Based on the spectroscopic data analysis, we have monitored the completion of a CuAAC reaction and, as a result, formation of the desired product, 2,5-bis((1-(2hydroxyethyl)-1H-1,2,3-triazol-4-yl)methoxy)terephthalaldehyde (Figure 4.1 (a blue highlight) and Figures 4.24 and 4.25). As a next step, we applied the developed conditions (*N*,*N*-diisopropylethylamine/CuI/THF/H_2O, 70 °C, 3 d) towards the reaction of 2-azidoethanol with the COF (1≡(34%)) instead of BPTA. To monitor the reaction progress, solid-state techniques, including FTIR and solid-state ^{13}C cross-polarization magic angle spinning (CP-MAS) NMR spectroscopies, were employed. In particular, we

observed the disappearance of 2120 cm^{-1} (C=C) and 3300 cm^{-1} (C≡C-H) resonances in the FTIR spectrum, indicative of reaction completion (Figure 4.26).[22] As a control experiment, we treated the COF under the same reaction conditions but without the presence of the azide-containing precursor. As expected, we observed preservation of both 2120 cm^{-1} (C=C) and 3300 cm^{-1} (H-C≡C) resonances in the FTIR spectrum (Experimental, Figure 4.29). Interestingly, in the case of the CuAAC reaction with bis(2-azidoethyl) malonate (that is, containing two azide groups, Figure 4.27), the disappearance of the stretch at 3300 cm^{-1} (H-C≡C) is evidence of the reaction progress, while the persistence of the stretch at 2100 cm^{-1} (N-N=N) is indicative of the preservation of the second azide group.[27]

After 2-azidoethanol and bis(2-azidoethyl) malonate, bulkier precursors such as dimethyl 5-azidoisophthalate and 1-azidopyrene (Figure 4.1) were probed for the CuAAC reaction under the developed experimental conditions. In both cases, the complete disappearance of the resonances at 2120 cm^{-1} and 3300 cm^{-1} was confirmed by FTIR spectroscopy (Experimental, Figures 4.28 and 4.29). In addition, presence of the characteristic carbonyl stretch at circa 1716 cm^{-1} in the case of dimethyl 5-azidoisophthalate after an extensive several-day washing procedure also supports successful reaction completion. After the development of the synthetic method for successful solid-state CuAAC reactions, we finally focused on integration of πBs, in particular, an azide-containing building block (πB-$C_{20}H_9N_3$, Main, Figure 4.1). Based on the combination of solid-state ^{13}C CP-MAS NMR and FTIR spectroscopic data, incorporation of the corannulene-based unit led to πB-$C_{20}H_9N_3$[1≡(50%)] formation (Figures 4.2 and Experimental, Figures 4.30 and 4.31). Even after πB incorporation, the

Brunauer–Emmett–Teller (BET) surface area was found to be 865 m^2g^{-1} according to the gas sorption analysis, which is the highest surface area reported for any corannulene-containing structure to date (Experimental, Figure 4.31).

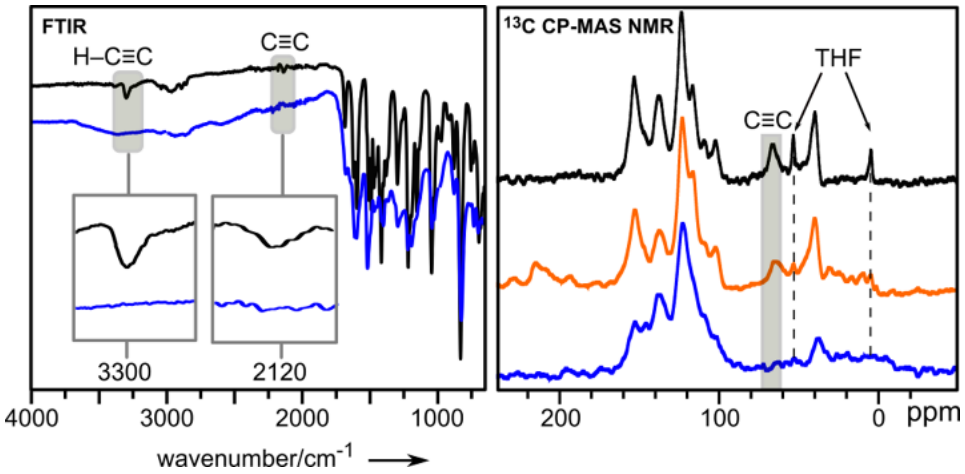

Figure 4.2. (left) FTIR spectra of **1≡(50%)** (black) and πB-$C_{20}H_9N_3$[**1≡(50%)**] (blue). Grey areas show H–C≡C and C≡C stretches, present in **1≡(50%)** and absent in πB-$C_{20}H_9N_3$[**1≡(50%)**]. (right) ^{13}C CP-MAS NMR spectra of **1≡(50%)** (black), a control experiment with **1≡(50%)** (orange), and πB-$C_{20}H_9N_3$[**1≡(50%)**] (blue).

Notably, the observed surface area is in line with corannulene integration since the measured surface area of the parent COF was found to be 1452 m^2g^{-1}. The synthesized material also maintains its crystallinity, resulting in the first example of a crystalline, porous corannulene-based COF. For a comparison, we performed non-coordinative immobilization of the πB inside 1-OMe. For that, we used a simpler 9-step synthetic route required for πB-$C_{20}H_{10}$ preparation rather than the 12-step procedure necessary for πB-$C_{20}H_9N_3$ preparation (Experimental, Figures 4.33–4.36).[25,26] An additional simplification is also found in πB$C_{20}H_{10}$@1-OMe synthesis. This was achieved through soaking 1-OMe in a πB-$C_{20}H_{10}$ solution for 5 days, followed by a thorough washing procedure to remove πB-$C_{20}H_{10}$ from the COF surface. Based on ^1H NMR

spectroscopic analysis of the digested COF, non-coordinative immobilization led to inclusion of one corannulene molecule per six -OMe units. The crystallinity of πB-$C_{20}H_{10}$@1-OMe after corannulene incorporation was confirmed by PXRD (Experimental, Figure 4.34). The measured BET surface area of π$BC_{20}H_{10}$@1-OMe was found to be 898 m^2g^{-1} (Experimental, Figure 4.35).

To probe the electronic structures of πB-containing materials, we employed diffuse reflectance (DR), steady state and time-resolved photoluminescence (PL), and X-ray photoelectron (XPS) spectroscopies, conductivity measurements, and theoretical calculations. Integration of corannulene moieties inside the COFs through CuAAC or noncoordinative integration resulted in a significant color change from pale-yellow to dark red (Figure 4.3).

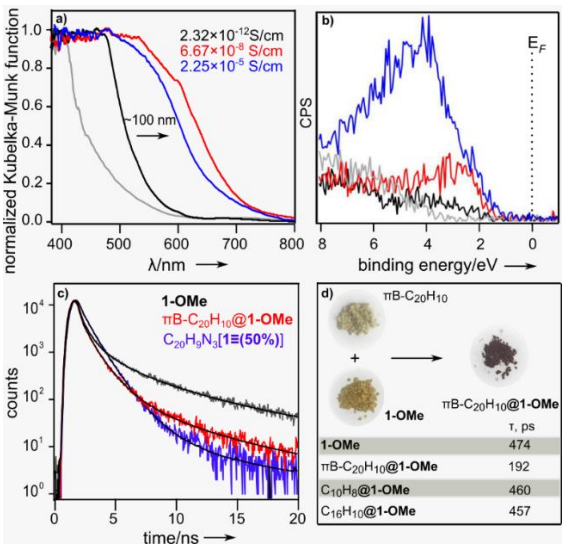

Figure 4.3. (a) Normalized diffuse reflectance spectra of πB-$C_{20}H_{10}$@**1-OMe** (red), **1-OMe** (black), πB-$C_{20}H_9N_3$[**1≡(50%)**] (blue), and πB-$C_{20}H_{10}$ (grey) with corresponding conductivity values. (b) XPS data for the valence band region for πB-$C_{20}H_{10}$@**1-OMe** (red), **1-OMe** (black), πB-$C_{20}H_9N_3$[**1≡(50%)**] (blue), and πB-$C_{20}H_{10}$ (grey). (c) Fluorescent decays of πB-$C_{20}H_{10}$@**1-**

OMe (red), πB-$C_{20}H_9N_3$[**1≡(50%)**] (blue), and **1-OMe** (grey). (d) Photographs of **1-OMe**, πB-$C_{20}H_{10}$, and πB-$C_{20}H_{10}$@**1-OMe**. The table shows the amplitude-weighted average lifetimes for **1-OMe**, πB-$C_{20}H_{10}$@**1-OMe**, and PAHs@**1-OMe**.

Indeed, DR spectroscopic analysis revealed that corannulene integration resulted in appearance of an additional absorption band (550–650 nm) leading to a bathochromic shift of the absorption profile of over 100 nm in comparison with both the pristine COF and corannulene units. Such a drastic change could be attributed to charge transfer (CT) between the covalent organic host and πB moieties, especially taking into account the electron donating character of the framework functional groups (for example,-OMe) and electron-accepting behavior of corannulene moieties.[22] This fact is in line with the results observed in the case of naphthalene ($C_{10}H_8$) and pyrene ($C_{16}H_{10}$) integration, both possessing higher-lying LUMOs than that of πB-$C_{20}H_{10}$ (-2.27 eV in contrast to -1.20 eV ($C_{10}H_8$)[28] and -1.48 eV ($C_{16}H_{10}$)[29]), which did not result in CT band formation. Integration of 1,4-dimethoxybenzene and 1,5-dimethoxynaphthalene exhibiting electron donating behavior also did not result in CT band formation. To further study the behavior of the prepared materials, we employed time-resolved PL spectroscopy. With the assumption that the PL decay rate consists of radiative, nonradiative, and CT components, analysis should reveal shortening of PL lifetimes of the host owing to integration of corannulene moieties.[30,31] Indeed, the amplitude-averaged lifetimes estimated by fitting the time-resolved PL decay curves were 474 ps (1-OMe) while πB-$C_{20}H_{10}$@1-OMe and πB-$C_{20}H_9N_3$[1≡(50%)] exhibited much shorter lifetimes of 192 ps and 167 ps, respectively, which is in line with the possibility of CT. Similar behavior was

previously reported for fullerene– porphyrin dyads in which the decrease in lifetime was attributed to an electron transfer from porphyrin moieties (D) to fullerene units (A).[30] Immobilization of planar PAHs (that is, naphthalene or pyrene) did not result in significant CT, and estimated lifetimes were similar to that of 1-OMe (Figure 4.3). As a next step, we employed XPS to probe the electronic structure of the πB-based materials by monitoring the density of states (DOS) near the Fermi level (E_F, binding energy = 0eV) as a fast and nondestructive pre-screening technique. This capability is especially crucial in the case of the multistep preparation of corannulene derivatives.[32] The valence band spectrum of πB-$C_{20}H_{10}$ itself exhibits behavior associated with insulating materials, given that there is zero intensity within 3eV of the Fermi level. The spectrum of 1OMe itself also shows nearly zero intensity at 2eV. In contrast, the XPS valence-band spectra for πB-$C_{20}H_{10}$@1OMe and πB-$C_{20}H_9N_3$[1≡(50%)] have much higher intensities within 2 eV of E_F; and this indicates a greater DOS near EF, which is associated with higher conductivity (see more details in the Supporting Information). The DOS curves obtained from the 4-unit computational models are quite similar for the "stack" and "pinwheel" orientations (see below) and show overall agreement with the DOS of pristine corannulene (see more details in the Supporting Information, Figures 4.39). To further shed light on the changes of electronic structure near E_F, we have performed pressed-pellet conductivity measurements as well as estimated the optical band gap values based on DR spectroscopic data. The bulk conductivity values for 1-OMe, πB-$C_{20}H_{10}$@1-OMe, and π$BC_{20}H_9N_3$[1≡(50%)] were found to be 2.32×10^{-12}, 6.67×10^{-8}, and 2.25×10^{-5} S/cm^{-1}, respectively, highlighting that conductivity of corannulene-integrated materials is circa 10000-fold higher in comparison to the parent framework.

This fact is consistent with the appearance of DOS in the XPS spectra as well as the trend observed for the optical band gap values derived from the Tauc plot.[33,34] The estimated band gaps for COF (**1-OMe**), πB-$C_{20}H_{10}$@**1-OMe**, and πB-$C_{20}H_9N_3$[**1≡(50%)**] were found to be 2.24 eV, 1.94 eV, and 1.93 eV, respectively. Thus, πB incorporation resulted in four orders of magnitude of enhancement of conductivity while preserving material crystallinity and porosity, thus providing a pathway to enhance semiconducting behavior in typically insulating porous COFs. To elucidate how πB packing (in addition to D-A interactions) could potentially promote charge transport, we explored the dependence of electronic properties as a function of possible πB arrangements inside the crystalline host. The πB organization could be defined by the interplay of electrostatic (dipole-dipole attractions, repulsions between electron clouds of π-surfaces, and attractions between the edges and bowl centers), dispersive (surface interactions), and interstack C-H···π interactions with distance between πBs ranging from 3.3 Å to 3.7 Å.[35,36] In addition, the open nature of the one-dimensional COF channels provides a structural basis for accommodation of guest molecules and their efficient confinement and packing. Furthermore, molecular dynamics and intermolecular distances of anchoring corannulene moieties are restricted by the COF interlayer distance of 3.5 Å (Figure 4.4).[22]

We employed theoretical calculations for a series of πB motifs by considering three main packing scenarios: convex-to-concave "stack" (Figure 4.4), concave-to-concave/convex-to-convex "clam", and "pinwheel" observed for the pristine corannulene in the solid state (Main, Figure 4.4 and Experimental, 4.36).[5,36] We evaluated the ground state CT in the chosen geometrical arrangements assuming a charge hopping mechanism, which involves transfer of charge through its relocation from charged to neutral

species.[37–40] The approach, based on the Hartree-Fock theory paired with 6-31+G* basis, yielded the electronic couplings and the frontier molecular orbitals (MOs) associated with the charge transport (see SI for more details).[41,42] Figure 4.4 illustrates the variation of frontier MOs associated with ground state CT.

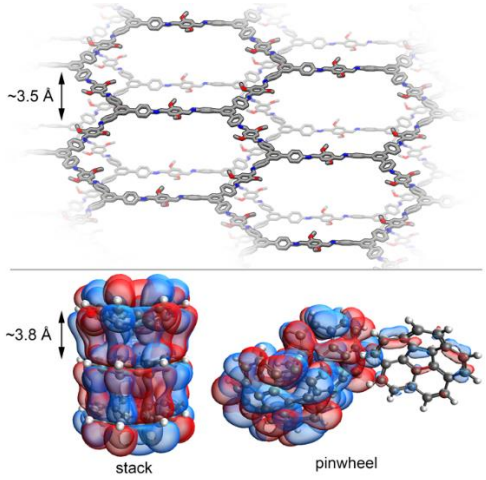

Figure 4.4. (top) Interlayer distance in **1-OMe**.[22] (bottom) Selected LUMOs, associated with the ground CT for the three πB-$C_{20}H_{10}$ units in "stack" and "pinwheel" orientations. (The theory level: LRC-wPBEh/6-31G*).

In the case of convex-to-concave corannulene stacks, frontier MOs form one π-column through all units, suggesting long-range π-interactions promoting charge transport. Our calculations do not show significant orbital delocalization for the cases of corannulene packing with disordered arrangements of units (e.g., "pinwheel", Main, Figures 4.4 and in the Experimental section, Figures 4.38 and 4.40). The latter fact is in agreement with previous studies that showed a strong correlation of molecular packing with charge transport.[41,43] To apply a more generalized approach and establish the

correlation of our suggested model to experimental conductivity data, we estimated CT constants according to the Marcus theory : $k = 2\pi/\hbar \cdot |V_c|^2/\sqrt{4\pi\lambda k_B T} \cdot \exp\left(-((-(\lambda + \Delta G^o)^2)/4\lambda k_B T\right)$,

where k – charge transfer rate, V_c – direct effective electron coupling, λ – reorganization energy of the system; see SI for more details.[44,45] By applying the Einstein relation ($\mu = eD/k_BT$, $D = kL^2/2$, where μ – mobility of charge transfer carriers, D – diffusion constant, L – mean length of particle movement) and assumption of the equal number of charge carriers in different packing motifs, we estimated the conductivity value ratio as a ratio of the corresponding k values. Within this model, we found that a shift from noncolumnar organization to a one-dimensional corannulene stack could result in a ~42 times increase in conductivity values (see SI for a detailed description). Therefore, the experimentally observed conductivity enhancement could be attributed not only to the πB integration and/or D-A corannulene-host communication inside the crystalline COF, but also to the mutual orientation of the corannulene moieties as shown in Figure 4.

The preceding results describe the properties of the first examples of corannulene-based (purely organic) crystalline and porous scaffolds with embedded πBs. Corannulene integration resulted in significant changes in the valence band structure and, thus, a four order of magnitude conductivity enhancement. Moreover, 1,3-cyloaddition, utilized for the first time for corannulene integration in the solid state, led to the formation of materials with the highest surface area reported for any corannulene-containing materials to date. Our theoretical analysis paves the way toward simulation of the electronic coupling constants as a function of corannulene mutual orientation. Overall, this work demonstrates the high potential of πBs for the development of materials with tunability of

electronic structures preserving material porosity and crystallinity; and this combination could be crucial for future technological advances in the fields of optoelectronic devices or highly efficient electrodes.

EXPERIMENTAL

Materials.

2,7-dihydroxynapthalene (99%, Chem-Impex International, Inc.), *N*,*N*-diethylcarbamoyl chloride (99%, Acros Organics), dichloro(1,3-bis(diphenylphosphino)propane)nickel (99%, Ark Pharm, Inc), methylmagnesium bromide (ACS grade, Alfa Aesar), aluminum bromide (99%, Strem Chemicals, Inc.), oxalyl chloride (98%, Alfa Aesar), Girard's Reagent T (99%, Acros Organics), 3-pentanone (>98%, Tokyo Chemical Industry Co, LTD), 2,5-norbornadiene (97%, Alfa Aesar), *N*-bromosuccinimide (96%, Oakwood Chemical), benzoyl peroxide (97%, Sigma-Aldrich), pyridine-4-boronic acid (95%, Matrix Scientific), sodium carbonate (ACS grade, Macron), tetrakis(triphenylphosphine)palladium(0) (98%, Matrix Scientific), sodium bicarbonate (ACS grade, Macron), 1,4-dimethoxybenzene (Reagent grade, Oakwood Chemical), bromine (reagent grade, Sigma-Aldrich), *n*-butyllithium (Reagent grade, Sigma-Aldrich), boron tribromide (reagent grade, Sigma-Aldrich), propargyl-bromide (80% weight in toluene, reagent grade, Oakwood Chemical), 1,3,5-tribromobenzene (98%, Sigma-Aldrich), 4-aminophenyl boronic ester (reagent grade, Oakwood Chemical), Aliquat 336 (reagent grade, Beantown chemical), terephthalaldehyde (95%, OxChem), palladium on carbon (10% on carbon, Alfa Aesar), ammonium formate (98%, Chem-Impex International), sodium nitrite (ACS grade, Fisher Scientific), sodium azide (reagent grade, Oakwood Chemical), *N*,*N*-dimethylformamide

(ACS grade, BDH), pyridine (99+%, Alfa Aesar), 1,4-dioxane (99+%, Alfa Aesar), diethyl ether (HPLC grade, Fisher Scientific), hydrochloric acid (ACS grade, EMD Chemicals), nitric acid (ACS grade, Fisher Scientific), hexane (ACS grade, BDH), diethyl ether (99%, Acros Organics), isopropanol (ACS grade, BDH), dichloromethane (ACS grade, Macron), methanol (HPLC grade, Fisher Scientific), acetic acid (ACS grade, Fisher Scientific), acetic anhydride (99%, Chem-Impex International, Inc.), cyclohexane (reagent grade, Malinckrodt), carbon tetrachloride (99%, Sigma-Aldrich), 1-butanol (reagent grade, Oakwood Chemical), *o*-dichlorobenzene (ACS grade, Alfa Aesar), ethanol (200 proof, Decon Laboratories, Inc.), chloroform (ACS grade, Macron), tetrahydrofuran (ACS grade, EMD Chemicals), benzene (ACS grade, EMD Chemicals), acetonitrile (ACS grade, Fisher Scientific), sodium hydroxide (ACS grade, Fisher Scientific), anhydrous magnesium sulfate (reagent grade, J.T. Baker® Chemicals), potassium hydroxide (ACS grade, Fisher Scientific), silica gel (Macron), sodium chloride (ACS grade, Fisher Scientific), chloroform-*d* (Cambridge Isotope Laboratories, Inc.), and DMSO-d_6 (Cambridge Isotope Laboratories, Inc.) were used as received.

The corannulene-based precursors and 1-azidocorannulene were prepared according to the literature procedures.[46,47] The COF-based linkers 2,5-dimethoxyterephthalaldehyde (DMTA), 1,3,5-tri-(4-aminophenyl)benzene (TAPB), and 2,5-bis(2-propynyloxy) terephthalaldehyde (BPTA) were synthesized based on modified literature procedures.[48-50] The **1-OMe** and **1≡(x%)** COFs were synthesized based on a modified literature procedures.[51]

Synthesis.

Tri-(4-aminophenyl)benzene ($C_{24}H_{21}N_3$, TAPB, Scheme 4.2).

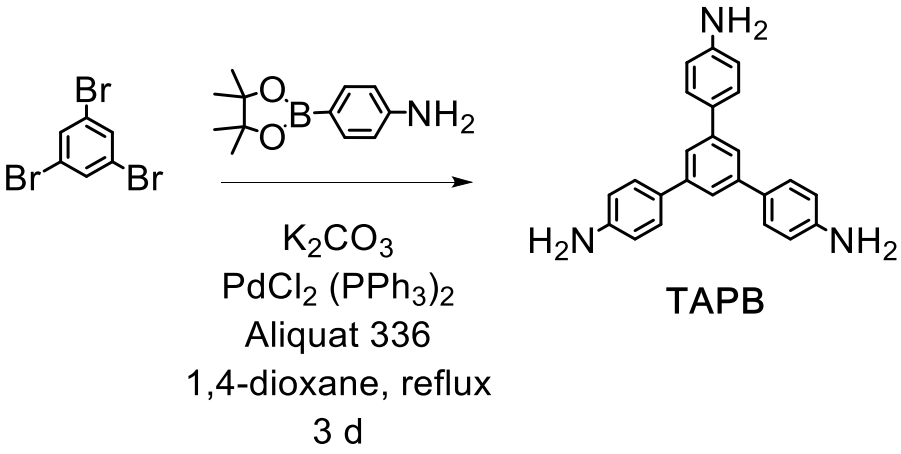

Scheme 4.2. Synthesis of 1,3,5-tri-(4-aminophenyl) benzene (TAPB).[48]

The TAPB linker was prepared according to a modified literature procedure.[48] For that, 1,3,5-tribromobenzene (1.00 g, 3.17 mmol), 4-aminophenyl boronic ester (2.31 g, 13.3 mmol), K_2CO_3 (2 M, 7.50 mL), $PdCl_2(PPh_3)_2$ (68.0 mg, 0.0971 mmol), and Aliquat 336 (100 µL) were heated at reflux in dioxane for 3 d. After cooling to room temperature, the reaction mixture was flushed through a silica plug with ethyl acetate, followed by recrystallization from methanol to afford TAPB in 62% yield. ^{1}H NMR (DMSO-d_6, 300 MHz): δ = 7.48 (6H, s), 7.45 (3H, s), 6.66 (6H, d, J = 8.46), 5.21 (6H, s) ppm (Figure 4.5). ^{13}C NMR (DMSO-d_6, 101 MHz): δ = 148.83, 142.04, 128.49, 127.90, 120.82, and 114.7 ppm (Figure S1). IR (neat, cm^{-1}): 668, 706, 822, 871, 951, 1126, 1176, 1279, 1406, 1448, 1513, 1606, 3210, 3355, and 3434 (Figure 4.6). HRMS (ESI, m/z) calculated for $C_{24}H_{21}N_3$ $[M+H]^+$ 352.1808, found 352.1806.

2,5-dimethoxyterephthalaldehyde ($C_{10}H_{10}O_4$, DMTA, Scheme 4.3).

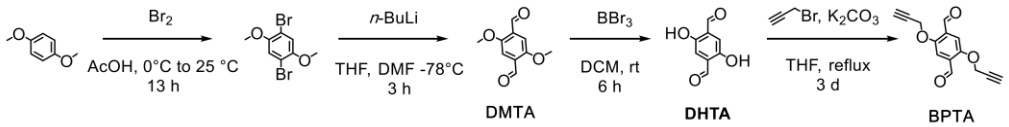

Scheme 4.3. Synthesis of 2,5-dimethoxyterephthalaldehyde (DMTA) and 2,5-bis(2-propynyloxy) terephthalaldehyde (BPTA).[50]

The DMTA linker was prepared according to a modified literature procedure.[49] To a solution of 1,4-dibromo-2,5-dimethoxybenzene (1.00 g, 30.0 mmol) in dry THF (20 mL) at –78 °C under a nitrogen atmosphere, *n*-butyllithium (2.5 M in hexane, 4.80 mL, 12.0 mmol) was added and stirred for 2 h. An additional 20 mL of THF was added along with DMF (3.0 mL, 39.0 mmol) and stirred for 1 h. When 3 M HCl (10 mL) was added, the reaction was warmed to room temperature and the product was filtered. After drying under vacuum, a yellow precipitate was obtained (DMTA) in 61% yield. ^{1}H NMR (DMSO-d_6, 300 MHz): δ = 10.39 (2H, s), 7.44 (2H, s), 3.93 (6H, s) ppm (Figure 4.7). ^{13}C NMR (DMSO-d_6, 101 MHz): δ = 189.44, 155.65, 129.20, 111.73, and 56.88 ppm (Figure 4.8). IR (neat, cm^{-1}): 875, 1018, 1127, 1166, 1210, 1300, 1393, 1408, 1480, 1671, 2869 (Figure 4.11). HRMS (ESI, m/z) calculated for $C_{10}H_{10}O_4$ $[M+H]^+$ 194.0579, found 194.0583.

2,5-bis(2-propynyloxy) terephthalaldehyde ($C_{14}H_{10}O_4$, BPTA, Scheme 4.4).

The BPTA linker was prepared according to a modified literature procedure.[50]To a solution of DMTA (0.200 g, 1.30 mmol) in dry dichloromethane (20 mL), BBr_3 (1 M in DCM, 2.30 mL, 2.30 mmol) was added dropwise at 0 °C under a nitrogen atmosphere.

After stirring for 3 h at room temperature, the reaction mixture was cooled to 0 °C and water (20 mL) was added to quench excess BBr_3. The organic layer was separated, while the aqueous layer was extracted with dichloromethane (3 × 25 mL) and dried over anhydrous Na_2SO_4, and after that the solvent was removed under reduced pressure. The crude material was recrystallized from acetone to yield the precursor, 2,5-dihydroxyterephthalaldehyde (DHTA) in 89% yield. To make desired BPTA, DHTA (150 mg, 0.900 mmol), and K_2CO_3 (624 mg, 4.51 mmol) were heated at reflux in THF for 30 min. Upon cooling to room temperature, propargyl bromide (0.408 mL) was added, and the reaction mixture was heated to reflux for 3 d. The reaction mixture was cooled to room temperature, followed by the addition of the equal volume of water, extracted with $CHCl_3$ (3 × 25 mL), washed with 5% NaOH (2 × 25 mL), washed with brine (25 mL), dried over Na_2SO_4, filtered, and the $CHCl_3$ was removed under reduced pressure to yield BPTA in 71% yield. ^{1}H NMR (DMSO-d_6, 300 MHz): δ = 10.79 (2H, s), 8.01(2H, s), 5.45 (4H, d, J = 2.13), 4.10 (2H, t, J = 2.16) ppm (Figure 4.9). ^{13}C NMR (DMSO-d_6, 101 MHz): δ = 189.16, 154.12, 129.93, 113.90, 79.91, 78.95, and 57.65 ppm (Figure 4.10). IR (neat, cm^{-1}): 705, 761, 800, 878, 931, 1012, 1097, 1139, 1163, 1202, 1260, 1295, 1359, 1403, 1423, 1449, 1480, 1682, 2121, 2881, 2963, 3282 (Figure 4.12). HRMS (ESI, m/z) calculated for $C_{14}H_{10}O_4$ $[M+H]^+$ 242.0579, found 242.0584. BPTA was recrystallized from a saturated dichloromethane solution. Single-crystal X-ray data for BPTA are shown in Table 4.1 and Figure 4.13.

Development of Synthetic Reaction Conditions for COF Preparation. To develop reaction conditions, we initially perform the condensation reactions in solution using the

molecular precursors as shown below, which allowed us to characterize the products by ^{1}H NMR spectroscopy.

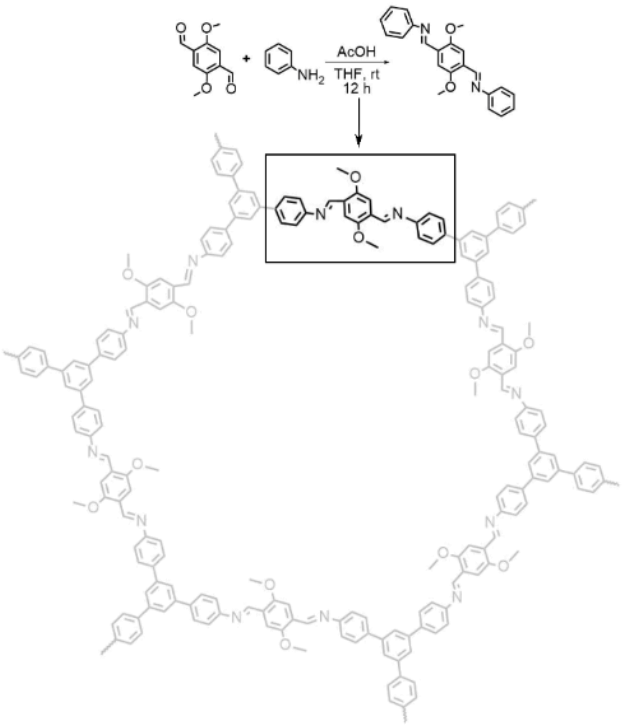

Scheme 4.4. (1*E*,1'*E*)-1,1'-(2,5-dimethoxy-1,4-phenylene)bis(*N*-phenylmethanimine), $C_{22}H_{20}O_2N_2$.

This reaction was performed to develop the methodology for **1-OMe** framework (see the main text).

In a 50 mL round bottom flask, DMTA (100 mg, 0.515 mmol) was dissolved in THF (2.0 mL) and aniline (118 µL, 1.29 mmol) was added to the mixture in the presence of 6M acetic acid catalyst (0.2 mL). After stirring overnight at room temperature, the solvent was removed under reduced pressure to afford a solid in a quantitative yield. ^{1}H NMR (DMSO-d_6, 300 MHz): 8.87 (2H, s), 7.73 (2H, s), 7.44 (4H, m), 7.28 (6H, m), 3.94 (6H, s) ppm (Figure 4.14).

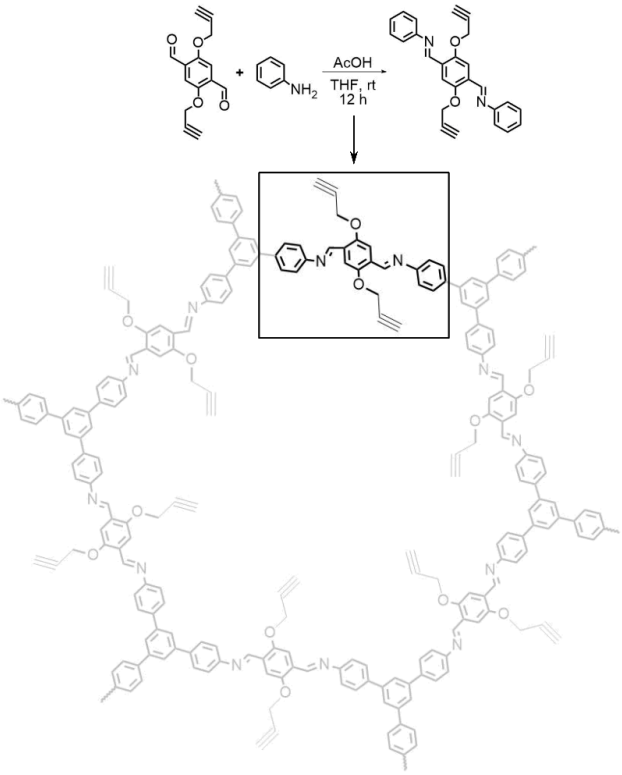

Scheme 4.5. (1*E*,1'*E*)-1,1'-(2,5-bis(prop-2-yn-1-yloxy)-1,4-phenylene)bis(*N*-phenylmethanimine), $C_{26}H_{20}O_2N_2$. This reaction was performed to develop the methodology for 1≡(x%) framework preparation (see the main text).

In a 50 mL round bottom flask, BPTA (100 mg, 0.413 mmol) was dissolved in THF (2.0 mL) and aniline (94 µL, 1.03 mmol) was added to the mixture in the presence of 6M acetic acid catalyst (0.2 mL). After stirring overnight at room temperature, the solvent was removed under reduced pressure to afford a yellow solid in a quantitative yield. ^{1}H NMR (DMSO-d_6, 300 MHz): 8.39 (2H, s), 7.88 (2H, s), 7.45 (4H, m), 7.29 (6H, m), 5.00 (4H, d, J = 1.95), 3.66 (2H, t, J = 2.19) ppm (Figure 4.15).

Synthesis of 1-OMe. The **1-OMe** framework was prepared according to a modified literature procedure.[51] In a pressure tube (10 mL), a mixture of TAPB (28.0 mg, 0.0800 mmol) and DMTA (23.3 mg, 0.120 mmol) in *o*-dichlorobenzene (*o*-DCB)/*n*-butanol (*n*-

BuOH) (1.00 mL/1.00 mL) mixture were heated at 120 °C for 3 d in the presence of acetic acid (6 M, 0.100 mL). Upon cooling to room temperature, the precipitate was collected, washed three times with THF (50 mL), and subjected to Soxhlet extraction (with THF as a solvent) to remove any unreacted precursors. The obtained powder was collected, dried at 120 °C under vacuum overnight to produce **1-OMe** in 80% yield. IR (neat, cm^{-1}): 2948, 1680, 1589, 1468, 1456, 1407, 1290, 1209, 1145, 1036, 972, 875, 827, 746, 691, and 659. Fitting the N_2 adsorption isotherm to the Brunauer-Emmett-Teller (BET) equation resulted in surface area of 1452 m^2/g. The PXRD pattern, FTIR spectrum, thermogravimetric, and gas sorption analysis are shown in Figures 4.16, 4.17, 4.18, 4.19, respectively.

Synthesis of 1≡(50%). The **1≡(50%)** framework was prepared according to a modified literature procedure.[51] In a glass tube (10 mL), a mixture of TAPB (28.0 mg, 0.080 mmol) and DMTA/BPTA (a total of 0.120 mmol) at a molar ratio of 50% in *o*-DCB/ *n*-BuOH (1 mL/1 mL) were held at room temperature for 3 d in the presence of an acetic acid (6 M, 0.100 mL). The precipitate was collected, washed three times with THF (50 mL) and subjected to the Soxhlet extraction procedure using THF as a solvent to remove any unreacted precursors. The powder was collected, dried at 120 °C under vacuum overnight to produce **1≡(50%)** in 78% yield. IR (neat, cm^{-1}): 3285, 2940, 1680, 1589, 1486, 1465, 1407, 1290, 1209, 1145, 1036, 972, 875, 827, 746, and 691. Fitting the N_2 adsorption isotherm to the BET equation resulted in surface area of 925 m^2/g. The PXRD pattern, FTIR spectrum, thermogravimetric, gas sorption analysis plots, and ^{13}C CP-MAS NMR data are shown in Figures 4.20, 4.21, 4.22, and Figure 4.2 (Main), respectively.

Synthesis of 1≡(34%). The **1≡(34%)** framework was prepared according to a modified literature procedure.[51] In a glass tube (10 mL), a mixture of TAPB (28.0 mg, 0.080 mmol) and DMTA/BPTA (a total of 0.120 mmol) at a molar ratio of 34% in *o*-DCB/*n*-BuOH (1 mL/1 mL) were held at room temperature for 3 d in the presence of an acetic acid catalyst (6 M, 0.100 mL). The precipitate was collected, washed three times with THF (50 mL) and subjected to Soxhlet extraction with THF to remove unreacted precursors. The powder was collected, dried at 120 °C under vacuum overnight to produce **1≡(34%)** in 78% yield. IR (neat, cm^{-1}): 3285, 2940, 1680, 1589, 1486, 1465, 1407, 1290, 1209, 1145, 1036, 972, 875, 827, 746, and 691 (Figure 4.23).

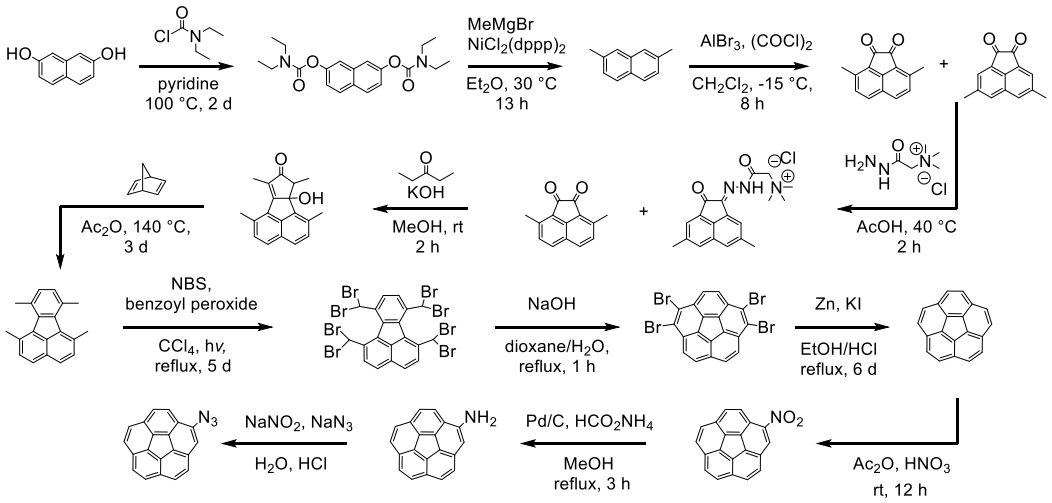

Scheme 4.6. Synthesis of πB-$C_{20}H_9N_3$.

Development of the Synthetic Conditions for CuAAC Reactions. For investigation of reaction conditions necessary to perform CuAAC using πB-$C_{20}H_9N_3$ with the extended insoluble structure **1≡(50%)**, we devised a stepwise approach starting at the molecular level, which includes development of the synthetic methodologies using less bulky and more affordable units (e.g., 2-azidoethanol) before pursuing the reaction with πB-$C_{20}H_9N_3$.

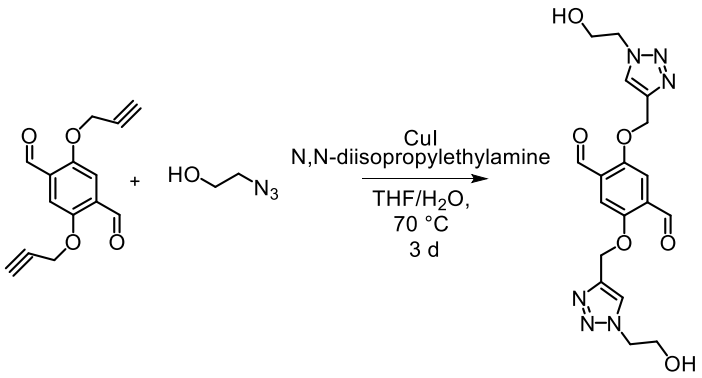

Scheme 4.7. 2,5-bis((1-(2-hydroxyethyl)-1*H*-1,2,3-triazol-4-yl)methoxy)terephthalaldehyde, $C_{18}H_{20}O_6N_6$.

Initially, we coupled just molecular species, such as 2-azidoethanol and BPTA, using THF/H_2O as a medium, which also provided us an access for monitoring the reaction progress by NMR spectroscopy.

In a 25-mL Schlenk tube, BPTA (10.0 mg, 41.0 µmol) and 2-azidoethanol (7.50 mg, 87.0 µmol) were dissolved with THF (0.320 mL) and water (0.110 mL). Next, CuI (2.99 mg, 10.0 µmol) and *N*,*N*-diisopropylethylamine (THF solution, 1 M, 33 µL) were added. Following degassing with three freeze-pump-thaw cycles, the mixture was reacted at 70 °C for 3 d. After removal of solvent under reduced pressure, the solids were stirred in water overnight, filtered, and dried under vacuum to afford a beige solid isolated in a quantitative yield. ^{1}H NMR (DMSO-d_6, 300 MHz): 10.36 (2H, s), 8.24 (2H, s), 7.68 (2H, s), 5.36 (4H, s), 5.03 (2H, t, J = 5.31), 4.41 (4H, t, J = 5.39), 3.78 (4H, q, J = 5.34) ppm (Figure 4.24). FTIR (neat, cm^{-1}): 3359 (broad), 2965, 1583, 1381, 1259, 1208, 1154, 1020, and 797 (Figure 4.25). The FTIR data highlights the disappearance of the alkyne triple bond stretches as shown in Figure 4.25. HRMS (ESI, m/z) calculated for $C_{18}H_{20}O_6N_6$ $[M+H]^+$ 417.1444, found 417.1438.

Stepwise approach for CuAAC reactions with ***1≡(x%)***

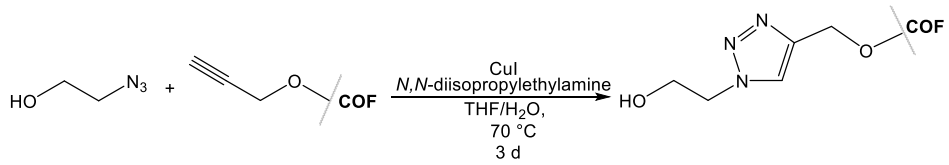

Scheme 4.8. Synthesis of 2-azidoethanol[1≡(34%)].

In a 25-mL Schlenk tube, CuI (1.50 mg, 7.50 µmol) and 1≡(34%) (15.0 mg) were added to a mixture of THF/water (2.00 mL/0.75 mL). To the resulting mixture, N,N-diisopropylethylamine (1 M, 75 µL) and 2-azidoethanol (4.40 mg, 50.0 µmol) were added. The flask was degassed through three freeze-pump-thaw cycles, and the reaction mixture was stirred at 70 °C for 3 d. Upon cooling to room temperature, the precipitate was collected, washed with THF/ACN, and dried under vacuum overnight to give a brown solid in a quantitative yield. IR (neat, cm-1) 2926, 1591, 1505, 1465, 1412, 1293, 1209, 1034, 823, and 697 (Figure 4.26). The FTIR data highlights the disappearance of the alkyne triple bond stretches as shown in Figure 4.26.

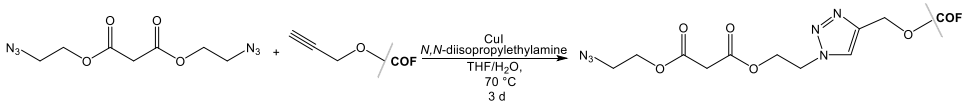

Scheme 4.9. Synthesis of bis(2-azidoethyl) malonate[1≡(34%)].

In a 25-mL Schlenk tube, CuI (1.50 mg, 7.50 µmol) and **1≡(34%)** (15.0 mg) were added to a mixture of THF/water (2.00 mL/0.750 mL). To the resulting mixture, *N,N*-diisopropylethylamine (1 M, 75 µL) and bis(2-azidoethyl) malonate (10.0 mg, 50.0 µmol) were added. The flask was degassed through three freeze-pump-thaw cycles and the mixture was stirred at 70 °C for 3 d. Upon cooling to room temperature, the precipitate was collected, washed with THF/ACN, and dried under vacuum overnight to give a brown solid in a quantitative yield. IR (neat, cm^{-1}): 2100, 1738, 1595, 1504, 1488,

1412, 1287, 1211, 1147, 1036, 829, 732, 698 (Figure 4.27). The FTIR data are shown in Figure S21, which highlights the disappearance of –C≡C– and –C≡C–H stretches.

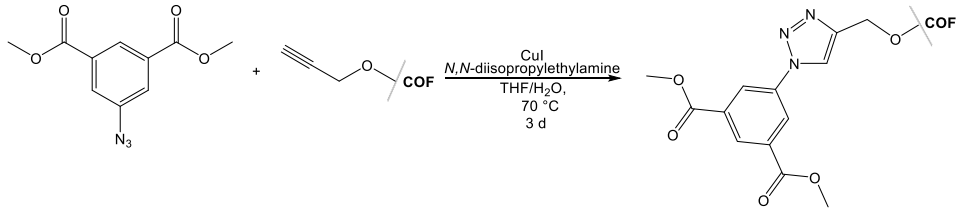

Scheme 4.10. Synthesis of dimethyl 5-azidoisophthalate[1≡(50%)].

In a 25-mL Schlenk tube, CuI (6.00 mg, 0.0315 mmol) and **1≡(50%)** (10.0 mg) were added to a mixture of THF/water (0.323 mL/ 0.107 mL). To this mixture, *N*,*N*-diisopropylethylamine (1 M, 17 µL) and dimethyl 5-azidoisophthalate (1 M, 25 µL) were added. The flask was degassed through three freeze-pump-thaw cycles, and the mixture was stirred at 70 °C for 3 d. Upon cooling to room temperature, the precipitate was collected, washed with THF/ACN and dried under vacuum overnight to give a brown solid in a quantitative yield. FTIR (neat, cm^{-1}): 1730, 1599, 1506, 1411, 1249, 1211, 1039, 879, 827, and 758 (Figure 4.28). The disappearance of –C≡C– and –C≡C–H stretches were observed.

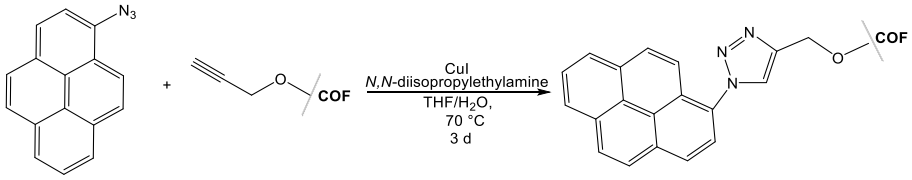

Scheme 4.11. Synthesis of 1-azidopyrene[1≡(50%)].

In a 25-mL Schlenk tube, CuI (6.00 mg, 0.0315 mmol) and **1≡(50%)** (10.0 mg) were added to a mixture of THF/H_2O (0.323 mL/0.107 mL). To resulting mixture, *N*,*N*-diisopropylethylamine (1 M, 17 µL) and 1-azopyrene (1 M, 25 µL) were also added. The

flask was degassed through three freeze-pump-thaw cycles, and the mixture was stirred at 70 °C for 3 d. Upon cooling to room temperature, the precipitate was collected, washed with THF/ACN, and dried under vacuum overnight to give a brown solid in a quantitative yield. IR (neat, cm^{-1}): 1682, 1593, 1506, 1488, 1464, 1409, 1289, 1210, 1183, 1143, 1038, 880, 828, and 694. (Figure 4.29). The FTIR data highlight the disappearance of the alkyne triple bond stretches as shown in Figure 4.29.

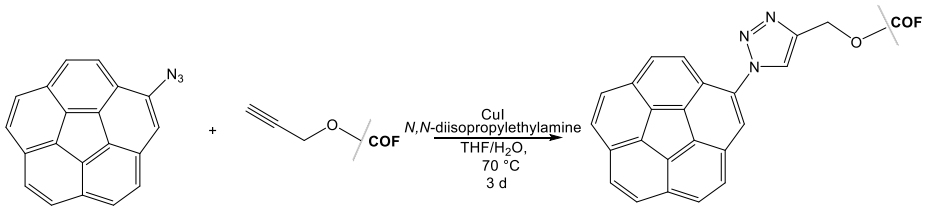

Scheme 4.12. Synthesis of πB-$C_{20}H_9N_3$[1≡(50%)].

In a 25-mL Schlenk tube, CuI (6.00 mg, 0.0315 mmol) and **1≡(50%)** (10.0 mg) were added to a mixture of THF/H_2O (0.323 mL/0.107 mL). To the resulting mixture, *N*,*N*-diisopropylethylamine (1 M, 17 µL) and 1-azidocorannulene (1 M, 18 µL) were added. The flask was degassed through three freeze-pump-thaw cycles, and the mixture was stirred at 70 °C for 3 d. Upon cooling to room temperature, the precipitate was collected, washed with THF/ACN, and dried under vacuum overnight to give a brown solid in a quantitative yield. FTIR (neat, cm^{-1}): 1673, 1596, 1510, 1458, 1394, 1284, 1210, 1185, 1029, 879, 824, 732, and 695. (Main Text, Figure 4.2). Fitting the N_2 adsorption isotherm to the BET equation resulted in surface area of 865 m^2/g (Figure 4.31). The PXRD pattern, gas sorption analysis plot, and FTIR spectrum are shown in Figures 4.30, 4.31, and Main Text Figure 4.2, respectively. ^{13}C CP-MAS NMR and FTIR data reveal disappearance of the alkyne resonances as shown in Figure 4.2 (Main Text).

A control experiment involving 1≡(50%). As a control experiment, we treated **1≡(50%)** under the same reaction conditions but without presence of the azide-containing precursor. As expected, we observed preservation of both 2120 cm^{-1} (C≡C) and 3300 cm^{-1} (H–C≡C) resonances in the FTIR spectrum (Figure 4.32).

In a 25-mL Schlenk tube, CuI (10 mg, 0.053 mmol) and **1≡(50%)** were added to a mixture of THF/H_2O (0.32 mL/0.11 mL). To the reaction mixture, *N*,*N*-diisopropylethylamine (1 M, 17 µL) was added. The flask was degassed through three freeze-pump-thaw cycles and the mixture was stirred at 70 °C for 3 d. Upon cooling to room temperature, the precipitate was collected, washed with THF/ACN, and dried under vacuum overnight to give a brown solid in a quantitative yield. IR (neat, cm^{-1}): 3300, 2120, 1673, 1596, 1510, 1458, 1394, 1284, 1210, 1185, 1029, 879, 824, 732, and 695 (Figure 4.32). ^{13}C CP-MAS NMR data highlight the preservation of 2120 (C≡C) and 3300 cm^{-1} (H–C≡C) resonances as shown in Figure 2 (Main Text).

Preparation of πB-$C_{20}H_{10}$@1-OMe. In a 0.5 dram vial, **1-OMe** (5.0 mg) was added to 0.20 mL THF followed by the addition of πB-$C_{20}H_{10}$ (5.0 mg, 0.020 mmol) in THF (45 µL). After 5 d, THF was used to remove any excess of corannulene. As a result, a red powder was obtained in a quantitative yield. ^1H NMR spectroscopic studies of a digested sample confirmed the presence of corannulene in **1-OMe** after washing, and it was found out presence of one corannulene molecule per six –OMe units (Figure 4.33). FTIR (neat, cm^{-1}): 660, 760, 865, 1064, 1093, 1256, 1388, 1408, 1440, 1496, 1597, and 1657. The PXRD pattern is shown in Figure 4.34. Fitting the N_2 adsorption isotherm to the BET equation resulted in surface area of 898 m^2/g (Figure 4.35).

Digestion Procedure for πB-$C_{20}H_{10}$@1-OMe. To study the amount of πB-$C_{20}H_{10}$ in πB-$C_{20}H_{10}$@**1-OMe**, a solution of 500 µL DMSO and 10 µL of concentrated HCl was added to ~5 mg of πB-$C_{20}H_{10}$@**1-OMe**, followed by heating at 100 °C for 3 d. Based on ^{1}H NMR spectroscopic analysis of the digested COF, non-coordinative immobilization led to inclusion of one corannulene molecule per six –OMe units (Figure 4.33)

Preparation of $C_{16}H_{10}$@1-OMe. In a 0.5 dram vial, **1-OMe** (5.00 mg) was added to 0.20 mL THF followed by the addition of pyrene (5.0 mg, 0.024 mmol) in THF (45 µL). After 5 d, solvent was replaced with fresh THF until the solution was clear to remove any excess of pyrene. As a result, an orange powder was obtained in a quantitative yield. Based on ^{1}H NMR spectroscopic analysis of the digested COF, non-coordinative immobilization led to inclusion of four pyrene molecule per six –OMe units.

Preparation of $C_{10}H_8$@1-OMe. In a 0.5 dram vial, **1-OMe** (5.0 mg) was added to 0.20 mL THF followed by the addition of naphthalene (5.0 mg, 0.039 mmol) in THF (45 µL). After 5 d, the sample was thoroughly washed with THF to remove any excess of naphthalene. As a result, a yellow powder was obtained in a quantitative yield. Based on ^{1}H NMR spectroscopic analysis of the digested COF, non-coordinative immobilization led to inclusion of three naphthalene molecules per six –OMe units.

X-ray crystal structure determination, BPTA ($C_{14}H_{10}O_4$).

X-ray intensity data from a yellow rectangular plate were collected at 100(2) K using a Bruker D8 QUEST diffractometer equipped with a PHOTON-100 CMOS area detector and an Incoatec microfocus source (Mo K_α radiation, λ = 0.71073 Å). The raw area detector data frames were reduced and corrected for absorption effects using the

Bruker APEX3, SAINT+ and SADABS programs.[7,8] Final unit cell parameters were determined by least-squares refinement of 5779 reflections taken from the data set. The structure was solved with SHELXT.[9,10] Subsequent difference Fourier calculations and full-matrix least-squares refinement against F^2 were performed with SHELXL-2018[9,10] using OLEX2.[11]

The compound crystallizes in the monoclinic system. The pattern of systematic absences in the intensity data was consistent with the space group $P2_1/c$, which was confirmed by the structure solution. The asymmetric unit consists of half of one molecule, which is located on a crystallographic inversion center. All non-hydrogen atoms were refined with anisotropic displacement parameters. Hydrogen atoms bonded to carbon were located in Fourier difference maps and refined freely. The largest residual electron density peak in the final difference map is 0.27 e/Å^3, located 0.69 Å from C3.

Table 4.1. X-ray structure refinement data for BPTA.[a]

compound	**BPTA**
formula	$C_{14}H_{10}O_4$
FW	242.22
T, K	100(2)
crystal system	monoclinic
space group	$P2_1/c$
Z	2
a, Å	9.8628(5)
b, Å	4.5525(2)
c, Å	12.7876(6)
α, °	90
β, °	100.550(2)
γ, °	90
V, Å^3	564.46(5)
d_{calc}, g/cm^3	1.425

μ, mm^{-1}	0.105
F(000)	252.0
crystal size, mm^3	0.26 × 0.2 × 0.09
theta range	6.482 to 56.924
index ranges	$-13 \leq h \leq 13$ $-6 \leq k \leq 6$ $-17 \leq l \leq 17$
refl. collected	17034
data/restraints/ parameters	1419/0/102
GOF on F^2	1.048
R_1/wR_2, $[I \geq 2\sigma(I)]^b$	0.0371/0.0833

Fluorescence spectroscopy.

An Edinburgh FS5 fluorescence spectrometer equipped with a 150 W Continuous Wave Xenon Lamp source for excitation was used to acquire steady-state emission spectra. Emission measurements on solid samples were collected on powders of the desired materials placed inside a 0.5 mm quartz sample holder using the front-facing module. Fluorescence lifetimes were measured using a Mini-τ lifetime spectrometer from Edinburgh Instruments equipped with a 365-nm picosecond-pulsed-light-emitting diode (EPLED 365).

Fitting of fluorescence decays.

The fluorescence decays for 1-OMe, $C_{20}H_{10}$πB@1-OMe, $C_{16}H_{10}$@1-OMe, $C_{10}H_8$@1-OMe, and πB-$C_{20}H_9N_3$[1≡(50%)] were fit with the triexponential function:

$$I(t) = \int_{-\infty}^{t} \mathrm{IRF}(t') \sum_{i=1}^{n} B_i e^{\left[-\frac{t-t'}{\tau_i}\right]} dt' \qquad \text{(eq. 4.1)}$$

where τ and B are lifetime and amplitude, respectively.

The amplitude-weighted average fluorescence lifetimes were calculated based on the following equation:

$$\langle \tau_{av} \rangle = \frac{B_1\tau_1 + B_2\tau_2 + B_3\tau_3}{B_1 + B_2 + B_3} \qquad \text{(eq. 4.2)}$$

	B_1	τ_1, ns	B_2	τ_2, ns	B_3	τ_3, ns	$<\tau_{av}>$, ns
1-OMe	0.111	0.242	0.0021	0.835	0.0658	0.855	0.474
πB-$C_{20}H_{10}$@1-OMe	0.267	0.144	0.0550	0.302	0.0350	0.375	0.192
$C_{16}H_{10}$@1-OMe	0.0228	0.200	0.0596	0.510	0.0567	0.514	0.461
$C_{10}H_8$@1-OMe	0.0133	0.262	0.0671	0.459	0.0619	0.497	0.457
πB-$C_{20}H_9N_3$[1≡(50%)]	0.523	0.0941	0.0157	0.217	0.0423	0.574	0.167

Other Physical Measurements.

NMR spectra were obtained on a Bruker Avance III-HD 300 and Bruker Avance III 400 MHz NMR spectrometers. 13C and 1H NMR spectra were referenced to natural abundance 13C peaks and residual 1H peaks of deuterated solvents, respectively. FTIR spectra were collected on a Perkin-Elmer Spectrum 100. Powder X-ray diffraction patterns were recorded from a Rigaku Miniflex II diffractometer with an accelerating voltage and current of 30 kV and 15 mA, respectively. Thermogravimetric analysis was performed on an SDT Q600 Thermogravimetric Analyzer using an alumina boat as the sample holder. Diffuse reflectance spectra were collected on a PerkinElmer Lambda 45

UV-vis spectrometer referenced to Spectralon®. The BET specific surface area was determined by measuring N2 adsorption at 75.6 K using a Micromeritics ASAP 2020. Prior to measurement, the samples were heated in vacuum (1.0×10-7 Torr) with a heating rate of 1 °C/min up to 60 °C, held for 3 h and subsequently heated to 80 °C at 10 °C/min and then held at this temperature for 9 h.

A two point method was employed to measure conductance σ (S/cm) of pressed pellets according to following equation:

$\sigma = Il/VA$,

where I – current, l – thickness of the pellets, V – voltage, A – surface area of the prepared pellets.

The electrical conductance in the prepared materials follows Ohm's law and was

The electrical conductance in the prepared materials follows Ohm's law and was measured by fitting a linear current (I)-voltage (V) curve obtained by using a source meter (Keithley Instruments GmbH, Germering, Germany, model 263) and an electrometer (Keithley Instruments GmbH, Germering, Germany, model 617).[12, 13] All samples were prepared consistently by using the same amounts of materials and the same pressing technique (30 mg of material, dried at 120°C for 3 days, were pressed under 4000 psi at room temperature for 5 minutes with an International Crystal Laboratory 20 Ton E-Z Hydraulic Laboratory PressTM), which relives the issue of deviations from the ideal configuration. The home-built setup was used to perform 2-contact probe conductivity measurements on the pressed pellets: the pellet was placed between two brass plates with attached contacts. A layer of double sided carbon tape

(Electron Microscopy Sciences) was added between a pellet and plates to improve contact.

Solid-state NMR spectra (^{13}C CP-MAS) were collected on a Bruker Avance III-HD 500 MHz spectrometer fitted with a 1.9 mm MAS probe. $^{13}C\{^{1}H\}$ CP-MAS NMR spectra (125.79 MHz) were collected at ambient temperature with a sample rotation rate of 20 kHz. For cross polarization, 2.0 ms contact time with linear ramping on the 1H channel and 62.5 kHz field on the 13C channel were used. 1H dipolar decoupling was performed with SPINAL64 modulation and 147 kHz field strength. Free induction decays (2048–5000 transients) were collected with a 27 ms acquisition time over a 400 ppm spectra width with a relaxation delay of 2.0 s. All XPS experiments were carried out with a Kratos AXIS Ultra DLD system, which was equipped with a monochromatic AlKα source, a hemispherical analyzer, a charge neutralizer for studying insulating samples, and a load lock chamber for rapid introduction of samples into the vacuum chamber. This system has been described in more detail elsewhere.[14, 15] Dwell times were 1000 ms and 600 ms for the valence band and C(1s) regions, respectively, and the step size for both regions was 0.06 eV. Absolute binding energies were set by fixing the C(1s) signal at 284.8 eV, which is the position for adventious carbon,[14, 15] but also has contribution from carbons in πB-C20H10 and 1-OMe. Valence band intensities were not normalized since the C(1s) intensities were comparable for both of the 1-OMe-corannulene containing samples (see Figure S35). Furthermore, normalizing the intensities of the valence band spectra to the total carbon signal does not change the fact that the πB-C20H10 and 1-OMe alone have very little intensity at the valence band edge compared to πB-C20H10@1-OMe and πB-C20H9N3[1≡(50%)]. 1-OMe only had a

C(1s) intensity that was slightly higher, which means that a normalized valence band spectrum would have even less relative intensity at EF. Although the corannulene C(1s) intensity was significantly lower than the other three samples, there is zero intensity between 0 and 3 eV.

Computational Details.

Molecular model. In theoretical analysis several arrangements of πB-$C_{20}H_{10}$ units are considered: convex-to-concave bowl orientation ("stack", Figure S30), concave-to-concave/convex-to-convex orientation ("clam", Figure S30) and the arrangement of pristine corannulene observed in the solid state ("pinwheel", Figure S30). The geometries have been taken from Ref. [16,17]. The nearest intramolecular carbon-to-carbon and unit center-to-center distances are listed in Table S2.

The ground state electron transfer properties are modeled assuming the hopping mechanism, i.e., an electron moves from a molecule to a molecule via a sequence of independent hops. For the stack geometry all hops are equivalent. For the "clam" geometry, there are two types of hops: concave-to-concave (unit A to unit B) and convex-to-convex (unit B to unit C) as shown in the central panel of Figure S30. To move the charge through the material, these two hops take place sequentially. In the case of the "pinwheel" structure, the charge transfer also involves two steps: a hop from unit *1* to *3* followed by a hop from to either unit *2* or to unit *4* (Figure S30, right). Therefore, to compare the charge transfer properties of different geometries, for the two-hop processes the geometric mean of single-hop rates is used.

The electronic couplings. To evaluate the electronic coupling, we employ a conventional two-state approach, which is termed "1+1" in Q-Chem.[18-21] The electron transfer from a donor molecule, *D*, to an acceptor molecule, *A*, ($D^-A \rightarrow DA^-$) is described in the basis of two electronic wavefunctions, representing the initial state *i* (D^-A) and the final state *f* (DA^-) of the electron donor-acceptor system. Minimization of the total energy in this basis is equivalent to the generalized eigenvalue problem,

$$\boldsymbol{H} = \boldsymbol{ES}. \tag{1}$$

In Eq. (1), $\boldsymbol{H}$ is the Hamiltonian matrix and $\boldsymbol{S}$ is the overlap matrix,

$$\boldsymbol{H} = \begin{pmatrix} H_{ii} & H_{if} \\ H_{if} & H_{ff} \end{pmatrix}, \boldsymbol{S} = \begin{pmatrix} S_{ii} & S_{if} \\ S_{if} & S_{ff} \end{pmatrix}. \tag{2}$$

The coupling V_c is determined as the off-diagonal element of $\boldsymbol{H}$ transformed into the orthogonal electronic basis, $\boldsymbol{H}^{eff} = \boldsymbol{S}^{-1/2}\boldsymbol{H}\ \boldsymbol{S}^{-1/2}$. If the electronic eigenstates are normalized to 1, then the coupling is expressed as,

$$V_c = H_{if}^{eff} = \frac{H_{if} - S_{if}(H_{ii}+H_{ff})/2}{1-S_{if}^2}. \tag{3}$$

The matrix elements in Eq. (4.2) are evaluated *directly* using the charge-localized determinants.[18-21] The charge-localized initial/final states are generated by using the fragment molecular orbitals with appropriate charges, i.e. D^-A as the initial state and DA^- as the final state. The direct coupling method is well-defined for the Hartree-Fock (HF) theory of the electronic structure. While the accuracy of the HF energies is limited by its mean-field character, the couplings are known to be more sensitive to the quality of the

basis set, rather than to the electron correlation.[22] Since the system has an overall negative charge, we use basis set 6-31+G* containing diffuse functions without relaxation of the fragment molecular orbitals. The couplings for all relative geometries of two πB-$C_{20}H_{10}$ molecules relevant to "stack", "clam" and "pinwheel" arrangements are listed in Table 4.2. The largest (by at least a factor of four) coupling is obtained for the stacked geometry. This trend is consistent with the LUMO character of the three-unit clusters shown in Figure S31: the LUMOs for the stack geometry are delocalized over all three units forming a "π-column"; for the clam geometry, LUMO is localized on two out of three fragments, while the LUMOs for the three units from the pinwheel geometry (Figure 4.38(d)) can be seen as an intermediate case.

Table 4.2. Analysis of the ground state electron transfer within the two-state direct coupling method (ES method is HF/6-31+G*).

	"stack"	**"clam"**		**"pinwheel"**					
		A→B	*B→C*	*1→2*	*1→3*	*1→4*	*2→3*	*2→4*	*3→4*
R_{cntr}, Å	3.80	8.59	5.14	8.45	3.89	11.60	7.16	8.55	10.61
R_{min}, Å	3.46	4.68	3.38	5.22	3.39	3.84	3.52	4.03	3.80
V_c, eV	0.2188	-0.0103	-0.0162	0.0002	0.0294	-0.0203	0.0549	-0.0043	0.0391

The electronic couplings obtained with the direct coupling method should be viewed as rough estimates: besides the limitations of the HF method, the electronic state

overlaps are very sensitive (exponential dependence) on the separation between the units as illustrated in Figure 4.37 for the "stack" geometry. Additional estimates can be made from the LUMO gap of two equivalent molecules, such as the neutral dimer of corannulene molecules in the "stack" geometry. Based on Koopmans' theorem, for two equivalent molecules[22-24] the frontier orbitals of the anionic dimer are the LUMO and LUMO+1 of the neutral system, and their splitting is related to the coupling between the equivalent initial and final states ($D^{-1}A$ and DA^{-1}),

$$E_{LUMO+1} - E_{LUMO} \approx 2V_c.$$

Since the diffuse functions tend to fill up the frontier orbitals, this coupling estimate is made using the valence basis 6-31G*. For the stack geometry the coupling is −0.217 eV (splitting between the two nearly degenerate pairs of LUMOs; for the *BC* and *AB* dimers, the couplings are −0.076 eV (LUMO and LUMO+1) and −0.0133 eV (nearly triply degenerate LUMO, LUMO+1, LUMO+2 vs LUMO+3). Given the simplicity of the energy gap method, getting the same magnitude for the couplings as with the direct coupling method, gives some support to our computational model.

Rate and diffusion constants, electron mobility.

According to the Marcus theory,[25] the electronic transfer rate for a nonadiabatic process is

$$k = \frac{2\pi}{\hbar}\frac{|V_c|^2}{\sqrt{4\pi\lambda k_B T}}\exp\left(-\frac{(\lambda+\Delta G^0)^2}{4\lambda k_B T}\right). \qquad (4)$$

In Eq. (4) λ - the reorganization energy of the system in response to "instantaneous" relocation of an electron from the donor to acceptor, ΔG° is the difference in the energies of the initial and final states, and T is the temperature. Eq. (4) is

applicable in the weak initial/final state coupling regime, $V_c << \lambda$. In the simplest picture, i.e. the influence of the molecular environment on the donor and acceptor states is neglected, the initial electronic state is $|i\rangle = |D^-\rangle \times |A\rangle$, and the final state is $|f\rangle = |D\rangle \times |A^-\rangle$. The energy of the initial state is

$$E_i = E_{D^-} + E_A \quad (5)$$

After the instantaneous electron "hop", i.e. the vertical electronic excitation, the energy of the initial state becomes

$$E_i^* = E_i - E_{D^-}^{HOMO} + E_A^{LUMO} \quad (6)$$

Upon relaxation, the system arrives at its final state of energy

$$E_f = E_D + E_{A^-} \quad (7)$$

Thus, the electronic reorganization energy is

$$\lambda = E_A^{LUMO} - E_{D^-}^{HOMO}, \quad (8)$$

while the total energy change is

$$\Delta E = E_i - E_f + \lambda = \Delta G_0 + \lambda. \quad (9)$$

For the identical donor and acceptor molecules $\Delta G^\circ = 0$. Within the theory used in direct coupling calculation (HF/6-31+G*), the reorganization energy of electron transfer between two corannulene molecules is $\lambda = 0.89$ eV. This estimate is the same for all arrangements of the corannulene molecules and is at least 3.3 times larger than the computed couplings.

For closer connection of theory and experiment we examine the ratios of conductivity values (σ) for different geometries. The conductivity is related to the charge transfer rates through the charge carrier mobility, μ

$$\sigma = n\mu e. \tag{10}$$

The latter is related to the charge transfer rates through the diffusion constant D and the mean length of the particle transfer

$$\mu = \frac{eD}{k_B T},\ D = \frac{kL^2}{2}, \tag{11}$$

Thus, assuming equal number of charge carriers in all packing motifs,

$$\frac{\sigma_i}{\sigma_j} = \frac{\mu_i}{\mu_j} = \frac{D_i}{D_j} = \frac{k_i L_i^2}{k_j L_j^2} \tag{12}$$

The shortest distance between carbon atoms of different πB-$C_{20}H_{10}$ units is used in Eq. (11), $L=R_{min}$ given in Table S2. The ratios of the rate and diffusion constants are given in Table S3 with respect to those of the most conducting "stack" geometry (k_o and D_o). According to these estimates the charge mobility for the stack geometry there is nearly 40 times larger than for the clam geometry and close to 300 times larger than for the "pinwheel" geometry. These results qualitatively agree with the conductivity measurements implying significant (10000) increase in charge mobility in corannulene integrated into COF compared to that of pristine corannulene. Overall, we argue that in the COF the corannulene molecules form conductive stack-like columns rather than maintaining "pinwheel" orientation associated with the pristine corannulene material.

Table 4.3. The ratios of the charge transfer rates and diffusion constants for different geometrical arrangements.

ratio[a,b]	k_{132}/k_o	k_{134}/k_o	k_{clam}/k_o	k_o/k_{132}	k_o/k_{134}	k_o/k_{clam}	D_o/D_{132}	D_o/D_{134}	D_o/D_{clam}
	0.0337	0.0241	0.0035	29.63	41.56	286.6	29.68	38.57	216.9

[a]The coupling constants are given in eV.
[b]Geometric averages are taken for couplings and distances for the two-step transfer in "clam" and "pinwheel" orientation of corannulene units.

The valence band density of states. In conjunction with the XPS results, we have generated the Density of States (DOS) for the valence band as a function of binding energy (Figure 4.39). The DOS was constructed from the energies of occupied molecular orbitals obtained with the Long-Range Corrected (LRC) ωPBEh density functional method for the 4-unit "stack" and "pinwheel" orientations. The chosen electronic structure method, i.e. LRC-ωPBEh/6-31G* has been shown to perform well for the ground and excited state properties including the charge-transfer states.[26] The DOS is simulated by summing the Gaussian functions centered at the energies of 260 occupied MOs. The standard deviation of the Gaussian function is 0.85 eV. On the plot the curves are shifted to have zero binding energy at the Fermi level. The two solid curves are shifted in accord with experimental calibration: the zero of energy is set to the center of the computed carbon gap of 5.87 eV (experimental value for the half-gap is 2.85 eV). The dashed curves are shifted according to the respective computed HOMO-LUMO gaps, which are 7.17 and 7.46 eV for the stack and pinwheel orientations. The simulated DOSs for the two geometries are quite similar to each other: the main difference is 0.3 eV (0.15

eV for the MO gap) peak shift. The shift is small, but it is in the direction of the XPS results for the pristine rather than COF-integrated corannulene. The overall shape is close to that of the pristine corannulene sample. Therefore, we attribute the lowest energy peak near 2.5 eV in the corannulene-COF samples to the COF states, modified by the interaction with guest molecules. This claim is supported by the fact that XPS of empty COF has significant DOS in this energy region. Extended molecular models for the pristine and COF-integrated corannulene are needed for a more definitive DOS analysis.

Excitation energies and LUMOs. To estimate the band gap in the corannulene-containing materials we have analyzed the excitation energies for the "cluster" models of corannulene materials, consisting of 3 and corannulene molecules for "stack", "clam", and "pinwheel" geometries as well as for the "stack", *AB* and *BC* corannulene dimers (Figure 4.36). The excitation energies are computed within the TDDFT formalism as implemented in Q-Chem. The long-range-corrected density functional with empirical GRIMME[27] correction and diffuse basis (LRC-ωPBEh-D3/6-31+G*) is selected to better capture the intramolecular interactions. As seen from Table S4, the lowest excitation energies for both, triplet and singlet states computed for the 3- and 4-unit models are in close agreement. The difference for the "stack" geometry is less than 0.5%; the difference with the dimer is on the order of 3%. Thus, within our computational method, the 4-unit cluster is a reasonable molecular model for the analysis of electronic excitations and band gaps. Our estimates for the band gaps are 2.95/2.87 eV (for the "stack"/"pinwheel" geometry, respectively) for the triplet state excitation, and 3.86/3.81 eV for the singlet state excitation. The computed values for the "stack"/"pinwheel", are higher than the experimentally assessed values of 2.24 and 1.94 eV for the COF-

integrated and pristine corannulene, respectively, which is typical for the cluster model calculations. Inclusion of more corannulene molecules is expected to reduce the energy gap. Nevertheless, even within our minimalistic 4-unit model, we see the experimentally observed trend of the stacked geometry having larger band gap compared to the material.

Table 4.4. The lowest excitation energies: method LRC-wPBEh/6-31+G*/EMPIRICAL-GRIMME3 (dispersion correction) in eV.

Units	geometry	Triplet	Singlet
2	stack	2.9868 (2.9990)	3.9323 (3.9788)
	A→*B*	3.0188 (3.0256)	4.0116 (4.0480)
	B→*C*	2.9981 (3.0045)	3.9587 3.9980)
3	"stack"	2.9609	3.8841
	"clam"	2.9967	3.9565
	1→*3*→*2*	2.8778	3.8210
	1→*3*→*4*	2.8727	3.8159
4	"stack"	2.9507	3.8644
	"clam"	2.9955	3.9543
	"pinwheel"	2.8740	3.8149

The character of the lowest singlet states for the 4-unit geometry is illustrated in Figure 4.40. Two most contributing virtual orbitals are shown for the three geometries. For the "stack" configuration four lowest virtual orbitals nearly equally contribute to a delocalized excited singlet. V2 and V4 (transition originates with HOMO) are shown. For

the clam shell the main contribution comes from LUMO to HOMO (transitions HOMO→V1 and HOMO-1 → V6, V1 and V6 are shown). For the pinwheel the main transitions are HOMO → V2 and HOMO → V5 which correspond to *1→3→4* charge transfer pathway of the direct coupling method. These excited states and the LUMOs from our charge transfer calculations (Figure 4.38) clearly show the same overall features (delocalization for the stack, localization on the *BC* pair for the clam and intermediate delocalization for the pinwheel geometries) supporting our attribution of high conductivity in corannulene-in-COF to the stacking of πB-$C_{20}H_{10}$ units. We expect increased excited state electron and energy transfer for corannulene-in-COF compared to the pristine material as well.

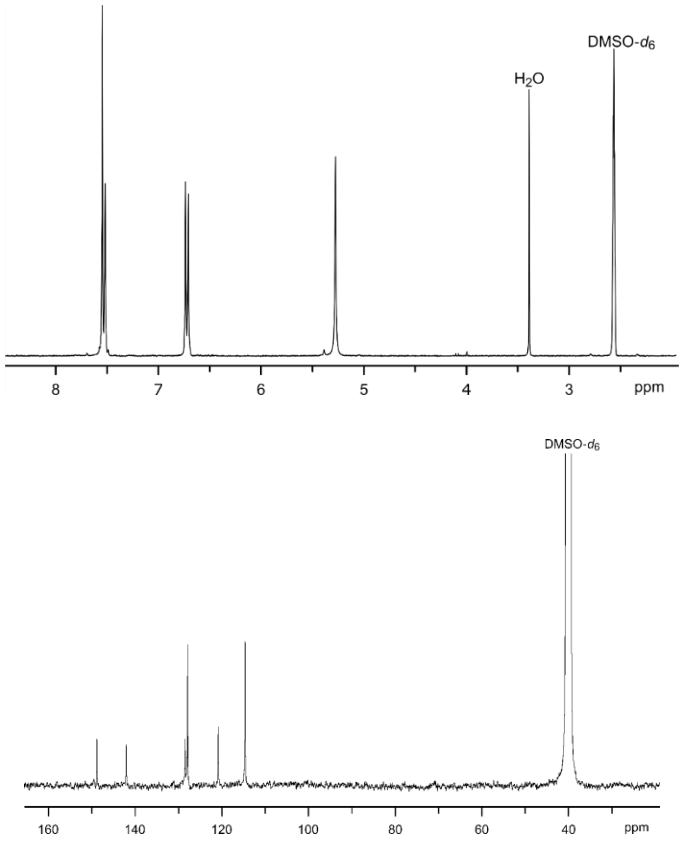

Figure 4.5. ^{1}H NMR (top) and ^{13}C NMR (bottom) spectra of TAPB in DMSO-d_6.

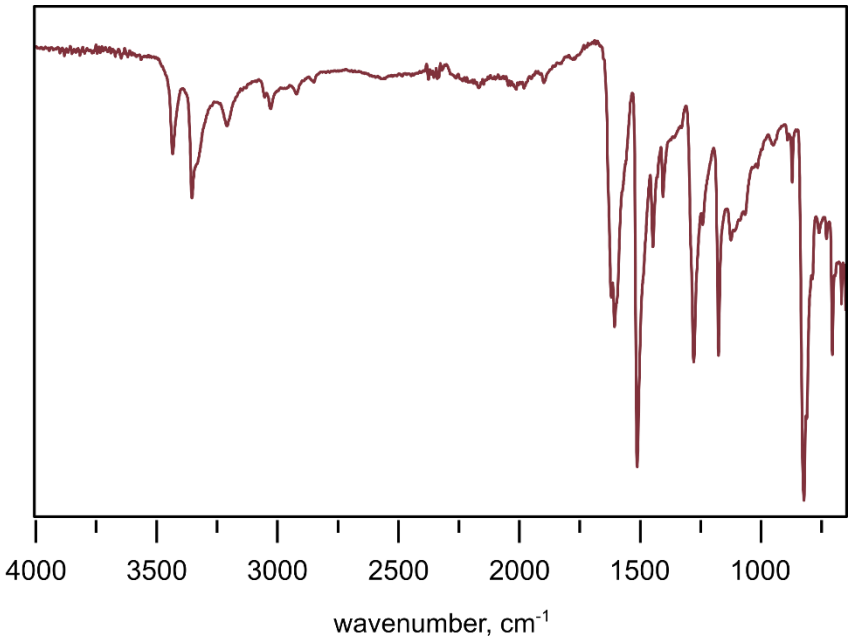

Figure 4.6. FTIR spectrum of TAPB.

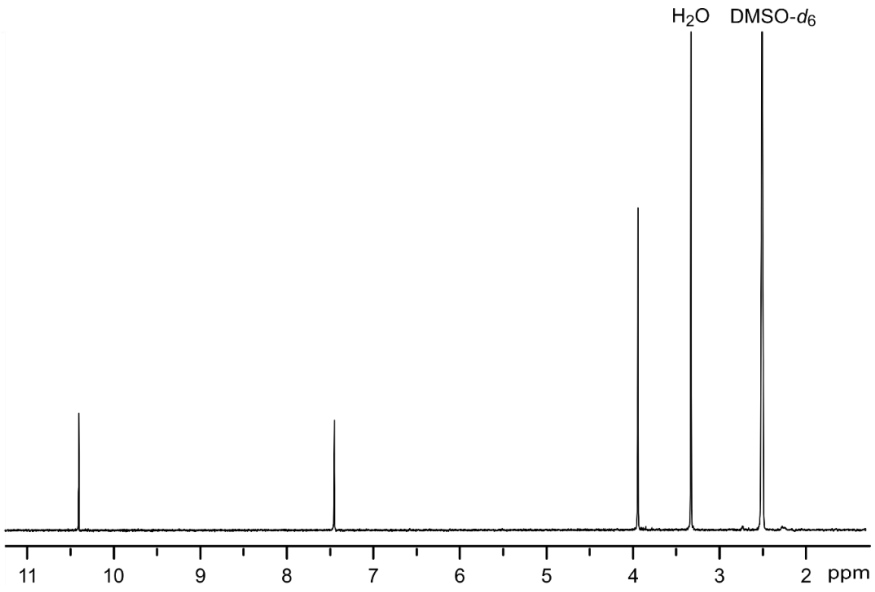

Figure 4.7. ^{1}H NMR spectrum of DMTA in DMSO-d_6.

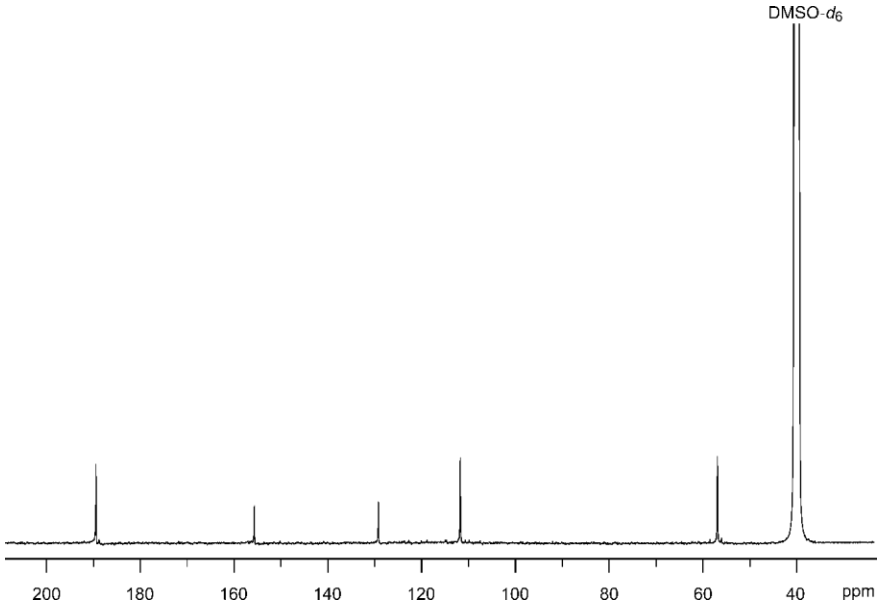

Figure 4.8. ^{13}C NMR spectrum of DMTA in DMSO-d_6.

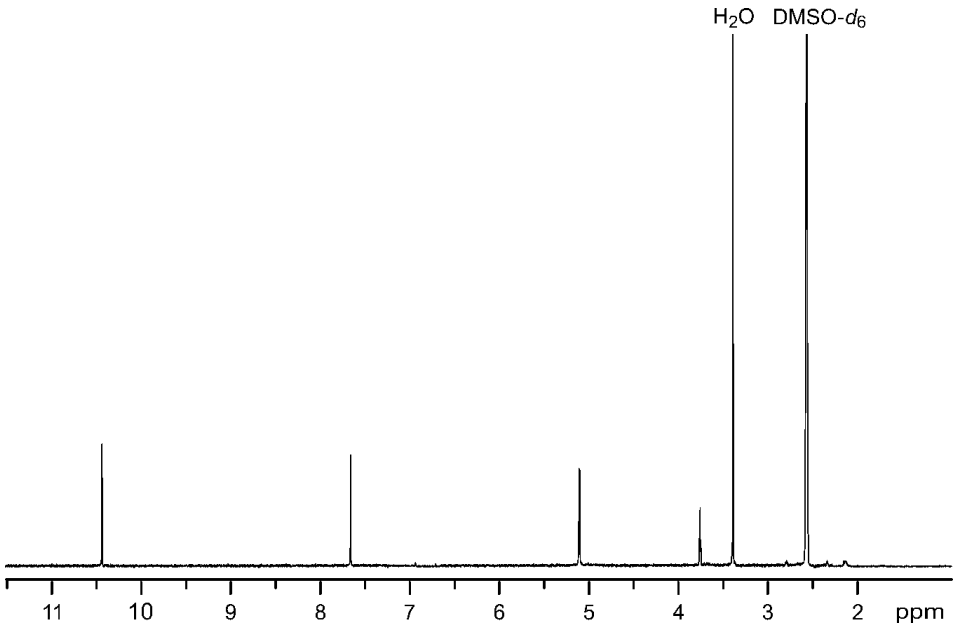

Figure 4.9. ^{1}H NMR spectrum of BPTA in DMSO-d_6.

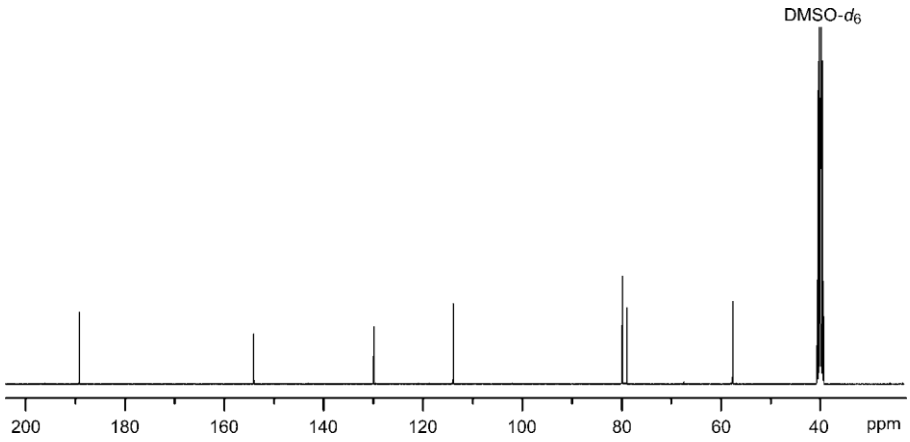

Figure 4.10. ^{13}C NMR spectrum of BPTA in DMSO-d_6.

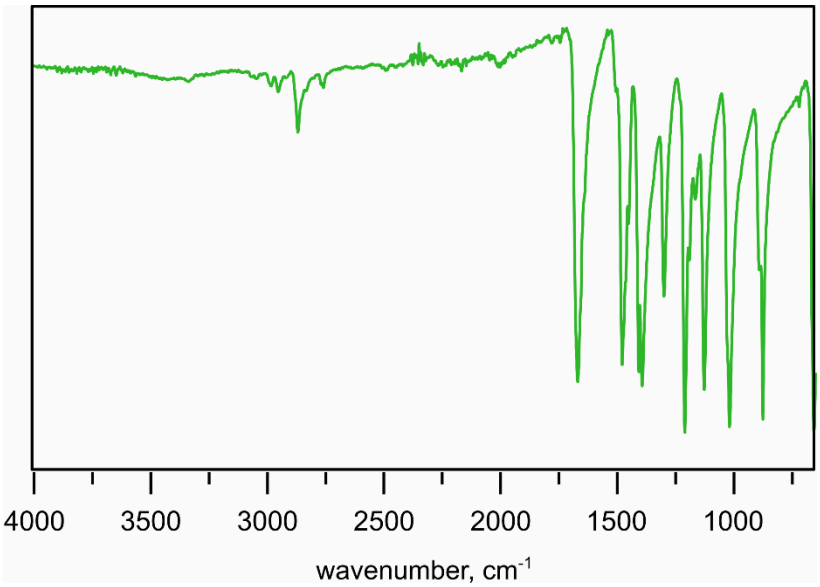

Figure 4.11. FTIR spectrum of DMTA.

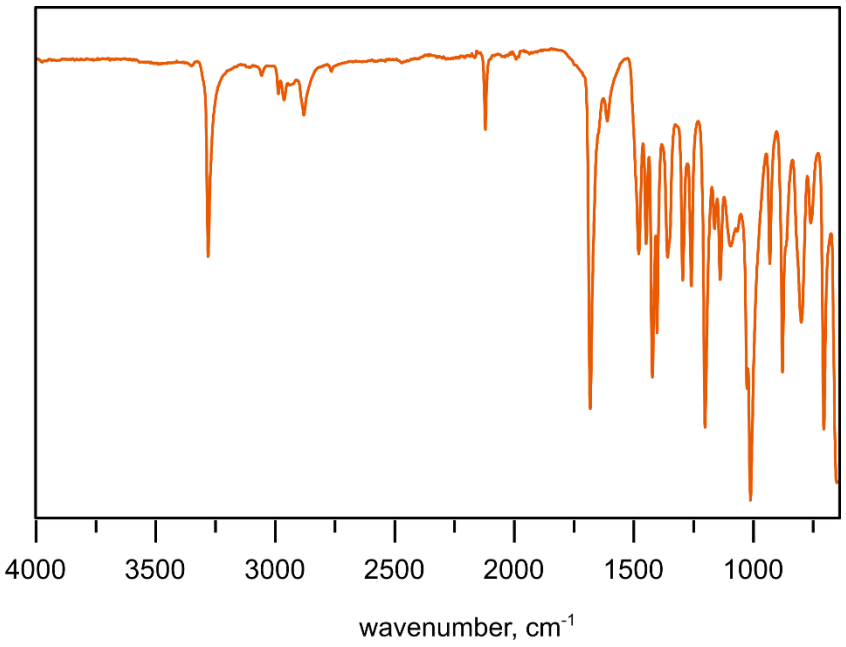

Figure 4.12. FTIR spectrum of BPTA.

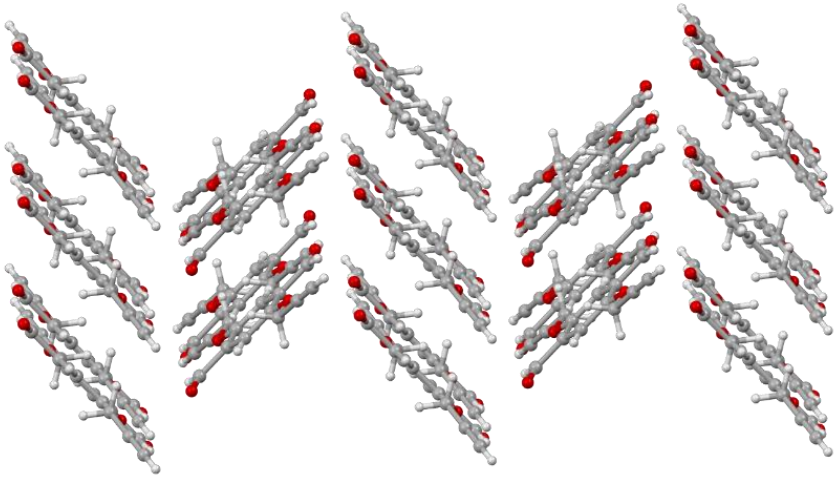

Figure 4.13. Crystal structure of BPTA and packing. Displacement ellipsoids are drawn at the 60% probability level. Red, grey, and white spheres correspond to oxygen, carbon, and hydrogen, respectively.

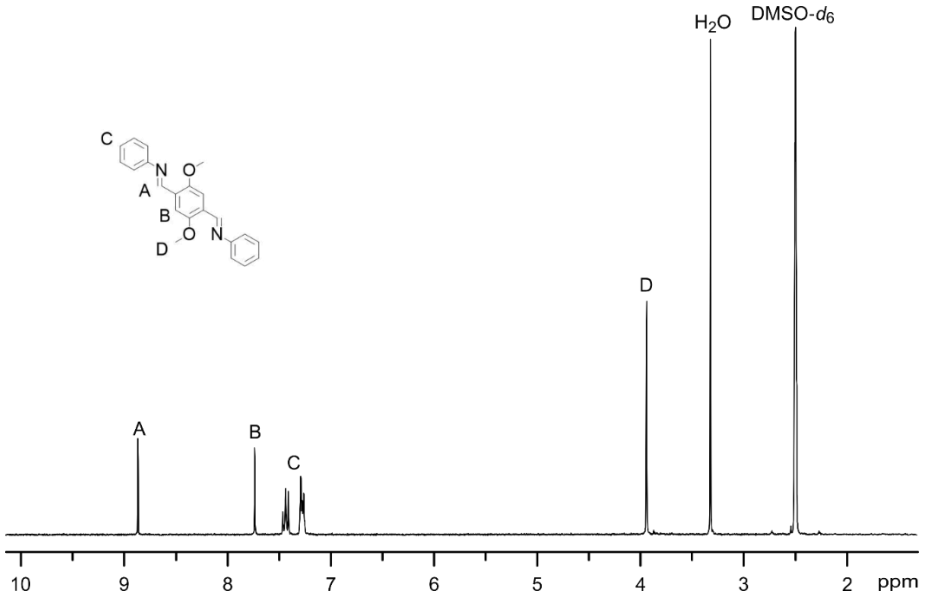

Figure 4.14. ^{1}H NMR spectrum of (1*E*,1'*E*)-1,1'-(2,5-dimethoxy-1,4-phenylene)bis(*N*-phenylmethanimine), $C_{22}H_{20}O_2N_2$.

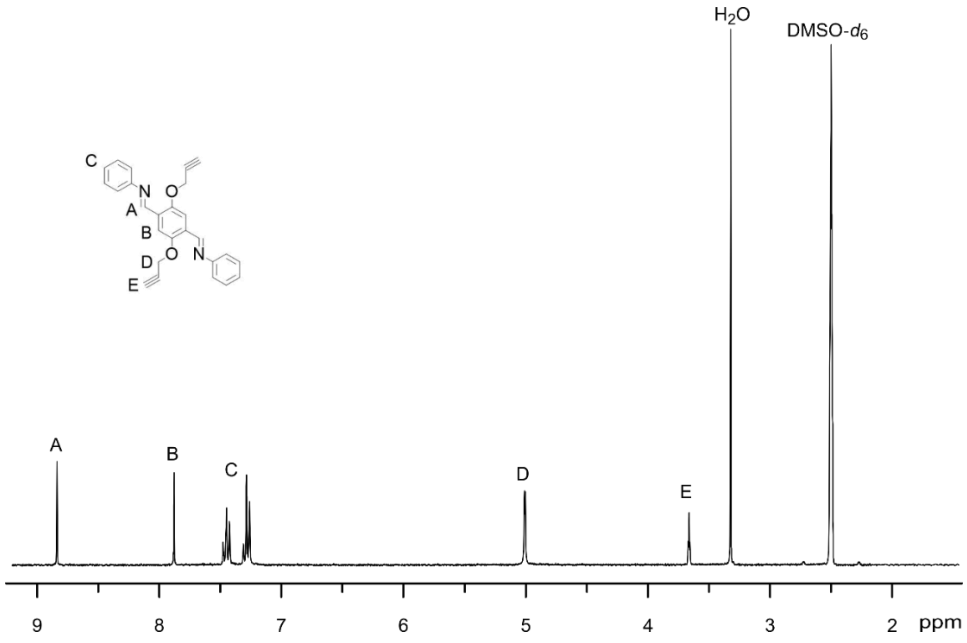

Figure 4.15. ^{1}H NMR spectrum of (1*E*,1'*E*)-1,1'-(2,5-bis(prop-2-yn-1-yloxy)-1,4-phenylene)bis(*N*-phenylmethanimine), $C_{26}H_{20}O_2N_2$.

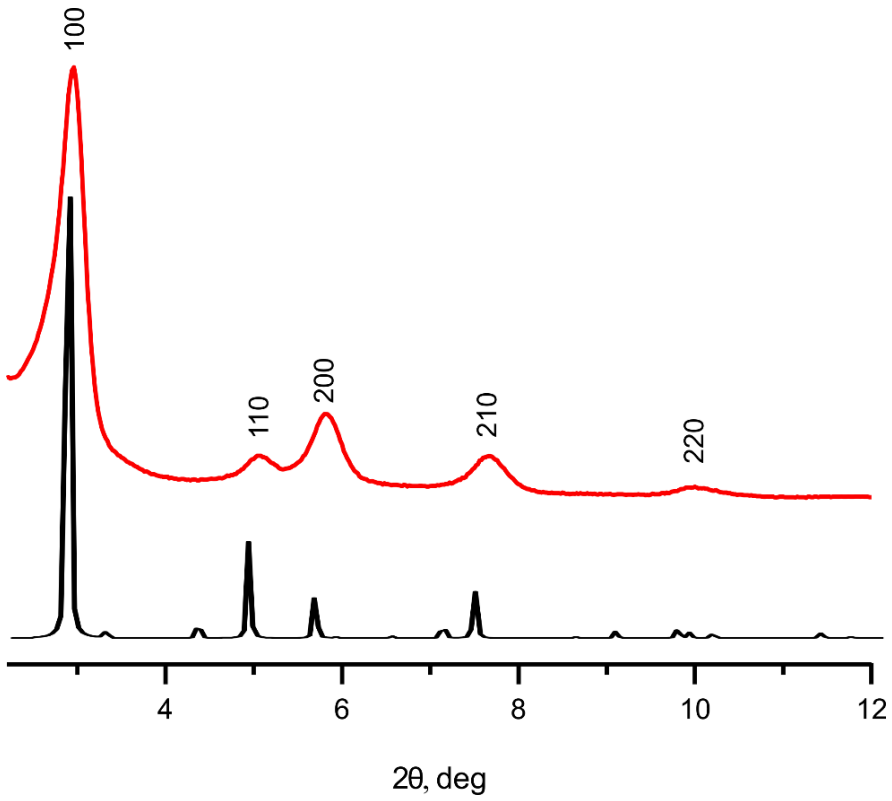

Figure 4.16. PXRD patterns of **1-OMe**: simulated (black) and experimental (red).

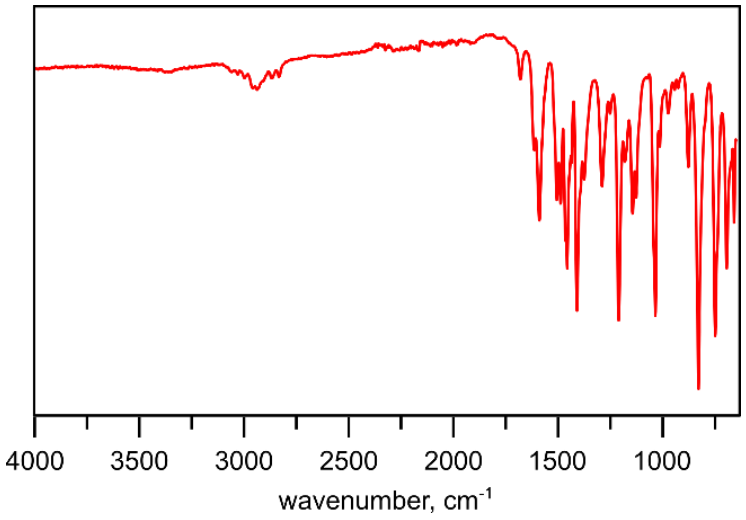

Figure 4.17. FTIR spectrum of **1-OMe**.

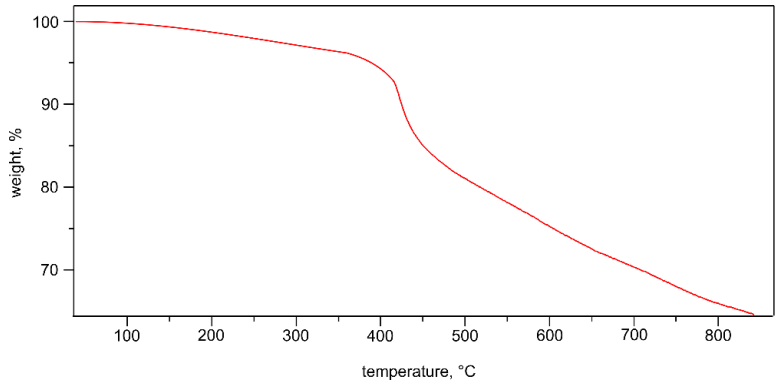

Figure 4.18. Thermogravimetric analysis plot of **1-OMe**.

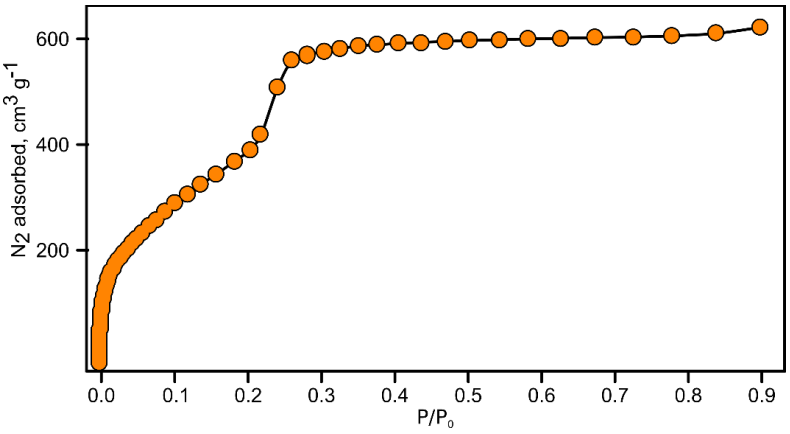

Figure 4.19. N_2 adsorption isotherm of **1-OMe**.

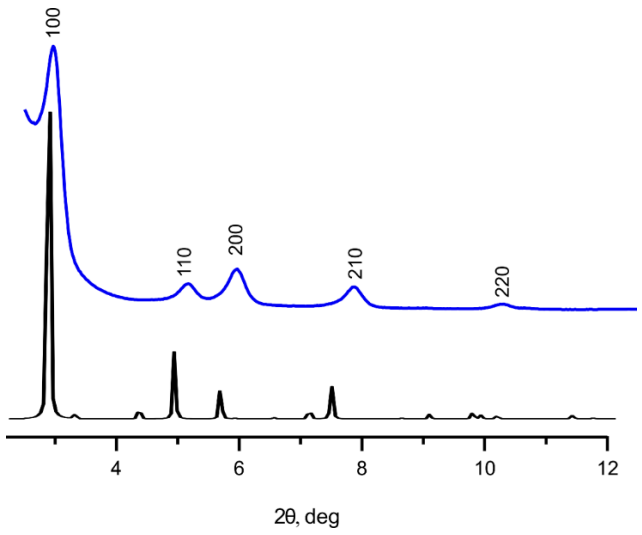

Figure 4.20. PXRD patterns of **1≡(50%)**:
simulated (black) and experimental (blue).

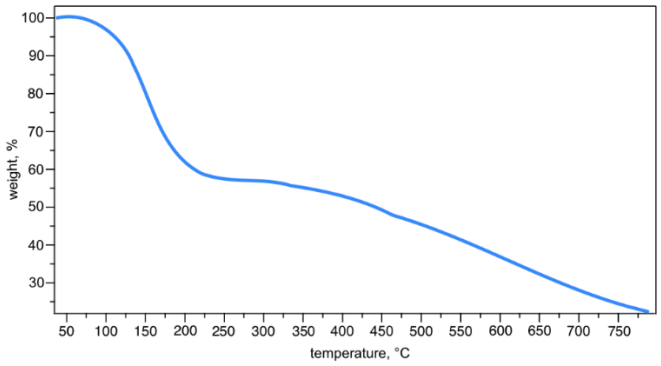

Figure 4.21. Thermogravimetric analysis plot of **1≡(50%)**.

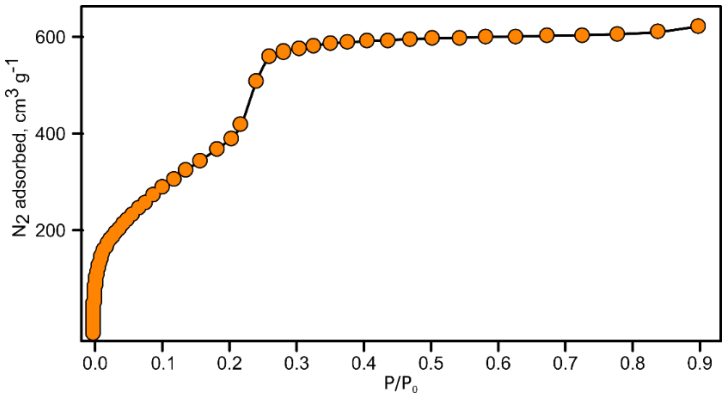

Figure 4.22. N_2 adsorption isotherm of **1≡(50%)**.

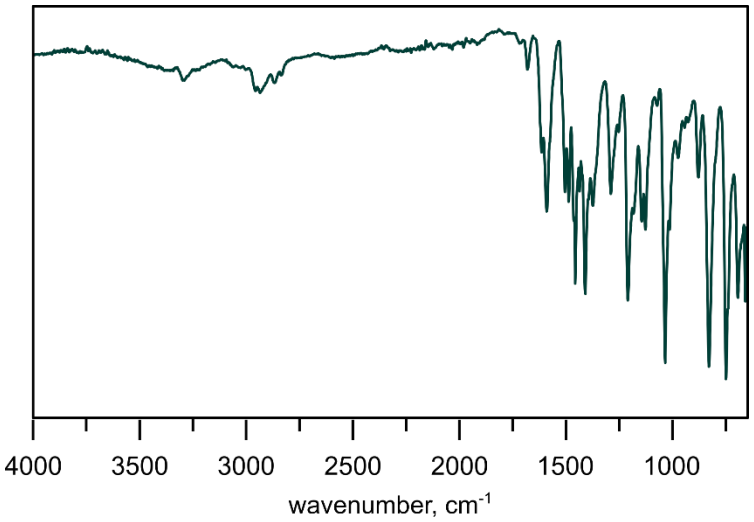

Figure 4.23. FTIR spectrum of **1≡(34%)**.

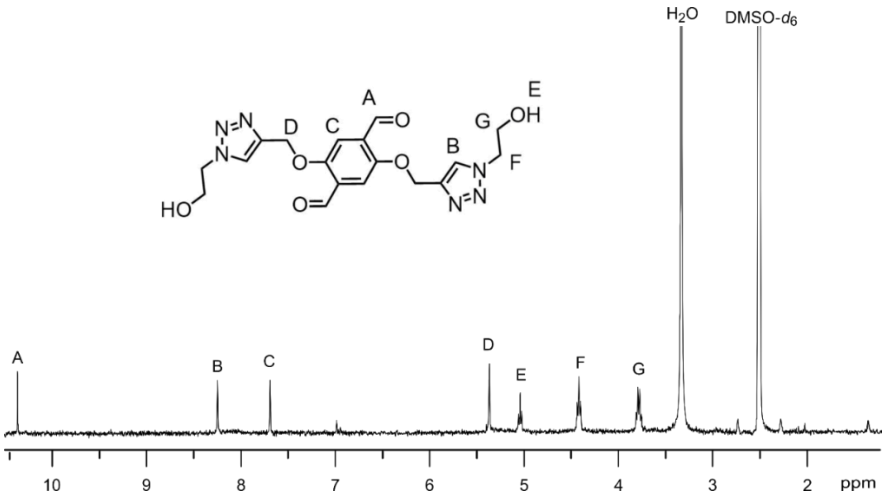

Figure 4.24. ^{1}H NMR spectrum of 2,5-bis((1-(2-hydroxyethyl)-1*H*-1,2,3-triazol-4-yl)methoxy)terephthalaldehyde, $C_{18}H_{20}O_6N_6$.

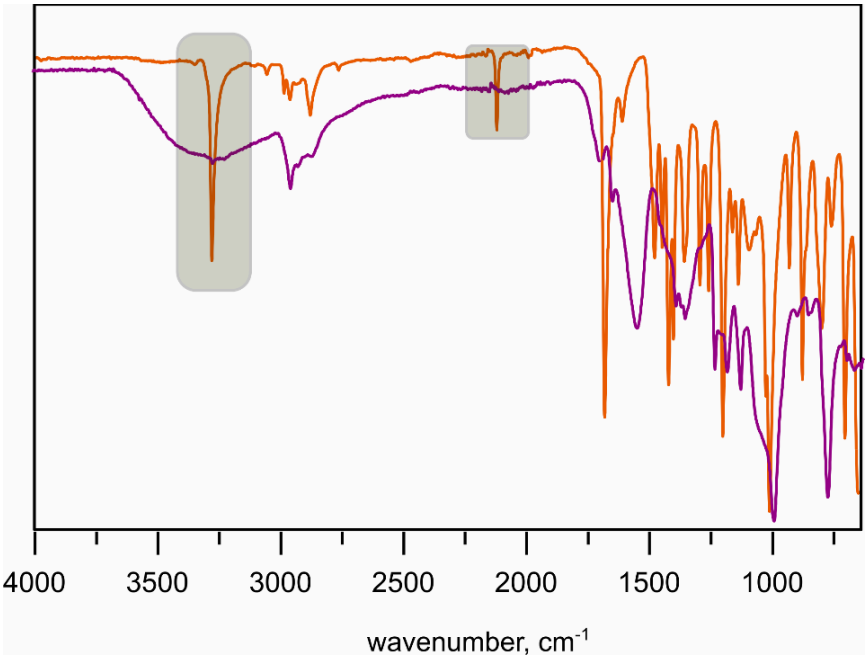

Figure 4.25. FTIR spectra of BPTA (orange) and 2,5-bis((1-(2-hydroxyethyl)-1*H*-1,2,3-triazol-4 yl)methoxy)terephthalaldehyde, $C_{18}H_{20}O_6N_6$ (purple). The grey areas highlight the absence of the H–C≡C stretch (3300 cm^{-1}) and the C≡C stretch (2120 cm^{-1}) in $C_{18}H_{20}O_6N_6$.

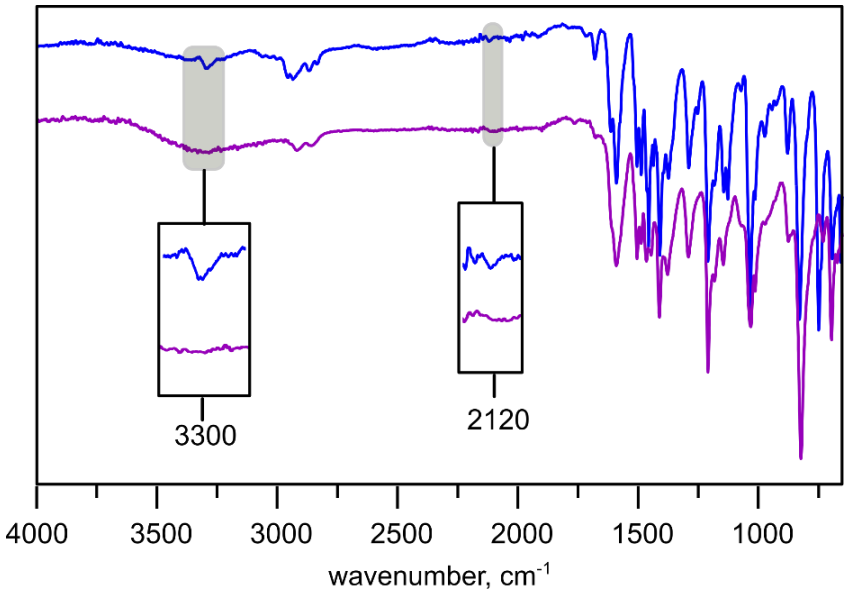

Figure 4.26. FTIR spectra of **1≡(34%)** (blue) and 2-azidoethanol[**1≡(34%)**] (purple). The grey areas highlight the absence of the H–C≡C (3300 cm^{-1}) and the C≡C (2120 cm^{-1}) stretches in $C_2H_5N_3O$[**1≡(34%)**].

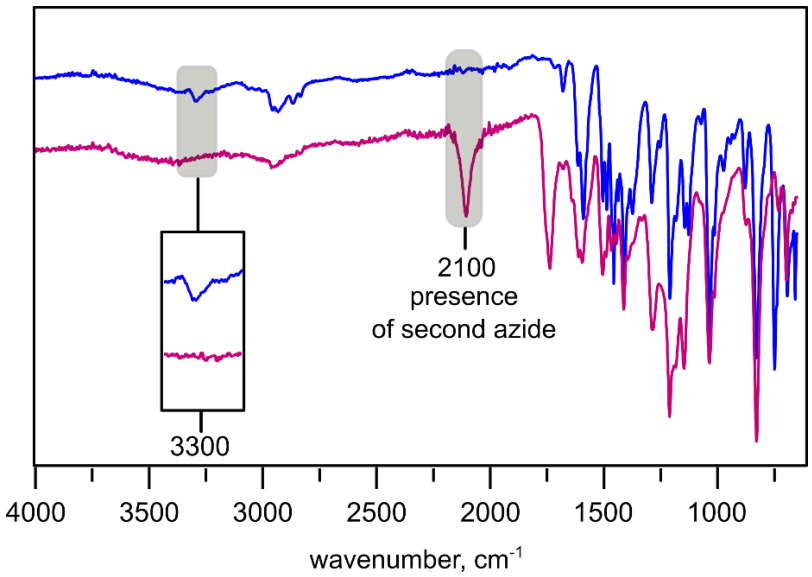

Figure 4.27. FTIR spectra of **1≡(34%)** (blue) and bis(2-azidoethyl) malonate[**1≡(34%)**] (pink). The grey areas highlight the absence of the H–C≡C stretch (3300 cm^{-1}) and the presence of the second azide group (2100 cm^{-1}) in $C_{18}H_{20}O_6N_6$ $C_7H_{10}N_6O_4$[**1≡(34%)**].

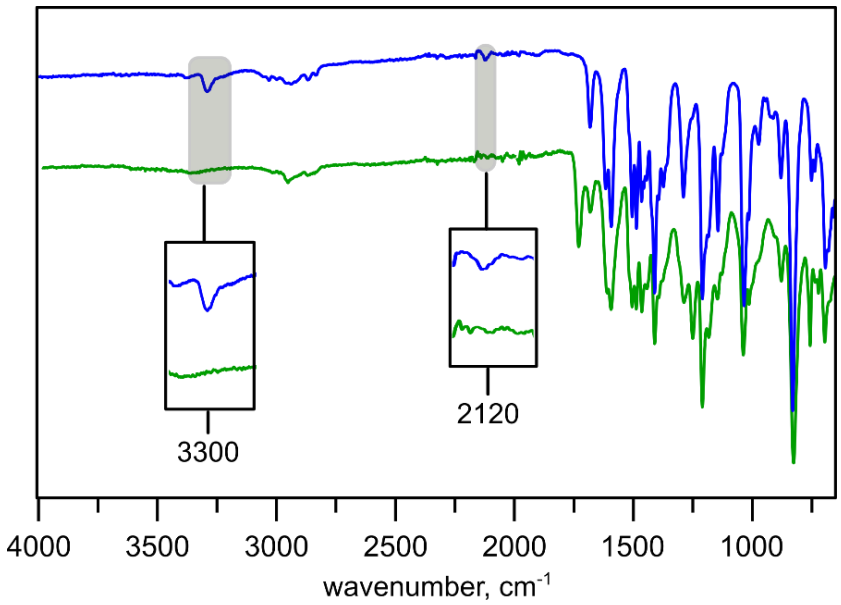

Figure 4.28. FTIR spectra of **1≡(50%)** (blue) and dimethyl 5-azidoisophthalate[**1≡(50%)**] (green). The grey areas highlight the absence of the H-C≡C stretch (3300 cm^{-1}) and the C≡C stretch (2120 cm^{-1}) in $C_{10}H_9N_3O_4$[**1≡(50%)**].

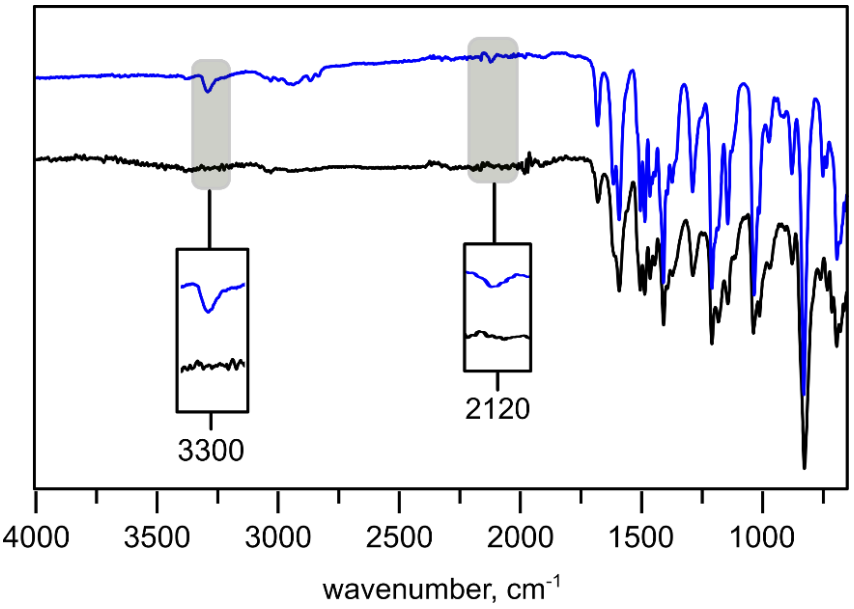

Figure 4.29. FTIR spectra of **1≡(50%)** (blue) and 1-azidopyrene[**1≡(50%)**] (black). The grey areas highlight the absence of the H–C≡C stretch (3300 cm^{-1}) and the C≡C stretch (2120 cm^{-1}) in $C_{16}H_9N_3$[**1≡(50%)**].

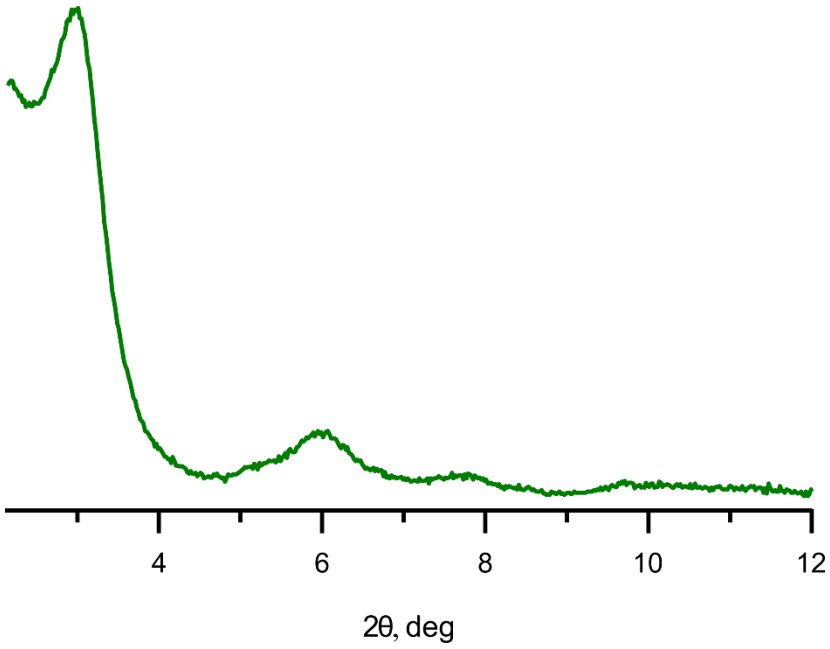

Figure 4.30. PXRD pattern of πB-$C_{20}H_9N_3$[**1≡(50%)**].

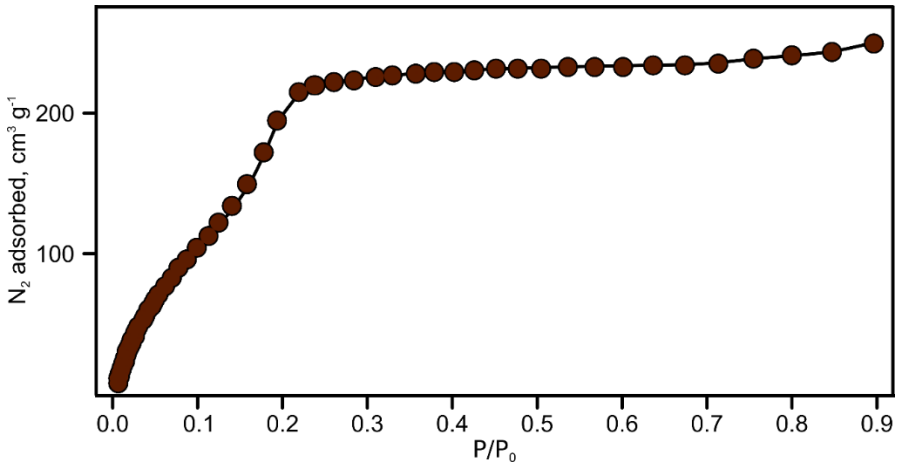

Figure 4.31. N_2 adsorption isotherm of πB-$C_{20}H_9N_3$[**1≡(50%)**].

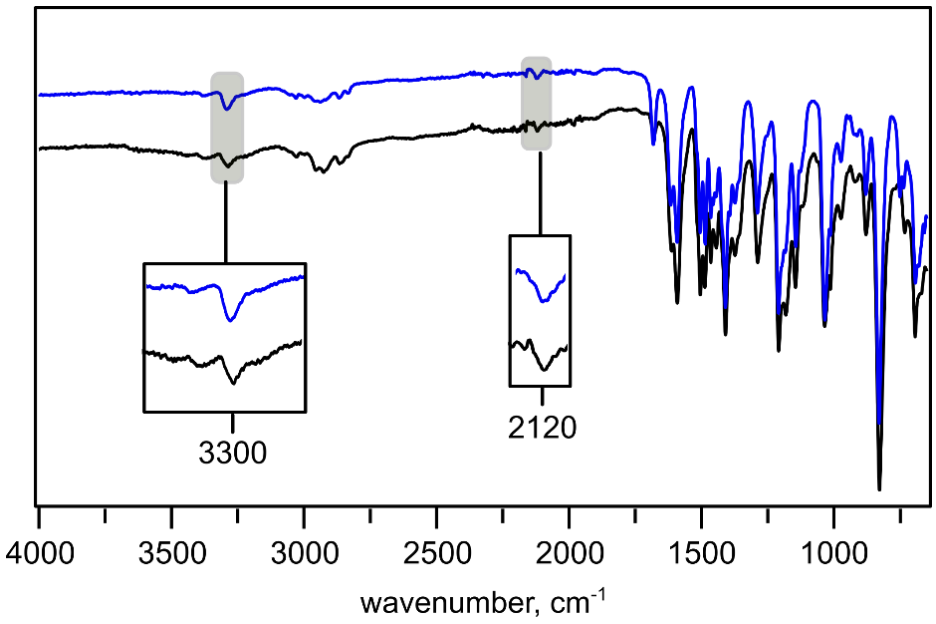

Figure 4.32. FTIR spectra of **1≡(50%)** (blue) and a control experiment involving **1≡(50%)** (black). The grey areas highlight the presence of the H–C≡C (3300 cm^{-1}) and the C≡C (2120 cm^{-1}) stretches in the control experiment performed with **1≡(50%)**.

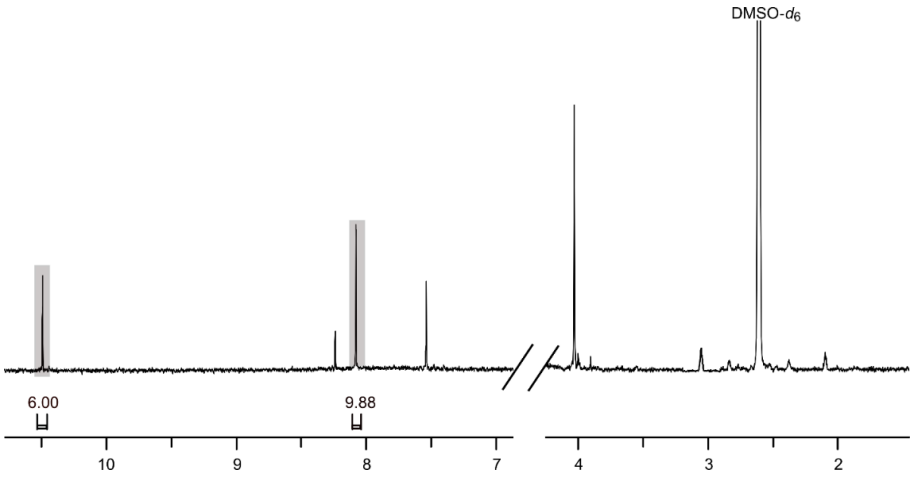

Figure 4.33. ^{1}H NMR spectrum of digested πB-$C_{20}H_{10}$@**1-OMe**. Based on ^{1}H NMR spectroscopic analysis of the digested COF, non-coordinative immobilization led to inclusion of one corannulene molecule per six –OMe units (grey).

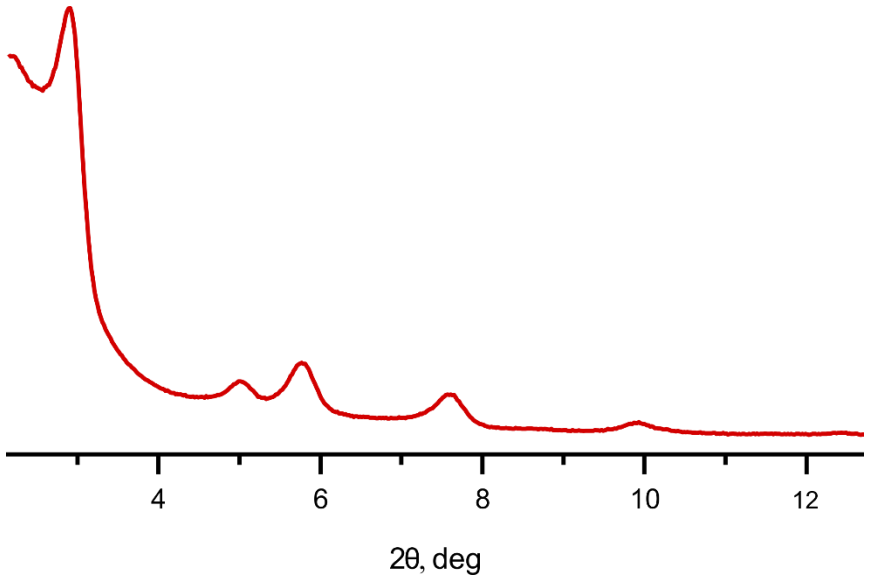

Figure 4.34. PXRD pattern of πB-$C_{20}H_{10}$@**1-OMe**.

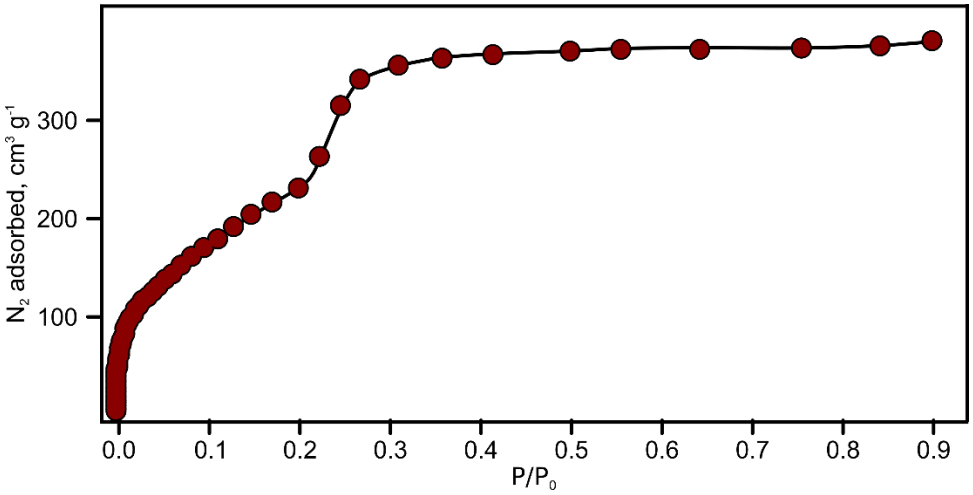

Figure 4.35. N_2 adsorption isotherm of πB-$C_{20}H_{10}$@**1-OMe**.

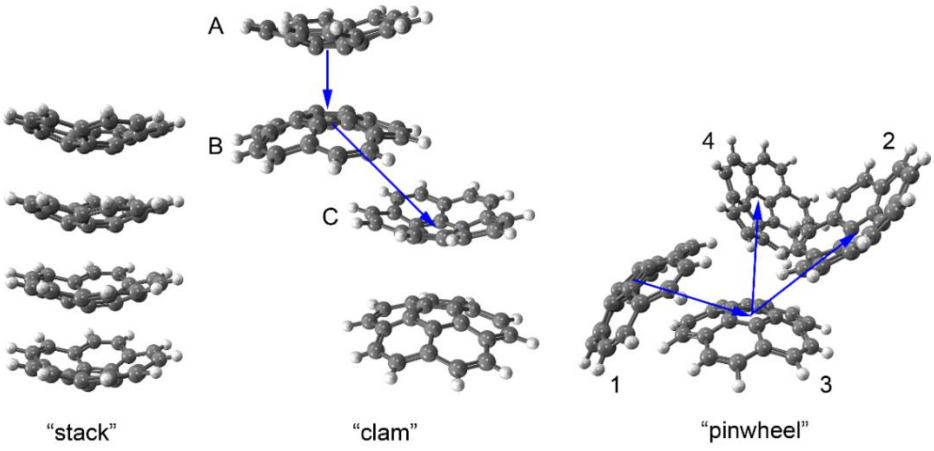

Figure 4.36. Molecular arrangements of πB-$C_{20}H_{10}$. Blue arrows represent possible electron hops during the charge transfer through the material. For the stack geometry all hops are equivalent. For the "clam" geometry charge transfer described through two sequential hops *A*→*B*→*C*. For "pinwheel" geometry charge transfer involves two steps *1*→*3* followed by a hop either to the unit *2* or to the unit *4*.

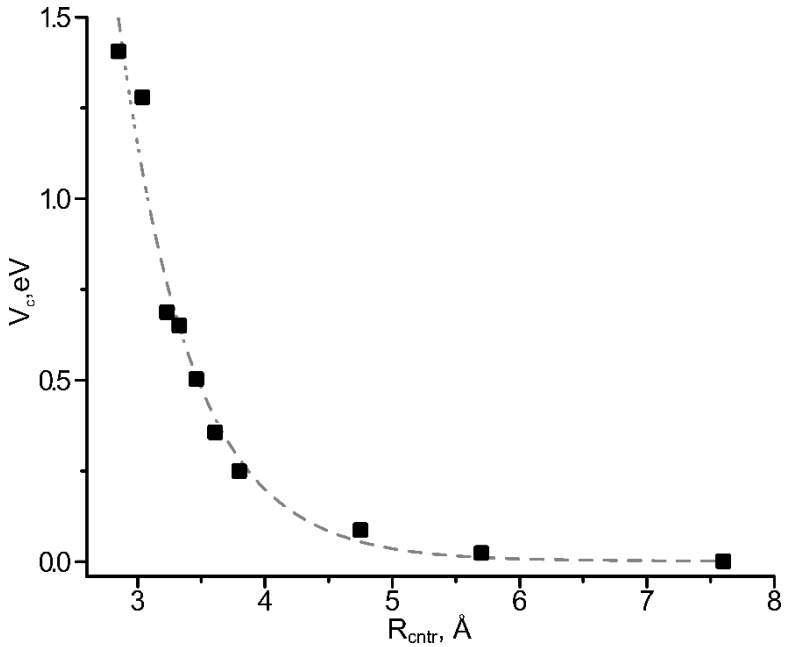

Figure 4.37. Dependence of coupling constants from the distance between πB-$C_{20}H_{10}$ units in the "stack" arrangement.

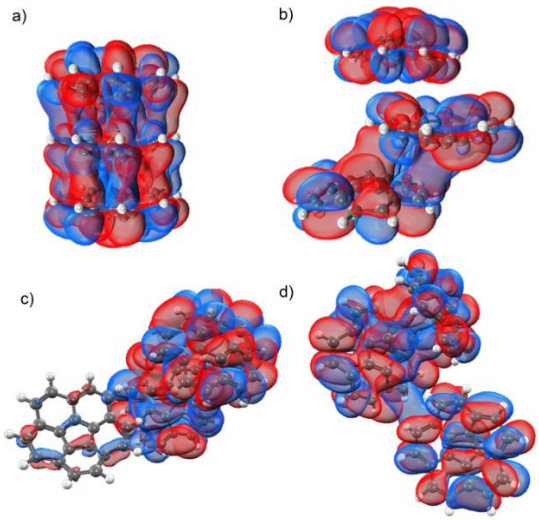

Figure 4.38. Selected LUMOs, associated with the ground state electron transport, for the three-unit πB-$C_{20}H_{10}$: a) "stack", b) "clam", c) "pinwheel"$_{1\rightarrow3\rightarrow2}$, and d) "pinwheel"$_{1\rightarrow3\rightarrow4}$. The theory level LRC-wPBEh/6-31G*. *1→3→2* and *1→3→4* represent the most probable charge transfer pathways in "pinwheel" geometry.

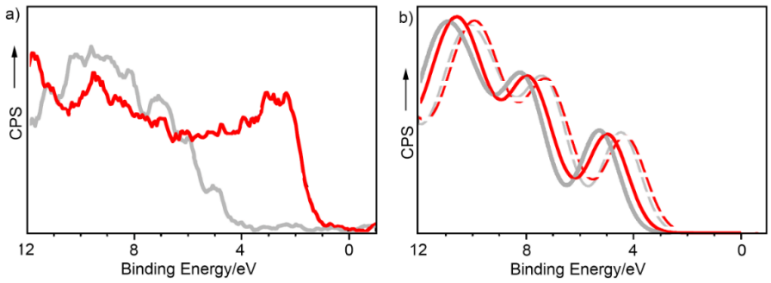

Figure 4.39. (a) XPS data for the valence band region for πB-$C_{20}H_{10}$ (grey) and πB-$C_{20}H_9N_3$**1≡(50%)**] (red). (b) Simulated density of states for the valence band for the "stack" (red) and "pinwheel" (grey) orientation of four πB-$C_{20}H_{10}$ units with LRC-wPBEh/6-31G* method. The zero energy of energy is set to the center of the respective HOMO-LUMO gaps (dashed lines) and carbon gap (solid line).

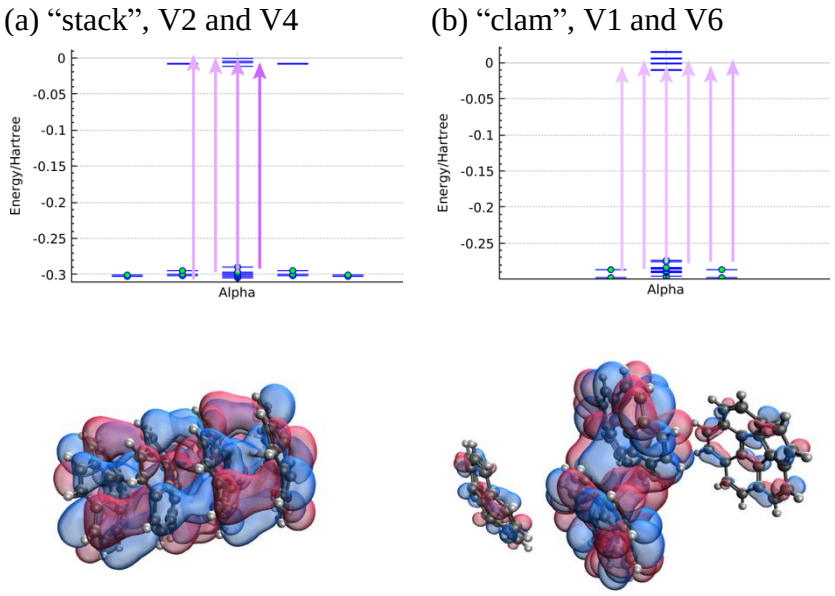

Figure 4.40. Decomposition of the lowest excited singlet state for the 4-unit geometry. Amplitudes of occupied to virtual (labeled V) MO transitions are shown in the middle, while two most contributing virtual orbitals are shown on the top.

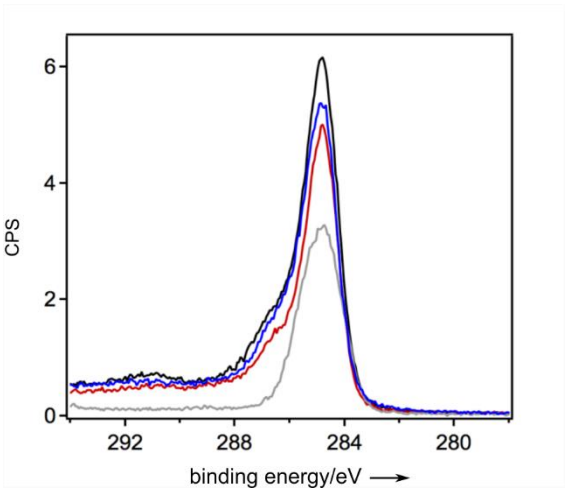

Figure 4.41. X-ray photoelectron spectroscopy data for the C(1s) region for: πB-$C_{20}H_{10}$@**1-OMe** (red); **1-OMe** (black); πB-$C_{20}H_9N_3$[**1≡(50%)**] (blue); and πB-$C_{20}H_{10}$ (grey).

Table 4.5. Atomistic coordinates for the 4-unit "stack" arrangement.

Atom	x	y	z
C	3.914914	3.277726	0.703212
C	3.033836	2.165272	0.699789
C	3.829303	0.988593	0.659475
C	5.191943	1.378526	0.652249
C	5.236532	2.791457	0.675068
C	2.177727	4.589734	1.657435
C	1.33767	3.500217	1.637658
C	1.778209	2.206559	1.252013
C	1.241358	0.910607	1.590879
H	0.324608	0.848676	1.833142
C	1.997587	-0.231666	1.578328
H	1.599853	-1.055111	1.832001
C	3.383413	-0.208729	1.18888
C	4.453549	-1.137685	1.499221
C	5.789436	-0.759221	1.487051
C	6.196087	0.589486	1.168343
C	7.398207	1.298246	1.549424
H	8.172272	0.805096	1.79473
C	7.441012	2.685946	1.563876
H	8.248965	3.119459	1.811844
C	6.301317	3.488748	1.214742
C	5.992762	4.842043	1.617881
H	6.704402	5.417767	1.868512
C	4.708598	5.319137	1.650208
H	4.549862	6.215981	1.921377
C	3.590306	4.481929	1.279016
H	0.296879	3.634938	1.92839
H	1.783058	5.557856	1.962225
H	4.20059	-2.166725	1.750238
H	6.551683	-1.499874	1.724398
C	3.914914	3.277726	4.506412
C	3.033836	2.165272	4.502989
C	3.829303	0.988593	4.462675
C	5.191943	1.378526	4.455449
C	5.236532	2.791457	4.478268
C	2.177727	4.589734	5.460635
C	1.33767	3.500217	5.440858
C	1.778209	2.206559	5.055213
C	1.241358	0.910607	5.394079
H	0.324608	0.848676	5.636342
C	1.997587	-0.231666	5.381528

H	1.599853	-1.055111	5.635201
C	3.383413	-0.208729	4.99208
C	4.453549	-1.137685	5.302421
C	5.789436	-0.759221	5.290251
C	6.196087	0.589486	4.971543
C	7.398207	1.298246	5.352624
H	8.172272	0.805096	5.59793
C	7.441012	2.685946	5.367076
H	8.248965	3.119459	5.615044
C	6.301317	3.488748	5.017942
C	5.992762	4.842043	5.421081
H	6.704402	5.417767	5.671712
C	4.708598	5.319137	5.453408
H	4.549862	6.215981	5.724577
C	3.590306	4.481929	5.082216
H	0.296879	3.634938	5.73159
H	1.783058	5.557856	5.765425
H	6.551683	-1.499874	5.527598
H	4.20059	-2.166725	5.553438
C	3.914914	3.277726	8.309612
C	3.033836	2.165272	8.306189
C	3.829303	0.988593	8.265875
C	5.191943	1.378526	8.258649
C	5.236532	2.791457	8.281468
C	2.177727	4.589734	9.263835
C	1.33767	3.500217	9.244058
C	1.778209	2.206559	8.858413
C	1.241358	0.910607	9.197279
H	0.324608	0.848676	9.439542
C	1.997587	-0.231666	9.184728
H	1.599853	-1.055111	9.438401
C	3.383413	-0.208729	8.79528
C	4.453549	-1.137685	9.105621
C	5.789436	-0.759221	9.093451
C	6.196087	0.589486	8.774743
C	7.398207	1.298246	9.155824
H	8.172272	0.805096	9.40113
C	7.441012	2.685946	9.170276
H	8.248965	3.119459	9.418244
C	6.301317	3.488748	8.821142
C	5.992762	4.842043	9.224281
H	6.704402	5.417767	9.474912
C	4.708598	5.319137	9.256608
H	4.549862	6.215981	9.527777
C	3.590306	4.481929	8.885416

H	0.296879	3.634938	9.53479
H	1.783058	5.557856	9.568625
H	4.20059	-2.166725	9.356638
H	6.551683	-1.499874	9.330798
C	3.914914	3.277726	12.112812
C	3.033836	2.165272	12.109389
C	3.829303	0.988593	12.069075
C	5.191943	1.378526	12.061849
C	5.236532	2.791457	12.084668
C	2.177727	4.589734	13.067035
C	1.33767	3.500217	13.047258
C	1.778209	2.206559	12.661613
C	1.241358	0.910607	13.000479
H	0.324608	0.848676	13.242742
C	1.997587	-0.231666	12.987928
H	1.599853	-1.055111	13.241601
C	3.383413	-0.208729	12.59848
C	4.453549	-1.137685	12.908821
C	5.789436	-0.759221	12.896651
C	6.196087	0.589486	12.577943
C	7.398207	1.298246	12.959024
H	8.172272	0.805096	13.20433
C	7.441012	2.685946	12.973476
H	8.248965	3.119459	13.221444
C	6.301317	3.488748	12.624342
C	5.992762	4.842043	13.027481
H	6.704402	5.417767	13.278112
C	4.708598	5.319137	13.059808
H	4.549862	6.215981	13.330977
C	3.590306	4.481929	12.688616
H	0.296879	3.634938	13.33799
H	1.783058	5.557856	13.371825
H	6.551683	-1.499874	13.133998
H	4.20059	-2.166725	13.159838
C	3.914914	3.277726	0.703212

Table 4.6. Atomistic coordinates for the 4-unit “clam” arrangement.

Atom	**x**	**y**	**z**
C	9.818961	32.46851	7.213393
C	9.094317	33.369452	6.40225
C	8.966938	34.588473	7.099038
C	9.607301	34.439838	8.35268
C	10.131716	33.136731	8.420265
C	10.55443	31.424879	6.717729

C	10.397403	31.209358	5.300204
H	10.796925	30.444736	4.90272
C	9.681509	32.085244	4.503731
H	9.597464	31.897114	3.576102
C	9.05672	33.275812	5.032748
C	8.635145	34.496744	4.347496
C	8.539911	35.715128	5.034629
C	8.82101	35.797726	6.468832
C	9.202901	36.932874	7.286495
H	9.024271	37.808548	6.965373
C	9.817745	36.786575	8.514557
H	10.039098	37.564362	9.01298
C	10.134226	35.492812	9.064765
C	11.103841	35.099141	10.060607
H	11.40635	35.746766	10.685672
C	11.606797	33.816844	10.136467
H	12.240316	33.606419	10.813569
C	11.197089	32.783829	9.212474
C	11.824973	31.518094	8.857998
C	11.532369	30.870894	7.649497
H	8.252125	36.614707	4.492543
H	8.391319	34.45912	3.28681
H	12.536787	31.065036	9.546461
H	12.042141	29.940959	7.401959
C	20.123361	32.46851	7.213393
C	19.398717	33.369452	6.40225
C	19.271338	34.588473	7.099038
C	19.911701	34.439838	8.35268
C	20.436116	33.136731	8.420265
C	20.85883	31.424879	6.717729
C	20.701803	31.209358	5.300204
H	21.101325	30.444736	4.90272
C	19.985909	32.085244	4.503731
H	19.901864	31.897114	3.576102
C	19.36112	33.275812	5.032748
C	18.939545	34.496744	4.347496
C	18.844311	35.715128	5.034629
C	19.12541	35.797726	6.468832
C	19.507301	36.932874	7.286495
H	19.328671	37.808548	6.965373
C	20.122145	36.786575	8.514557
H	20.343498	37.564362	9.01298
C	20.438626	35.492812	9.064765
C	21.408241	35.099141	10.060607
H	21.71075	35.746766	10.685672

C	21.911197	33.816844	10.136467
H	22.544716	33.606419	10.813569
C	21.501489	32.783829	9.212474
C	22.129373	31.518094	8.857998
C	21.836769	30.870894	7.649497
H	18.556525	36.614707	4.492543
H	18.695719	34.45912	3.28681
H	22.346541	29.940959	7.401959
H	22.841187	31.065036	9.546461
C	6.378122	31.23229	5.325532
C	7.102765	30.331348	6.136675
C	7.230145	29.112327	5.439887
C	6.589782	29.260962	4.186246
C	6.065367	30.564069	4.118661
C	5.642652	32.275921	5.821196
C	5.79968	32.491442	7.238722
H	5.400157	33.256064	7.636206
C	6.515574	31.615556	8.035194
H	6.599619	31.803686	8.962824
C	7.140362	30.424988	7.506177
C	7.561938	29.204056	8.191429
C	7.657171	27.985672	7.504296
C	7.376073	27.903074	6.070094
C	6.994181	26.767926	5.25243
H	7.172812	25.892252	5.573552
C	6.379338	26.914225	4.024368
H	6.157984	26.136438	3.525946
C	6.062856	28.207988	3.47416
C	5.093241	28.601659	2.478319
H	4.790732	27.954034	1.853253
C	4.590286	29.883956	2.402458
H	3.956766	30.094381	1.725356
C	4.999993	30.916971	3.326452
C	4.37211	32.182706	3.680927
C	4.664713	32.829906	4.889429
H	3.660298	32.635764	2.992463
H	4.154941	33.75984	5.136967
H	7.944955	27.086092	8.046382
H	7.805765	29.24168	9.252114
C	16.682522	31.23229	5.325532
C	17.407165	30.331348	6.136675
C	17.534545	29.112327	5.439887
C	16.894182	29.260962	4.186246
C	16.369767	30.564069	4.118661
C	15.947052	32.275921	5.821196

C	16.10408	32.491442	7.238722
H	15.704557	33.256064	7.636206
C	16.819974	31.615556	8.035194
H	16.904019	31.803686	8.962824
C	17.444762	30.424988	7.506177
C	17.866338	29.204056	8.191429
C	17.961571	27.985672	7.504296
C	17.680473	27.903074	6.070094
C	17.298581	26.767926	5.25243
H	17.477212	25.892252	5.573552
C	16.683738	26.914225	4.024368
H	16.462384	26.136438	3.525946
C	16.367256	28.207988	3.47416
C	15.397641	28.601659	2.478319
H	15.095132	27.954034	1.853253
C	14.894686	29.8836	2.402458
H	14.261166	30.094381	1.725356
C	15.304393	30.916971	3.326452
C	14.67651	32.182706	3.680927
C	14.969113	32.829906	4.889429
H	14.459341	33.75984	5.136967
H	13.964698	32.635764	2.992463
H	18.249355	27.086092	8.046382
H	18.110165	29.24168	9.252114
C	9.818961	32.46851	7.213393
C	9.094317	33.369452	6.40225

Table 4.7. Atomistic coordinates for the 4-unit “pinwheel” arrangement.

Atom	x	y	z
C	1.00949	3.706383	4.988249
C	-1.423684	3.863123	4.742847
C	2.553042	5.513023	4.730015
C	3.350967	4.961485	5.722853
C	3.360244	3.337512	7.785518
C	2.565437	2.500777	8.544181
C	0.170017	1.526158	8.842514
C	-1.101221	1.559156	8.329253
C	-2.623636	2.578558	6.465477
C	-2.626721	3.444756	5.37961
C	-1.153913	5.06755	3.964936
C	1.853983	3.159559	5.985899
C	0.113323	5.568412	3.812562

C	1.045481	2.289826	6.752582
C	-0.259554	2.307503	6.242529
C	-0.280955	3.196092	5.143831
C	1.258555	4.939093	4.404415
C	2.93916	3.790056	6.467081
C	1.307055	2.028199	8.074227
C	-1.404279	2.047055	7.015628
H	2.8939	6.45818	4.298556
H	4.080488	5.456455	5.982691
H	4.076326	3.806555	8.260284
H	2.90722	2.227365	9.350962
H	0.44463	1.260995	9.832144
H	-1.82285	1.237425	8.901859
H	-3.502004	2.368785	6.993172
H	-3.588155	3.72406	5.180722
H	-1.935316	5.53895	3.640941
H	0.496188	6.399255	3.239956
C	8.652975	8.078618	11.051137
C	11.08615	7.921877	11.29654
C	7.109424	6.271977	11.309371
C	6.311499	6.823515	10.316533
C	6.302221	8.447488	8.253868
C	7.097029	9.284223	7.495205
C	9.492449	10.258843	7.196873
C	10.763687	10.225845	7.710133
C	12.286102	9.206442	9.57391
C	12.289187	8.340245	10.659776
C	10.816378	6.71745	12.07445
C	7.808483	8.625442	10.053487
C	9.549143	6.216588	12.226824
C	8.616985	9.495174	9.286805
C	9.92202	9.477497	9.796857
C	9.943421	8.588908	10.895555
C	8.403911	6.845907	11.634971
C	6.723306	7.994944	9.572306
C	8.355411	9.756801	7.965159
C	11.066745	9.737946	9.023759
H	6.768566	5.32682	11.740831
H	5.581978	6.328545	10.056695
H	5.58614	7.978445	7.779102
H	6.755246	9.557635	6.688424
H	9.217836	10.524005	6.207242
H	11.485316	10.547575	7.137527
H	13.16447	9.416215	9.046214
H	13.25062	8.06094	10.858664

H	11.597782	6.24605	12.398446
H	9.166278	5.385745	12.79943
C	1.903237	7.03211	8.314818
C	2.402639	9.379682	7.878547
C	-0.005647	5.874823	7.527284
C	0.007732	5.09937	8.691743
C	0.822444	4.960307	11.166621
C	1.531056	5.655622	12.138607
C	2.828109	7.878273	12.631017
C	3.263886	9.065022	12.100113
C	3.289789	10.508685	9.909133
C	2.871057	10.539326	8.56824
C	1.541928	9.258296	6.73975
C	1.891978	6.231908	9.488901
C	0.813059	8.098652	6.500763
C	2.627456	6.942544	10.476927
C	3.080098	8.168184	9.905925
C	2.621458	8.196468	8.577864
C	0.92192	6.95315	7.349247
C	0.912342	5.322106	9.776006
C	2.370485	6.781089	11.827443
C	3.300514	9.303079	10.6694
H	-0.859398	5.810005	6.832779
H	-0.724935	4.54901	8.725426
H	0.008178	4.254385	11.436082
H	1.351041	5.46824	13.0721
H	2.795756	7.56597	13.537242
H	3.583627	9.911185	12.494682
H	3.555231	11.26646	10.18501
H	2.750505	11.466805	8.212166
H	1.143185	10.146885	6.159124
H	0.242495	8.190575	5.806258
C	5.973962	1.13961	15.744262
C	5.47456	3.487182	16.180533
C	7.882846	-0.017677	16.531795
C	7.869467	-0.79313	15.367336
C	7.054755	-0.932193	12.892459
C	6.346142	-0.236878	11.920472
C	5.04909	1.985773	11.428063
C	4.613313	3.172522	11.958966
C	4.58741	4.616185	14.149947
C	5.006142	4.646826	15.490839
C	6.335271	3.365796	17.319329
C	5.985221	0.339408	14.570178
C	7.06414	2.206152	17.558316

C	5.249743	1.050044	13.582152
C	4.797101	2.275684	14.153154
C	5.255741	2.303968	15.481216
C	6.955279	1.06065	16.709833
C	6.964857	-0.570394	14.283073
C	5.506713	0.888589	12.231636
C	4.576684	3.410579	13.38968
H	8.736596	-0.082495	17.226301
H	8.602133	-1.34349	15.333653
H	7.869021	-1.638115	12.622997
H	6.526158	-0.42426	10.98698
H	5.081443	1.67347	10.521837
H	4.293572	4.018685	11.564397
H	4.321968	5.37396	13.874069
H	5.126694	5.574305	15.846914
H	6.734014	4.254385	17.899955
H	7.634704	2.298075	18.252822
C	1.00949	3.706383	4.988249
C	-1.423684	3.863123	4.742847

REFERENCES

1) A. V Zabula, A. S. Filatov, S. N. Spisak, A. Y. Rogachev, M. A. Petrukhina, *Science* **2011**, *333*, 1008–1011.

2) C. Dubceac, A. S. Filatov, A. V. Zabula, A. Y. Rogachev, M. A. Petrukhina, *Chem. - Eur. J.* **2015**, *21*, 14268–14279.

3) Z. Zhou, S. N. Spisak, Q. Xu, A. Y. Rogachev, Z. Wei, M. Marcaccio, M. A. Petrukhina, *Chem.-Eur. J.* **2018**, *24*, 3455–3463.

4) E. Nestoros, M. C. Stuparu, *Chem. Commun.* **2018**, *54*, 6503–6519.

5) Y. T. Wu, J. S. Siegel, *Chem. Rev.* **2006**, *106*, 4843–4867.

6) H. Yokoi, Y. Hiraoka, S. Hiroto, D. Sakamaki, S. Seki, H. Shinokubo, *Nat. Commun.* **2015**, *6*, 8215.

7) A. G. Gagorik, J. W. Mohin, T. Kowalewski, G. R. Hutchison, *Adv. Funct. Mater.* **2015**, *25*, 1996–2003.

8) L. K. San, T. T. Clikeman, C. Dubceac, A. A. Popov, Y.- S. Chen, M. A. Petrukhina, S. H. Strauss, O. V. Boltalina, *Chem.-Eur. J.* **2015**, *21*, 9488–9492.

9) M. Saito, H. Shinokubo, H. Sakurai, *Mater. Chem. Front.* **2018**, *2*, 635–661.

10) J. Mack, P. Vogel, D. Jones, N. Kaval, A. Sutton, *Org. Biomol. Chem.* **2007**, *5*, 2448–2452.

11) H. Wang, X. Dong, J. Lin, S. J. Teat, S. Jensen, J. Cure, E. V Alexandrov, Q. Xia, K. Tan, Q. Wang, D. H. Olson, D. M. Proserpio, Y. J. Chabal, T. Thonhauser, J.

Sun, Y. Han, J. Li, *Nat. Commun.* **2018**, *9*, 1745.

12) Q.-G. Zhai, X. Bu, X. Zhao, D.-S. Li, P. Feng, *Acc. Chem. Res.* **2017**, *50*, 407–417.

13) S.-T. Zheng, J. T. Bu, Y. Li, T. Wu, F. Zuo, P. Feng, X. Bu, *J. Am. Chem. Soc.* **2010**, *132*, 17062–17064.

14) A. J. Howarth, A. W. Peters, N. A. Vermeulen, T. C. Wang, J. T. Hupp, O. K. Farha, *Chem. Mater.* **2017**, *29*, 26–39.

15) S. M. Cohen, *J. Am. Chem. Soc.* **2017**, *139*, 2855–2863.

16) M. K. Smith, K. A. Mirica, *J. Am. Chem. Soc.* **2017**, *139*, 16759–16767.

17) C. R. DeBlase, W. R. Dichtel, *Macromolecules* **2016**, *49*, 5297–5305.

18) M. Matsumoto, R. R. Dasari, W. Ji, C. H. Feriante, T. C. Parker, S. R. Marder, W. R. Dichtel, *J. Am. Chem. Soc.* **2017**, *139*, 4999–5002.

19) C. H. Hendon, A. J. Rieth, M. D. Korzyński, M. Dincă, *ACS Cent. Sci.* **2017**, *3*, 554–563.

20) A. Béziau, S. A. Baudron, G. Rogez, M. W. Hosseini, *Inorg. Chem.* **2015**, *54*, 2032–2039.

21) M. W. Logan, J. D. Adamson, D. Le, F. J. Uribe-Romo, *ACS Appl. Mater. Interfaces* **2017**, *9*, 44529–44533.

22) H. Xu, J. Gao, D. Jiang, *Nat. Chem.* **2015**, *7*, 905–912.

23) A. M. Rice, E. A. Dolgopolova, N. B. Shustova, *Chem. Mater.* **2017**, *29*, 7054–

7061.

24) A. A. K. Karunathilake, C. M. Thompson, S. Perananthan, J. P. Ferraris, R. A. Smaldone, *Chem. Commun.* **2016**, *52*, 12881–12884.

25) A. M. Butterfield, B. Gilomen, J. S. Siegel, *Org. Process Res. Dev.* **2012**, *16*, 664–676.

26) N. Niamnont, N. Kimpitak, K. Wongravee, P. Rashatasakhon, K. K. Baldridge, J. S. Siegel, M. Sukwattanasinitt, *Chem. Commun.* **2013**, *49*, 780–782.

27) A. Nagai, Z. Guo, X. Feng, S. Jin, X. Chen, X. Ding, D. Jiang, *Nat. Commun.* **2011**, *2*, 536.

28) J. C. Bachman, R. Kavian, D. J. Graham, D. Y. Kim, S. Noda, D. G. Nocera, Y. Shao-Horn, S. W. Lee, *Nat. Commun.* **2015**, *6*, 7040.

29) V. Rajeshkumar, M. Courte, D. Fichou, M. C. Stuparu, *Eur. J. Org. Chem.* **2016**, 6010–6014.

30) F. D'Souza, O. Ito, *Coord. Chem. Rev.* **2005**, *249*, 1410–1422.

31) D. E. Williams, E. A. Dolgopolova, D. C. Godfrey, E. D. Ermolaeva, P. J. Pellechia, A. B. Greytak, M. D. Smith, S. M. Avdoshenko, A. A. Popov, N. B. Shustova, *Angew. Chem. Int. Ed.* **2016**, *55*, 9070–9074.

32) E. A. Dolgopolova, A. J. Brandt, O. A. Ejegbavwo, A. S. Duke, T. D. Maddumapatabandi, R. P. Galhenage, B. W. Larson, O. G. Reid, S. C. Ammal, A. Heyden, M. Chandrashekhar, V. Stavila, D. A. Chen, N. B. Shustova *J. Am. Chem.*

Soc. **2017**, *139*, 5201–5209.

33) R. López, R. Gómez, *J. Sol-Gel Sci. Technol.* **2012**, *61*, 1–7.

34) M. Usman, S. Mendiratta, S. Batjargal, G. Haider, M. Hayashi, N. R. Gade, J.-W. Chen, Y.-F. Chen, K.-L. Lu, *ACS Appl. Mater. Interfaces* **2015**, *7*, 22767–22774.

35) A. Sygula, S. Saebø, *Int. J. Quantum Chem.* **2009**, *109*, 65–72.

36) A. S. Filatov, L. T. Scott, M. A. Petrukhina, *Cryst. Growth Des.* **2010**, *10*, 4607–4621.

37) K. Ohta, G. L. Closs, K. Morokuma, N. J. Green, *J. Am. Chem. Soc.* **1986**, *108*, 1319–1320.

38) A. Farazdel, M. Dupuis, E. Clementi, A. Aviram, *J. Am. Chem. Soc.* **1990**, *112*, 4206–4214.

39) M. D. Newton, *Chem. Rev.* **1991**, *91*, 767–792.

40) L. Y. Zhang, R. A. Friesner, R. B. Murphy, *J. Chem. Phys.* **1997**, *107*, 450–459.

41) S. Sanyal, A. K. Manna, S. K. Pati, *ChemPhysChem* **2014**, *15*, 885–893.

42) J. Luo, Z. Q. Xue, W. M. Liu, J. L. Wu, Z. Q. Yang, *J. Phys. Chem. A* **2006**, *110*, 12005–12009.

43) B. -T. Wang, M. A. Petrukhina, E. R. Margine, *Carbon* **2015**, *94*, 174–180.

44) Y.-Z. Liu, K. Yuan, Z. Yuan, Y.-C. Zhu, S.-D. Zhao, L.-L. Lv, *RSC Adv.* **2017**, *7*, 27960–27968.

45) K. M. Pelzer, Á. Vázquez-Mayagoitia, L. E. Ratcliff, S. Tretiak, R. A. Bair, S. K. Gray, T. Van Voorhis, R. E. Larsen, S. B. Darling, *Chem. Sci.* **2017**, *8*, 2597–2609.

46) A. M. Butterfield, B. Gilomen, J. S. Siegel, *Org. Process Res. Dev.* **2012**, *16*, 664–676.

47) N. Niamnont, N. Kimpitak, K. Wongravee, P. Rashatasakhon, K. K. Baldridge, J. S. Siegel, M. Sukwattanasinitt, *Chem. Commun.* **2013**, *49*, 780–782.

48) M. G. Schwab, M. Hamburger, X. Feng, J. Shu, H. W. Spiess, X. Wang, M. Antonietti, K. Müllen, *Chem. Commun.* **2010**, *46*, 8932–8934.

49) J. I. Kadokawa, Y. Tanaka, Y. Yamashita, K. Yamamoto, *Eur. Polym. J.* **2012**, *48*, 549–559.

50) S. Jeon, S. Park, J. Nam, Y. Kang, J. M. Kim, *ACS Appl. Mater. Interfaces* **2016**, *8*, 1813–1818.

51) H. Xu, J. Gao, D. Jiang, *Nat. Chem.* **2015**, *7*, 905–912.

CHAPTER 5

"BROKEN-HEARTED" BOWL: STRAIN ENERGY RELEASE VIA AN ELECTRON SHUTTLE REACTION

Rice, A. M.; Yarbrough, B. J.; Leith, G. A.; Ly, R. T.; Morris, N. A.; Dhull, P.; Adams, R. D.; Smith, M. D.; Garashchuk, S.; Shustova, N. B. *Angew. Chem. Int. Ed*. **2018**, *submitted*.

In this chapter, we report the first example of multiple reductions and a subsequent C–C bond cleavage leading to π-bowl "unzipping" occurring in one step via an electron shuttle reaction. Such ring opening is unprecedented in the literature and has not been observed for any π-bowls to date. Theoretical modeling was utilized to support the experimental results and to shed light on possible energetics of the observed processes. The 9-step solution-based routes have also been developed for preparation of two novel "unzipped" corannulene-based derivatives. The presented solid-state and solution methodologies are the first steps toward understanding possible avenues to inaccessible classes of compounds through targeted C–C bond "unzipping".

Unzipping nanotubes,[1–3] buckyballs,[4–7] or annulenes[8–10] is driven by the revived interest in fundamental understanding and practical access to novel structural transformations[11] leading to unique electronic profiles. For instance, cutting and unravelling of nanotubes led to formation of nanoribbons, which electronic properties can be varied as a function of their width, and therefore, applied in a variety of electronic devices including field effect transistors, light emitting diodes, or transparent conductive electrodes.[3,12] However, promotion of selective C–C bond cleavage in graphitic materials is challenging,[13,14] and although there has been examples of structural changes due to periphery modifications of, for instance, buckybowls,[15–18] reactions involving C–C bond cleavage of strained π-bowls themselves are very limited.[13,19,20] Despite the fact that strain energy release could

be a driving force for planarization of the naturally curved buckybowl surface (e.g., $C_{20}H_{10}$ corannulene), there is no direct route to cleave a C–C bond (except uncontrollable flash vacuum pyrolysis[13]) without the presence of a directing group attached to the corannulene core. [18–20]

Therefore, the first example of a one-step solid-state reaction achieved via utilization of an electron shuttle (7,7,8,8-tetracyanoquinodimethane (TCNQ)) that is reported here could potentially lead to new mechanisms for access to a class of compounds which are not available to date. This process is accompanied with the release of ~200 kJ/mol through buckybowl planarization according to our estimation discussed below. We also offer more "conventional" solution-based 9-step synthetic routes for preparation of two novel "unzipped" corannulene analogs.

The C–C bond cleavage and consecutive corannulene planarization to form 5,6-dimethyl-benzo[ghi]fluoranthene (planar corannulene analog (P-$C_{20}H_{14}$), Scheme 5.1) was achieved through a solid state reaction, in which corannulene (15 mg, 0.060 mmol), TCNQ (an electron shuttle; 14 mg, 0.068 mmol), and zinc powder (a reducing agent; 50 mg, 0.76 mmol) were ground together.

After that, the reaction mixture was placed in a glass tube, a drop of hydrochloric acid was added, and the glass tube was flame-sealed under dynamic vacuum (4×10^{-5} mbar). Heating the reaction mixture at 200 °C for six days resulted in formation of dark brown needles suitable for single-crystal X-ray diffraction analysis (Scheme 5.1). As shown in Scheme 5.1, such treatment resulted in planarization of the corannulene bowl through partial hydrogenation and formation of P-$C_{20}H_{14}$. X-ray crystallographic studies

revealed that packing consists of alternating columns of TCNQ and P-$C_{20}H_{14}$ along the *c* axis direction while $C_{20}H_{10}$ surrounds these columns (Figure 5.12).

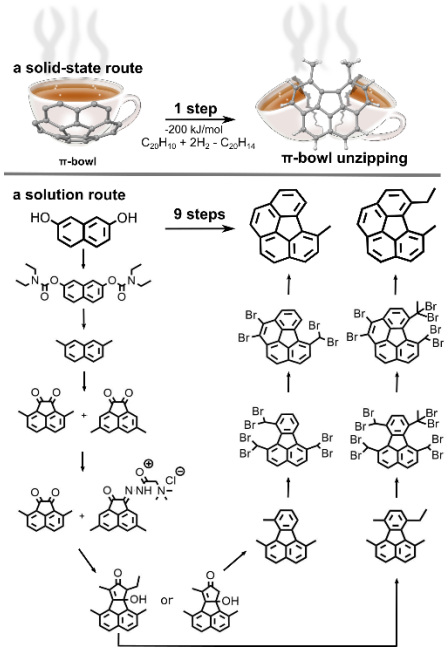

Scheme 5.1. (top) A schematic representation of π-bowl unzipping through a solid-state route. Single-crystal X-ray structure of corannulene (left) and X-ray structure of 5,6-dimethyl-benzo[*ghi*]fluoranthene (P-$C_{20}H_{14}$) ("unzipped corannulene, right). (bottom) Developed solution routes for the preparation of planar "heart-broken" corannulene analogs.

While "unzipped" corannulene is planar, the corannulene surrounding the P-$C_{20}H_{14}$ column still possesses the typical bowl depth (0.87 Å[22]). Photoluminescence and epifluorescence microscopy studies demonstrated that the obtained (corannulene)·(P-$C_{20}H_{14}$)·(TCNQ) (**1**) crystals exhibit red emission (λ_{max} = 705 nm, λ_{ex} = 365 nm) in contrast to their components ((TCNQ) = undetectable emission and λ_{max} (corannulene) =

490 nm, λ_{ex} = 365 nm, Figure 5.1 (Main Text)). Such a bathochromic shift could be attributed to charge transfer,[23,24] especially taking into account the electron-accepting ability of TCNQ. To shed light on the observed emission profiles of **1**, we also performed optical excitations of isolated corannulene, planar P-$C_{20}H_{14}$, TCNQ, and the relevant dimers, employing B3LYP-D3/6-311+G** with the dispersion correction in the direct TDDFT calculations. The acquired results on the TCNQ/P-$C_{20}H_{14}$ stacks are in line with the experimentally observed red emission. In particular, the considered TCNQ/P-$C_{20}H_{14}$ "stack" is the only species with excitation energies of appreciable strength around 1.8 eV (690 nm), which is in agreement with experimentally determined λ_{max} = 705 nm (Figure 5.17).

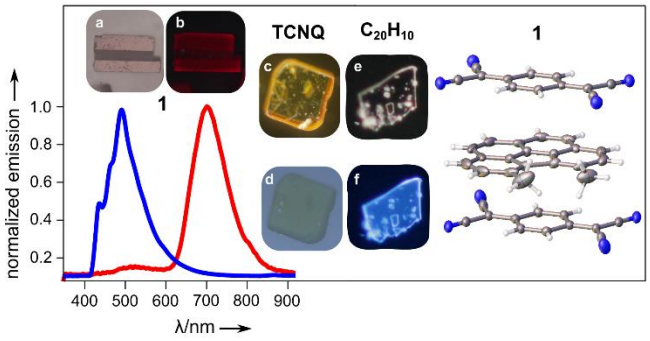

Figure 5.1. (left) The normalized emission spectra of **1** (red) and corannulene ($C_{20}H_{10}$, blue) collected on corresponding single crystals. Epifluorescence images for single crystals of **1** (a), TCNQ (c), and $C_{20}H_{10}$ (e), and after λ_{ex} = 360 nm of **1** (b), TCNQ (d), and $C_{20}H_{10}$ (f). (right) The single-crystal X-ray structure of **1** showing an alternating column of TCNQ and P-$C_{20}H_{14}$.

The lowest excitations for TCNQ, π-bowl, and $C_{20}H_{14}$ are 3 eV, 4.3 and 3.6 eV (413, 288 and 344 nm), respectively (Figure 5.17). More computational details can be found in the Supplementary information. A similar CT process was previously reported for complexes consisting of flat arenes and TCNQ molecules.[23] Moreover, the possibility of CT is also in line with the appearance of a new band (550 nm) in the diffuse reflectance (DR) profile of **1** in comparison with DR profiles of pristine corannulene and TCNQ (Figure 5.16).

To shed light on the plausible mechanism of corannulene "unzipping", we initially tested the hypothesis whether *all* components of the reaction mixture are necessary to perform the solid-state C–C bond cleavage. Indeed, absence of one of the components of the reaction mixture resulted in either the absence of any type of transformations or formation of $(corannulene)_2$·(TCNQ) previously reported in the literature.[25] Packing of $(corannulene)_2$·TCNQ co-crystals consists of two types of columns along the *c* axis (Figure 5.13): one with an alternating column with a repeating unit of one corannulene and one TCNQ (similar to alternation of P-$C_{20}H_{14}$ and TCNQ molecules in **1**, Figures 5.1 (Main Text) and Experimental Section Figures 5.11 and 5.12) and a separate column of corannulene itself (Figures 5.13 and 5.14).[25] In the alternating TCNQ/corannulene columns, the bowl depth of corannulene was reduced to 0.80 Å in comparison with that of parent corannulene (0.87 Å).[22] The π-orbital axis vector (POAV) pyramidalization angle, another parameter for curvature estimation, was found to be 10% decreased for the alternating TCNQ/corannulene columns.[25] Such corannulene planarization is in line with our calculations (see the Supplementary Information) as shown in Table 5.2-5.5. Addition of the negative charge to the bowl flattens the bowl, stretches the C–C bonds along its

rim up to 5%, and lowers the inversion barrier to 25 kJ/mol for $C_{20}H_{10}^{2-}$. These properties of charged corannulene may also contribute to the C–C bond-cleavage mechanism and formation of planar P-$C_{20}H_{14}$.

Several control experiments were carried out involving a different redox mediator (e.g., methyl viologen) as well as a series of flat polycyclic aromatic hydrocarbons (PAHs) as a substituent of corannulene. Our studies demonstrated that although TCNQ and methyl viologen have both been used as electron shuttles in various biological applications,[26–29] only TCNQ resulted in corannulene "unzipping" (P-$C_{20}H_{14}$, Scheme 5.1 (a solid-state route)). The estimated enthalpy of the reaction, $C_{20}H_{10} + 2H_2 = C_{20}H_{14}$, was found to be –190 kJ/mol (–239 and –180 kJ/mol for just the electronic and the ZPE-corrected electronic energies, respectively (see the Supplementary Information for more details).

The high strain energy (100 kJ/mol)[30] of corannulene could also be a key factor to facilitate the C–C bond cleavage reaction as evident by the relief of strain in P-$C_{20}H_{14}$. To study this possibility, reactions with PAHs including pyrene, anthracene, naphthalene, phenanthrene, or acenaphthylene have been carried out under similar conditions (see more details and X-ray structure of pyrene:TCNQ in the Supplementary Information). However, no bond cleavage was detected in any of these systems. For instance, utilization of the less strained phenanthrene instead of corannulene under the same reactions conditions resulted in formation of 1:1 phenanthrene:TCNQ co-crystals with no traces of the cleaved PAH, the structure of which has previously been reported in the literature (Figure 5.2).[31] This could be attributed to the fact that phenanthrene's strain energy is only 4.89 kJ/mol[32] versus 100 kJ/mol[30] calculated for corannulene. For a

rough estimation of the "electronic strain component" only, we calculated the energy difference of the π-bowl with the methyl units (curved) versus fully relaxed $C_{20}H_{14}$, which was found to be 202 kJ/mol.

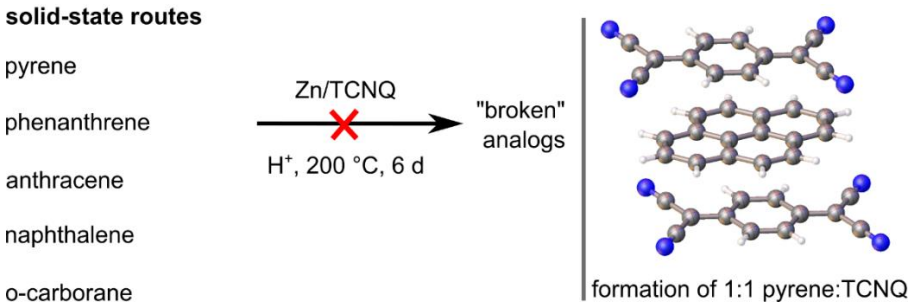

Figure 5.2. Polycyclic aromatic hydrocarbons probed for "unzipping."

We also probed the reaction conditions previously utilized for the ring-opening of other nonplanar structures such as *o*-carborane.[33–35] For that, we used a triosmium carbonyl complex, $Os_3(CO)_{10}(NCMe)_2$, which is a known C–H bond activation agent.[33–35] However, no ring-opening of corannulene was observed even at high temperatures (220 °C), while successful *o*-carborane unzipping occurred at 150 °C in a nonane reflux.[35]

We have also heated the developed system (corannulene/TCNQ/Zn/HCl) in a set of organic solvents trying to utilize a more conventional solution-based route. We started with solvents possessing low boiling points such as dichloromethane or methanol transitioning to dichloromethane/water or methanol/water mixtures and then attempted heating in the higher boiling glycerol (b.p. = 290 °C) or ethylene glycol (b.p. = 197 °C) to more closely match the reaction temperature (200 °C) of the solid-state synthesis (vide supra). In all reactions, no evidence of P-$C_{20}H_{14}$ was detected based on ^{1}H NMR spectroscopy or mass spectrometry. Replacement of the electron shuttle, TCNQ, to more widely used methyl viologen[27] still did not result in the desired product formation

according to spectroscopic studies. Attempts to electrochemically cleave the C–C bond by bulk electrolysis of a corannulene solution in *N*,*N*-dimethylformamide or acetonitrile for 24 and 48 hours, respectively, were also not successful. Notably, TCNQ was not used in the performed electrochemical reactions due to its low reduction potential (i.e., its reduction would occur prior to corannulene itself). Furthermore, attempts to reduce the C–C bond of corannulene using a combination of previously explored conditions, such as a sodium dithionite[36] as a reducing agent (instead of the zinc powder) and methyl viologen [37] were unsuccessful (see Supplementary Information for more details).

Based on these results, the reaction is specific to the developed set of conditions, and in order for four electrons to be added to the system, a series of one-electron reductions mediated by TCNQ should occur. As a potential first step in the preliminary mechanism, $C_{20}H_{10}$ could be reduced to form a radical anion, followed by a second reduction and cleavage of the C–C bond. Interestingly, it is possible that zinc plays a dual role, as it not only reduces corannulene, but also TCNQ to its aromatic 6π electron core form that has the capacity to serve as an electron carrier for multiple reductions. When TCNQ is excluded from the system, no reaction occurs portending its ability to mediate the reduction. At the same time, we are not excluding the possibility that intermolecular interactions with the π-planar TCNQ molecules and corannulene can also contribute to the flattering of the bowl depth attributing to the greater susceptibility to cleave. We have also found that the presence of the proton source is crucial for the formation of **1**.

In contrast to the one-pot solid-state reaction, the developed “conventional” synthetic methodology for preparation of planar "broken” analogs consist of nine steps (Schemes 5.1, 5.2, and 5.8). Instead of 3-pentanone used for corannulene preparation,[38] we used 2-

butanone (route 1, step 5, Scheme 5.3) and 3-hexanone (route 2, step 5, Scheme 5.9). The single-crystal X-ray structures of precursors, 1,6,7-trimethylfluoranthene (**VII**, Scheme 5.4) and 7-ethyl-1,6,10-trimethylfluoranthene (**VII'**, Scheme 5.10), are shown in Figures 5.2 and 5.9-5.10, respectively.

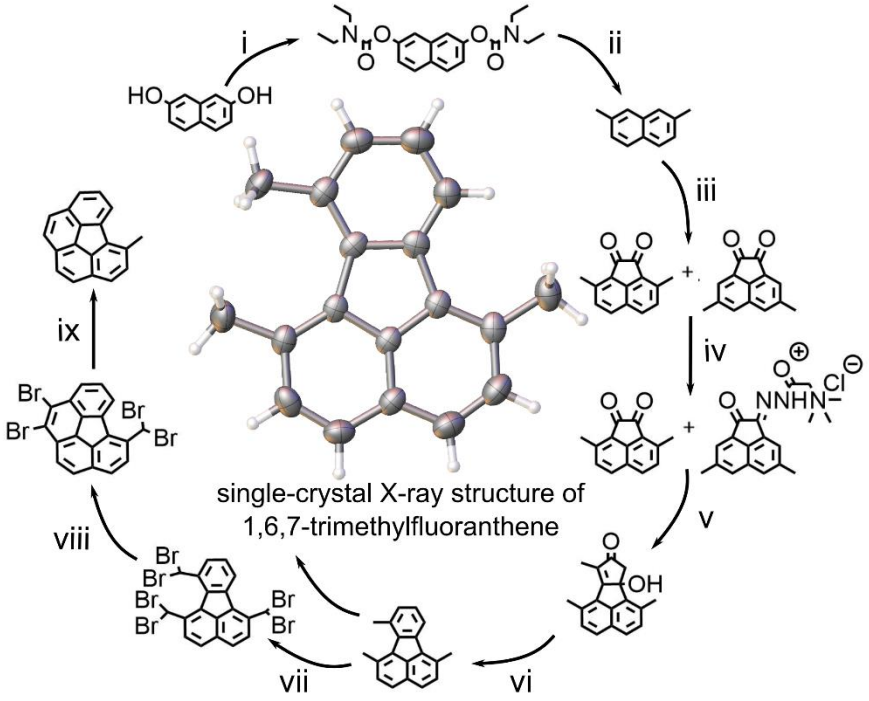

Figure 5.3. (middle) Single-crystal X-ray structure of 1,6,7-trimethylfluoranthene utilized for synthesis of 5-methylbenzo[*ghi*]fluoranthene. The thermal ellipsoids are shown at 40% probability level (periphery) Synthesis of 5-methylbenzo[*ghi*]fluoranthene through a solution route: (i) diethylcarbamoyl chloride, pyridine, 100 °C, 2 d; (ii) MeMgBr, $NiCl_2(dppp)_2$, Et_2O, 30 °C, 13 h; (iii) $AlBr_3$, $(COCl)_2$, CH_2Cl_2, –15 °C, 8h; (iv) Girard's reagent T, AcOH, 40 °C, 2h; (v) 2-butanone, KOH, MeOH, 2h; (vi) norbornadiene, Ac_2O, 140 °C, (vii) NBS, benzoyl peroxide, CCl_4, h*v*, 77 °C, 6 d; (viii) NaOH, dioxane/H_2O, 100 °C, 1h; (ix) Zn dust, KI, EtOH/H_2O, 100 °C, 7 d.

The additional methyl group (route 1) and ethyl group (route 2) in comparison with corannulene synthesis allowed us to close only one side of the ring resulting in formation

of 5-methylbenzo[*ghi*]fluoranthene and 5-ethyl-6-methylbenzo[*ghi*]fluoranthene, respectively (Figure 5.3). Sublimation of the produced yellow powder (Scheme S1) in a sealed glass tube at 200 °C allowed for the formation of single-crystals suitable for X-ray diffraction. As shown in Figure 5.3, this structure of "unzipped" corannulene possess a planar geometry with the POAV angle = 0° for 5-methylbenzo[*ghi*]fluoranthene versus 0.87 Å for parent corannulene.

To summarize, we report the first example of a unique one-step C–C bond cleavage in the very robust π-bowl occurring via an electron shuttle reaction. Attempts to mimic this successful product formation by applying more conventional solution routes even under harsh conditions (> 200 °C) or through utilization of a very strong C–H bond activation reagent $Os_3(CO)_{10}(NCMe)_2$, did not result in product formation. Moreover, such ring opening is unprecedented in the literature and has not been observed for π-bowls (e.g., corannulene) to date (with exception of uncontrollable brute force vacuum pyrolysis[13]). Furthermore, access to a one-pot synthesis through electron-shuttle reactions is a very intriguing concept, which can surpass the conventional synthetic routes through revealing novel mechanisms. Theoretical modeling was utilized to support the experimental results and to shed light on possible energetics of the observed processes. The 9-step solution-based routes have also been developed for preparation of two novel "unzipped" corannulene-based derivatives. Thus, the presented solid-state and solution methodology are the first steps toward understanding possible avenues to barely accessible structures by "unzipping" the corannulene core and application of the latter for molecular electronic development.

EXPERIMENTAL SECTION

Materials.

2,7-dihydroxynaphthalene (99%, Chem-Impex International, Inc.), *N*,*N*-diethylcarbamoyl chloride (99%, Acros Organics), pyridine (99+%, Alfa Aesar), dichloro(1,3-bis(diphenylphosphino)propane)nickel (99%, Ark Pharm, Inc), methylmagnesium bromide (ACS grade, Alfa Aesar), diethyl ether (HPLC grade, Fisher Scientific), aluminum bromide (99%, Strem Chemicals, Inc.), oxalyl chloride (98%, Alfa Aesar), dichloromethane (ACS grade, Macron), Girard's Reagent T (99%, Acros Organics), acetic acid (ACS grade, Fisher Scientific), methyl ethyl ketone (99.9%, Oakwood), 3-hexanone (>98%, Tokyo Chemical Industry Co, LTD), potassium hydroxide (ACS grade, Fisher Scientific), methanol (HPLC grade, Fisher Scientific), 2,5-norbornadiene (97%, Alfa Aesar), acetic anhydride (99%, Chem-Impex International, Inc.), cyclohexane (reagent grade, Malinckrodt), silica gel (Macron), *N*-bromosuccinimide (96%, Oakwood Chemical), benzoyl peroxide (97%, Sigma-Aldrich), carbon tetrachloride (ACS grade, Fisher Scientific), 1,4-dioxane (99+%, Alfa Aesar), sodium hydroxide (ACS grade, Fisher Scientific), zinc (97.5%, BeanTown Chemical), potassium iodide (ACS grade, Fisher Scientific), ethanol (200 proof, Decon Laboratories, Inc.), pyridine-4-boronic acid (95%, Matrix Scientific), sodium carbonate (ACS grade, Macron), tetrakis(triphenylphosphine)palladium(0) (98%, Matrix Scientific), sodium bicarbonate (ACS grade, Macron), 1,4-dimethoxybenzene (reagent grade, Oakwood Chemical), bromine (reagent grade, Sigma-Aldrich), *n*-butyllithium (reagent grade, Sigma-Aldrich), boron tribromide (reagent grade, Sigma-Aldrich), propargyl-bromide (80% weight in toluene, reagent grade, Oakwood Chemical), 1,3,5-tribromobenzene (98%, Sigma-

Aldrich), 4-aminophenyl boronic ester (reagent grade, Oakwood Chemical), Aliquat 336 (reagent grade, Beantown chemical), hexane (ACS grade, BDH), hydrochloric acid (ACS grade, EMD Chemicals), tetrahydrofuran (ACS grade, EMD Chemicals), 1-butanol (reagent grade, Oakwood Chemical), *o*-dichlorobenzene (ACS grade, Alfa Aesar), acetonitrile (ACS grade, Fisher Scientific), anhydrous magnesium sulfate (reagent grade, J.T. Baker® Chemicals), corning Pyrex glass tubing (O.D. = ½"), chloroform-*d* (Cambridge Isotope Laboratories, Inc.), and DMSO-d_6 (Cambridge Isotope Laboratories, Inc.) were used as received.

Synthesis.

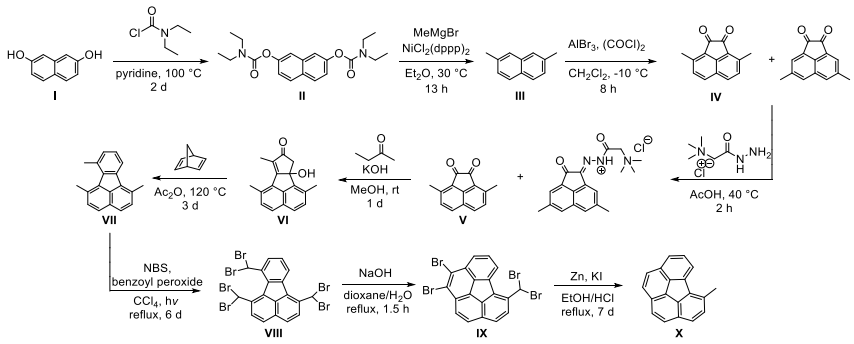

Scheme 5.2. Synthesis of 5-methylbenzo[*ghi*]fluoranthene (**X**).

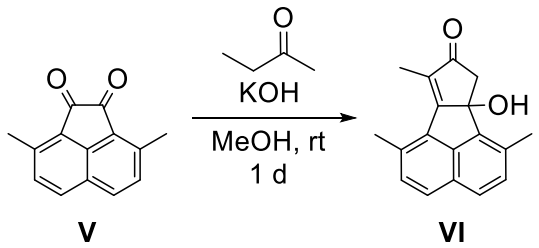

Scheme 5.3. Synthesis of 7-dihydro-8H-cyclopenta[*a*]acenaphthylen-8-one ($C_{18}H_{16}O_2$ (**VI**)).

First, potassium hydroxide (0.35 g, 6.2 mmol) was dissolved in dry methanol (0.64 mL, 16 mmol) in a 5-mL Schlenk flask purged with nitrogen. Then, 2-butanone

(0.22 mL, 2.5 mmol) and 3,8-dimethylacenaphthylene-1,2-dione (V) (54 mg, 0.26 mmol) were also added to the flask under a nitrogen flow. The resulting mixture was stirred at room temperature overnight, and then the mixture was diluted with equal volume of water. The desired compound was extracted from the aqueous layer using dichloromethane (3 × 10 mL). The combined organic layers were neutralized with hydrochloric acid (1 mL, 3 M), and then washed with water (3 × 10 mL), and dried using magnesium sulfate. Dichloromethane was removed under reduced pressure, resulting in a brown oil, which was used without further purification.

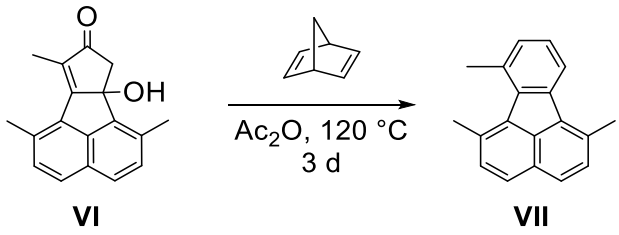

VI **VII**

Scheme 5.4. Synthesis of 1,6,7-trimethylfluoranthene ($C_{19}H_{16}$ (**VII**)).

Norbornadiene (0.18 mL, 1.8 mmol), 7-dihydro-8*H*-cyclopenta[*a*]acenaphthylen-8-one (**VI**) (54 mg, 0.26 mmol), and acetic anhydride (2.2 mL, 23 mmol) were added in a 5-mL round bottom flask. The reaction mixture was heated at reflux for three days, and cooled down to room temperature, and then 10% sodium hydroxide was added to quench the excess of acetic anhydride. The desired compound was extracted from the aqueous layer with dichloromethane (3 × 10 mL). The combined organic layers were washed with water (3 × 10 mL), dried using magnesium sulfate, and then dichloromethane was removed under reduced pressure. The resulting product was purified by column chromatography using cyclohexane to give 1,6,7-trimethylfluoranthene (**VII**) (35 mg, 68%) as a yellow solid. ^{1}H NMR ($CDCl_3$, 300 MHz): 7.89 (1H, d, J = 7.53), 7.71-7.67

(2H, m), 7.38-7.28 (3H, m), 7.17 (1H, d, J = 7.59), 2.99 (3H, s), 2.89 (6H, s) (Figure 5.4). HRMS (ESI, m/z) calculated for $C_{19}H_{16}$ $[M+H]^+$ 244.1303, found 244.1306.

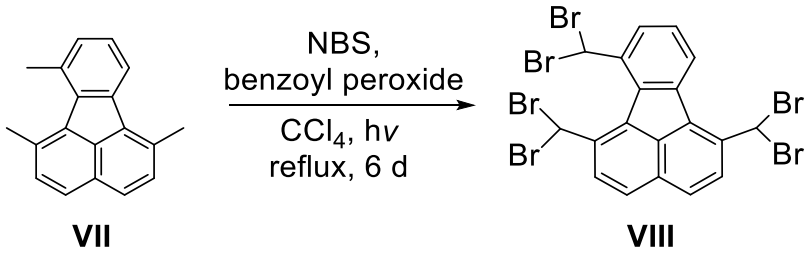

VII **VIII**

Scheme 5.5. Synthesis of 1,6,7-tris(dibromomethyl)fluoranthene ($C_{19}H_{10}Br_6$ (**VIII**)).

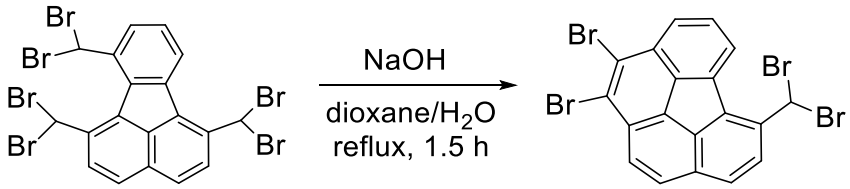

VIII **IX**

Scheme 5.6. Synthesis of 1,2-dibromo-6-(bromomethyl)benzo[*ghi*]fluoranthene ($C_{19}H_8Br_4$ (**IX**)).

Sodium hydroxide pellets (24 mg, 0.59 mmol), 1,6,7-tris(dibromomethyl)fluoranthene (**VIII**) (51 mg, 0.071 mmol), dioxane (2.0 mL, 23 mmol), and water (0.79 mL, 44 mmol) were added to a 50-mL round bottom flask. The resulting mixture was heated at reflux for one and a half hours, cooled down to room temperature, followed by the addition of equal volume of water, and neutralized using 3 M hydrochloric acid. The precipitate was filtered, washed with water, and dried under reduced pressure. The resulting product (1.0 mg, 27%) was used without further purification. HRMS (ESI, m/z) calculated for $[C_{19}H_8Br_4+H]^+$: 555.7320, found 555.7321.

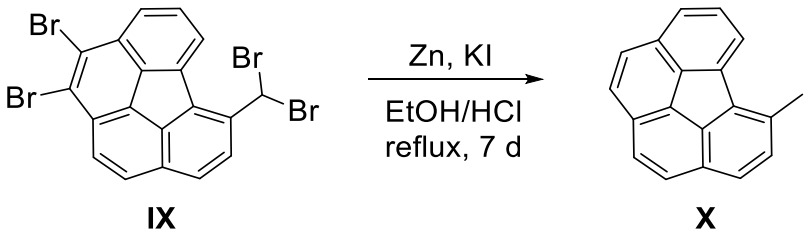

Scheme 5.7. Synthesis of 5-methylbenzo[ghi]fluoranthene ($C_{19}H_{12}$ (**X**)).

Zinc (0.71 g, 11 mmol), 1,2-dibromo-6-(bromomethyl)benzo[*ghi*]fluoranthene (**IX**) (59 mg, 0.11 mmol), potassium iodide (0.25 g, 1.5 mmol), ethanol (10 mL, 0.18 mol), and 4% hydrochloric acid (0.59 mL, 16 mmol) were added to a 15-mL round bottom flask. The reaction mixture was heated at reflux for seven days. Once the reaction mixture was cooled to room temperature, solvent was removed under reduced pressure. The crude product was purified by the Soxhlet extraction procedure using dichloromethane as the solvent. The solvent was removed under reduced pressure, and the product was isolated as a yellow solid (13 mg, 52 %). ^{1}H NMR ($CDCl_3$, 400 MHz): 8.14 (1H, d, J = 7.00), 7.99-7.84 (6H, m), 7.71 (1H, t, J = 7.54), 7.48 (1 H, d, J = 8.12), 2.97 (3H, s) (Figure 5.6). HRMS (ESI, m/z) calculated for $[C_{19}H_{12}+H]^+$: 240.0939, found 240.0942.

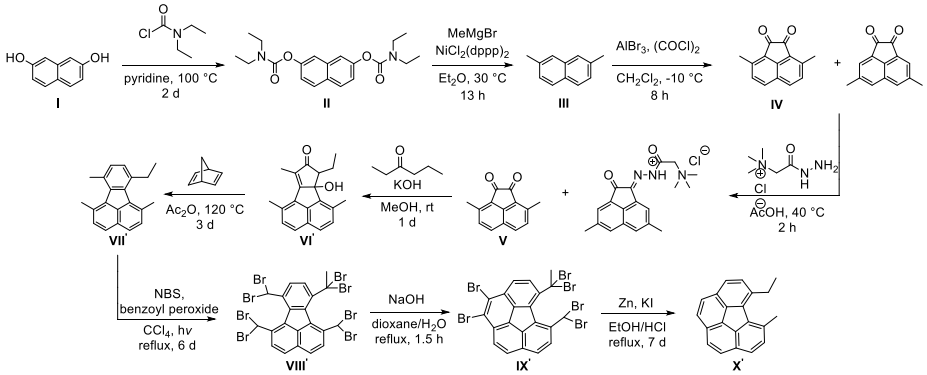

Scheme 5.8. Synthesis of 5-ethyl-6-methylbenzo[ghi]fluoranthene ($C_{21}H_{16}$ (**X'**)).

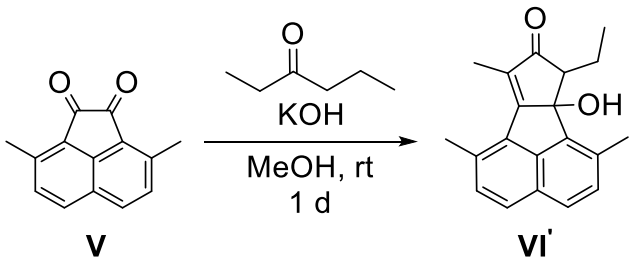

Scheme 5.9. Synthesis of 7-ethyl-6b-hydroxy-1,6,9-trimethyl-6b,7-dihydro-8H- cyclopenta[*a*] acenaphthylen-8-one ($C_{20}H_{20}O_2$ (**VI'**).

First, potassium hydroxide (0.35 g, 6.2 mmol) was dissolved in dry methanol (0.64 mL, 16 mmol) in a 5-mL Schlenk flask purged with nitrogen. Then, 3-hexanone (0.24 mL, 2.5 mmol) and 3,8-dimethylacenaphthylene-1,2-dione (**V**) (0.054 g, 0.26 mmol) were also added to the flask under a nitrogen flow. After that, the resulting mixture was stirred overnight at room temperature. Then, the mixture was diluted with equal volume of water, and the desired compound was extracted from the aqueous layer using dichloromethane (3 × 10 mL). The combined organic layers were neutralized with hydrochloric acid (1 mL, 3 M), washed with water (3 × 10 mL), dried using magnesium sulfate, and dichloromethane was removed under reduced pressure, resulting in a brown oil, which was used without further purification.

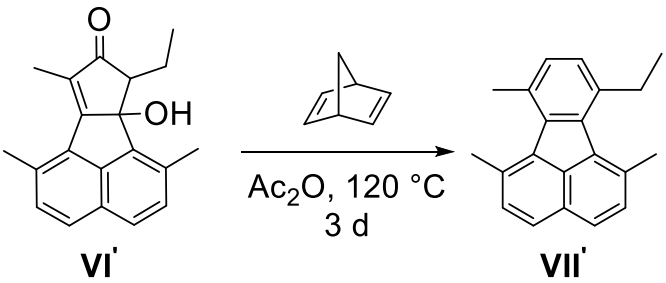

Scheme 5.10. Synthesis of 7-ethyl-1,6,10-trimethylfluoranthene ($C_{21}H_{20}$ (**VII'**)).

Norbornadiene (0.18 mL, 1.8 mmol), 7-ethyl-6b-hydroxy-1,6,9-trimethyl-6b,7-dihydro-8H-cyclopenta[*a*]acenaphthylen-8-one (**VI´**) (0.075 g, 0.26 mmol), and acetic anhydride (2.2 mL, 23 mmol) were added to a 5-mL round bottom flask. The resulting mixture was heated at reflux for three days, cooled down to room temperature, and a sodium hydroxide solution (10%) was added to quench the acetic anhydride. The desired compound was extracted from the aqueous layer with dichloromethane (3 × 10 mL), which was washed with water (3 × 10 mL), and dried using magnesium sulfate. Dichloromethane was removed under reduced pressure. The resulting crude product was purified by column chromatography using cyclohexane to give 7-ethyl-1,6,10-trimethylfluoranthene (**VII´)** (57 mg, 81%) as a yellow powder. ^{1}H NMR ($CDCl_3$, 300 MHz): δ = 7.68 (2H, d, J = 8.25), 7.37 (2H, dd, J = 8.25, 2.73), 7.19 (2H, sext, J = 6.30), 3.13 (2H, q, J = 7.50), 2.84 (3H, s), 2.81 (3H, s), 2.75 (3H, s), and 1.31 (3H, t, J = 7.50) ppm (Figure 5.5).

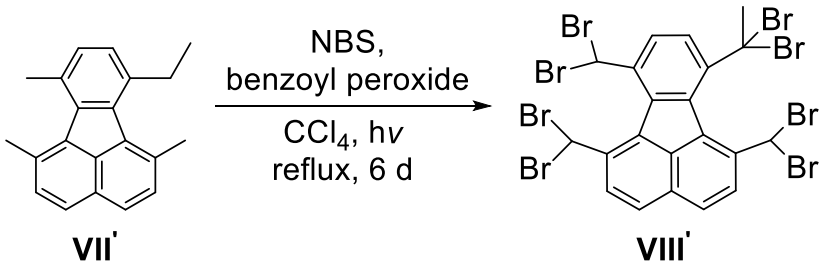

Scheme 5.11. Synthesis of 7-(1,1-dibromoethyl)-1,6,10-tris(dibromomethyl)fluoranthene ($C_{21}H_{12}Br_8$ (**VIII'**)).

Benzoyl peroxide (0.35 mg, 0.0015 mmol), 7-ethyl-1,6,10-trimethylfluoranthene (**VII´)** (0.040 g, 0.15 mmol), *n*-bromosuccinimide (0.26 g, 2.1 mmol), and carbon tetrachloride (3.0 mL, 31 mmol) were added to a 5-mL Schlenk flask purged with nitrogen. The reaction mixture was heated at reflux while irradiated with a 300 W lamp

for six days. After that, the solvent was removed under reduced pressure, and the solid was purified by the Soxhlet extraction procedure using ethanol as the solvent resulting in a brown powder (70 mg, 52%).

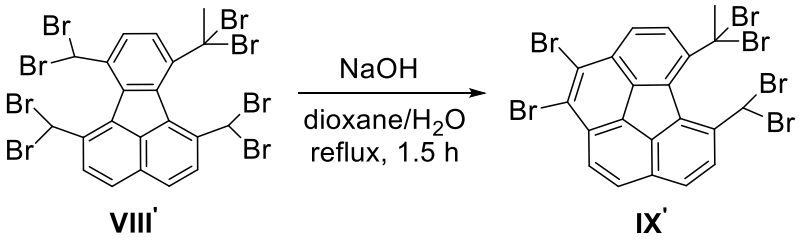

Scheme 5.12. Synthesis of 1,2-dibromo-5-(1,1-dibromoethyl)-6-(dibromomethyl)benzo[ghi]fluoranthene ($C_{21}H_{10}Br_6$ (**IX**').

Sodium hydroxide (0.12 g, 3.0 mmol), 7-(1,1-dibromoethyl)-1,6,10-tris(dibromomethyl)fluoranthene (**VIII´**) (0.025 g, 0.030 mmol), dioxane (3 mL, 35 mmol), and water (1 mL, 56 mmol) were added to a 10-mL round bottom flask. The reaction mixture was heated at reflux for one and a half hours, cooled down to room temperature, followed by the addition of water (4 mL), and neutralized using 3 M hydrochloric acid. The obtained precipitate was filtered, washed with water, and dried under reduced pressure. The resulting product (17 mg, 82 %) was then used without further purification.

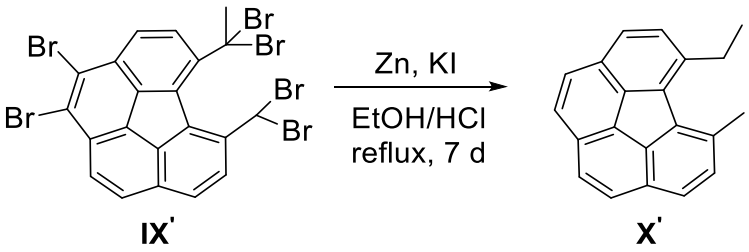

Scheme 5.13. Synthesis of 5-ethyl-6-methylbenzo[ghi]fluoranthene ($C_{21}H_{16}$ (**X'**)).

Zinc (0.36 g, 5.5 mmol), 1,2-dibromo-6-(bromomethyl)benzo[*ghi*]fluoranthene (0.040 g, 0.053 mmol) (**IX´**), potassium iodide (0.13 g, 0.78 mmol), ethanol (5.0 mL, 0.090 mol), and 4% hydrochloric acid (0.29 mL, 8.0 mmol) were added to a 10-mL round bottom flask. The reaction mixture was heated at reflux for seven days, cooled down to room temperature, and the solvent was removed under reduced pressure. The crude product was purified by the Soxhlet extraction procedure using dichloromethane as the solvent. The solvent was removed under reduced pressure, and the product was isolated as a yellow powder.

Synthesis of $C_{20}H_{10}\cdot C_{20}H_{14}\cdot C_{12}H_4N_4$ *(*$C_{52}H_{28}N_4$*,* ***1****).*

A mixture of corannulene (15 mg, 0.060 mmol), TCNQ (14 mg, 0.068 mmol), and zinc (50 mg, 0.76 mmol) was ground together followed by the addition of 12 M HCl (3 µL). Then, the resulting mixture was placed in a borosilicate glass ampule (diameter = 12.7 mm; length = 130 mm), which was flame-sealed under vacuum (4×10^{-5} mbar). The tube was placed in a sand bath at 200 °C, and the top end of the tube was wrapped with aluminum foil. After six days, brown rod-like crystals (**1**) were formed. The obtained crystals were suitable for single-crystal X-ray analysis (Figures 1 (main text), S8-S9). Table S1 contains crystallographic refinement data for **1**. More detailed description of the crystal structure can be found in the *X-ray Crystal Structure Determination section* (vide infra). The MS data are shown in Figures S4. The epifluorescence microscopy image of **1** and an emission spectrum of **1** collected from a single crystal are shown in Figure 1. Corannulene was also studied using the epifluorescence microscopy and photoluminescence spectroscopy (Figure 1).

Synthesis of $(C_{20}H_{10})_2 \cdot C_{12}H_4N_4$ ($C_{52}H_{28}N_4$).

A mixture of corannulene (15 mg, 0.060 mmol) and TCNQ (14 mg, 0.068 mmol) was ground together. Then, the resulting mixture was placed in a borosilicate glass ampule (diameter = 12.7 mm; length = 130 mm), which was flame-sealed under vacuum (4×10^{-5} mbar). The tube was placed in a sand bath at 200 °C, and the top end of the tube was wrapped with aluminum foil.

After six days, brown rod-like crystals were formed. The obtained crystals were suitable for single-crystal X-ray analysis (Figures 1 (main text), Figure 5.13-5.14). Table 5.1 contains crystallographic refinement data for $(C_{20}H_{10})_2 \cdot C_{12}H_4N_4$. More detailed description of the crystal structure can be found in the *X-ray Crystal Structure Determination section* (vide infra). The MS spectroscopic data are shown in Figures 5.8.

Synthesis of $C_{16}H_{10} \cdot C_{12}H_4N_4 \cdot$ ($C_{28}H_{14}N_4$, pyrTCNQ).

The pyrene and TCNQ (pyrTCNQ) cocrystals were prepared according to a modified literature procedure.[1] Pyrene (0.010 g, 0.050 mmol) and TCNQ (0.010 g, 0.050 mmol) were heated at reflux in a benzene/toluene mixture (1 mL / 1 mL) for two hours in a 5-mL round bottom flask. The reaction mixture was cooled to room temperature, and after one day of slow evaporation of the solvent, black crystals were obtained. The obtained crystals were suitable for single-crystal X-ray analysis (Figure 5.15). Table 5.1 contains crystallographic refinement data for $C_{16}H_{10} \cdot C_{12}H_4N_4$. More detailed description of the crystal structure can be found in the *X-ray Crystal Structure Determination section* (vide infra).

Synthesis of $C_{14}H_{10}$·$C_{12}H_4N_4$·($C_{26}H_{14}N_4$, phenanTCNQ).

The phenanthrene and TCNQ (phenanTCNQ) co-crystals were prepared according to a modified literature procedure.[1] Phenanthrene (13 mg, 0.074 mmol) and TCNQ (15 mg, 0.074 mmol) were ground together, and the resulting mixture was placed in a borosilicate glass ampule (diameter = 12.7 mm; length = 13 cm) before flame-sealing under vacuum (4×10^{-5} mbar). The tube was then placed in a sand bath at 200 °C with the top end of the tube wrapped with aluminum foil. After six days, brown rod-like crystals were isolated, and match closely to the reported one and their crystal structure.[1]

Solution Reactions.

A series of reactions were investigated in solution in attempts to repeat the results of the reduction reaction that occurred with corannulene in a sealed ampule. Starting with relatively lower boiling point solvents, such as dichloromethane and methanol, the same equivalents of the reagents were used (i.e. corannulene, TCNQ, Zn, HCl), and heated at reflux in the solvent for six days. No evidence of the planar 5,6-dimethyl-benzo[*ghi*]fluoranthene was found through ^{1}H NMR spectroscopy or mass spectrometry. In order to more closely match the successful high temperature (200 °C) reaction conditions resulting in the formation of **1**, solvents such as ethylene glycol and glycerol were used. In this case, no evidence of the planar 5,6-dimethyl-benzo[*ghi*]fluoranthene was also found through ^{1}H NMR spectroscopy or mass spectrometry.

In order to investigate if the type of electron shuttle used could make a difference in solution-based reactions, TCNQ, which was used in the formation of **1**, was replaced with methyl viologen, another common electron shuttle.[2] Using the same conditions as

above, still no product was observed through ^{1}H NMR spectroscopy and mass spectrometry.

In addition, the reducing agent zinc, was replaced with sodium dithionite under the aforementioned reaction conditions, and there was no evidence of product formation.

X-ray Crystal Structure Determination.

Single-Crystal X-ray Structure of 1,6,7-trimethylfluoranthene ($C_{19}H_{16}$).

X-ray intensity data from a colorless needle were collected at 100(2) K using a Bruker D8 QUEST diffractometer equipped with a PHOTON-100 CMOS area detector and an Incoatec microfocus source (Mo Kα radiation, λ = 0.71073 Å). The raw area detector data frames were reduced and corrected for absorption effects using the Bruker APEX3, SAINT+, and SADABS programs.[3,4] The structure was solved with SHELXT.[5] Subsequent difference Fourier calculations and full-matrix least-squares refinement against F^2 were performed with SHELXL-2018[4] using OLEX2.[5]

The compound crystallizes in the orthorhombic system. The pattern of systematic absences in the intensity data was uniquely consistent with the space group $P2_12_12_1$, which was confirmed by structure solution. The asymmetric unit consists of one molecule. All non-hydrogen atoms were refined with anisotropic displacement parameters. Hydrogen atoms bonded to carbon were located in difference Fourier maps before being placed in geometrically idealized positions and included as riding atoms with d(C–H) = 0.95 Å and U_{iso}(H) = 1.2U_{eq}(C) for aromatic hydrogen atoms and d(C–H) = 0.98 Å and U_{iso}(H) = 1.5U_{eq}(C) for methyl hydrogens. The methyl hydrogens were

allowed to rotate as a rigid group to the orientation of maximum observed electron density. The largest residual electron density peak in the final difference map is 0.19 e/Å^3, located 1.11 Å from C3. Because of the absence of heavy atoms in the crystal, the absolute structure was not determined.

Single-Crystal X-ray Structure of 7-ethyl-1,6,10-trimethylfluoranthene ($C_{21}H_{20}$).

X-ray intensity data from a colorless block were collected at 100(2) K using a Bruker D8 QUEST diffractometer equipped with a PHOTON-100 CMOS area detector and an Incoatec microfocus source (Mo Kα radiation, λ = 0.71073 Å). The raw area detector data frames were reduced and corrected for absorption effects using the Bruker APEX3, SAINT+, and SADABS programs.[3,4] The structure was solved with SHELXT.[5] Subsequent difference Fourier calculations and full-matrix least-squares refinement against F^2 were performed with SHELXL-2018[5] using OLEX2.[6]

The compound crystallizes in the orthorhombic system. The pattern of systematic absences in the intensity data was consistent with the space groups *Pnma* and *Pna*2$_1$. The acentric group *Pna*2$_1$ was assigned by the solution program XT and was confirmed by structure solution. The asymmetric unit consists of one molecule. All non-hydrogen atoms were refined with anisotropic displacement parameters. Hydrogen atoms bonded to carbon were located in difference Fourier maps before being placed in geometrically idealized positions and included as riding atoms with d(C–H) = 0.95 Å and U_{iso}(H) = 1.2U_{eq}(C) for aromatic hydrogen atoms, d(C–H) = 0.99 Å and U_{iso}(H) = 1.2U_{eq}(C) for methylene hydrogen atoms, and d(C–H) = 0.98 Å and U_{iso}(H) = 1.5U_{eq}(C) for methyl hydrogens. The methyl hydrogens were allowed to rotate as a rigid group to the orientation of maximum observed electron density. The largest residual electron density

peak in the final difference map is 0.56 e/Å^3, located 0.72 Å from H19B. Because of the absence of heavy atoms in the crystal, Friedel opposites were merged during refinement and no attempt made to determine the absolute structure.

*Single-Crystal X-ray Structure of $C_{20}H_{10}$·$C_{20}H_{14}$·$C_{12}H_4N_4$ ($C_{52}H_{28}N_4$, **1**).*

X-ray intensity data from a dark brown needle were collected at 100(2) K using a Bruker D8 QUEST diffractometer equipped with a PHOTON-100 CMOS area detector and an Incoatec microfocus source. All of several crystals screened were found to be twinned by non-merohedry. From the crystal judged to be the best quality, all reflections from a trial set of 569 could be indexed to two domains using the Cell_Now program.[3] Orientation matrices for the two domains along with the twin law relating the domains were also derived using Cell_Now. The twin law is (-1 0 0.147 / 0 -1 0 / 0 0 1), corresponding to a two-fold rotation around the real-space [001] axis. The raw area detector data frames were reduced, scaled, and corrected for absorption effects using the Bruker APEX3, SAINT+, and TWINABS programs.[3] The reported unit cell parameters were determined by least-squares refinement of 8512 reflections taken from both domains. The structure was solved by direct methods with SHELXT.[7] Subsequent difference Fourier calculations and full-matrix least-squares refinement against F2 were performed with SHELXL-2014[5] using OLEX2.[6] The major twin domain volume fraction refined to 0.633(3).

The compound crystallizes in the triclinic system. The space group P-1 (No. 2) was confirmed by structure solution. The asymmetric unit consists of one $C_{20}H_{10}$ (corannulene) molecule, one $C_{20}H_{14}$ molecule and half each of two $C_{12}H_4N_4$ (TCNQ) molecules. Both TCNQ molecules are located on crystallographic inversion centers. The

corannulene molecule is disordered and was modeled with two orientations (A/B). The disorder takes the form of a near-180° rotation around an axis perpendicular to the central five-membered ring. Total group occupancy was constrained to sum to unity and refined to A/B = 0.611(5)/0.389(5). Similar sets of bonds between the two components were restrained to have approximately the same distances, using SHELX SADI instructions. These are: the two sets of five bonds each of the central C5 rings (e.g., C1–C2), the two sets of five bonds radiating from each central C5 ring (e.g., C1-C6), the two sets of five bonds outermost in each phenyl ring (e.g., C7-C8), and the remaining two sets of ten phenyl C–C bonds (e.g., C6–C7, C8–C9). Some atoms which appear nearly superimposed were assigned equal displacement parameters. In total 367 restraints were used in the disorder modeling. All non-hydrogen atoms were refined with anisotropic displacement parameters. Most hydrogen atoms bonded to carbon, including the methyl hydrogens of the $C_{20}H_{14}$ molecule, were located in Fourier difference maps before being placed in geometrically idealized positions and included as riding atoms (d(C–H) = 0.95 Å and $U_{iso}(H) = 1.2U_{eq}(C)$ for aromatic hydrogen atoms and d(C-H) = 0.98 Å and $U_{iso}(H) = 1.5U_{eq}(C)$ for methyl hydrogens). The methyl hydrogens were allowed to rotate as a rigid group to the orientation of maximum observed electron density. Anti-bumping restraints (d(H---H) > 2.0 Å) were applied to two sets of H atoms, H50A-H8B and H50A-H49C. The largest residual electron density peak in the final difference map is 0.43 e/Å^3, located 1.13 Å from H49A. This peak and the next highest peak lie between C49 and C50 and, though small in magnitude, were considered carefully. Ultimately, no reasonable alternative molecular model could be achieved; they most likely arise from a minor whole-molecule disorder component of this species.

Single-Crystal X-ray structure of $(C_{20}H_{10})_2 \cdot C_{12}H_4N_4$, $(C_{52}H_{24}N_4)$.

X-ray intensity data from a thin brown plate were collected at 100(2) K using a Bruker D8 QUEST diffractometer equipped with a PHOTON-100 CMOS area detector and an Incoatec microfocus source (Mo Kα radiation, λ = 0.71073 Å). The raw area detector data frames were reduced and corrected for absorption effects using the Bruker APEX3, SAINT+ and SADABS programs.[3,4] Weak diffraction was observed from the thin plate crystal despite using a long scan rate of 120s/°. The mean reflection I/σ(I) fell below 1.5 at d = 0.87 Å, at which point the dataset was truncated. Final unit cell parameters were determined by least-squares refinement of 5689 reflections taken from the data set. The structure was solved with SHELXT.[7] Subsequent difference Fourier calculations and full-matrix least-squares refinement against F2 were performed with SHELXL-2017[5] using OLEX2.[6]

The compound crystallizes in the monoclinic system. The pattern of systematic absences in the intensity data was consistent with the space groups P21 and P21/m. The best solution was obtained in the centrosymmetric group P21/m. The asymmetric unit consists of half of one TCNQ molecule and half each of two independent corannulene molecules. All species are located on crystallographic mirror planes. One corannulene molecule (C11A-C31A) is disordered. Considerable difficulty was encountered in modeling the disorder. The best model utilized one complete corannulene molecule component disordered over two positions by symmetry across the mirror plane. This model proved superior to models involving two or more independent half-molecules. A similar disorder was observed by removing the mirror plane and refining in space group P21. The molecular geometry of the independent component (C11A-C31A) was

restrained to be similar to that of the ordered corannulene using a SHELX SAME instruction. Atoms C11A-C31A were refined with half-occupancy. Anisotropic displacement parameters of disordered atoms were restrained with DELU and SIMU instructions. After disorder modeling and anisotropic refinement, several relatively large residual electron density peaks were left in the difference Fourier map with magnitudes 1.60 –0.96 e/ Å3. Most are located near the periphery of both corannulene molecules. The peaks could not be fitted to any reasonable species. The two largest peaks are located 1.29 and 1.45 Å from C29A and C9, respectively. All non-hydrogen atoms were refined with anisotropic displacement parameters. Hydrogen atoms were placed in geometrically idealized positions and included as riding atoms with d(C–H) = 0.95 Å and U_{iso}(H) = 1.2U_{eq}(C). The reported structural model is non-ideal in several respects: high final R-factors, the necessity of many strict restraints, large unassigned peaks in the difference electron density map, and the existence of a 'void' of volume ~100 $Å^3$ identified by PLATON. The void contains small electron density peaks which could not be fit to any plausible species. These issues arise because of crystallinity and data limitations, and precise structural details should be regarded as approximate. General features of the average structure, such as the stoichiometry of two corannulene molecules per one TCNQ and the absence of any planar polycyclic molecules are well established.

Single-Crystal X-ray structure of $C_{16}H_{10}$·$C_{12}H_4N_4$, ($C_{28}H_{14}N_4$·pyrTCNQ).

X-ray intensity data from a dark brown plate were collected at 100(2) K using a Bruker D8 QUEST diffractometer equipped with a PHOTON-100 CMOS area detector and an Incoatec microfocus source (Mo Kα radiation, λ = 0.71073 Å). The raw area detector data frames were reduced and corrected for absorption effects using the Bruker

APEX3, SAINT+ and SADABS programs.[3,4] Final unit cell parameters were determined by least-squares refinement of 9208 reflections taken from the data set. The structure was solved with SHELXT.[7] Subsequent difference Fourier calculations and full-matrix least-squares refinement against F^2 were performed with SHELXL-2018[5] using OLEX2.[6]

Table 5.1. X-ray structure refinement data[a] for **1**, $(C_{20}H_{10})_2 \cdot C_{12}H_4N_4$, $C_{16}H_{10} \cdot C_{12}H_4N_4 \cdot$pyrTCNQ.

compound	**$C_{19}H_{16}$**	**$C_{21}H_{20}$**	**1**
formula	$C_{19}H_{16}$	$C_{21}H_{20}$	$C_{52}H_{28}N_4$
FW	244.32	272.37	708.78
T, K	100(2)	100(2)	100(2)
crystal system	orthorhombic	orthorhombic	triclinic
space group	$P2_12_12_1$	$Pna2_1$	P-1
Z	4	4	2
a, Å	5.0524(4)	9.8601(4)	10.5126(12)
b, Å	15.7417(11)	9.0281(4)	13.2993(15)
c, Å	15.7910(11)	16.8983(6)	13.3298(15)
α, °	90	90	88.442(3)
β, °	90	90	84.692(3)
γ, °	90	90	69.641(3)
V, Å^3	1255.91(16)	1504.3(10)	1739.7(3)
d_{calc}, g/cm^3	1.292	1.203	1.353
μ, mm^{-1}	0.073	0.068	0.080
F(000)	520.0	548.0	736.0
crystal size, mm^3	0.22 × 0.06 × 0.04	0.18 × 0.14 × 0.08	0.4 × 0.06 × 0.06
theta range	5.16 to 50.088	5.116 to 55.106	4.47 to 50.052
index ranges	$-6 \le h \le 6$ $-17 \le k \le 18$ $-18 \le l \le 18$	$-12 \le h \le 12$ $-11 \le k \le 11$ $-21 \le l \le 21$	$-12 \le h \le 12$ $-15 \le k \le 15$ $0 \le l \le 15$
refl. collected	16295	62323	6143
data/restraints / parameters	2212/0/176	3461/1/194	6143/367/666

The compound crystallizes in the monoclinic system. The pattern of systematic absences in the intensity data was consistent with the space group $P2_1/n$, which was confirmed by structure solution. The asymmetric unit consists of half of one pyrene molecule and half of one TCNQ molecule, both located on crystallographic inversion centers. All non-hydrogen atoms were refined with anisotropic displacement parameters. Hydrogen atoms bonded to carbon were located in Fourier difference maps and refined freely. The largest residual electron density peak in the final difference map is 0.23 e/Å^3, located 0.72 Å from C3.

Other Physical Measurements.

An Edinburgh FS5 fluorescence spectrometer equipped with a 150 W Continuous Wave Xenon Lamp source for excitation was used to acquire steady-state emission spectra. Emission measurements on solid samples were collected on powders of the desired materials placed inside a 0.5 mm quartz sample holder using the front-facing module. In addition, emission measurements on single crystals were collected on an Ocean Optics JAZ spectrometer was also used to record the emission response. In this case, a mounted highpower 365 nm LED (M365L2, Thorlabs) was used as an excitation source. Epifluorescence microscopy images were collected on an Olympus BX51 microscope with a 120 W mercury vapor short arc excitation light source (Figure 5.1, Main Text). NMR spectra were obtained on a Bruker Avance III-HD 300 and Bruker Avance III 400 MHz NMR spectrometers. ^{13}C and ^{1}H NMR spectra were referenced to natural abundance ^{13}C peaks and residual ^{1}H peaks of deuterated solvents, respectively. FTIR spectra were collected on a Perkin-Elmer Spectrum 100. Diffuse reflectance spectra

were collected on a Perkin Elmer Lambda 45 UV-vis spectrometer referenced to Spectralon®.

Computational Details.

A neutral corannulene molecule is shaped as a bowl of 0.87 Å depth; the barrier to the bowl inversion through a planar transition state is ~ 40 kJ/mol. According to the electronic structure analysis it can accommodate up to 4 electrons into its doubly degenerate low-lying LUMO. Experiments with Li and Cs sandwiched between the corannulene bowls confirm this expectation. Within our ES method (B3LYP/6-31+G*) the LUMO energy is -1.9 eV and the HOMO-LUMO gap is 4.38 eV. Another low-lying doubly-degenerate orbital LUMO+1 at -1.8 eV, may also contribute to the charge transfer properties and hydrogenation upon the bond-breaking in corannulene. As shown in Table 2, addition of the negative charge to the bowl flattens the bowl, stretches the CC bonds along its rim up to 5% and lowers the inversion barrier to 25 kJ/mol for $C_{20}H_{10}^{-2}$. These properties of charged corannulene may contribute to the CC bond-cleavage and formation of $C_{20}H_{14}$, characterized by the planar arrangement of the carbon atoms. Formally, the standard enthalpy change during this process

$$C_{20}H_{10} + 2H_2 \rightarrow C_{20}H_{14}$$

is -190 kJ/mol (-239 and -180 kJ/mol for just the electronic and the ZPE-corrected electronic energies, respectively). The 'geometric strain' energy (electronic energy only), computed as the energy difference of the π-bowl with just the methyl units relaxed, and of the fully relaxed $C_{20}H_{14}$ is 202 kJ/mol. We have also examined optical excitations of isolated corannulene, broken corannulene and TCNQ, and f the relevant dimers,

employing B3LYP-D3/6-311+G** with the dispersion correction in the direct TDDFT calculation. The results, while based on minimalistic representation of the TCNQ/corannulene stacks, agree with the experimentally observed red emission: the TCNQ/$C_{20}H_{14}$ 'stack' is the only species with excitation energies of appreciable strength around 1.8 eV (690 nm). The lowest excitations for TCNQ, π-bowl and $C_{20}H_{14}$ are 3 eV, 4.3 and 3.6 eV (413, 288 and 344 nm), respectively.

Table 5.2. The bowl depth and the bowl-inversion barrier for an isolated corannulene molecule, computed at B3LYP/6-31+G* level of the electronic structure theory.

charge	0	-1	-2
Depth [Å]	0.87	0.83	0.78
$E^{\dagger}$ [kJ/mol]	39.0	30.9	25.4

Table 5.3. Calculations for charged bowls.

Charge	0	-1	2	-2 triplet	-3
Depth [Å]	0.866	0.829	0.782	0.758	0.695
CC top [Å]	1.415	1.415	1.415	1.414	1.412
CC rim (lng) [Å]	1.383	1.407 (1.423)	1.425 (1.463)	1.427 (1.427)	1.413 (1.435)
CC n/bnd	2.621	2.632	2.641	2.643	2.664

[Å]					
E^{3D} a.u.	- 768.1727	- 768.1956	- 768.0793	- 767.8552	- 767.8553
E^{2D} a.u.	- 768.1578	- 768.1838	- 768.0696	- 767.8552	- 767.8552
ΔE kJ/mol	39.0	30.88	25.37	20.48	34.35

Table 5.4. Electronic excitations contributing to UV. Method: direct TDDFT B3LYP/6-311+G** with the dispersion correction Grimme D3. Red 1.65-2 eV; Violet 2.75-3.26 eV; nm =1240/ eV.

cor3D	4.316 (0.201)	4.323 (0.190)	5.180 (0.460)
cor broken	3.606 (0.028)	3.637 (0.108)	4.443 (0.144)
TCNQ	3.058 (1.978)	5.109 (0.087)	
TCNQ-$C_{20}H_{10}$	1.6580 (0.01)	3.3684 (0.633)	3.5407 (0.2125)
TCNQ-$C_{20}H_{14}$	1.8421 (0.105)	2.5924 (0.015)	3.2241 (0.380)
TCNQ-$C_{20}H_{14}$-TCNQ	1.811 (0.122)	2.816 (0.146)	2.969 (0.766)

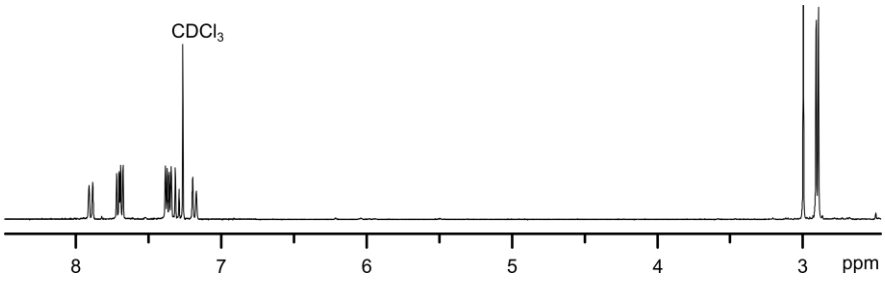

Figure 5.4. ^{1}H NMR and ^{13}C NMR spectrum of 1,6,7-trimethylfluoranthene.

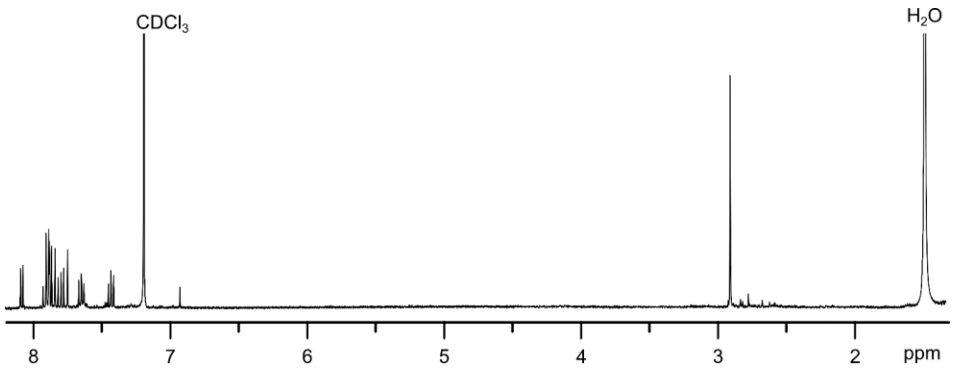

Figure 5.5. ^{1}H NMR and ^{13}C NMR spectrum of 7-ethyl-1,6,10-trimethylfluoranthene.

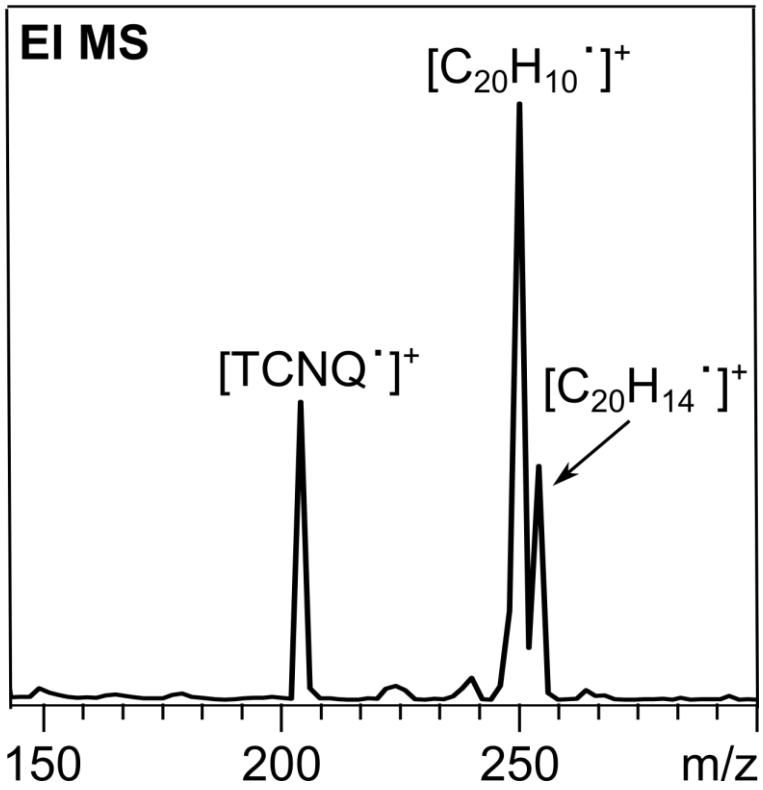

Figure 5.6. ESI MS of **1**.

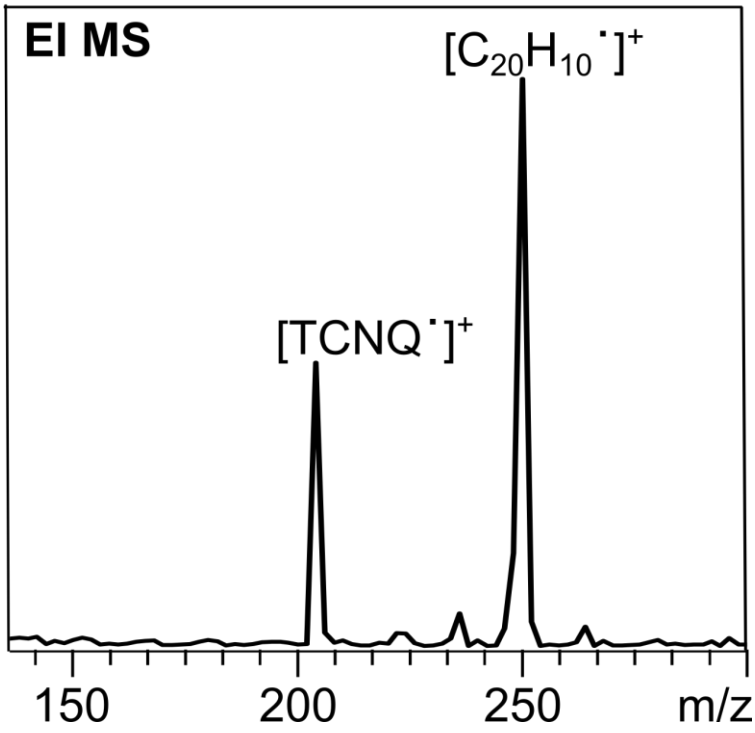

Figure 5.7. ESI MS of $(C_{20}H_{10})_2 \cdot C_{12}H_4N_4$.

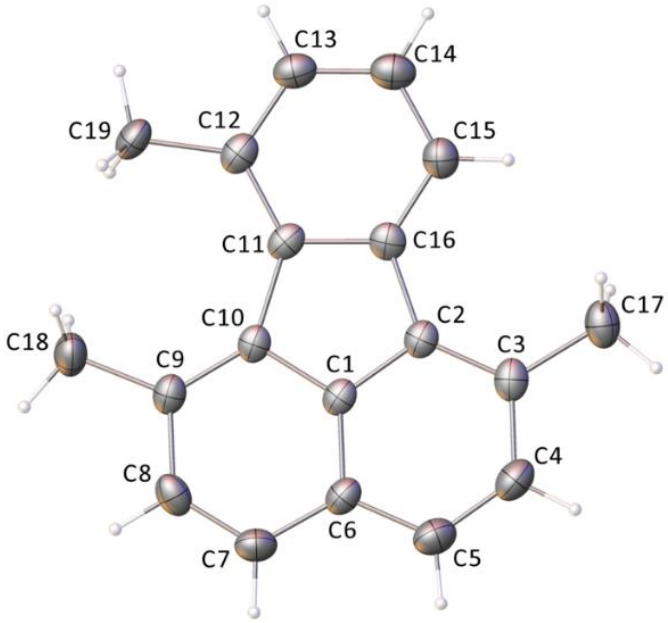

Figure 5.8. Crystal structure of 1,6,7-trimethylfluoranthene ($C_{19}H_{16}$). Displacement ellipsoids drawn at the 50% probability level. Grey and white

spheres correspond to carbon and hydrogen atoms, respectively.

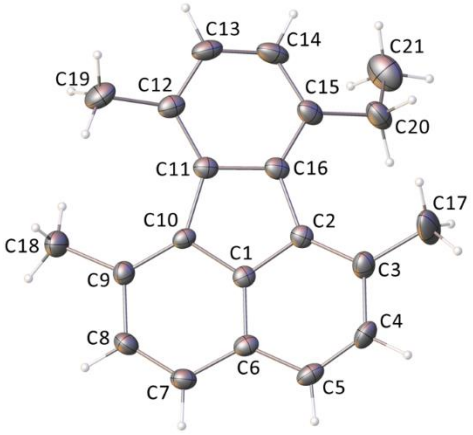

Figure 5.9. Crystal structure of 7-ethyl-1,6,10-trimethylfluoranthene ($C_{21}H_{10}$). Displacement ellipsoids drawn at the 50% probability level. Grey and white spheres correspond to carbon and hydrogen atoms, respectively.

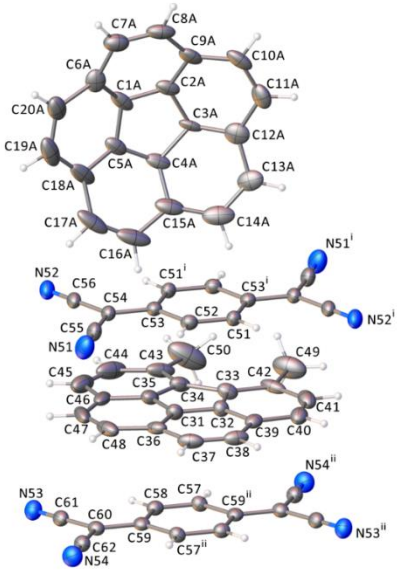

Figure 5.10. Crystal structure of **1**. Displacement ellipsoids drawn at the 40% probability

level. Grey, blue, and white spheres correspond to carbon, nitrogen, and hydrogen atoms, respectively.

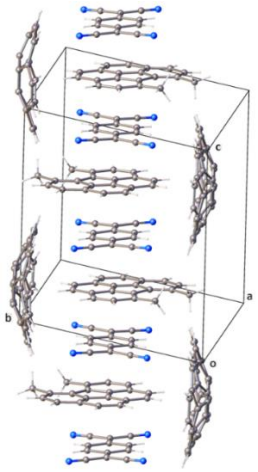

Figure 5.11. Packing of **1** along the *c* axis. Grey, blue, and white spheres correspond to carbon, nitrogen, and hydrogen atoms, respectively.

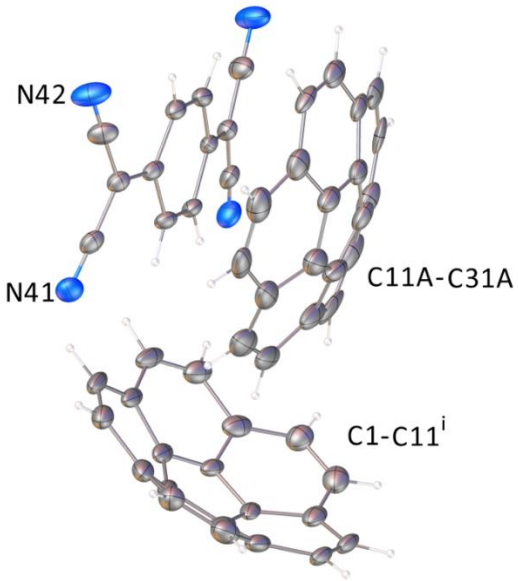

Figure 5.12. Crystal structure of $(C_{20}H_{10})_2 \cdot C_{12}H_4N_4$. Displacement

ellipsoids drawn at the 40% probability level. Grey, blue, and white spheres correspond to carbon, nitrogen, and hydrogen atoms, respectively.

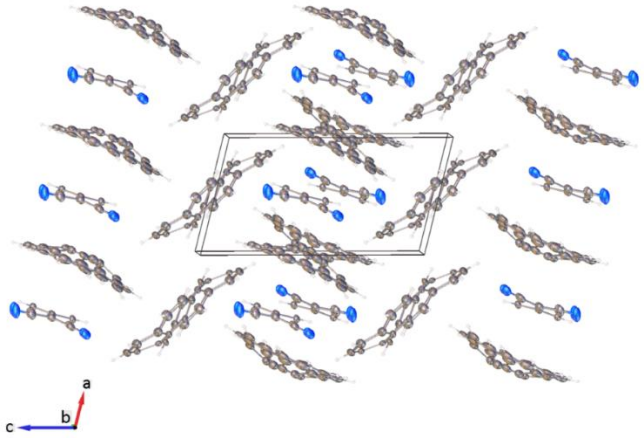

Figure 5.13. Packing of $(C_{20}H_{10})_2 \cdot C_{12}H_4N_4$ along the *c* axis. Grey, blue, and white spheres correspond to carbon, nitrogen, and hydrogen atoms, respectively.

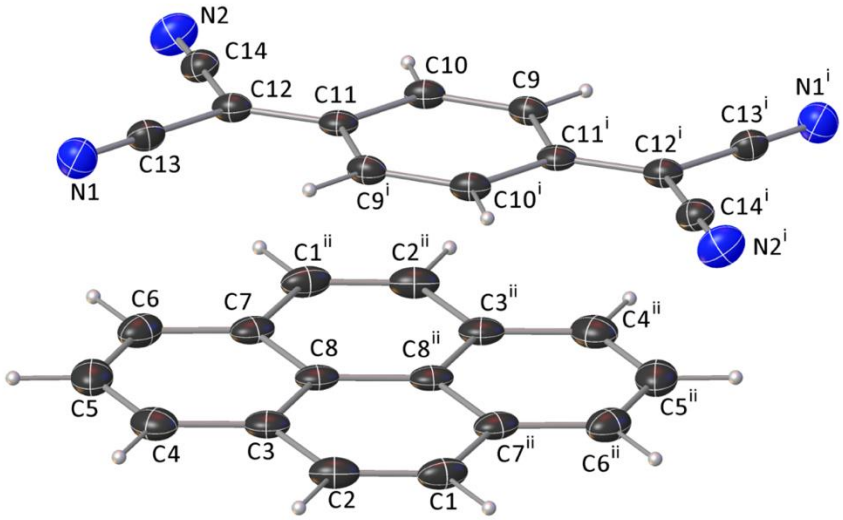

Figure 5.14. Crystal structure of $C_{16}H_{10} \cdot C_{12}H_4N_4$. Displacement ellipsoids drawn at the 50% probability level. Grey, blue, and white spheres correspond to carbon, nitrogen, and hydrogen atoms, respectively.

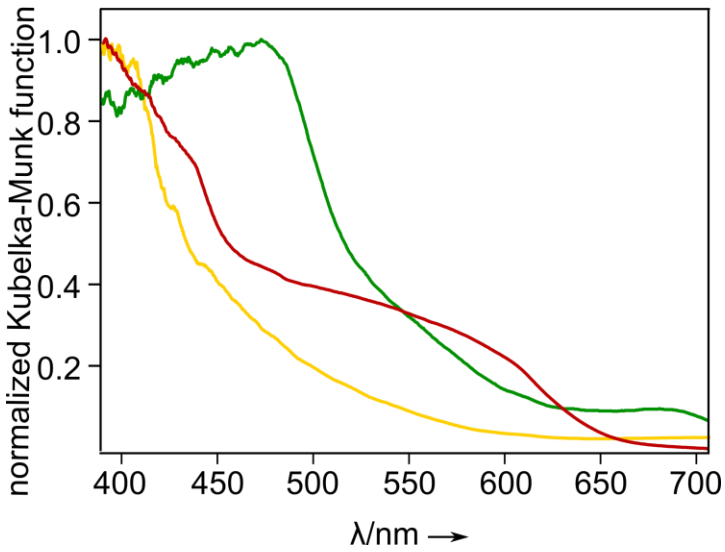

Figure 5.15. Normalized diffuse reflectance spectra of $C_{20}H_{10}$ (yellow), TCNQ (green), and **1** (red).

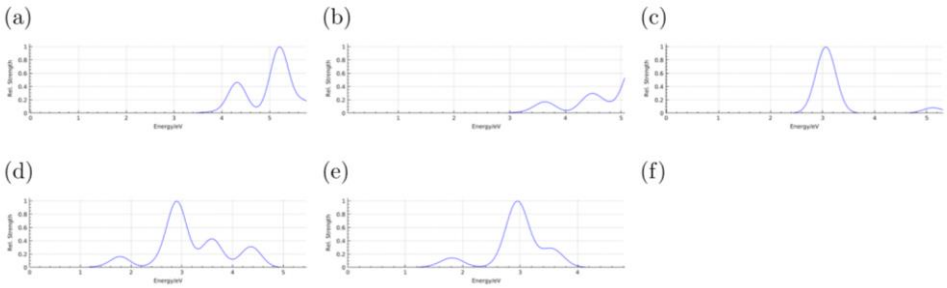

Figure 5.16. Optical transitions strength: (a) π-bowl; (b) $C_{20}H_{14}$; (c) TCNQ; (d) TCNQ-$C_{20}H_{14}$; (e) TCNQ-$C_{20}H_{14}$-TCNQ.

REFERENCES

1) J. Gao, F. J. Uribe-Romo, J. D. Saatho, H. Arslan, C. R. Crick, S. J. Hein, B. Itin, P. Clancy, W. R. Dichtel, Y. Loo, ACS Nano 2016, 10, 4847−4856.

2) M. K. Smith, K. E. Jensen, P. A. Pivak, K. A. Mirica, Chem. Mater. 2016, 28, 5264−5268.

3) M. Terrones, ACS Nano 2010, 4, 1775–1781.

4) O. V Boltalina, A. A. Popov, I. V Kuvychko, N. B. Shustova, S. H. Strauss, Chem. Rev. 2015, 115, 1051−1105.

5) M. A. Petrukhina, L. T. Scott, Eds. , Fragments of Fullerene and Carbon Nanotubes-Designed Synthesis, Unusual Reactions, and Coordination Chemistry, John Wiley And Sons, Inc., Hoboken, 2011.

6) A. Hirsch, The Chemistry of Fullerenes, John Wiley And Sons, Inc., 2008.

7) A. M. Rice, E. A. Dolgopolova, N. B. Shustova, Chem. Mater. 2017, 29, 7054–7061.

8) A. V Zabula, A. Y. Rogachev, M. A. Petrukhina, Science (80-.). 2011, 333, 1008–1011.

9) C. Dubceac, A. S. Filatov, A. V. Zabula, A. Y. Rogachev, M. A. Petrukhina, Chem. - A Eur. J. 2015, 21, 14268–14279.

10) Z. Zhou, S. N. Spisak, Q. Xu, A. Y. Rogachev, Z. Wei, M. Marcaccio, M. A. Petrukhina, Chem. - A Eur. J. 2018, 24, 3455–3463.

11) A. Béziau, S. A. Baudron, G. Rogez, M. W. Hosseini, Inorg. Chem. 2015, 54, 2032−2039.

12) I. Martin-Fernandez, D. Wang, Y. Zhang, Nano Lett. 2012, 12, 6175–6179.

13) A. Borchardt, A. Fuchicello, L. Jolla, K. V Kilway, K. K. Baldridge, J. S. Siegel, J. Am. Chem. Soc. 1992, 114, 1921–1924.

14) Z. Chen, J. A. M. Mercer, X. Zhu, J. A. H. Romaniuk, R. Pfattner, L. Cegelski, T. J. Martinez, N. Z. Burns, Y. Xia, Science (80-.). 2017, 479, 475–479.

15) Y. T. Wu, J. S. Siegel, Chem. Rev. 2006, 106, 4843–4867.

16) B. M. Schmidt, B. Topolinski, M. Yamada, S. Higashibayashi, M. Shionoya, H. Sakurai, D. Lentz, Chem. - A Eur. J. 2013, 19, 13872–13880.

17) L. T. Scott, E. A. Jackson, Q. Zhang, B. D. Steinberg, M. Bancu, B. Li, J. Am. Chem. Soc. 2012, 134, 107–110.

18) E. Nestoros, M. C. Stuparu, Chem. Commun. 2018, 54, 6503–6519.

19) S. Attar, D. M. Forkey, M. M. Olmstead, A. L. Balch, Chem. Commun. 1998, 1255–1256.

20) T. Hayama, Y. Wu, A. Linden, K. K. Baldridge, J. S. Siegel, J. Am. Chem. Soc. 2007, 129, 12612–12613.

21) S. Tashiro, M. Yamada, M. Shionoya, Angew. Chemie Int. Ed. 2015, 54, 5351–5354.

22) J. C. Hanson, C. E. Nordman, Acta Crystallogr. 1976, 32, 1147–1153.

23) R. J. Dillon, C. J. Bardeen, J. Phys. Chem. A 2012, 116, 5145−5150.

24) H. N. Ghosh, J. Phys. Chem. B 1999, 103, 10382–10387.

25) Y. Yoshida, K. Isomura, N. Yuto, H. Kishida, G. Saito, Chem. Lett. 2015, 44, 709–711.

26) M. Wang, C. Wölfer, L. Otrin, I. Ivanov, T. Vidaković-Koch, K. Sundmacher, Langmuir 2018, 34, 5435−5443.

27) F. P. Van Der Zee, F. J. Cervantes, Biotechnol. Adv. 2009, 27, 256–277.

28) M. D. Peterson, S. C. Jensen, D. J. Weinberg, E. A. Weiss, ACS Nano 2014, 8, 2826–2837.

29) L. Striepe, T. Baumgartner, Chem. Eur. J 2017, 23, 16924–16940.

30) M. A. Dobrowolski, A. Ciesielskiab, M. K. Cyranski, Phys. Chem. Chem. Phys. 2011, 13, 20557–20563.

31) M. A. Dobrowolski, G. Garbarino, M. Mezouar, A. Ciesielski, M. K. Cyrański, CrystEngComm 2014, 16, 415–429.

32) Y. Nagano, M. Nakano, J. Chem. Thermodyn. 2003, 35, 1403–1412.

33) R. D. Adams, J. Kiprotich, D. V Peryshkov, Y. Onn, Chem. Eur. J 2016, 22, 6501–6504.

34) R. D. Adams, E. J. Kiprotich, M. D. Smith, Chem. Commun. 2018, 54, 3464–3467.

35) R. D. Adams, J. Kiprotich, D. V Peryshkov, Y. O. Wong, Inorg. Chem. 2016, 55, 8207−8213.

36) J. M. Khurana, S. Singh, J. Indian Chem. Soc. 1996, 73, 487–488.

37) K. K. Park, C. H. Oh, W. K. Joung, Tetrahedron Lett. 1993, 34, 7445–7446.

38) A. M. Butterfield, B. Gilomen, J. S. Siegel, Org. Process Res. Dev. 2012, 16, 664–676.

APPENDIX A: COPYRIGHT PERMISSIONS

Chapter 1.

Chapter 2.

Chapter 3.

Chapter 4